PONTIFÍCIA UNIVERSIDADE CATÓLICA
DO RIO DE JANEIRO

Kaio César Borges Benedetti

Global analysis of stochastic nonlinear dynamical systems

an Adaptative phase-space discretization strategy

Tese de doutorado

Thesis presented to the Programa de Pós-Graduação em Engenharia Civil of PUC-Rio in partial fulfillment of the requirements for the degree of Doutor em Ciências – Engenharia Civil

Advisor: Prof. Paulo Batista Gonçalves
Co-supervisor: Prof. Stefano Lenci
Co-supervisor: Prof. Giuseppe Rega

Rio de Janeiro
August, 2022

PONTIFÍCIA UNIVERSIDADE CATÓLICA
DO RIO DE JANEIRO

Kaio César Borges Benedetti

Global analysis of stochastic nonlinear dynamical systems

an Adaptative phase-space discretization strategy

Thesis presented to the Programa de Pós-Graduação em Engenharia Civil of PUC-Rio in partial fulfillment of the requirements for the degree of Doutor em Ciências – Engenharia Civil. Approved by the Examination Committee

Prof. Paulo Batista Gonçalves
Advisor
Department of Civil and Environmental Engineering – PUC-Rio

Prof. Stefano Lenci
Co-supervisor
Università Politecnica delle Marche – Ancona

Prof. Giuseppe Rega
Co-supervisor
University of Rome

Profª. Deane de Mesquita Roehl
Department of Civil and Environmental Engineering – PUC-Rio

Prof. Ivan Fabio Mota de Menezes
Department of Mechanical Engineering – PUC-Rio

Prof. Carlos Eduardo Nigro Mazzilli
USP

Prof. Americo Barbosa da Cunha Junior
UERJ

Prof. Frederico Martins Alves da Silva
UFG

Rio de Janeiro, August 25th, 2022

Kaio César Borges Benedetti

Holds a Bachelor's degree in Civil Engineering from Universidade Federal de Goiás, in 2016, and obtained his M.Sc. degree in Civil Engineering from the same university in 2018. Worked as an assistant researcher at Tecgraf institute from 2018 to 2022, developing software for nonlinear analysis of structures and numerical simulation of seismic wave propagation. Granted the scholarship Faperj nota 10 – doutorado, from 2020 to 2022. Attended many conferences in the area of dynamics of structures and was awarded the Ali H. Nayfeh honors mention at the Second International Nonlinear Dynamics Conference in 2021 for his contribution in the nondeterministic effects over global dynamical structures.

Bibliographic data

Benedetti, Kaio César Borges

Global analysis of stochastic nonlinear dynamical systems : an adaptative phase-space discretization strategy / Kaio César Borges Benedetti ; advisor: Paulo Batista Gonçalves ; co-supervisors: Stefano Lenci, Giuseppe Rega. – 2022.
265 f. : il. color. ; 30 cm

Tese (doutorado)–Pontifícia Universidade Católica do Rio de Janeiro, Departamento de Engenharia Civil e Ambiental, 2022.
Inclui bibliografia

1. Engenharia Civil e Ambiental – Teses. 2. Dinâmica global não linear. 3. Método de Ulam. 4. Discretização adaptativa. 5. Incerteza de parâmetros e ruído. 6. Integridade dinâmica. I. Gonçalves, Paulo Batista. II. Lenci, Stefano. III. Rega, Giuseppe. IV. Pontifícia Universidade Católica do Rio de Janeiro. Departamento de Engenharia Civil e Ambiental. V. Título.

CDD: 624

To my sweet little star, my dear Laura,
whose smile always fills me with joy.

Acknowledgements

I hereby express my gratitude to my advisor, professor Paulo Gonçalves. Thank you for your support during my years at PUC-Rio. You always inspired and helped me dream of new ideas and possibilities. You allowed me to outbrave my constraints, which culminated in participation in many conferences and collaborations with other researchers, both in Brazil and abroad. I am eager to continue this fruitful work in the years to come.

I would like to thank professors Stefano Lenci and Giuseppe Rega, my co-advisors in this research. Through many discussions and exchange letters, you helped me lapidate my ideas, solidifying this contribution. I am looking forward to strengthening our relationship and developing the new scientific contributions that will come.

During my years at PUC-Rio, I got the opportunity to work with professor Deane Roehl in the Multiphysics Modeling and Simulation group at Tecgraf. This gave me a diverse experience in different fields of study, and the discussions with all my colleagues contributed significantly to my development. For that, I am truly grateful.

To all the professors of the department of Civil and Environmental Engineering in PUC-Rio, my gratitude.

To my professor Frederico Silva, who first gave me the opportunity, in my undergraduate days, to do science, always inspiring me with new and different possibilities.

To my friends Matheus Cavalcanti, Pedro Rassi, Natan Reis, Edson Amaral, Raphael Sales, Felipe Sales, Jessica Motta, Alexandre Amaral, Diana Mota, and Julio Brito, that, together with my brother Marco Benedetti, helped me pass through difficult times.

To my mom, Valéria de Oliveira, and my sister, Ana de Souza, for always supporting me and bringing joy when we meet.

To my dear wife, Fabiane Benedetti, who helped me during all stages of this research and gave me my most precious gift, my daughter Laura Benedetti.

I would also like to thank the presence of the Professors members of this thesis committee for their availability and careful reading of this study.

This study was financed in part by the Coordenação de Aperfeiçoamento de Pessoal de Nível Superior - Brasil (CAPES) - Finance Code 001, CNPq, FAPERJ, and PUC-Rio.

Abstract

Benedetti, Kaio César Borges; Gonçalves, Paulo Batista; Lenci, Stefano; Rega, Giuseppe. **Global analysis of stochastic nonlinear dynamical systems: an adaptative phase-space discretization strategy.** Rio de Janeiro, 2022, 265p. Doctoral thesis – Civil and Environmental Engineering Department, Pontifical Catholic University of Rio de Janeiro.

The aim of this thesis is to provide tools for the global analysis of nondeterministic dynamical systems with competing attractors considering parameter uncertainty and noise and apply them to real-world engineering problems. For this, an adaptative phase-space discretization strategy based on the classical Ulam method is proposed. Initially, a review of the mathematical definitions of dynamical systems, parametric uncertainty, and noise is presented, and the effect of randomness on the global dynamical structures is highlighted. Discretized transfer operators with the necessary modifications due to parameter uncertainty are derived. The stochastic basin of attraction and attractors' distributions replace the usual basin and attractor concept. For parameter uncertainty cases, the phase-space is augmented with the corresponding probability space, resulting in a collection of transfer operators for which mean results are obtained. Two adaptative phase-space discretization strategies are proposed, one which only considers the attractors' distribution and stochastic basins, and another that discretizes the stable and unstable manifolds. The first method is initially applied to the Helmholtz and Duffing oscillators under harmonic or parametric excitation with uncertain parameters or added load noise. They demonstrate the adaptive capabilities of the proposed methods, increasing the quality without overly increasing the computational cost. The time-dependency of stochastic responses is demonstrated, with long-transients influencing the global behavior. Finally, the effect of uncertainties and noise on the basins' areas, attractors distributions, and basin boundaries are discussed, which can be used to evaluate the dynamic integrity of the competing basins. Then, two electrically actuated Microelectromechanical Systems (MEMS), an imperfect microcantilever and microarch, are investigated. The effect of added noise and parametric uncertainty on both structures is demonstrated. The results highlight the importance of randomness on the global dynamics of dynamical systems with competing attractors.

Keywords

Global nonlinear dynamics; Ulam method; Adaptative discretization; Parameter uncertainty and noise; Dynamic integrity

Resumo

Benedetti, Kaio César Borges; Gonçalves, Paulo Batista; Lenci, Stefano; Rega, Giuseppe. **Análise global de sistemas dinâmicos estocásticos não lineares: uma estratégia adaptativa de discretização do espaço de fase.** Rio de Janeiro, 2022, 265p. Tese de Doutorado – Departamento de Engenharia Civil e Ambiental, Pontifícia Universidade Católica do Rio de Janeiro.

O objetivo desta tese é fornecer ferramentas para a análise global de sistemas dinâmicos não determinísticos com atratores coexiostentes considerando incerteza paramétrica ou ruído e aplicá-las a problemas de engenharia. Para isso, é proposta uma estratégia de discretização adaptativa no espaço de fase baseada no método clássico de Ulam. Inicialmente, apresenta-se uma revisão das definições matemáticas de sistemas dinâmicos, incerteza paramétrica e ruído, destacando-se o efeito da aleatoriedade nas estruturas dinâmicas globais. Operadores de transferência discretos são derivados com as modificações necessárias devido à incerteza dos parâmetros. Bacias de atração estocásticas e distribuição dos atratores substituem o conceito usual de bacia e atrator. Para casos de incerteza paramétrica, o espaço de fase é aumentado com o espaço de probabilidade correspondente, resultando em uma coleção de operadores de transferência dos quais médias são obtidas. São propostas duas estratégias de discretização adaptativa no espaço de fase, uma que considera apenas a distribuição dos atratores e bacias estocásticas, e outra que discretiza as variedades estáveis e instáveis. O primeiro método é aplicado inicialmente aos osciladores de Helmholtz e Duffing sob excitação harmônica ou paramétrica com parâmetros incertos ou ruído adicionado ao carregamento determinístico. Eles demonstram as capacidades adaptativas dos métodos propostos, aumentando a qualidade sem aumentar demasiadamente o custo computacional. A dependência do tempo das respostas estocásticas é demonstrada, com longos transientes influenciando o comportamento global. Por fim, discute-se o efeito das incertezas e ruídos nas áreas das bacias, distribuições de atratores e limites das bacias, que podem ser usados para avaliar a integridade dinâmica de sistemas com bacias coexistentes. Em seguida, dois Sistemas Micro-Eletro-Mecânicos (MEMS) atuados eletricamente, uma microviga em balanço e um microarco imperfeitos, são investigados. O efeito do ruído adicionado e da incerteza paramétrica em ambas as estruturas é demonstrado. Os resultados destacam a importância da aleatoriedade na dinâmica global de sistemas dinâmicos com atratores coexistentes.

Palavras-chave

Dinâmica global não linear; Método de Ulam; Discretização adaptativa; Incerteza de parâmetros e Ruído; Integridade dinâmica

Table of contents

List of figures

List of tables

List of symbols

Deterministic dynamical systems

$\mathbb{X}$	Abstract phase-space
$x \in \mathbb{X}$	Abstract point in phase-space
$\mathbb{T}$	General time-space
$t \in \mathbb{T}$	Time
φ	Dynamical system's flow law
$(\mathbb{X}, \mathbb{T}, \varphi_t)$	Dynamical system tuple definition, with a phase-space $\mathbb{X}$, a time-space $\mathbb{T}$, and a flow law φ
$\circ$	Composition operator
$\mathfrak{B}(\cdot)$	Borel σ-algebra of a space $(\cdot)$
$\mathrm{id}_{\mathbb{X}}$	Identity operator over $\mathbb{X}$
$f(x,t)$	Continuous or discontinuous vector field
$\partial_t \varphi_s x$	Flow law time-derivative
$\mathbb{N}, \mathbb{Z}, \mathbb{R}$	Number sets (natural, integer, real)

Probability

$\mathbb{L}$	Abstract sample space
$\lambda \in \mathbb{L}$	Elements of the sample space $\mathbb{L}$
$\mathfrak{S}$	General σ-algebra of $\mathbb{L}$
$A \in \mathfrak{S}$	Elements of the σ-algebra $\mathfrak{S}(\mathbb{L})$
$\mathbb{P}_\lambda$	Probability measure on $\mathfrak{S}(\mathbb{L})$
$d\mathbb{P}_\lambda$	Probability density function of parameter λ
$(\mathbb{L}, \mathfrak{S}, \mathbb{P}_\lambda)$	Probability tuple, with a sample space $\mathbb{L}$, a σ-algebra $\mathfrak{S}(\mathbb{L})$, and a probability measure $\mathbb{P}_\lambda$
$2^{\mathbb{L}}$	Power set of $\mathbb{L}$

Nondeterministic dynamical system

$(\mathbb{L},\mathfrak{S},\mathbb{P}_\lambda,\mathbb{X},\mathbb{T},\varphi_t)$	General dynamical system with uncertain parameter $\lambda\in(\mathbb{L},\mathfrak{S},\mathbb{P}_\lambda)$
$\varphi_t(\lambda)$	Flow law of a parametric uncertain dynamical system
Ω	Abstract noise space
$\mathfrak{F}$	Countably generated σ-algebra of Ω
$\mathbb{P}_\omega$	Probability measure on $\mathfrak{F}(\Omega)$
$(\Omega,\mathfrak{F},\mathbb{P}_\omega)$	Countably generated probability space, applicable for noise systems
$(\Omega,\mathfrak{F},\mathbb{P}_\omega,\mathbb{T},\theta_t)$	Metric dynamical system over the probability space $(\Omega,\mathfrak{F},\mathbb{P}_\omega)$; model for the noise
$\theta_t\omega$	Flow law of a metric dynamical system
$(\mathbb{X},\mathfrak{B},\mathbb{T},\varphi_t)$	Random dynamical system
$\varphi_t(\omega)$	Random dynamical system's flow law, defined as a cocycle over $\theta_t\omega$
$f(\theta_t\omega,x,t)$	Continuous or discontinuous noise-driven vector field
$\varphi_t(\lambda,\omega)x$	General dynamical system with random parameter λ and noise ω

Invariant structures and global perspective of DS

A	Attractor
g_A	Basin of attraction of A
$\mathcal{P}_t$	Perron-Frobenius operator
$\mathcal{P}_t(\lambda)$	Parameter-dependent Perron-Frobenius operator
$L^1(\mathbb{X})$	Space of distributions over $\mathbb{X}$
$f_A\in L^1(\mathbb{X})$	Distribution of attractor A
δ_C	Dirac delta distribution over C
$\mathcal{K}_t$	Koopman operator
$\mathcal{K}_t(\lambda)$	Parameter-dependent Koopman operator
$L^\infty(\mathbb{X})$	Space of observables
$g_A(\varepsilon)\in L^\infty(\mathbb{X})$	General stochastic basin of attraction of attractor A for a time-horizon $1/\varepsilon$
$\mathcal{F}_t$	Foias operator

Operator discretization

$\mathbb{B}_i$	Phase-space disjoint partition at depth level i
$\mathbb{S}_i$	Phase-space partition subset at depth level i
$\Delta_h \subset L^1(\mathbb{X})$	Discrete subspace spammed by unitary distributions over all $b_i \in \mathbb{B}$, with characteristic length h
$Q_h : L^1(\mathbb{X}) \to \Delta_h$	Projection operator from continuous function space $L^1(\mathbb{X})$ to the discretized space Δ_h
f_h	Discretized distribution over Δ_h
P_h	Discretized Perron-Frobenius operator over Δ_h
F_h	Discretized Foias operator over Δ_h
K_h	Discretized Koopman operator over Δ_h
p_{ij}	Transfer operator matrix *ij*-entry
c_f	Heuristic minimum distribution constraint
$c_g^{(1,2)}$	Heuristic minimum (1) and maximum (2) basin values
Λ	Discrete probability space
P_Λ	Discrete probability measure
$\bar{\mathcal{P}}_t$	Markov open flow operator with $\mathrm{fix}(\bar{\mathcal{P}}_t) = \varnothing$
$\bar{\mathcal{K}}_t$	Dual Markov open flow operator with $\mathrm{fix}(\bar{\mathcal{K}}_t) = \varnothing$
$\bar{P}_h$	Discretized open flow Markov operator over Δ_h
c_x	Minimal ratio of distribution's support and phase-space window
c_p	Minimum quasidistribution constraint

Archetypal oscillators

x	Mechanical system degree of freedom
t	Time variable
δ	Damping term
α	Linear stiffness
β	Nonlinear stiffness
A	Amplitude of excitation
Ω	Frequency of excitation
λ	Truncated standard normal distribution random variable
σ	Random stiffness scaling factor
$\dot{W}$	Standard white noise process

s	Noise standard deviation

Microbeams

d	Actuation plate distance
L	Beam length
b	Beam width
h	Beam thickness
ε	Free space permittivity
V_{dc}	Direct current voltage
V_{ac}	Alternating current voltage
A	Alternating current voltage amplitude
Ω	Alternating current voltage frequency
P	Axial load
u_B	Initial axial displacement
F_i	i^{th} natural mode of vibration
ω	Natural vibration frequency
C_i	i^{th} normalization constant
w_i	Modal displacement
w_0, w_s, w_d	Initial, static and dynamic displacement components
y_0	Central microarch initial displacement
ξ	Critical damping ratio
σ	Stochastic amplitude of excitation
$[a, b]$	Critical damping ratio value interval

General beam problem

(X, Y, Z)	Reference system
$\{i_X, i_Y, i_Z\}$	Reference system unit vectors
(ξ, η, ζ)	Deformed configuration
$\{i_\xi, i_\eta, i_\zeta\}$	Deformed configuration unit vectors
(ξ_0, η_0, ζ_0)	Undeformed, stress-free configuration
$\{i_{\xi 0}, i_{\eta 0}, i_{\zeta 0}\}$	Undeformed configuration unit vectors
s	Undeformed arc-length
$\tilde{s}$	Deformed arc-length
ψ, θ, ϕ	Euler rotations from the undeformed to the deformed frame
ψ_0, θ_0, ϕ_0	Euler rotations from the reference system to the undeformed frame

$\bar{\psi}, \bar{\theta}, \bar{\phi}$	Euler total rotations, from the reference system to the undeformed frame
$[T_0]$	Rotation matrix from the reference system to the undeformed frame
$[T]$	Rotation matrix from the reference system to the deformed configuration
$\kappa_{\xi_0}, \kappa_{\eta_0}, \kappa_{\zeta_0}$	Curvatures of the undeformed configuration
$\bar{\kappa}_\xi, \bar{\kappa}_\eta, \bar{\kappa}_\zeta$	Curvatures of the deformed configuration
$\omega_\xi, \omega_\eta, \omega_\zeta$	Angular velocities of the deformed configuration
u, v, w	Axial and transversal displacements from the undeformed to the deformed configuration
v_0, w_0	Initial transversal displacements, from the reference to the undeformed configuration
$\bar{v}, \bar{w}$	Total transversal displacements, from the reference system to the deformed configuration
Δ_e	Axial elongation
ε	Small strain tensor
σ	Cauchy stress tensor
$\mathbf{C}$	Fourth-order elastic constitutive tensor
m	Linearly distributed mass
J_ξ, J_η, J_ζ	Linearly distributed rotational inertias
ρ	Density
A	Cross-sectional area
$D_u, D_\xi, D_\eta, D_\zeta$	Stiffness constants
$\mu_{1,2}$	Lamé parameters
λ	Lagrange multiplier for $\Delta_e \approx 0$; axial energy term $-2D_u\Delta_e$
T	Kinetic energy
U	Potential strain energy
$\mathcal{L}, \ell$	Lagrangian integral and kernel
$\mathcal{H}$	Hamiltonian
W_{nc}	Nonconservative energy terms
$Q_u^{nc}, Q_v^{nc}, Q_w^{nc}, Q_\phi^{nc}$	Nonconservative forces
Q_u, Q_v, Q_w, Q_ϕ	External forces
c_u, c_v, c_w, c_ϕ	Viscous damping

1
Introduction

In recent decades nonlinear phenomena have become increasingly relevant in engineering design due to the increasing demand for high-performance engineering structures and devices. In addition, for nonlinear engineering problems, nondeterministic aspects have become increasingly important due to the sensitivity of nonlinear systems to parameter values, noise, and mathematical modeling hypotheses, among others. Small changes and variations can lead to unpredicted outcomes in a nonlinear problem, impacting the system's performance and safety. This is particularly important in the analysis of time-varying nonlinear engineering problems.

The global dynamic analysis gives an understanding of the underlying nonlinear dynamics of complex engineering systems, showing how stable solutions are limited by other possible coexisting solutions. However, this type of analysis is nowadays impractical for large-scale systems due to the computational cost, being limited to reduced order models with a small number of degrees of freedom.

The uncertainty quantification of engineering problems is a thriving research area, with contributions from many researchers to different aspects of the problem. Uncertainty analysis is known to be computationally demanding, increasing the model dimensionality in a global dynamic analysis. This hinders the applicability of this type of analysis, leaving the adoption of safety factors and lower bound estimates of design loads as the default engineering practice in the design process. Robust analyses that consider both global nonlinear dynamics and nondeterministic effects are rarely found in the literature, needing both theoretical and numerical developments to become feasible from a design point of view. There are plenty of examples that would benefit from such an analysis, such as the case of microstructures.

In the next sections, a review of the literature related to this line of research is presented.

1.1. The nondeterminism in engineering dynamic analysis

The nondeterministic design needs to account for aleatoric uncertainties, such as variability in material properties, and epistemic uncertainties, including errors due to imperfect analysis tools [1]. In real-life applications, both uncertainties are indistinguishable, and their added effect must be considered for a safe design. Generally, the mathematical model of a physical problem can be concisely written as

$$\mathcal{N}_{\lambda,\omega}\{u\} = f_{\lambda,\omega} \tag{1.1}$$

where u is the dependent variables, f is the non-homogeneous terms, and $\mathcal{N}$ is a (differential) operator. Uncertainty is a lack of knowledge in $\mathcal{N}$ or f, represented here through random parameters λ or noise terms ω. Examples of other uncertainty types are: structural, that is, related to the underlying physics of the problem; algorithmic, coming from numerical errors and approximations in the computer model; and experimental, arising from measurement variability or interpolation errors.

In the context of structural engineering, the need to include parameter uncertainties and noise in dynamic analyses has long been recognized [2, 3]. Many systems are highly sensitive to small variations in their material/geometrical properties, such as damping parameters or material constants, imperfections, boundary and initial conditions, and natural frequencies [2–5]. Koiter's work in the field of structural stability, for example, has shown the drastic influence of unknown geometric imperfections on the load capacity of many engineering structures [6, 7]. Since then, imperfection sensitivity analysis has become an important topic in structural stability analysis [8]. The added influence of uncertainties has also been addressed [9]. Such sensitivities are particularly relevant in nonlinear dynamics. Gonçalves and Santee [10] have shown that different types of uncertainties, including geometric imperfections, can cause a decrease in the load-carrying capacity of structures liable to buckling under dynamic excitation, similar to that observed in the static case.

In addition, deterioration or evolution of the structure during its lifetime leads to increasing uncertainties which can affect its dynamic behavior. In structural dynamics, parameters such as the natural frequencies or damping are subject to uncertainty. This uncertainty may stem from a lack of knowledge of the parameter values and a lack of understanding of the behavior of the actual system. The problem can be stated in a probabilistic framework to account for the uncertainty in system parameters, leading to differential equations whose coefficients are modeled as random variables.

Various techniques have been developed for the analysis of uncertainties in structural problems. For an overview of classical methodologies, such as Monte Carlo sampling, perturbation, moment equations, operator of the governing equations, generalized polynomial chaos (GPC), stochastic Galerkin, and collocation, refer to Xiu [11]. Long-time integration, a common analysis in nonlinear dynamics, suffers from accuracy loss if usual expansions of the random space are employed. More recent developments were devoted to mitigating this limitation and included the time-dependent GPC methodology presented by Gerritsma et al. [12], the stochastic time-warping polynomial chaos, and nonlinear autoregressive polynomial chaos proposed by Mai [13], and GPC with flow composition proposed by Luchtenburg et al. [14].

The study of time-dependent uncertainty is also important for structural dynamics, representing noisy loads and parametric excitations. Various sampling-based methods have been developed where the governing systems are reformulated as stochastic differential equations. Arnold [15] presents the mathematical foundation of the theory of random dynamical systems, stochastic bifurcations, and their multiplicative ergodic theory. Han and Kloeden [16] discuss the numerical simulation and analysis of random ordinary differential equations. These works point out that noisy excitation represents a major difficulty in the uncertainty analysis, requiring the analyst to ponder the meaning of the results, either numeric or analytic.

Overall, uncertainty considerations translate into analyzing responses distributed in probability space, that is, a macro view of all the possible outcomes of a given physical problem. Depending on the dynamical system, such distributions could evolve with time, and fixed-point distributions can change due to uncertainty. Fortunately, such evolutions are also dynamical systems governed by a transfer operator [17]. Such operators are Markov type and thus linear, positive, and mass conserving. Ulam [18] hypothesized that transfer operators could be discretized and distributions approximated by histograms, defining what today is known as the Ulam method. Later, Hsu [19, 20] developed the generalized cell-mapping in an algorithmic perspective, which was proven to be equivalent to the Ulam method by Guder and Kreuzer [21].

Several advances followed the cell-mapping theory developed by Hsu [19, 20]. Hsu and Chiu combined the generalized cell-mapping with a previously developed simpler version, called simple cell-mapping, denominated hybrid cell-mapping [22, 23]. There is already a separation between stochastic and parametric uncertainties in these works, with specific methodologies to deal with them focused on global dynamics. However, a proper probabilistic framework is missing. Later, Sun and Hsu [24] developed a short-time Gaussian approximation for nonlinear random vibration analysis. Han and coworkers explored this strategy extensively, considering nonautonomous cases [25] under colored noise [26], stochastic bifurcations in a turbulent swirling flow [27], and a combination with digraph algorithms [28]. The simple and generalized cell-mapping was recently reformulated by Yue et al. [29], the so-called compatible cell-mapping method. This method employs adaptative refinement of the phase-space, increasing the resolution of global attractors of random dynamical systems. In [30], Yue et al. demonstrated that this method refines stable and unstable manifolds similar to the subdivision and selection method developed by Dellnitz and coworkers [31–33], but with digraph algorithms instead. Another cell-mapping method is found in [34–36], designed with two distinct scales of cell spaces. The similarities between the transfer probability distributions obtained by Yue et al. [36] and the generalized committor functions defined by Linder and Hellmann [37] are evident. However, the latter is adequate for transient analysis, describing how transfer probabilities evolve with time. Finally, the phase-space dimension of engineering problems demands high-performance computing (HPC), as described by Andonovski [38] and Belardinelli and Lenci [39, 40]. Parallel computing strategies are fundamental, employing even general-purpose graphic cards (GPU) to this end [41].

The Ulam method was the focus of various works. Klus et al. [42] compared different numerical approximations of the Perron-Frobenius operator and its dual, the Koopman operator. Dellnitz and coworkers [31–33] developed a subdivision strategy with box-covering to approximate complicated numerical behavior, implemented in the software package GAIO [43]. Further developments include the detection of transport barriers [44], the analysis of dynamical systems with parameter uncertainty [45], invariant sets of infinite-dimensional dynamical systems [46, 47], and a set-oriented path-following method for computation of parameter-dependent attractors [48]. Koltai and coworkers developed methods for global analysis without trajectory integration focused on basins of attraction [49, 50] and nonautonomous systems [51]. A comparison of data-driven model reductions for dynamical systems based on the approximation of the transfer operators is given by Klus et al. [52]. Independently, Ding and coworkers investigated the original Ulam method and approximations of the Perron-Frobenius operator by piecewise linear and quadratic functions [53] and higher-order approximations in [54]. Recently, Jin and Ding [55] and Bangura et al. [56] applied spline and least-squares approximation for random maps. Specifically, they considered the Foias operator, which governs the mean flow of random maps [17].

1.2. Global dynamics and dynamical integrity considering uncertainty and noise

The concept of elastic stability in statics began with the work of Euler on the critical buckling load of columns [57]. However, he left the concept of stability undefined. Later, Lagrange stated that a stable equilibrium point of a conservative system corresponds to a minimum of the total potential energy. The Lagrange theorem implicitly implies the local stability concept in the sense of Lyapunov. Still, only at the beginning of the twentieth century were the mathematical definitions of stability for a dynamical system, as well as stability theorems for nonlinear systems, first formulated by Lyapunov [58, 59]. According to the Lyapunov stability concept, dynamical systems are said to be stable if small infinitesimal perturbations of the initial conditions lead to small deviations of the response, i.e., they cannot alter the system's time-asymptotic behavior [58]. While in this classical definition of stability, perturbations are infinitesimal, in the real world, as observed by Thompson and co-workers [60–62], perturbations have finite magnitudes. Thus, the system should be able to withstand finite, although small, changes in the initial conditions, returning asymptotically to the desired state. Consequently, beyond questions of local stability, a central role in the study of instability phenomena is played by the global features of phase-space, such as basins of attraction.

Additionally, nonlinear dynamical systems usually display multistability due to local or global bifurcations or the presence of multiple potential wells. This is characterized by the occurrence of multiple attractors in the phase-space, each with its own set of converging initial conditions, denominated basin of attraction [63–65]. The basin topology can vary remarkably as a function of systems' parameters, with their boundaries being smooth or fractal, depending on the stable and unstable invariant manifolds of the saddles lying on it [66]. Furthermore, the complexity of the interwoven basins of attraction increases with the number of coexisting solutions. In such cases, responses become extremely sensitive to any perturbation, with the final state depending crucially on the initial conditions. As an example, the basins of attraction of the coexisting solutions of an axially loaded cylindrical shell are depicted in Figure 1.1, for two different load parameters, see [65]. This is a complex structure with a prebuckling potential well and two additional pos-critical potential wells, with intense competition in phase-space. Although the prebuckling well is the dominant one [65], the basins of the coexisting solutions within this well (black, violet and blue) are swiftly eroded, and fractality increases, as shown in Figure 1.1(a), due to the incursion and increasing competition of the basins of the out-of-well solutions, as observed in Figure 1.1(b). This explains the high imperfection sensitivity of axially loaded cylindrical shells, which leads to a loss of their load carrying capacity even in the static case [7].

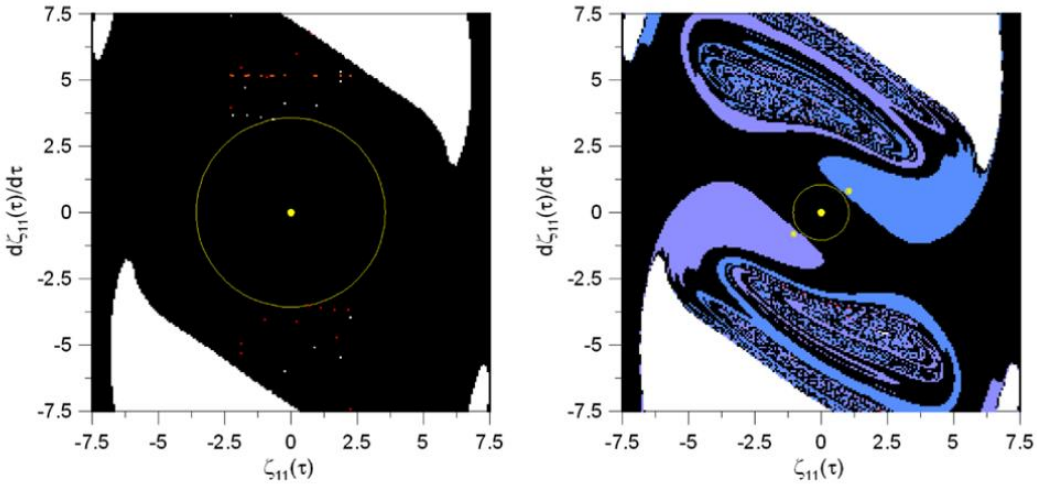

(a) In-well pre-buckling attractors and basins

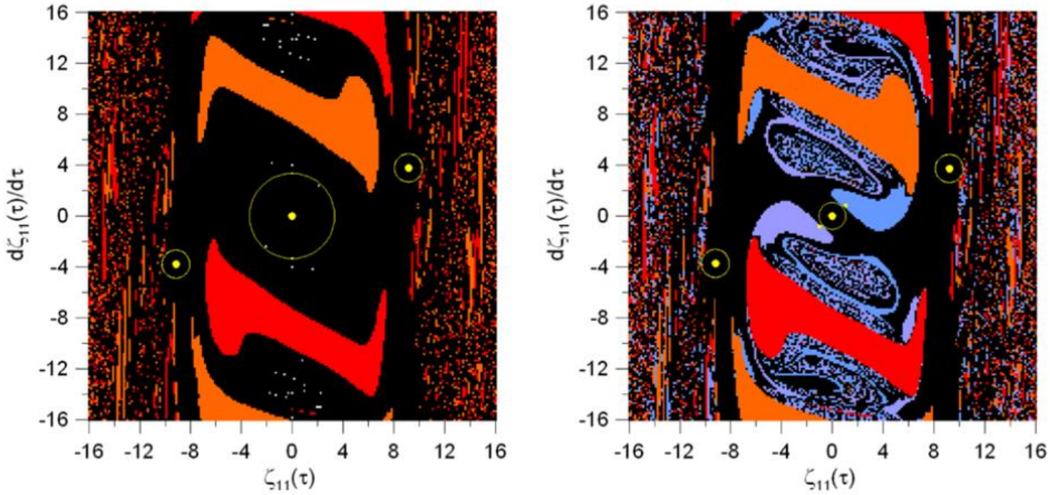

(b) Enlarged view containing out-of-well attractors

Figure 1.1 – Example of the complex basin topology of the competing oscillatory solutions of an axially loaded cylindrical shell [65]

Due to many nonlinear phenomena, compact basin regions can decrease, become fractal or disappear from the phase-space. This loss of basin robustness is identified as a loss of dynamic integrity of the respective attractor [60]. This is an important concept because attractors can only be observable if they are resilient to finite perturbations, that is, if their basins are robust enough and, therefore, they have an acceptable integrity value. If a basin is not robust enough, small unavoidable perturbations may lead the system to converge to another (sometimes undesirable) attractor or even escape to infinity. As an example, Figure 1.2 compares the theoretical and experimental escape boundaries for an electrically actuated capacitive accelerometer studied by Lenci, Rega, and Ruzziconi [67]. The discrepancy between the theoretical and experimental escape boundaries is explained by the swift erosion of the orange and green basins, as observed by comparing the basins of points Q and P. This issue can be correctly addressed by integrity profiles which measure the basins erosion process as a function of a relevant design parameter. As exemplified here, unless an attractor has a robust, compact basin, it will not be physically observable, and the adopted design parameters must take this into account.

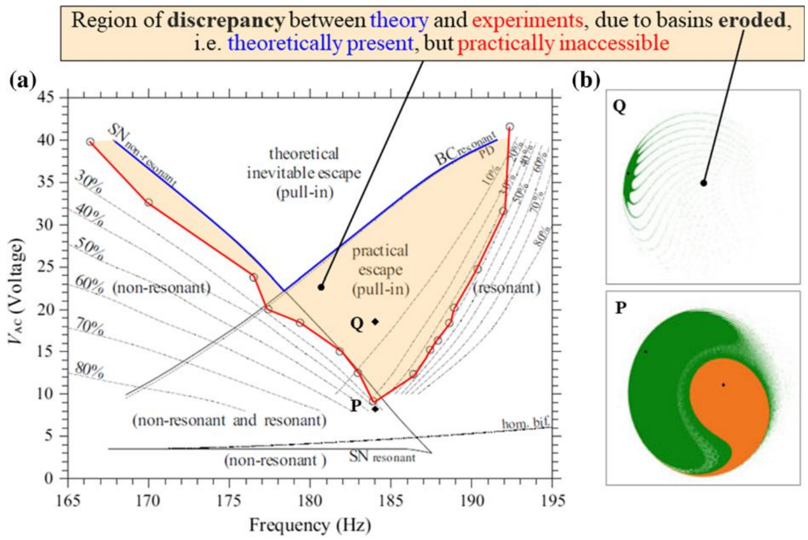

Figure 1.2 – Response of an electrically actuated capacitive accelerometer. (a) Stability chart with theoretical (in blue), experimental (in red) escape boundaries, and integrity contour lines (dashed). (b) Basins of attraction at points P and Q [68]

Thompson and co-workers introduced the concept of dynamical integrity based on the systematic study of the topology and evolution of basins of attraction as a function of system parameters quantified by different integrity measures [60, 61, 69]. In particular, they explored the erosion of basins of attraction due to fractal intrusions [70, 71]. Later, Rega and Lenci proposed the use of integrity measures as a tool to evaluate the actual safety of engineering systems in a dynamic environment. They developed and explored various integrity measures for safety quantification and applied these ideas to several mechanical systems [65, 67, 72–75]. They also have shown how global control strategies [63, 64, 76] can be used to prevent the basin erosion phenomenon. Figure 1.3 is a depiction of the three main integrity measures in the literature, which are the *Global Integrity Measure* (GIM), the *Local Integrity Measure* (LIM), and the *Integrity Factor* (IF). The GIM is the hypervolume (area in $\mathbb{R}^2$); the LIM is the minimum attractor-basin boundary distance; the IF is the radius of the maximum inscribed hypersphere (circle in $\mathbb{R}^2$) in the basin [77].

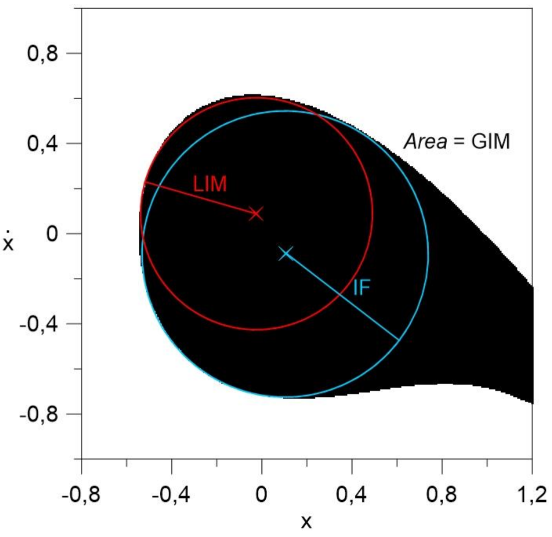

Figure 1.3 – Illustration of the three main integrity measures, the Global Integrity Measure (GIM), the Local Integrity Measure (LIM), and the Integrity Factor (IF)

The variation of an attractor's dynamic integrity measure against a relevant design parameter can be observed through integrity profiles [78]. Figure 1.4 gives a typical integrity profile up to the critical load of an attractor as a function of a chosen governing parameter. The Lyapunov local stability criterion states that the system is stable up to the bifurcation point. However, as shown in Figure 1.2 and Figure 1.4, it is not able to detect the erosion process. The integrity profile depicts an initial plateau corresponding to the uneroded basin, followed by a rapid integrity loss due to basin erosion. The rapid integrity loss has been usually termed a Dover cliff profile [79], an important phenomenon prior to the attractor loss of stability, which, for practical purposes, serves to indicate the unsafe region.

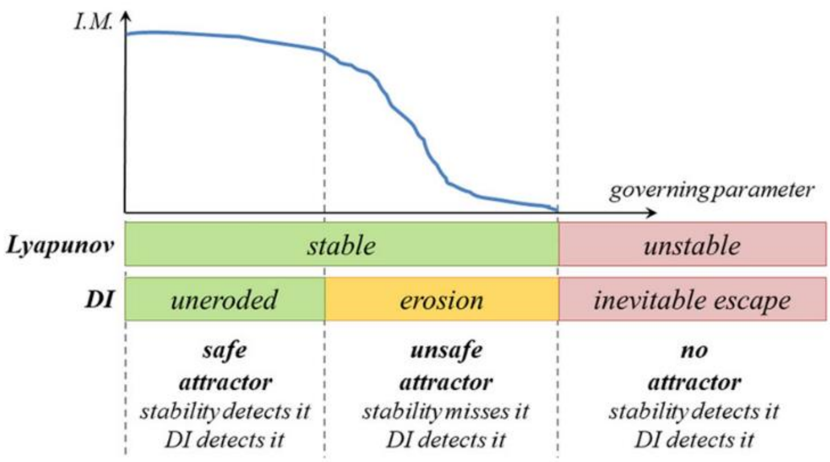

Figure 1.4 – Classic integrity profile demonstrating the difference between Lyapunov stability concept and integrity loss of an attractor as a function of a governing parameter [78]

Dynamical integrity measure is not a simple quantity to obtain. Its practical implementation is far from trivial since no direct connection exists between the coexisting asymptotic states and their basins of attraction [72, 73, 80]. However, despite the growing difficulties in terms of numerical costs of the simulations as the number of dof increases, changing the paradigm from local to global dynamics leads to a deeper knowledge of system safety, as discussed in the lectures published in [78]. In this context, the derivation of low but reliable reduced order models (ROMs) becomes increasingly important [81–83].

In recent years, a growing number of applications have relied on multistable systems capable of assuming different equilibrium configurations without damage [84]. Detailed reviews of this topic and applications were recently published by Hu and Burgueño [85], Cao et al. [86], and Fang et al. [87], with applications including actuators, energy harvesters, composite structures, microelectromechanical systems (MEMS), robotics, energy absorbers, deployable structures, and programmable metamaterials. This enhances the importance of global dynamics in engineering analysis. Another growing research area where global dynamics can become an essential tool is the analysis of metastable systems found in physics, chemistry, biology, etc. Metastability is defined as the phenomenon where a system, under the influence of stochastic dynamics, explores its state space on different time scales [88, 89].

However, not only finite perturbations in initial conditions should be considered. Dynamical systems are inevitably influenced by unavoidable noise and uncertainties, which complicates the already complex deterministic dynamics of multistable nonlinear systems by introducing new dynamical behavior and a number of stochastic phenomena [90]. These phenomena are not accounted for in the set of differential equations that models the idealized deterministic system. Noise is also intrinsic to observations made on real systems, as illustrated by the vast literature on system identification [91–94]. Poon and Grebogi [95] showed that noise might move the system away from the neighborhood of the attractor towards the basin boundary and over a nearby saddle point to another basin of attraction, increasing the competition between the attractors. Noise may also cause the basins to merge or disappear [96], and when the noise amplitude is above a critical value, the distinction between two coexisting attractors is lost. In addition, noise may lead to stochastic bifurcations and a shift of the bifurcation point [97, 98]. The global stability of a state in the presence of noise depends on both the size of the basin of attraction and the dynamical behavior. Soliman and Thompson [99] showed that the addition of noise could affect the robustness of attractors, and stochastic integrity measures could assess the sensitivity of an attractor to noise-induced jumping. However, when multiple steady states coexist in a system, little is known about what governs the stability of each state under the effects of random perturbations. Parameter and model uncertainties, especially in the vicinity of bifurcation points, are also of importance [2–5].

Many authors explored the effects of noise excitations. The bifurcation scenarios of the noisy Duffing-van der Pol oscillator were studied by, among others, Schenk-Hoppé [100] and Sharma [101]. Later, the global analysis of the stochastic bifurcations in Duffing, previously considered by Ueda, and Duffing–Van der Pol oscillators, were studied by the generalized cell mapping method by Xu et al. [102–104] and He et al. [105]. Basins were considered in the same sense as in deterministic problems through the generalized cell mapping (GCM) with partially ordered sets (posets) and directed graphs (digraphs) [106]. The impact of randomness on the basin boundaries is evident, showing how it diffuses as noise increases, eventually destroying the attractor. Although the results clarify the influence of noise on the attractor and basin evolution and possible bifurcations, the adopted basin definition lacks a proper stochastic description. Green et al. [107] studied the effect of white noise on an energy harvester described by Duffing-type nonlinearities, using the Fokker–Planck–Kolmogorov equation. However, the mono-stable system had just one global attractor, thus basin analysis was not needed. Local investigations of a softening-type Duffing oscillator with noise were conducted by Agarwal et al. [108]. Recently, the short-time Gaussian GCM approximation [24] was applied to the global analysis of a Duffing oscillator by Han et al. [28], but the deterministic definition of basins of attraction was maintained and, therefore, the results lack further quantification of the basin randomness. The path-integral methodology was applied to Duffing-type oscillators with noise by Cui et al. [109], Agarwal et al. [110], and Cilenti and Balachandran [111], but they also maintained the same deterministic interpretation for basins of attraction. Noise effects on the dynamic integrity were investigated in a Helmholtz-Duffing oscillator by Orlando et al. [112], and Helmholtz-type oscillator by Silva and Gonçalves [113], where also the parametric uncertainty was considered. Sets sensitive to random noise were considered in the evaluation of safe basins and their dynamic integrity analysis as depicted in white in Figure 1.5, where a system with three coexisting attractors (black, blue and red basins) is investigated. Again, the results demonstrated the effect of randomness on the basin of attraction qualitatively, but the proper description is still an open issue. Stochastic perturbation methods can be applied to formulate the statistics' governing equations in the case of parameter uncertainty, but restricted to local dynamics, as shown by Kamiński and Corigliano [114].

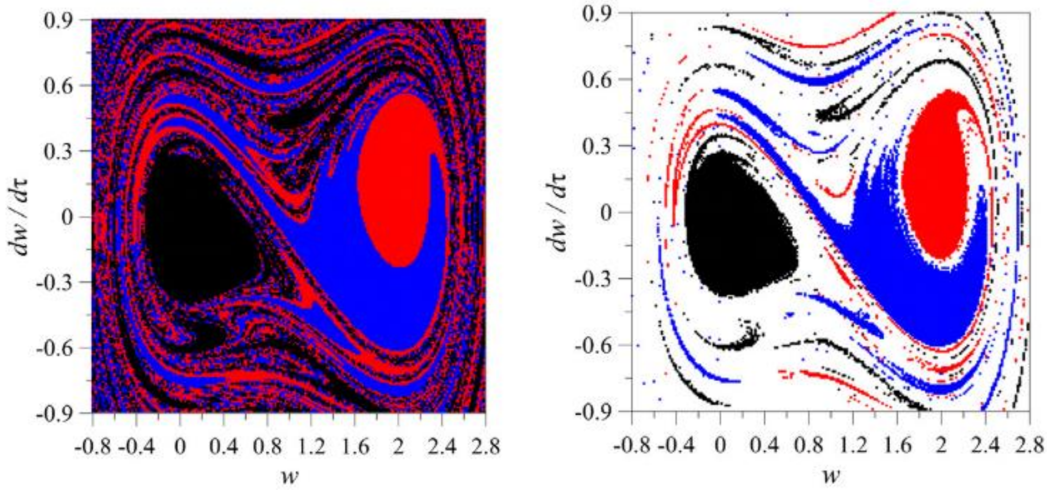

(a) Noise-free case (b) Noise-excited case

Figure 1.5 – Three coexisting basins of attraction of a dynamical system under harmonic load for (a) noise-free and (b) noise-excited cases, with sensitive initial conditions marked in white [112].

1.3. Parametric uncertainty and noise in microstructures

As an interesting example presenting diverse physical phenomena and applied in various fields, microelectromechanical systems (MEMS) are important devices with a broad range of applications [115–117]. Their theoretical analysis is diverse, with contributions from different fields, such as structural mechanics, electrostatics and electrodynamics, electromagnetism, piezoelectricity, electrothermal effects, and optics, to name a few. Also, these systems are rather flexible and can undergo large displacements due to their small scale in the presence of electrostatic and electrodynamic loads. Therefore, MEMS requires complex multidisciplinary analysis to correctly capture all the physical phenomena involved. For this purpose, various techniques are employed, for example, finite element and boundary element methods [115, 118, 119], shooting method [120], reduced-order models [121–124], and perturbation methods [125–127]. Notably, the multiple time scales method combined with a Galerkin procedure is a powerful strategy in order to obtain theoretical internal resonances, which have been validated by experimental results [127]. Numerical techniques have also been applied in the study of microbeams, such as pseudo-arclength continuation method with nonlocal constitutive relations [128–130]. These models are validated by comparing their results with experimental results and finite-element solutions available in the literature.

Younis and Nayfeh [125], Abdel-Rahman et al. [131], and Younis et al. [132] studied through an analytical approach and a reduced-order model (macromodel) the behavior of electrically actuated microbeam-based MEMS, with emphasis on their nonlinear resonant behavior. They modeled the beam as a partial integro-differential equation. Only nonlinearities due to midplane stretching and electrostatic load were considered, with displacements assumed to be small [133]. It is evident from the equation of motion that electrostatic loads result in strong nonlinearities with singularities. The analysis is carried out by dividing the actuation into a static part, due to the direct current voltage V_{dc}, and a dynamic part, due to an alternating current voltage V_{ac}. The static problem is solved numerically by the shooting method, and pull-in voltages are obtained under varying axial force. Natural frequencies are also obtained, and they exhibited a good agreement with experimental results even near the pull-in voltage. Forced vibration and various internal resonance conditions were addressed by the multiple scales method [125]. In [125, 131], the dynamic problem is considered using Taylor-series expansion superimposed on the static solution. However, they fail to represent the electric force at voltages close to pull-in since the neglected terms in the Taylor-series expansion become significant. Younis et al. [131, 132] then proposed an alternative approach capable of describing the strong nonlinearities exactly, which shows better agreement with experimental data using fewer mode shapes.

The described analytic procedure is relevant to this day, being applied to other MEMS problems, as reported in a recent review paper by Hajjaj et al. [115], such as arch resonators [123, 126, 127, 134, 135], arches over flexible supports [136], functionally graded viscoelastic microbeams with imperfections [137], cantilever resonators [138–140], narrow microbeams subject to fringing fields [118, 119, 141] and microscale beams described by the modified couple stress theory [120, 128–130, 133, 142–144]. Also, in a recent contribution, Ilyas et al. [145] investigated the response of MEMS resonators under generic electrostatic loadings theoretically. The qualitative resonant behavior was analytically demonstrated by the multiple scale method, showing that the nonlinear electrostatic load leads to softening-type nonlinearity. In a companion paper, Ilyas et al. [146] investigated the simultaneous excitation of primary and subharmonic resonances of similar strength experimentally by using different combinations of AC and DC voltages, and two potential applications are experimentally demonstrated.

Several types of uncertainties may be found in practical applications and may have a substantial influence on the behavior of MEMS, given their multi-physical nature. In [147], Vig and Kim enumerate some noise sources, including fluctuations in temperature, adsorbing/desorbing molecules, outgassing, Brownian motion, Johnson noise, drive power, and self-heating. The reduced dimension of the microbeam intensifies all noise effects and instabilities that are negligible in macro-scale devices. Experimental investigations corroborate these conclusions [123, 148, 149]. The global dynamic analysis has shown to be a powerful tool to predict and quantify finite instability, which considers, heuristically, uncertainties in initial conditions, as evidenced by the works of Alsaleem et al. [149], Ruzziconi et al. [150], and Lenci et al. [67]. The influence of material parameters and their uncertainties on the nonlinear response has been highlighted in [151–153], and the influence of uncertainties in geometric nonlinearities in [154–156]. Parametric uncertainties are also of interest in the analysis of MEMS [114, 157], such as geometric [126, 129, 130] and constitutive [133] uncertainties, which can be represented through a Monte Carlo approach, stochastic perturbation, or stochastic collocation. However, further investigation is needed to understand the effects of uncertainties on the response of MEMs, particularly on their global dynamics, where a stochastic framework is still to be developed. The coupling between global dynamics and parametric uncertainty in a probabilistic framework is yet to be discussed.

1.4.
Objectives

Global dynamic analysis is computationally expensive, increasing exponentially together with the phase-space dimension. The nondeterministic analysis is also, generally, computationally expensive. Therefore, the effects of noise and parameter uncertainty on the global dynamics of engineering structures have rarely been conducted, with the few known works devoted to the qualitative analysis of low-dimensional systems. In this scenario, the objective of this thesis is to present adaptative alternatives within an operator-oriented approach of the Ulam method for the global analysis of nonlinear dynamical systems with competing attractors. The stochastic basin of attraction definition by Linder and Hellmann [37] is adopted since it is, from the present point of view, the most natural with respect to the transfer operator's theory. Here a hierarchical discretization of the phase-space is proposed, refining basin's boundaries, attractors' distributions, and manifolds to reduce de computational cost. Also, a procedure to obtain global structures in the mean sense of systems with parametric uncertainties is presented. These tools are applied to the analysis of two archetypal models, the Helmholtz and Duffing oscillators, and two MEMS structures, a microcantilever, and a microarch, to demonstrate the efficiency of the proposed methodologies in exploring the global behavior and safety of noisy and uncertain systems. Finally, the dynamic integrity analysis of these systems is conducted through a new integrity measure based on a given probability threshold.

1.5.
Structure of the thesis

This thesis is subdivided into seven chapters, including this introduction, where basic concepts, bibliographic review, and objectives are presented.

Chapter 2 presents the mathematical background of deterministic and nondeterministic dynamical systems, the axiomatic view of probability, the invariant phase-space structures, and the global operators, necessary for the understanding of nondeterministic global dynamics. The discretization of the transfer operators in the space of indicator functions is derived, and the necessary modifications for stochastic or parametric uncertainty systems are discussed.

Chapter 3 presents the refinement procedures of the phase-space, one focusing only on the basin boundaries and another considering the phase-space manifolds. The case of parametric uncertainty is discussed in more detail. A comparison of two subdivision strategies, one as a binary tree and another as a general r-tree, is given.

In chapter 4, the numerical developments are applied to two archetypal systems, the Helmholtz and the Duffing oscillators, covering different bifurcation scenarios and coexisting solutions. The deterministic case, the parameter uncertainty case, and the additive white noise case are studied. Distinct global dynamics are analyzed, such as multiple wells, harmonic and parametric excitations, multiperiodic and chaotic solutions. Finally, the nondeterministic effect on the dynamic integrity is highlighted.

In chapter 5, an imperfect microcantilever under electric actuation, whose equations are obtained from a three-dimensional Rayleigh beam formulation presented in Appendix A, is analyzed. The static and dynamic responses of a reduced-order model are presented. The global dynamics are analyzed with and without the phase-space local refinement, demonstrating the advantages of the proposed algorithm, specifically when there is an additive noise component. Finally, the dynamic integrity with noise is depicted.

In chapter 6, an initially curved microarch under electric actuation is studied, formulated from a three-dimensional Rayleigh beam formulation presented in Appendix A. The static and dynamic responses are investigated, and a reduced order model (ROM) is derived using the nonlinear normal modes theory. The global dynamics of this ROM are investigated, and parametric uncertainty in the critical damping ratio and additive white noise is considered. The time dependency of the dynamic integrity in stochastic dynamics is demonstrated. The effect of nondeterminism on the manifolds is also discussed.

Finally, chapter 7 presents the conclusions and suggestions for future works.

2
Mathematical background

This chapter presents concise mathematical definitions of deterministic and nondeterministic dynamical systems. The discussion starts with the different flow definitions of deterministic dynamical systems, followed by the axiomatic view of probability and nondeterministic dynamical systems. Then, the influence of nondeterministic effects on invariant phase-space structures is discussed. The chapter ends with the discretization procedure of global phase-space operators, namely, the Perron-Frobenius, Foias, and Koopman operators.

2.1. Definitions of deterministic dynamical systems

The theory of dynamic systems is vast and complex, being an amalgam of several research fields, such as topological dynamics, ergodic theory, measure theory, and bifurcation theory [66, 158–162], among others. In a few words, a dynamic system is a representation of systems that change through time. Precisely, a dynamic system $(\mathbb{X}, \mathbb{T}, \varphi_t)$ consists of a phase-space $\mathbb{X}$, a time-space (additive semigroup) $\mathbb{T}$, and a flow φ such that

$$
\begin{aligned}
&\varphi : \mathbb{X} \times \mathbb{T} \to \mathbb{X} \\
&(x, t) \mapsto \varphi_t x,
\end{aligned}
\tag{2.1}
$$

with properties

$$
\begin{aligned}
&1. \quad \varphi_0 x = \mathrm{id}_{\mathbb{X}}, \\
&2. \quad \varphi_{s+t} x = (\varphi_t \circ \varphi_s) x, \qquad \forall s, t \in \mathbb{T},
\end{aligned}
\tag{2.2}
$$

where $\circ$ means composition, $\mathrm{id}_{\mathbb{X}}$ is the identity in $\mathbb{X}$, with $\varphi_0 x = x$, and the second equation is the flow property. Usually, the dynamical system is referred to by its flow φ. Also, the state of a dynamical system at time t can be designated as x_t for simplicity. These structures are depicted in Figure 2.1.

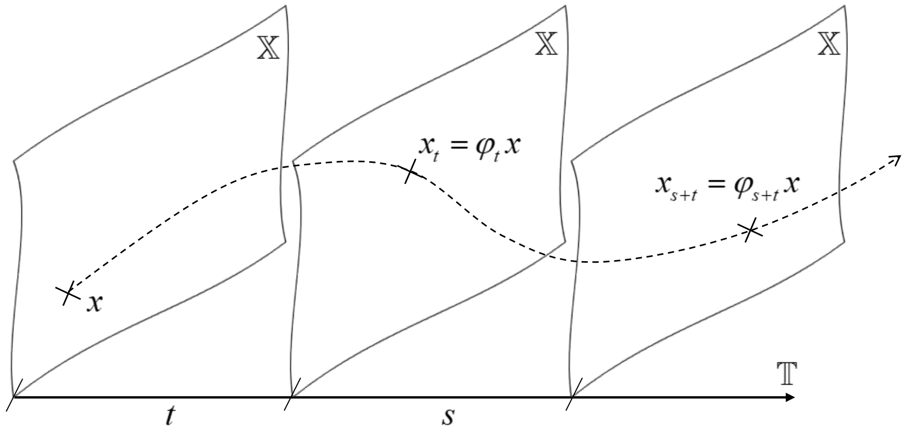

Figure 2.1 – General structures of a dynamical system

The phase-space $\mathbb{X}$ is usually endowed with some extra structure, such as manifolds or a (probability) measure [161]. Examples of such structures are the invariant manifolds of a fixed point, its evolution through time, and its distribution over the phase-space. The case where the phase-space $\mathbb{X}$ is a Euclidean space $\mathbb{R}^n, n \in \mathbb{N}^*$, is particularly important, describing several problems in the literature [66, 163].

Deterministic dynamical systems with continuous time-spaces $\mathbb{T}$, such as the real line or the positive real numbers, have been extensively studied in the literature. The Duffing equation [164] and the Helmholtz oscillator [63, 76] are important examples of such dynamical systems found in engineering. They are defined as differential equations

$$\dot{x} = f\left(x, t\right), \tag{2.3}$$

where $f(x, t)$ are continuous vector fields smooth in t [66, 163]. For such cases, the flow is defined as

$$\varphi_t x = x_0 + \int_{t_0}^{t} f\left(\varphi_s x, s\right) ds, \tag{2.4}$$

and the differential eq. (2.3) is its generator structure. Such flows are *diffeomorphisms*:

$$
\begin{aligned}
&1.\quad \varphi_t : \mathbb{X} \to \mathbb{X}, \qquad \forall t \in \mathbb{R},\\
&2.\quad \exists \partial_t \varphi \quad \text{where} \quad \partial_t \varphi_s x = f\left(x, s\right) \in C^n,\ n \geq 1,\\
&3.\quad \exists \varphi_t^{-1} x = \varphi_{-t}\, x.
\end{aligned}
\tag{2.5}
$$

Note that the flow is assumed to be invertible, which means that the corresponding dynamical system can evolve backward in time. Also, smooth dynamical systems are defined when all endowed manifolds are smooth, i.e., at least of class C^1 [15].

Discrete dynamical systems are another essential case, where $\mathbb{T} = \mathbb{Z}$ and evolution occurring in discrete time steps. The logistic equation and the Hénon map are examples [163]. For these cases, the generator structures are difference equations,

$$
x_{t+1} = f\left(x_t, t\right), \tag{2.6}
$$

where $f(x_t, t)$ are discontinuous vector fields in t [66, 163]. The flows for such cases are the vector fields themselves,

$$
\varphi_t x = f\left(x_t, t\right). \tag{2.7}
$$

Furthermore, these flows are *automorphisms*:

$$
\begin{aligned}
&1.\quad \varphi_n : \mathbb{X} \to \mathbb{X}, \qquad \forall n \in \mathbb{Z},\\
&2.\quad \varphi_n x = \left(\varphi_n \circ \varphi_{n-1} \circ \ldots \circ \varphi_1 \circ \varphi_0\right) x,\\
&3.\quad \exists \varphi_n^{-1} x = \varphi_{-n}\, x.
\end{aligned}
\tag{2.8}
$$

The flow is also assumed invertible, which implies the existence of a dynamical system $\varphi_{-n}, \forall n \in \mathbb{Z}$ that evolves backward in time.

For noninvertible discrete maps, the time set is $\mathbb{T} = \mathbb{Z}^+$. The respective flows are *endomorphisms*:

$$
\begin{aligned}
&1.\quad \varphi_n : \mathbb{X} \to \mathbb{X}, \qquad \forall n \in \mathbb{Z}^+,\\
&2.\quad \varphi_n x = \left(\varphi_n \circ \varphi_{n-1} \circ \ldots \circ \varphi_1 \circ \varphi_0\right) x.
\end{aligned}
\tag{2.9}
$$

Since the inverse map does not exist, the past state of these systems cannot be reconstructed from the present. Root finding algorithms are important examples of such flows, where fixed points are their solutions [161].

Dynamical systems can also be generated in functional phase-spaces $\mathbb{X}$, such as Banach spaces [165–167]. Well-posed evolutionary partial differential equations are examples of generator structures for such cases, where flows are families of bounded operators on $\mathbb{X}$ to $\mathbb{X}$. Such families are C_0-semigroups, with properties (2.2) extended to Banach spaces. In the general sense, the time space is restricted to $\mathbb{R}^+$ since the inverse flow is not guaranteed to exist. Other examples of generator structures with Banach spaces are functional equations, delayed differential equations, and integro-differential equations.

Functional phase-spaces, in contrast to dynamical systems where $\mathbb{X} \subseteq \mathbb{R}^n, n \in \mathbb{N}^*$, possess infinite dimensions. This represents a significant difficulty since a discretization technique, such as the Galerkin method [168, 169], must be applied to the functional space.

The spatial discretization of a deterministic time-dependent system results in a system of nonlinear ordinary differential equations. In this thesis, this system is assumed as a diffeomorphism, with flow given by (2.4). Their time-discretization through numerical methods, such as Euler, trapezoidal rule, or Runge-Kutta, results in noninvertible maps, with flows that are endomorphisms where the time-set $\mathbb{T} = \mathbb{Z}^+$ corresponds to the number of integrated time-steps. The endomorphic construction is necessary to understand the transfer operators that are discussed in section 2.5.

2.2. Axiomatic view of probability

Before nondeterministic dynamical systems are discussed, some concepts from the theory of probability must be addressed. This discussion follows an axiomatic view of probability and can be checked in more detail in [170].

A random experiment is modeled with a sample space $\mathbb{L}$, an event space $\mathfrak{S} \subset 2^{\mathbb{L}}$, and a probability measure[1] $\mathbb{P}_\lambda$. They are organized in a tuple $\left(\mathbb{L}, \mathfrak{S}, \mathbb{P}_\lambda\right)$, which is also named probability space[2]. The sample space $\mathbb{L}$ is generally arbitrary, with elements λ. The event space $\mathfrak{S} \subset 2^{\mathbb{L}}$ is a σ-algebra of $\mathbb{L}$, with elements A. Specifically,

$$
\begin{aligned}
&1. \quad \mathbb{L} \in \mathfrak{S}, \\
&2. \quad A \in \mathfrak{S} \Rightarrow A^c \in \mathfrak{S}, \\
&3. \quad A_i \in \mathfrak{S}, \forall i = 1, 2, \ldots, \Rightarrow \left\{ \bigcup_{i=1}^{\infty} A_i \right\} \in \mathfrak{S}.
\end{aligned}
\tag{2.10}
$$

Also, from the last two properties and De Morgan's law [170], the event space is closed under countable intersections,

$$
A_i \in \mathfrak{S}, \forall i = 1, 2, \ldots, \Rightarrow \left\{ \bigcap_{i=1}^{\infty} A_i \right\} \in \mathfrak{S}, \tag{2.11}
$$

which implies that $\{\varnothing\} \in \mathfrak{S}$ since it is also valid for a countable collection of disjoint sets. At last, the probability measure is a positive function $\mathbb{P}_\lambda : \mathfrak{S} \to [0,1]$ such that

---

[1] A measure is a generalization of concepts such as length, area, volume, probability, etc. Generally, given a measurable space $(\mathbb{X}, \mathfrak{S})$, the set function $\mathbb{P}$ is a measure if the following properties are verified,

1. Non-negativity	$\mathbb{P}(b) \geq 0, \forall\, b \in \mathfrak{S}(\mathbb{X}),$
2. Null-empty set	$\mathbb{P}(\varnothing) = 0,$
3. Countable additivity	$\left.\{b_i \cap b_j\}\right\vert_{i \neq j} = \{\varnothing\} \Leftrightarrow \mathbb{P}\left(\bigcup_i b_i\right) = \sum_i \mathbb{P}(b_i),$

If $\mathbb{P}(\mathbb{X}) = 1$, then it is also a probability measure. The first property, however, is relaxed for the eigenmeasures of the transfer operators in section 2.5, and $\mathbb{P}$ can be signed or even complex-valued.

[2] For general measures, the tuple $(\mathbb{X}, \mathfrak{S}, \mathbb{P})$ is called a measure space.

$$\begin{aligned}
&1. \quad \mathbb{P}_\lambda\{A\} \geq 0, \qquad \forall A \in \mathfrak{S}, \\
&2. \quad \mathbb{P}_\lambda\{\mathbb{L}\} = 1, \\
&3. \quad \left.\{A_i \cap A_j\}\right|_{i \neq j} = \{\varnothing\} \Leftrightarrow \mathbb{P}_\lambda\left\{\bigcup_i A_i\right\} = \sum_i \mathbb{P}_\lambda\{A_i\}.
\end{aligned} \tag{2.12}$$

The expressions in (2.12) are also denominated axioms of Kolmogorov [170]. All conclusions from the theory of probability are defined directly or indirectly from these axioms. These structures are depicted in Figure 2.2.

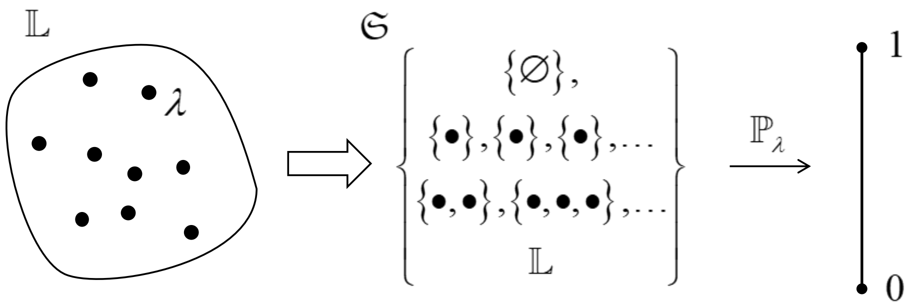

Figure 2.2 – General probability space $(\mathbb{L}, \mathfrak{S}, \mathbb{P}_\lambda)$

The event space $\mathfrak{S}$ is implicitly defined in some cases, with only the sample space $\mathbb{L}$ and the probability measure $\mathbb{P}_\lambda$ specified. For such cases, the event space $\mathfrak{S}$ is assumed as the Borel σ-algebra of the sample space, $\mathfrak{B}(\mathbb{L})$. Also, probability measures can be defined as

$$\mathbb{P}_\lambda\{A\} = \int_A d\mathbb{P}_\lambda, \qquad \forall A \in \mathfrak{B}(\mathbb{L}), \tag{2.13}$$

for both continuous and discrete sample spaces. The derivative $d\mathbb{P}_\lambda$ is the probability density or mass distribution, an essential structure in the analysis of random events.

2.3. Definitions of nondeterministic dynamical systems

Two separate cases must be considered to expand for nondeterministic systems, namely, the parameter uncertainty case and the stochastic case. In the parameter uncertainty case, parameters λ are defined in a probability space $(\mathbb{L}, \mathfrak{S}, \mathbb{P}_\lambda)$, where $\mathbb{L}$ is the parameter space of dimension p, $\mathfrak{S}(\mathbb{L})$ is a σ-algebra, and $\mathbb{P}_\lambda$ is a probability measure [171]. A dynamical system with such a parameter is

$$\begin{aligned}&\varphi:\mathbb{X}\times\mathbb{T}\times\mathbb{L}\to\mathbb{X}\\&\left(x,t;\lambda\right)\mapsto\varphi_t\left(\lambda\right)x,\end{aligned}\tag{2.14}$$

explicitly written as $\left(\mathbb{L},\mathfrak{S},\mathbb{P}_\lambda,\mathbb{X},\mathbb{T},\varphi_t\right)$ and existing in the product space $\left(\mathbb{X},\mathfrak{B}\right)\times\left(\mathbb{L},\mathfrak{S},\mathbb{P}_\lambda\right)$. For simplicity, such dynamical systems are represented by the flow $\varphi_t\left(\lambda\right)$, where the parameter dependency is given explicitly.

A point, evolving according to eq. (2.14), is *n* + *p* dimensional. Each λ-value defines a dynamical system $\varphi_t\left(\lambda\right)$, evolving independently from all other dynamical systems. Generally, the flow $\varphi_t\left(\lambda\right)$ depends nonlinearly on the parameter λ, and care must be taken to choose the correct methodology to represent the probability space [172]. For example, stochastic Galerkin and polynomial chaos methods are known to lose convergence in the second moment for long time-integration [11]. Nevertheless, statistics can be obtained from the collection of dynamic systems $\varphi_t\left(\lambda\right),\lambda\in\mathbb{L}$, such as the mean attractors and mean basins of attraction, when they can be defined.

The generator structures of dynamical systems $\varphi_t\left(\lambda\right)$ with $\mathbb{X}\subseteq\mathbb{R}^n, n\in\mathbb{N}^*$ are, for continuous time $\mathbb{T}=\mathbb{R}$,

$$\dot{x}=f\left(x,t;\lambda\right),\tag{2.15}$$

and for discontinuous time $\mathbb{T}=\mathbb{Z}^{(+)}$

$$x_{t+1}=f\left(x_t,t;\lambda\right),\tag{2.16}$$

where the vector fields depend explicitly on the probability space $\left(\mathbb{L},\mathfrak{S},\mathbb{P}_\lambda\right)$. For continuous-time systems $\mathbb{T}=\mathbb{R}$, flows are diffeomorphisms

$$\begin{aligned}&1.\quad \varphi_t\left(\lambda\right):\mathbb{X}\to\mathbb{X}, \qquad \forall t\in\mathbb{R},\lambda\in\left(\mathbb{L},\mathfrak{S},\mathbb{P}_\lambda\right),\\&2.\quad \exists\partial_t\varphi\left(\lambda\right)\quad\text{where}\quad \partial_t\varphi_s\left(\lambda\right)x=f\left(x,s;\lambda\right)\in C^n, n\geq 1,\\&3.\quad \exists\varphi_t^{-1}\left(\lambda\right)x=\varphi_{-t}\left(\lambda\right)x.\end{aligned}\tag{2.17}$$

For $\mathbb{T}=\mathbb{Z}^{(+)}$, flows are

$$
\begin{aligned}
&1.\quad \varphi_n(\lambda):\mathbb{X}\to\mathbb{X}, \qquad \forall n\in\mathbb{Z},\lambda\in(\mathbb{L},\mathfrak{S},\mathbb{P}_\lambda),\\
&2.\quad \varphi_n(\lambda)x=(\varphi_n\circ\varphi_{n-1}\circ\ldots\circ\varphi_1\circ\varphi_0)(\lambda)x,\\
&3.\quad \exists\varphi_n^{-1}(\lambda)x=\varphi_{-n}(\lambda)x \quad \text{if } \mathbb{T}=\mathbb{Z},
\end{aligned}
\tag{2.18}
$$

which are automorphisms for $\mathbb{T}=\mathbb{Z}$ or endomorphisms for $\mathbb{T}=\mathbb{Z}^+$. In both structures (2.17) and (2.18), flows are also samples, having a one-to-one correspondence with each realization λ of the random parameter. Thus, a family of flows is generated by the probability space $(\mathbb{L},\mathfrak{S},\mathbb{P}_\lambda)$. A representation of the generated flows is depicted in Figure 2.3.

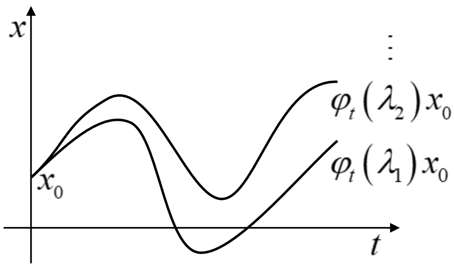

Figure 2.3 – Family of flows generated by a probability space

Therefore, the family of flows has the following properties

$$
\begin{aligned}
&1.\quad (\varphi_t\circ\varphi_s)(\lambda)x=\varphi_{s+t}(\lambda)x,\\
&2.\quad \varphi_0(\lambda)x=\mathrm{id}_{\mathbb{L}\times\mathbb{X}},\\
&3.\quad \varphi_t(\lambda)x \text{ is } \mathfrak{B}(\mathbb{X})\otimes\mathfrak{B}(\mathbb{T})\otimes\mathfrak{S},\mathfrak{B}(\mathbb{X})-\text{measurable.}^3
\end{aligned}
\tag{2.19}
$$

The previous structure belongs to the broader class of *measurable dynamical systems*. Given a time set $\mathbb{T}$, a probability space $(\Omega,\mathfrak{F},\mathbb{P})$, and a function θ, the flow is defined as

$$
\begin{aligned}
&\theta:\Omega\times\mathbb{T}\to\Omega\\
&(\omega,t)\mapsto\theta_t\omega,
\end{aligned}
\tag{2.20}
$$

---

[3] A transformation $\varphi_t:\mathbb{X}\to\mathbb{X}$ over a measure space $(\Omega,\mathfrak{F},\mathbb{P})$ is $\mathfrak{F}(\Omega)-$measurable if $\varphi_t^{-1}(b)\in\mathfrak{F}(\Omega)$ for all $b\in\mathfrak{F}(\Omega)$.

a measurable dynamical system $(\Omega,\mathfrak{F},\mathbb{P},\mathbb{T},\theta_t)$ is such that the following properties hold,

$$
\begin{aligned}
&1.\quad (\theta_s \circ \theta_t)\omega = \theta_{s+t}\omega,\\
&2.\quad \theta_0\omega = \mathrm{id}_\Omega,\\
&3.\quad \theta_t\omega \text{ is } \mathfrak{F}\otimes\mathfrak{B}(\mathbb{T}),\mathfrak{F}-\text{measurable.}
\end{aligned}
\tag{2.21}
$$

Furthermore, this dynamical system is measure-preserving if it is an endomorphism with $\theta_t(\mathbb{P}) = \mathbb{P}$. The measure $\mathbb{P}$ is called *invariant*. Such measure is fundamental in the steady-state analysis, and endomorphic measurable dynamic systems are denominated *metric dynamical systems.*

As an example, the dynamical system $(\mathbb{X},\mathbb{T},\varphi_t)$ generated by an ordinary differential eq. (2.3) is considered. The flow is the differential equation solution, $\theta_t x = \varphi_t x = x(t)$. The phase-space is endowed with the Borel σ-algebra $\mathfrak{B}(\mathbb{X})$ by definition. Suppose that the system is conservative in the sense that the phase volume is preserved in time. For such systems, the Liouville's theorem is applicable [17]:

$$\nabla_x \rho \cdot f = 0, \tag{2.22}$$

where $\rho(x,t)$ is the phase-space density, normalized as $\int_{\mathbb{X}} \rho dx = 1$. Equation (2.22) has a solution for all continuous vector fields $f(x,t)$ smooth in $(\mathbb{X},\mathbb{T})$. A measure with density $d\mathbb{P} = \rho dx$ is then defined. Then, with the phase-space having a σ-algebra and a measure, one can conclude that the dynamical system generated by a conservative differential equation is measurable with $(\mathbb{X},\mathfrak{B}(\mathbb{X}),\mathbb{P},\mathbb{T},\varphi_t)$. Even further, the Liouville's theorem dictates that the density is constant in time [17], which implies the existence of an invariant measure. Therefore, this is a metric dynamical system.

The previous example is vital since various physical models constitute conservative dynamical systems, such as planetary orbits, frictionless harmonic oscillators, among others. However, the dynamical systems generated by non-conservative physical models can also be measurable since phase-space sets $\mathbb{X}$

will, in general, be Lebesgue measurable [158, 159]. Then, all dynamical systems will be assumed measurable from now on.

Another class of dynamical systems with random parameters has the product $\mathbb{L}\otimes\mathbb{X}$ as a separable Banach space. Examples of generator structures are stochastic partial differential equations with spatial white noise and partial differential equations with random spatial properties [172–174]. These are much more complicated to analyze, with a discretization procedure taking place in both physical and probabilistic spaces.

Stochastic cases were considered by Arnold [15]. He defines random dynamical systems as cocycles over stochastic processes, with the latter being measurable dynamical systems. Specifically, considering a metric dynamical system $(\Omega,\mathfrak{F},\mathbb{P}_\omega,\mathbb{T},\theta_t)$ over the probability space Ω (with given σ-algebra $\mathfrak{F}$ and probability measure $\mathbb{P}_\omega$), a random dynamical system $(\mathbb{X},\mathfrak{B},\mathbb{T},\varphi_t)$ over $(\Omega,\mathfrak{F},\mathbb{P}_\omega,\mathbb{T},\theta_t)$ is defined as

$$\begin{aligned}&\varphi:\mathbb{X}\times\mathbb{T}\times\Omega\to\mathbb{X}\\&(x,t;\omega)\mapsto\varphi_t(\omega)x,\end{aligned}\tag{2.23}$$

with the following properties

$$\begin{array}{ll}1. & \varphi \text{ is } \mathfrak{B}(\mathbb{X})\otimes\mathfrak{B}(\mathbb{T})\otimes\mathfrak{F},\mathfrak{B}(\mathbb{X})-\text{measurable,}\\ 2. & \varphi_t(\omega):\mathbb{X}\to\mathbb{X} \text{ form a cocyle over } \theta_t\omega:\\ & \text{i.}\quad \varphi_0(\omega)=\mathrm{id}_{\mathbb{X}}, \qquad\qquad \forall\omega\in\Omega,\\ & \text{ii.}\quad \varphi_{s+t}(\omega)=\varphi_s(\theta_t\omega)\circ\varphi_t(\omega), \quad \forall s,t\in\mathbb{T},\omega\in\Omega.\end{array}\tag{2.24}$$

The cocycle property 2.ii. can also be written as $\varphi_{s+t}(\omega)x=\varphi_s(\theta_t\omega)\varphi_t(\omega)x$. The conclusion is that random dynamical systems evolve together with a random space when the underlying metric dynamical system has a probability law. Therefore, the flow $\varphi_t(\omega)$ obeys a probability law and is distributed accordingly. One could argue that the injective property of the flow $\varphi_t(\omega)$ is violated in stochastic cases, but as can be concluded through property 1, there is one outcome for each sample ω, thus maintaining this property.

The random dynamical system definition (2.23) and properties (2.24) are interesting by also being able to describe general nonautonomous dynamics. For example, if the underlying metric dynamical system θ_t is a deterministic harmonic function, the probability measure is a Dirac delta for phase-angles between 0 and 2π, evolving with the excitation frequency, ω, and the resulting dynamics $\varphi_t(\omega)x$ is harmonic.

It is worth visualizing the evolution of a random dynamical system on $\Omega \otimes \mathbb{X}$. While ω evolves with the flow θ_t, the cocycle $\varphi_t(\omega)$ moves the point x along the fibers $\{\omega\} \times \mathbb{X}$. The cocycle property is also depicted.

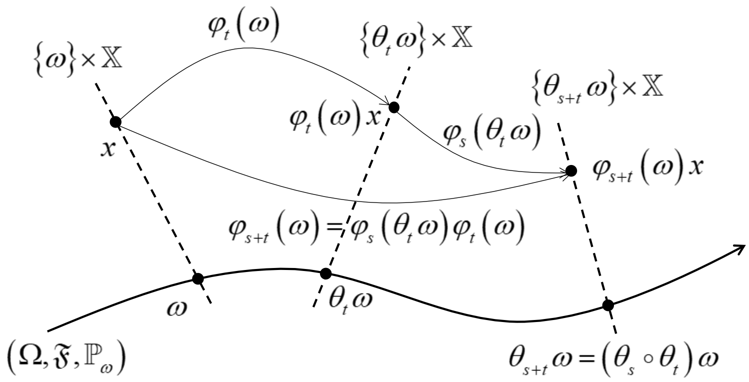

Figure 2.4 – Evolution of a random dynamical system

The generator structures with $\mathbb{X} \subseteq \mathbb{R}^n, n \in \mathbb{N}^*$ are separated into three main categories [15]: random maps with $\mathbb{T} = \mathbb{Z}^{(+)}$,

$$x_{t+1} = f(\theta_t \omega, x_t, t), \tag{2.25}$$

random differential equations with $\mathbb{T} = \mathbb{R}$,

$$\dot{x} = f(\theta_t \omega, x, t), \tag{2.26}$$

and stochastic differential equations with $\mathbb{T} = \mathbb{R}$,

$$dx = f(x,t)dt + g(x,t)dW. \tag{2.27}$$

The white noise dW is the formal derivative of the Wiener process [175]. It is not physically feasible, possessing constant power spectral density [176] and, as such, different methods of analysis must be applied. The flows for the random map, the random differential equation, and the stochastic differential equation are, respectively,

$$\varphi_t(\omega)x = f(\theta_t\omega, x_t, t), \tag{2.28}$$

$$\varphi_t(\omega)x = x_0 + \int_{t_0}^{t} f(\theta_s\omega, \varphi_s(\omega), s)ds, \tag{2.29}$$

$$\varphi_t(\omega)x = x_0 + \int_{t_0}^{t} f(x,s)ds + \int_{t_0}^{t} g(x,s)dW, \tag{2.30}$$

Also, the continuous-time flows are diffeomorphisms. In contrast, the discrete-time flows are endomorphisms, for noninvertible flows with $\mathbb{T} = \mathbb{Z}^{+}$, or automorphisms, for invertible flows with $\mathbb{T} = \mathbb{Z}$.

As in the deterministic case, random dynamical systems can also be generated when $\mathbb{X}$ is a functional phase-space. However, the abstract setting is much more complicated due to the cocycle nature, with the underlying noise also being defined over a Banach space, usually, a Hilbert space [177], and the generator structure is a stochastic partial differential equation. It is known that stochastic differential equations with linear multiplicative noise effectively generate random dynamical systems. However, the case with nonlinear multiplicative noise is unclear. Stochastic partial differential equations usually are crude cocycles, whereas random dynamical systems are perfect cocycles. A perfection procedure makes changes in the space definitions, particularly in sets with zero probability, defining a time subset in which the crude cocycle is indistinguishable from the perfect cocycle [15]. Therefore, the cocycle perfection will be assumed in the analysis of continuous systems under stochastic excitations.

The probabilistic framework represents a significant computational difficulty. Special techniques must be employed to access the full randomness of stochastic systems. According to some probability law, all deterministic quantities, namely attractors, repellors, saddles, and basins, become randomly distributed. Such facts arise from the interplay between the random parameter λ, the stochastic system θ_t, and the flow φ_t, being particularly difficult to obtain in nonlinear cases. Therefore, one must resort to numerical strategies to verify such structures in a probabilistic sense.

To summarize, the flow $\varphi_t x$ of general nondeterministic dynamics is assumed to be dependent on some random event, such as a random parameter value λ in a probability space $\mathbb{L}$ or a noise sample ω in a probability space Ω, with the latter evolving according to another dynamical system θ_t. The flow of those systems is generally labelled as $\varphi_t(\lambda,\omega)x$ to specify that the evolution law is a function of these random events. It is also implied that the noise sample evolves according to θ_t together with the flow φ_t, with this dependence suppressed in the notation. The complete structure is given in eq. (2.31).

$$\begin{aligned}
&\varphi : \mathbb{X}\times\mathbb{T}\times\mathbb{L}\times\Omega \to \mathbb{X} \\
&(x,t;\lambda,\omega) \mapsto \varphi_t(\lambda,\omega)x.
\end{aligned} \tag{2.31}$$

The spatial discretization of a nondeterministic time-dependent system can result in many different complex nondeterministic dynamical systems, see Zhang and Karniadakis [174] for explorations with white noise cases and Le Maître and Knio [172] for parameter uncertainty cases. In this thesis, the nondeterminism is assumed to be small, so that the spatial discretization is performed deterministically. Then, nondeterminism is applied to the ensuing dynamical system, resulting in structures such as (2.15) for random parameters or (2.27) for white noise cases.

2.4. Invariant structures of dynamical systems

Moving on to the description of the invariant objects, one has, initially, attractors and their basins. Attractors are usually defined in the pushforward sense as regions A in the phase-space $\mathbb{X}$ to which initial conditions converge asymptotically as $t \to \infty$. Other definitions of attractors exist in the literature, see Arnold [15], but the restriction to pushforward convergence allows the operator perspective, focus of this thesis, to be addressed naturally. Likewise, the set of all initial conditions that converge to a given attractor is defined as its basin, g_A. Specifically,

$$g_A = \left\{ x \in \mathbb{X} \mid \lim_{t \to \infty} \varphi_t x \subseteq A \right\}. \tag{2.32}$$

As specified in Section 2.3, nondeterminism can be assumed in two different ways, namely *parametric* and *stochastic*. The resulting dynamical system for an uncertain parameter λ is augmented by the probability space, with uncertainty as an additional initial condition. On the other hand, the stochastic dynamic case is governed by a random dynamical system, i.e., a deterministic law driven by a stochastic process. The last case is theoretically more involved, inserting a diffusion of the solutions over $\mathbb{X}$. The distinction is necessary because stochastic dynamics can be globally approximated by an operator named Foias. In contrast, the parameter uncertainty case cannot, requiring a collection of Perron-Frobenius operators to obtain valid statistics. Therefore, two different random parameters are adopted, λ for the parameter uncertainty and ω for stochastic dynamics, following the definitions in section 2.3.

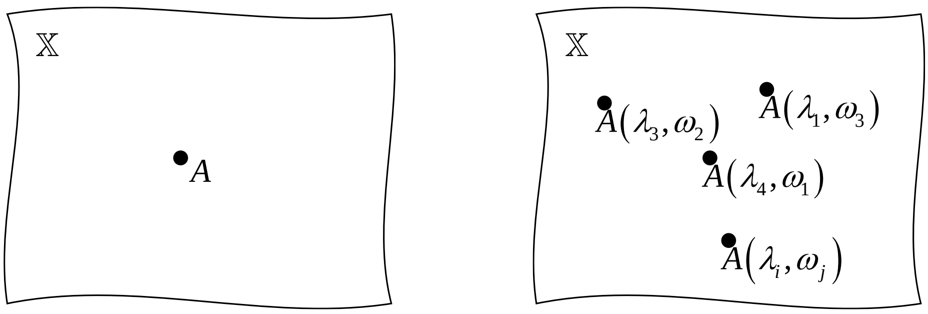

(a) Deterministic fixed-point (b) Nondeterministic fixed-point samples

Figure 2.5 – Comparison between deterministic and random fixed-point attractors

For general nondeterministic dynamics, the flow $\varphi_t x$ is assumed to be dependent on some random event, such as a random parameter value λ in a probability space $\mathbb{L}$ or a noise sample ω in a probability space Ω, which evolves according to another dynamical system θ_t. The flow of those systems is generally labeled as $\varphi_t(\lambda, \omega)x$ to specify that the evolution law is a function of these random events. It is also implied that the noise sample evolves according to θ_t together with the flow φ_t, but this dependence is suppressed. Likewise, attractors can be described as dependent on random events λ and ω. This dependence is denoted as $A(\lambda, \omega)$. Of course, attractors are also time-dependent if the flow is noise-driven, see Ochs [178], but this dependence is suppressed for clarity. As an example, fixed-point attractors become random points in $\mathbb{X}$ [15], see Figure 2.5.

Because the outcome is not unique, the definition of convergence must be changed as well. Specifically, a random attractor is a phase-space set $A(\lambda,\omega)$ such that the distance between it and some neighbor converges to zero in probability as $t \to \infty$. This set attractor $A(\lambda,\omega)$ plays an important role in nondeterministic dynamics, being accompanied by a phase-space distribution f_A. Figure 2.6 illustrates the distributions for the deterministic and nondeterministic cases, where the former was lifted to the random space $\mathbb{L}\times\Omega$ considering its distribution as a Dirac delta. Although the attractor $A(\lambda,\omega)$ is random, its distribution f_A is not. Ochs [178] discusses the numerical approximation of attractors and invariant measures for random dynamical systems. He also presents an existence theorem for attractors and comments on their robustness under perturbations. In our framework, these correspond to stochastically driven systems with attractors $A(\lambda,\omega)$.

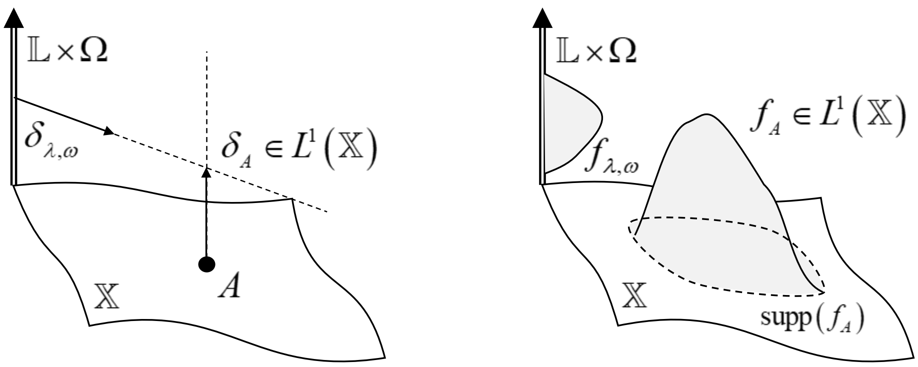

(a) Deterministic attractor (b) nondeterministic attractor

Figure 2.6 – Comparison between deterministic and nondeterministic periodic attractor's distributions

The definition of basins of attraction for nondeterministic dynamical systems is much more complicated to address. Distinct definitions and methods for stochastic basins of attraction are found in the literature. Ochs [178] defines them as forward invariant random sets $g_A(\lambda,\omega)$ under the flow $\varphi_t(\lambda,\omega)x$ in the probabilistic sense,

$$g_A(\lambda,\omega)=\left\{x\in\mathbb{X}\mid \lim_{t\to\infty}\mathbb{P}_\lambda\left[\varphi_t(\lambda,\omega)x\notin A(\lambda,\theta_t\omega)\right]=0\right\}, \tag{2.33}$$

the probability of a solution $\varphi_t(\lambda,\omega)x$ not being in the attractor set goes to zero as time increases. Therefore, for each $A(\lambda,\omega)$, there is a respective random set $g_A(\lambda,\omega)$, which is its basin of attraction in the probabilistic sense. It is evident that this definition gives a one-to-one relation between a random event, the flow, the attractors and the basins. Of course, this random inclusion represents a major computational difficulty, increasing the system dimensionality.

Xu et al. [103] investigated the Ueda system with additive white noise, considering basins in the same sense as the deterministic problems through the generalized cell mapping (GCM) with partially ordered sets (posets) and directed graphs (digraphs) [106]. The impact of randomness on the basin boundaries is evident, showing how it diffuses as noise increases, eventually destroying the attractor. Although the results clarify the influence of noise on the attractor and basin evolution and possible bifurcations, the adopted basin definition lacks a proper stochastic description. Recently, the short-time gaussian GCM approximation [24] was applied to a Duffing oscillator by Han et al. [28], but the definition of basins was maintained and, therefore, the results lack further quantification of the basin randomness. Another strategy was followed by Silva et al. [179] and Orlando et al. [112], which considered random noise, but did not investigate its effect on the safe basin and dynamic integrity with an actually stochastic approach. Again, the results demonstrated the effect of randomness on the basin of attraction qualitatively, but the proper description is still an open issue.

Later, Linder and Hellmann [37] proposed a generalization of stochastic basins of attraction of a stable state based on the fixed spaces of the Perron-Frobenius $\mathcal{P}_t$ and the Koopman $\mathcal{K}_t$ operators in phase-space. Succinctly, they explored the coupling between general dynamical systems with two linear systems, one over the space of phase-space distributions *f*, with operator $\mathcal{P}_t$, and another over the space of phase-space observables *g*, with operator $\mathcal{K}_t$. Their duality property and the Ulam method [180] enable the derivation of the discretized operators P_h and $K_h = P_h^T$. Then, stochastic basins of attraction can be defined as

$$\begin{aligned} &g_A(\varepsilon): \mathbb{X} \to [0,1], \\ &x \mapsto g_A(\varepsilon)x \end{aligned} \tag{2.34}$$

that is, a value between 0 and 1 is assigned to each phase-space point $x \in \mathbb{X}$. This value is the probability that *x*, evolving according to a given dynamical system $\varphi_t(\lambda,\omega)$, stays at *A* until a predefined time $t = 1/\varepsilon$, denominated the time-horizon. The limit case $g_A(0)$ corresponds to the classical (i.e., deterministic) definition of basin of attraction for $t \to \infty$. Linder and Hellmann [37] call the functions $g_A(\varepsilon)$ ε-committors. Markov operators, such as the Foias operator $\mathcal{F}_t$, can be adopted for stochastic dynamic system analyses [17]. Figure 2.7 presents the deterministic and stochastic cases of functions $g_A(\varepsilon)$. It is clear that it is an indicator function in the deterministic case while presenting values between 0 and 1 for the stochastic case.

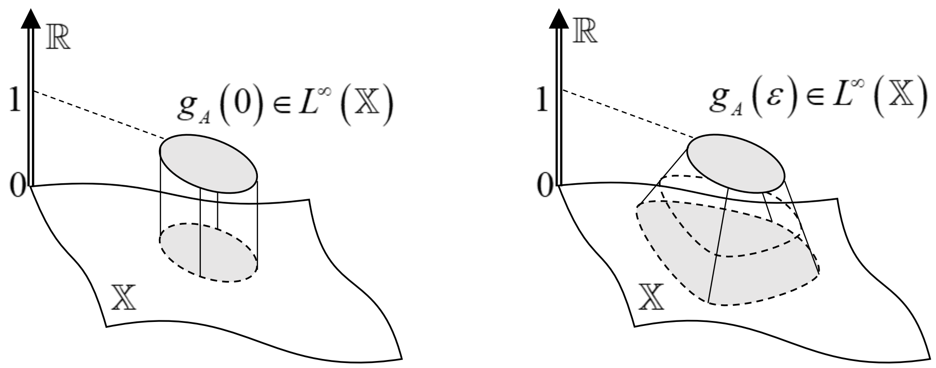

(a) Deterministic basin (b) General stochastic basin

Figure 2.7 – Comparison between deterministic and stochastic basin of attraction

2.5. Global perspective and projection onto discretized phase-spaces

The local analysis of dynamical systems is generally conducted from a geometric perspective. Specifically, the changes in the flow topology φ_t given a parameter space $\mathbb{L}$ can be described by bifurcation diagrams, where the relation of fixed points of the steady-state solutions with the varying control parameters is depicted [163]. Stability is evaluated in the Lyapunov (infinitesimal) sense.

This approach can be understood from a material (Lagrangian) perspective, following specific orbits as they change in time and in the parameter space. Although fundamental, this analysis becomes computationally prohibitive when large ensembles of orbits are of interest. Examples of such cases occur in stochastic dynamics [15] and parameter uncertainty, with non-unique outcomes.

The natural alternative to the Lagrangian analysis is to investigate regions in phase-space $\mathbb{X}$ as orbits evolve in a spatial (Eulerian) perspective. The theoretical development is, however, more involved, needing the definition of *flux operators* in the phase-space. Some of these concepts, following [17, 42, 181–183], are reviewed.

First, the deterministic case is considered. Associated with a given dynamical system $(\mathbb{X},\mathfrak{B},\mathbb{T},\varphi_t)$ is another dynamical system over the space $L^1(\mathbb{X})$, namely the space of distributions *f* over $\mathbb{X}$, that is

$$\begin{aligned}&\mathcal{P}_t : L^1(\mathbb{X}) \to L^1(\mathbb{X}),\\ &f \mapsto \mathcal{P}_t[f],\end{aligned} \tag{2.35}$$

with $\mathcal{P}_t$ defined by

$$\int_B \mathcal{P}_t[f]dx = \int_{\varphi_t^{-1}B} f\,dx, \qquad \forall B \in \mathfrak{B}, \tag{2.36}$$

being known as the Perron-Frobenius operator. Stationary solutions *f* of eq. (2.36) are such that

$$\mathcal{P}_t[f] = f, \tag{2.37}$$

and they specify how attractors are localized in the phase-space [17]. For example, fixed points, periodic orbits, and limit-cycle attractors are described by Dirac distributions $\delta_C(.)$ supported on *C* such that

$$\int_A \delta_C(x)dx = \begin{cases}0, & C \not\subset A\\ 1, & C \subseteq A\end{cases}. \tag{2.38}$$

The Perron-Frobenius operator $\mathcal{P}_t$ can be understood as a transport of distributions under the flow φ_t. Given an initial distribution *f* in the phase-space, $\mathcal{P}_t$ drives it through the dynamics, as depicted in Figure 2.8.

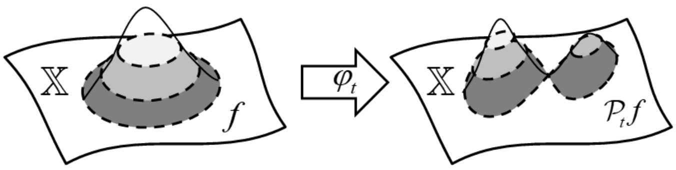

Figure 2.8 – Evolution of a distribution *f* under the Perron-Frobenius operator $\mathcal{P}_t$

The function $\varphi_t^{-1}B$ is the preimage of the set *B* under the flow φ_t, i.e., the collection of all *x* that map to *B* under φ_t, that is

$$\varphi_t^{-1}B = \bigcup \left\{ x \middle| \varphi_t x \in B \text{ given } t \in \mathbb{T}, A \in \mathfrak{B} \right\}. \tag{2.39}$$

The Perron-Frobenius operator is also a Markov operator; therefore, it is linear, positive $\left(f \geq 0 \Leftrightarrow \mathcal{P}_t f \geq 0 \right)$, and non-expansive $\left(\left\| \mathcal{P}_t f \right\|_{L^1} = \left\| f \right\|_{L^1} \right)$. Its adjoint (dual) is the Koopman operator $\mathcal{K}_t$, which defines a dynamical system in $L^\infty(\mathbb{X})$, the space of observables *g* over $\mathbb{X}$,

$$\begin{aligned} &\mathcal{K}_t : L^\infty(\mathbb{X}) \to L^\infty(\mathbb{X}), \\ &g \mapsto \mathcal{K}_t[g], \end{aligned} \tag{2.40}$$

explicitly given by

$$\mathcal{K}_t[g] = g(\varphi_t x). \tag{2.41}$$

Stationary solutions of eq. (2.41) are given by

$$\mathcal{K}_t[g] = g, \tag{2.42}$$

and they govern the basins of attraction distributions over the phase-space [37]. Finally, the duality property $\left\langle \mathcal{P}_t f, g \right\rangle = \left\langle f, \mathcal{K}_t g \right\rangle$ between the two operators is expanded as [17]

$$\int_{\mathbb{X}} g\mathcal{P}_t[f]dx = \int_{\mathbb{X}} \mathcal{K}_t[g]f\,dx, \qquad \forall f \in L^1(\mathbb{X}), g \in L^\infty(\mathbb{X}). \tag{2.43}$$

Systems with *parameter uncertainty* are described with a one-to-one relationship between the operators and the elements $\lambda \in (\mathbb{L}, \mathfrak{S}, \mathbb{P}_\lambda)$. Therefore, the operators are written as $\mathcal{P}_t(\lambda)$ and $\mathcal{K}_t(\lambda)$ for all $\lambda \in (\mathbb{L}, \mathfrak{S}, \mathbb{P}_\lambda)$. Specifically, the Perron-Frobenius operator is given by

$$\begin{aligned} &\mathcal{P}_t(\lambda) : L^1(\mathbb{X}) \to L^1(\mathbb{X}), \\ &f \mapsto \mathcal{P}_t(\lambda)[f], \\ &\int_B \mathcal{P}_t(\lambda)[f]dx = \int_{\varphi_t^{-1}(\lambda)B} f\,dx, \qquad \forall B \in \mathfrak{B}, \lambda \in \mathbb{L}, \end{aligned} \tag{2.44}$$

where the inverse flow is

$$\varphi_t^{-1}(\lambda)B = \bigcup \left\{ x \middle| \varphi_t(\lambda)x \in B \text{ given } t \in \mathbb{T}, B \in \mathfrak{B}, \lambda \in \mathbb{L} \right\}. \tag{2.45}$$

The Koopman operator with parameter uncertainty is

$$\begin{aligned} &\mathcal{K}_t(\lambda) : L^\infty(\mathbb{X}) \to L^\infty(\mathbb{X}), \\ &g \mapsto \mathcal{K}_t(\lambda)[g], \\ &\mathcal{K}_t(\lambda)[g] = g(\varphi_t(\lambda)x). \end{aligned} \tag{2.46}$$

and the duality property is also defined locally, i.e., for each $\lambda \in (\mathbb{L}, \mathfrak{S}, \mathbb{P}_\lambda)$,

$$\int_{\mathbb{X}} g\mathcal{P}_t(\lambda)[f]dx = \int_{\mathbb{X}} \mathcal{K}_t(\lambda)[g]f\,dx, \qquad \forall f \in L^1(\mathbb{X}), g \in L^\infty(\mathbb{X}). \tag{2.47}$$

With these definitions, the global analysis of flows $\varphi_t(\lambda)$ can be conducted independently for each $\lambda \in (\mathbb{L}, \mathfrak{S}, \mathbb{P}_\lambda)$. Therefore, the one-to-one relationship between parameter values λ and flows $\varphi_t(\lambda)$ is maintained.

The generalization for *stochastic* systems is obtained by the Foias operator [17, 55, 56]. First, notice that the indicator function of a set A is defined as

$$\mathrm{id}_A(x) = \begin{cases} 0, & x \notin A \\ 1, & x \in A \end{cases}, \tag{2.48}$$

and has the following property for any dynamic system,

$$\mathrm{id}_B\left(\varphi_t x\right)=\mathrm{id}_{\varphi_t^{-1}B}\left(x\right), \tag{2.49}$$

which allows rewriting eq. (2.36) as

$$\int_B \mathcal{P}_t\left[f\right]dx=\int_{\mathbb{X}}\mathrm{id}_B\left(\varphi_t x\right)f\,dx. \tag{2.50}$$

For the case of random dynamical systems, the flow $\varphi_t\left(\omega\right)$ depends on a probability space $\left(\Omega,\mathfrak{F},\mathbb{P}_\omega\right)$. By taking the mean of eq. (2.50) in $\left(\Omega,\mathfrak{F},\mathbb{P}_\omega\right)$, one obtains

$$\mathbb{E}\left\{\int_B \mathcal{P}_t\left[f\right]dx\right\}=\int_\Omega\left\{\int_{\mathbb{X}}\mathrm{id}_B\left[\varphi_t\left(\omega\right)x\right]f\,dx\right\}\mathbb{P}_\omega\left(d\omega\right), \tag{2.51}$$

and the Foias operator is defined by changing the order of integration,

$$\int_B \mathcal{F}_t\left[f\right]dx=\int_{\mathbb{X}}\left\{\int_\Omega\mathrm{id}_B\left[\varphi_t\left(\omega\right)x\right]\mathbb{P}_\omega\left(d\omega\right)\right\}f\,dx. \tag{2.52}$$

Also, the notation can be simplified considering the subset of the probability space $\Omega_x\left(B\right)$ for which the dynamical system is in B under the flow $\varphi_t\left(\omega\right)$ [45],

$$\Omega_x\left(B\right)=\left\{\omega\in\Omega:\varphi_t\left(\omega\right)x\in B\right\}, \tag{2.53}$$

resulting in

$$\int_B \mathcal{F}_t\left[f\right]dx=\int_{\mathbb{X}}\left\{\int_{\Omega_x(B)}\mathbb{P}_\omega\left(d\omega\right)\right\}f\,dx. \tag{2.54}$$

The Foias operator $\mathcal{F}_t$ is associated with random dynamical systems $\varphi_t\left(\omega\right)$ taking values in a phase-space $\left(\mathbb{X},\mathfrak{B}\right)$ and a probability space $\left(\Omega,\mathfrak{F},\mathbb{P}_\omega\right)$ at each time step. The case of stochastic processes $\left(\Omega,\mathfrak{F},\mathbb{P}_\omega,\theta_t\right)$, which are systems that sample the probability space $\left(\Omega,\mathfrak{F},\mathbb{P}_\omega\right)$ continuously in time, is developed through the cocycle property, resulting in

$$\int_B \mathcal{F}_{s+t}\left[f\right]dx=\int_{\mathbb{X}}\left\{\int_\Omega\mathrm{id}_B\left[\varphi_s\left(\theta_t\omega\right)\circ\varphi_t\left(\omega\right)x\right]\mathbb{P}_\omega\left(d\omega\right)\right\}f\,dx. \tag{2.55}$$

with the composition property given by its differentiation. These developments show that the Foias operator $\mathcal{F}_t$ gives a good generalization in the mean sense for the Eulerian analysis of random dynamical systems with continuous or discrete time. Furthermore, the adjoint operator is obtained by setting

$$\mathcal{K}_t[g] = \int_\Omega g\left(\varphi_t(\omega)x\right)\mathbb{P}_\omega(d\omega), \qquad \forall, g \in L^\infty(\mathbb{X}). \tag{2.56}$$

which is a mean Koopman operator over the probability space $(\Omega, \mathfrak{F}, \mathbb{P}_\omega)$.

The *discretization* of $\mathcal{P}_t$ is given by the Ulam method [37, 42, 180], equivalent to the generalized cell-mapping [21]. Let $\mathbb{B} = \{b_1, \ldots, b_k\}$ be a disjoint partition of the phase-space $\mathbb{X}$ into k sets. Additionally, consider the subspace $\Delta_h \subset L^1(\mathbb{X})$ spanned by the normalized indicator functions of $\mathbb{B}$, i.e., it has basis $\{1_1, \ldots, 1_k\}$, where $1_i = \mathrm{id}_{b_i} / m(b_i)$. $m(b_i)$ is the measure in $\mathbb{X}$ and h is the characteristic size of the partition. A projection $Q_h : L^1(\mathbb{X}) \to \Delta_h$ is then given by

$$Q_h f = \sum_{i=1}^{k} \left\{ \int_{b_i} f\, dx \right\} 1_i = \sum_{i=1}^{k} f_i 1_i. \tag{2.57}$$

Therefore, the discretized (projected) distribution is $f_h = Q_h f$. Following [180], the projection of $\mathcal{P}_t$ is $P_h : \Delta_h \to \Delta_h$, $P_h = Q_h \mathcal{P}_t$. Substituting $\mathcal{P}_t[f]$ into eq. (2.57) results in

$$
\begin{aligned}
Q_h \mathcal{P}_t[f] &= \sum_{i=1}^{k} f_i Q_h \mathcal{P}_t[1_i], \\
&= \sum_{i=1}^{k} f_i \sum_{j=1}^{k} \left\{ \int_{b_j} \mathcal{P}_t[1_i]\, dx \right\} 1_j, \\
&= \sum_{i=1}^{k} f_i \sum_{j=1}^{k} \left\{ \int_{\varphi_t^{-1} b_j} 1_i\, dx \right\} 1_j, \\
&= \sum_{i,j=1}^{k} \frac{f_i}{m(b_i)} \left\{ \int_{\varphi_t^{-1} b_j} \mathrm{id}_{b_i}\, dx \right\} 1_j \\
&= \sum_{i,j=1}^{k} f_i \frac{m\left(b_i \cap \varphi_t^{-1} b_j\right)}{m(b_i)} 1_j, \\
&= \sum_{i,j=1}^{k} f_i p_{ij} 1_j.
\end{aligned}
\tag{2.58}
$$

Then, the projected operator P_h is defined as

$$
P_h 1_i = \sum_{j=1}^{k} p_{ij} 1_j,\; p_{ij} = \frac{m\left(b_i \cap \varphi_t^{-1} b_j\right)}{m(b_i)},
\tag{2.59}
$$

and, by observing (2.58), (2.59) is identified as a row-stochastic matrix. This expression coincides with the classical definition of the Ulam method [180], and the difference with the generalized cell mapping [21], which gives a column stochastic transfer matrix, is purely a computational implementation. Here, the Eigen C++ template library for linear algebra, available at http://eigen.tuxfamily.org, which presents both storage orders, is used. The column-major storage with the transposed formulation is chosen, following [21], since it is the standard for Eigen.

Finally, the evolution of discretized distribution is then given by

$$
\begin{aligned}
&\sum_{i=1}^{k} f_i' 1_i = \sum_{i,j=1}^{k} f_i p_{ij} 1_j, \\
&\sum_{i=1}^{k} f_i' 1_i = \sum_{i=1}^{k} f_i P_h 1_i, \\
&\therefore\; f_h' = f_h P_h.
\end{aligned}
\tag{2.60}
$$

These discretization results can be applied directly for parameter uncertainty systems. Of course, the probability space must also be discretized so that operators $P_h(\lambda_i)$ for all $\lambda_i \in (\Lambda, \mathfrak{S}_\Lambda, P_\Lambda)$ can be calculated.

Now the discretization of the Foias operator $\mathcal{F}_t$ can be obtained. Considering the same subspace of normalized indicator functions $\Delta_h \subset L^1(\mathbb{X})$ and the projection operator $Q_h : L^1(\mathbb{X}) \to \Delta_h$, and substituting $\mathcal{F}_t[f]$ into eq. (2.57), results in

$$\begin{aligned}
Q_h\mathcal{F}_t[f] &= \sum_{i=1}^{k} f_i Q_h \mathcal{F}_t[1_i], \\
&= \sum_{i=1}^{k} f_i \sum_{j=1}^{k} \left(\int_{b_j} \mathcal{F}_t[1_i]\, dx \right) 1_j, \\
&= \sum_{i=1}^{k} f_i \sum_{j=1}^{k} \left\{ \int_{\mathbb{X}} \left\{ \int_{\Omega_x(b_j)} \mathbb{P}_\omega(d\omega) \right\} 1_i\, dx \right\} 1_j, \\
&= \sum_{i,j=1}^{k} \frac{f_i}{m(b_i)} \int_{b_i} \left\{ \int_{\Omega_x(b_j)} \mathbb{P}_\omega(d\omega) \right\} dx\, 1_j, \\
&= \sum_{i,j=1}^{k} f_i p_{ij} 1_j,
\end{aligned} \tag{2.61}$$

where the projected operator $F_h : \Delta_h \to \Delta_h, F_h = Q_h\mathcal{F}_t$ is defined as

$$F_h 1_i = \sum_{j=1}^{k} p_{ij} 1_j,\ p_{ij} = \frac{1}{m(b_i)} \int_{b_i} \left\{ \int_{\Omega_x(b_j)} \mathbb{P}_\omega(d\omega) \right\} dx. \tag{2.62}$$

The Foias operator is a generalization for any random dynamical system in the mean sense, representing the global evolution of dynamical systems subject to a time-dependent random perturbation. Therefore, its discretization is an approximation in the mean sense of the flow for such systems, evolving mean distributions according to (2.49). Also, cases with both parameter uncertainty and stochastic dynamics can be represented similarly to $P_h(\lambda_i)$, that is, one discretized Foias $F_h(\lambda_i)$ operator is calculated for each $\lambda_i \in (\Lambda, \mathfrak{S}_\Lambda, P_\Lambda)$.

The discretized Koopman operators K_h for both deterministic and nondeterministic cases are given by the transpose of P_h and F_h, respectively, thanks to their dual relations. It encodes the basins of attraction in its fixed space, $gK_h = g$, for an initial condition $g_0 = \mathrm{id}_f$, where f is an attractor's distribution. Through the computation of ε-committor functions, the basins of attractions can be estimated and generalized for random dynamical systems [37]. For parameter uncertainty, the collections $f(\lambda_i)$ and $g(\lambda_i)$ can be used in the computation of means in the space $(\Lambda, \mathfrak{S}_\Lambda, P_\Lambda)$, approximating the mean statistics of the global dynamics.

3
Theoretical and numerical developments for adaptative phase-space refinement

In this chapter, adaptative procedures are developed within the set-oriented approach of the Ulam method for the global analysis of nonlinear dynamical systems with competing attractors. The stochastic basin of attraction definition by Linder and Hellmann [37] is adopted since it is, from the present point of view, the most natural with respect to the transfer operator's theory. Alternatives are also proposed to hierarchically discretize the phase-space in the stochastic basin of attractions' boundaries. The procedure to obtain basins and attractors in the mean sense of systems with parametric uncertainties is also presented. Finally, a comparison of two discretized phase-space structures is presented.

3.1. Boundary and attractor refinement procedures: the deterministic and stochastic case

The evaluation of the projected operators P_h, eq. (2.59) and F_h, eq. (2.62), involves a considerable number of time integrations when a Monte Carlo [37, 45] or quasi-Monte Carlo [180] strategy is employed. Thus, the discretized operators P_h and F_h converge weakly to the continuous operators $\mathcal{P}_t$ and $\mathcal{F}_t$, respectively, as $h \to 0$ [180]. However, the phase-space discretization inserts a numerical diffusion in the dynamical system [37, 49, 51], which inevitably changes the dynamics to a certain degree. A remedy is to increase the resolution, but this would impact the computational cost significantly.

A possible and efficient strategy is proposed here involving identifying regions for further discretization, taking advantage that the projection operator

Q_h, eq. (2.57), is not limited to cells of equal size, but only to disjoint partitions. To start the process, a disjoint partition of the phase-space into k boxes, $\mathbb{B}_i = \{b_1, \ldots, b_k\}$, is defined, covering the phase-space window of interest, $\mathbb{X}$. Also, the subindex $i = \{0, 1, 2, \ldots\}$ indicates the refinement level of the partition. A subset $\mathbb{S}_i \subseteq \mathbb{B}_i$ is also defined, including the boxes in which the flow φ_t must be evaluated to construct the entries of P_h, eq. (2.59), or F_h, eq. (2.62). Initially, it is presumed that no information regarding the phase-space flow is known, and therefore the flow is evaluated in all boxes, thus $\mathbb{S}_0 \equiv \mathbb{B}_0$. Then, the transfer matrices $P_h^{(i)}$ or $F_h^{(i)}$ are calculated. The flow φ_t of selected initial conditions in each $b \in \mathbb{S}_i$ is computed, and then the integrals in eq. (2.59) or (2.62) are approximated through the Monte-Carlo or quasi Monte-Carlo approach.

The *attractors' distributions* are calculated from the transfer matrix $P_h^{(i)}$ or $F_h^{(i)}$. Recall that $P_h^{(i)}$ and $F_h^{(i)}$ are (row) stochastic matrices, and the fixed distributions corresponding to the attractors are eigenvectors with eigenvalues equal to 1 [37]. Therefore, an eigenvalue problem, $f^{(i)} P_h^{(i)} = f^{(i)}$ or $f^{(i)} F_h^{(i)} = f^{(i)}$, must be solved. Since $P_h^{(i)}$ and $F_h^{(i)}$ are sparse, asymmetric in general, and indefinite, this is a difficult computational problem, requiring specialized algorithms. Additionally, the unitary eigenvalue has geometric multiplicity equal to the number of identified attractors in the partition $\mathbb{B}_i$. This poses a difficulty for the definition of the eigenvectors since geometric multiplicity means that they are not uniquely defined. To address this issue, the methodology proposed in [33] is adopted to construct a meaningful fixed eigenvector space in the sense of the problem, i.e., composed of distributions $f^{(i)} \geq 0, \left\| f^{(i)} \right\|_{L^1(\mathbb{X})} = 1$.

The *basins of attraction* $g^{(i)}$ are obtained next. Lindner and Hellmann [37] demonstrated that the basin structure is described by the fixed space of the Koopman operator $\mathcal{K}_t$. Since this operator is approximated by the transpose of the discretized transfer operators, $K_h^{(i)} = \left[P_h^{(i)} \right]^T$ or $K_h^{(i)} = \left[F_h^{(i)} \right]^T$, the basins of attraction are the solutions to the dual eigenvalue problem $g^{(i)} K_h^{(i)} = g^{(i)}$. The distributions $f^{(i)}$ and basins of attraction $g^{(i)}$ are the left and right eigenvectors of $P_h^{(i)}$, respectively, with unitary eigenvalues. Numerically, $g^{(i)}$ are obtained interactively or as a solution to an ill-conditioned linear problem. Starting from a known attractor distribution, the distribution function indicator, $g_0^{(i)} = \mathrm{id}_f$, is defined according to eq. (2.48). The interactive strategy consists in solving, recursively, the equation $g_{k+1}^{(i)} K_h^{(i)} = g_k^{(i)}$ until $\left\| g_{k+1}^{(i)} - g_k^{(i)} \right\|_{L^\infty} \leq \varepsilon$. In the limit, $\lim_{k\to\infty} g_k^{(i)} = g^{(i)}$. Therefore, the observable $g_k^{(i)}$ converges to the basin of attraction of $f^{(i)}$. The alternative strategy is to calculate basins of attraction as ε-committor functions by solving the ill-conditioned linear system [37]

$$\left(I - \left(1-\varepsilon\right) P_h^{(i)}\right) g^{(i)}\left(\varepsilon\right) = \varepsilon\,\mathrm{id}_f, \tag{3.1}$$

as employed by Benedetti and Gonçalves in [96].

The functions $g^{(i)}\left(\varepsilon\right)$ are discretizations of functions $g_A\left(\varepsilon\right)$ in eq. (2.34), where the latter is defined over continuous phase-spaces, and the former is defined over discretized phase-spaces. As previously stated, the limit $\lim_{\varepsilon\to 0} g^{(i)}\left(\varepsilon\right) = g^{(i)}$ corresponds to the basin of attraction of $f^{(i)}$ in the classical sense, see section 2.4. Each component of $0 \leq g_j^{(i)}\left(\varepsilon\right) \leq 1$ gives the probability that a trajectory initially in box b_j converges to the distribution $f^{(i)}$ at time $1/\varepsilon$. The time defined by $1/\varepsilon$ is the number of interactions of the transfer operator $P_h^{(i)}$ or $F_h^{(i)}$. It gives a useful generalization for basins of attraction, encompassing both deterministic and stochastic (noise-driven) cases. Transient effects can be considered, adopting distinct initial states of attractors' distributions and/or $\varepsilon > 0$. The problem of parameter uncertainty will be discussed in the next section since the ε-committor function is not directly generalized to such cases.

Once the distributions $f^{(i)}$ and basins of attraction $g^{(i)}$ are calculated, they can be used to identify and flag subdivision and flow recalculation boxes. The attractors' phase-space locations tend to have a high-density value, identified by a large value in a component of $f^{(i)}$. Therefore, the heuristic constraint

$$f_j^{(i)} \geq c_f, \tag{3.2}$$

is adopted to identify such regions. This strategy is straightforward since it only depends on the computed density in the j^{th} box, whereas strategies considering the local upper bound L^1 error need information about neighboring boxes [184]. However, it does not clearly define when the process should stop, needing a threshold discretization level to finish the process.

Regarding the basins' boundaries, if a saddle's stable manifold passes through a box b_j, then there will be values between 0 and 1 in the j^{th} element of one of the associated basins $g^{(i)}$. That is, trajectories passing through boxes b_j can converge to distinct attractors. This effect is also known as numeric diffusion [183] for deterministic systems, caused by discretization. For nondeterministic systems, both numeric and real diffusion can happen, and such regions increase as the uncertainty increases. Therefore, a second constraint is defined,

$$0 < c_g^{(1)} \leq g_j^{(i)} \leq c_g^{(2)} < 1, \tag{3.3}$$

identifying boxes that can converge to more than one attractor with significant probability. Again, this strategy depends only on the computed basin in the j^{th} box. Other methodologies consider the neighbor´s information [185], but are computationally more involved. To the authors' knowledge, there is no upper bound local error definition for basins analogous to the upper bound L^1 error for densities, as presented in [184]. Therefore, a heuristic criterion to stop the subdivision strategy must be adopted. In the analyzed examples, the highest i^{th} level is defined *a priori*.

Figure 3.1 illustrates the selection and subdivision process where the disjoint set and the flow field at two subsequent refinement levels i (left) and $i+1$ (right) are reported in the upper (a) and lower (b) parts, respectively. Figure 3.1(a) (left) presents the i-th partition, with the $b_j^{(i)}$ attractor or boundary boxes identified through (3.2) or (3.3) marked in green. In the corresponding flow of Figure 3.1(b) (left), the red arrows are those to be recomputed in the next step, either because of being directed inward/outward of the green boxes to be subdivided or because of coming from neighboring boxes as colored in red in Figure 3.1(a) (left). The newly formed collection of boxes (in yellow in Figure 3.1(a) (right)) defines the subset $\mathbb{S}_{i+1}$ in which the flow will be computed at level $i+1$. Together with the white boxes, they form the new partition $\mathbb{B}_{i+1}$, with the redefined flow given by Figure 3.1(b) (right). Density and boundary boxes are again identified through (3.2) or (3.3) and the selection and subdivision process repeats. The proposed procedure is summarized in Table 3.1

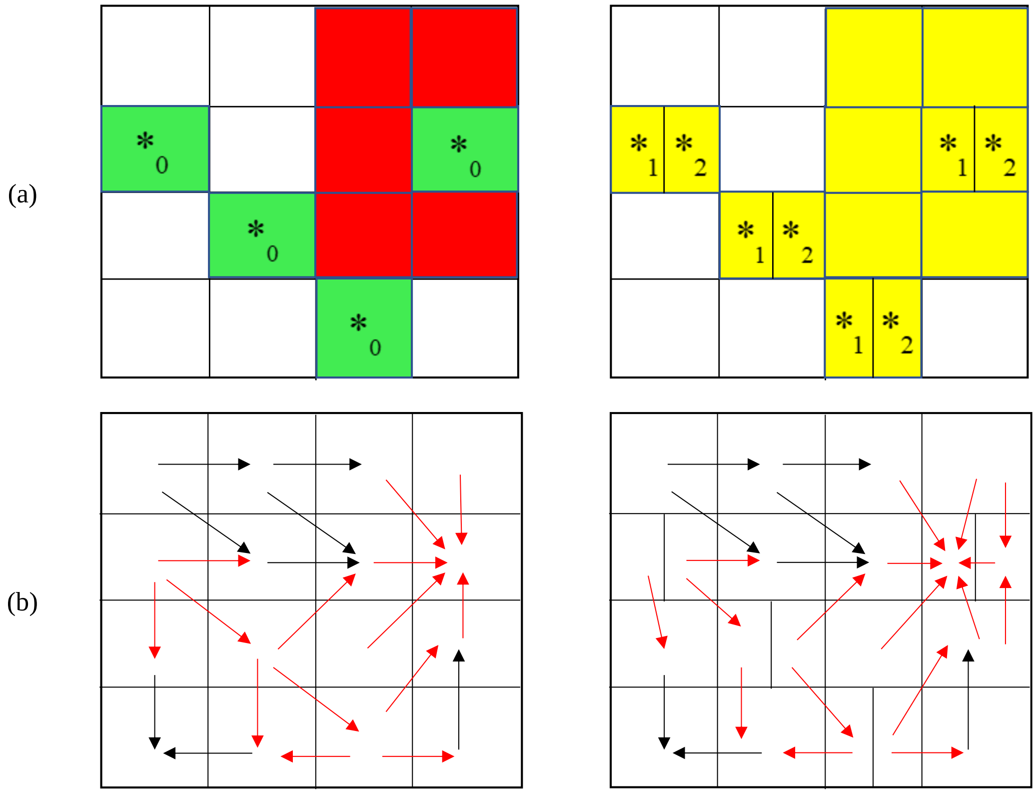

Figure 3.1 – (a) Disjoint sets $\mathbb{B}_i$ (left) and $\mathbb{B}_{i+1}$ (right). Left: boxes for subdivision in green, labelled as $*_0 = b_j^{(i)}$, and preimage boxes in red. Right: subset of boxes $\mathbb{S}_{i+1}$ that will be computed, and child boxes $*_1 = b_{2j}^{(i+1)}$ and $*_2 = b_{2j+1}^{(i+1)}$. (b) Corresponding initial (left) and updated (right) flow fields.

The phase-space subdivision algorithm is organized in a binary tree structure [32], where $b_j^{(i)}$ at a certain level i is the parent box of its subdivided boxes $b_{2j}^{(i+1)}$ and $b_{2j+1}^{(i+1)}$ at level $i+1$, such that $b_j^{(i)} = b_{2j}^{(i+1)} \cup b_{2j+1}^{(i+1)}$ and $b_{2j}^{(i+1)} \cap b_{2j+1}^{(i+1)} = \varnothing$. Examples of this structure are depicted in Figure 3.1(a). This allows optimal storage, subdivision, and search of elements. This strategy was previously used in the software GAIO [43].

The proposed procedure refines important phase-space regions, where crude discretizations would result in significantly different outcomes and can be applied to external or parametric excitation problems with noise. The fundamental hypothesis is that the sequence of transfer matrices $P_h^{(i)}$ and $F_h^{(i)}$ converge in the $L^1(\mathbb{X})$ space, formally denoted as $\lim_{i\to\infty}\left\|P_h^{(i)}-\mathcal{P}_t\right\|_{L^1(\mathbb{X})}=0$ and $\lim_{i\to\infty}\left\|F_h^{(i)}-\mathcal{F}_t\right\|_{L^1(\mathbb{X})}=0$, and that their transpose $K_h^{(i)}$ converges in the $L^\infty(\mathbb{X})$ space, formally denoted as $\lim_{i\to\infty}\left\|K_h^{(i)}-\mathcal{K}_t\right\|_{L^\infty(\mathbb{X})}=0$.

Table 3.1 – Refinement algorithm for box space

0.	Construct collection $\mathbb{S}_0$ and partition $\mathbb{B}_0$ of phase-space $\mathbb{X}$; set i = 0
1.	Update $P_h^{(i)}$ or $F_h^{(i)}$ with the new collection $\mathbb{S}_i$ from partition $\mathbb{B}_i$
2.	Obtain invariant distributions (attractors) $f^{(i)}$ solving the eigenvalue problem $f^{(i)}P_h^{(i)}=f^{(i)}$ or $f^{(i)}F_h^{(i)}=f^{(i)}$
3.	Calculate basins of attraction $g^{(i)}$ of each distribution $f^{(i)}$
4.	If $i=i_{\max}$ then finish, else continue
5.	Identify sets for subdivision, corresponding to basins boundaries, eq. (3.3), and attractors distributions, eq (3.2)
6.	Refine identified sets and construct new collection $\mathbb{S}_{i+1}$ and partition $\mathbb{B}_{i+1}$
7.	Set i = i + 1 and go to step 1

3.2.
Refinement procedure for parameter uncertainty

Here, the procedure for obtaining the mean results for dynamical systems with parameter uncertainty is outlined. Since the aim is to deal with general nonlinear dynamical problems, sparse sampling strategies of the parameter space are not adequate, given that the dynamical system may depend strongly on it, particularly when close to bifurcation points, as shown by Le Maître and Knio [172]. Since the analysis is limited to bounded parameter spaces, only a window of the phase-space is considered in all cases.

If a parameter set $\Lambda=\{\lambda_1,\lambda_2,\ldots,\lambda_n\}$ is defined with a constant interval $\Delta\lambda=\lambda_i-\lambda_{i-1}$, a continuous probability measure $\mathbb{P}_\lambda$ can be discretized as

$$P_\Lambda(\lambda_i) = \mathbb{P}_\lambda\left[\left(\lambda_i - \frac{\Delta\lambda}{2}\right) \le \lambda \le \left(\lambda_i + \frac{\Delta\lambda}{2}\right)\right], \tag{3.4}$$

resulting in a discretization of the continuous bounded parameter space $\left[\lambda_1 - \Delta\lambda/2, \lambda_n + \Delta\lambda/2\right]$. Therefore, the continuous probability space $\left(\mathbb{L}, \mathfrak{S}, \mathbb{P}_\lambda\right)$ can be effectively substituted by the discrete probability space $\left(\Lambda, \mathfrak{S}_\Lambda, P_\Lambda\right)$, where $\mathfrak{S}_\Lambda$ is a σ-algebra over Λ. The resulting problem is a collection of deterministic or stochastic dynamical systems, pondered by the discrete probability measure P_Λ. Finally, the algorithm in Table 3.1 is applied to all Λ, and statistics are computed according to P_Λ. The mean values are calculated according to the rectangle rule,

$$\mathbb{E}\left[f(\lambda)\right] = \int_{\mathbb{L}} f(\lambda; x)\, d\mathbb{P}_\lambda \approx \sum_{i=1}^{n} f(\lambda_i; x) P_\Lambda(\lambda_i), \tag{3.5}$$

where $f(\lambda; x)$ represents any dynamical structure dependent on the parameter λ, such as attractors' distributions, basins of attraction, or manifolds. Eq. (3.5) is an approximation of an integral by a weighted sum, a strategy that has been used in uncertainty quantification [172]. No continuation procedure is necessary if the discretization methodology covers the entire phase-space window, identifying all existing attractors (which is not always the case, in particular when one wants to "zoom" around certain attractors/basins of interest). It is only required to determine to which branch the identified attractors with a parameter λ_i belong.

The distance between the distributions of two attractors is calculated through the Lukaszyk-Karmowski metric [186],

$$D(A_1, A_2) = \int_{\mathbb{X}}\int_{\mathbb{X}} d(x, y)\, f_{A_1}(\lambda; x)\, f_{A_2}(\lambda; y)\, dx dy, \tag{3.6}$$

where the function $d(x, y)$ is the distance between two points x and y in $\mathbb{X}$ and $f_A(\lambda; x)$ are the attractors' distributions calculated by the subdivision algorithm given a parameter λ. A small $D(A_1, A_2)$ value means that the attractors A_1 and A_2 belong to the same branch. This choice has two justifications: first, the operator approach always results in a discrete distribution, even in the deterministic case, and second, this approach can theoretically be applied also to noise-induced dynamics.

If a smaller phase-space window is adopted, attractors outside of it are flagged as escape solutions. Escape solutions are identified previously and do not enter in the metric calculation, eq. (3.6). Also, there is no distinction between escape solutions and attractors outside the window, and basin structures that do belong to those attractors are also flagged as escape solutions. This can be an issue if an attractor moves outside the phase-space due to the parameter variation, altering the resulting density and basin.

The parameter space subdivision procedure takes advantage of the fact that bounded probability spaces can be, by definition, decomposed into a countable set of discrete points. It can be viewed as an extension of the Ulam method but with a general probability measure instead of the usual Lebesgue measure. Also, it can be generalized to multidimensional parameter spaces. Adaptative discretization of the parameter space can reduce the computational cost of the discretization refinement [172].

3.3. Modifications to the refinement algorithm for the discretization of stable and unstable manifolds

Traditionally, a flow $\varphi : \mathbb{X} \times \mathbb{T} \to \mathbb{X}$ of a given dynamical system is assumed as a closed flow, that is, the density is conserved over time. This leads to the existence of constant distributions *f* given by eq. (2.37). The set of all linearly independent *f* that are solutions of eq. (2.37) defines the Perron-Frobenius fixed space, see [17, 42, 181–183].

The recent developments of Klünker et al. [187] demonstrated that the Ulam method could be applied to the analysis of the stable and unstable manifolds, structures that organize the flow in the phase-space [181]. From the discretized operator P_h, an open flow system is defined by eliminating boxes b_j with the probability of the flow returning to them equal to 1. Numerically, this can also be achieved by setting zero the j^{th} lines and columns of P_h, forming a new operator

$\bar{P}_h$. Distinct from the closed system operator P_h, this new operator $\bar{P}_h$ is a row-substochastic matrix, with a constant outflow of densities [187]. This matrix governs all transient states in the phase-space $\mathbb{X}$, with density decaying to zero everywhere in a finite time. The spectrum of $\bar{P}_h$ contains the stable and unstable manifolds, obtained as the eigenvectors with real and positive eigenvalues smaller than one. They are solutions of the systems

$$\mu p = p\bar{P}_h, \tag{3.7}$$

$$\mu q = \bar{P}_h q, \tag{3.8}$$

where the left-eigenvectors *p* (respectively right-eigenvectors *q*) with larger real part governs the unstable manifolds (respectively stable manifolds). The corresponding continuous set is obtained by considering a Markov operator $\bar{\mathcal{P}}_t$ as

$$\begin{aligned} &\bar{\mathcal{P}}_t : L^1(\mathbb{X}_o) \to L^1(\mathbb{X}_o), \\ &f \mapsto \bar{\mathcal{P}}_t[f], \end{aligned} \tag{3.9}$$

where $\mathbb{X}_o \subset \mathbb{X}$ is the phase-space minus the attractors' regions, which are given by $\mathrm{fix}(\mathcal{P}_t)$. The flow in $\mathbb{X}_o$ is open, that is, there is a continuous outflow of mass from $\mathbb{X}_o$ to $\mathrm{fix}(\mathcal{P}_t)$. Similarly, the dual operator is defined as

$$\begin{aligned} &\bar{\mathcal{K}}_t : L^\infty(\mathbb{X}_o) \to L^\infty(\mathbb{X}_o), \\ &g \mapsto \bar{\mathcal{K}}_t[g]. \end{aligned} \tag{3.10}$$

Instead of using only conditions (3.2) and (3.3), the *p* and *q* eigenvectors of the open flow operator $\bar{P}_h$ are considered as additional criteria for the subdivision strategy. To this end, the algorithm in Table 3.1 is modified, specifically after step 5, where the sets for subdivision are identified, adding the construction of $\bar{P}_h$, the calculus of its left and right eigenvectors, and the selection of boxes for subdivision.

The open flow operator $\bar{P}_h$ is constructed from the original operator P_h and its invariant distributions *f*. It should be observed that the original strategy in [187] assumes that attractor sets b_j are such that $P_{h;j.j} = 1$, which is based only on the discrete setting. However, it can miss periodic, quasi-periodic, and chaotic attractors, since, as demonstrated by Lasota and Mackey [17], and by Hsu [188], their distributions are spread over many sets b_j, all with $P_{h;j,j} < 1$. This is also problematic for stochastic systems, where attractors are diffused over large regions of the phase-space, as shown by Sun and Hsu [24]. Therefore, the boxes that cover the entire support of the attractors' distributions, $\operatorname{supp}(f)$, are considered, allowing other types of attractors to be analyzed. Still, it was observed that if f is too concentrated, then its vicinity could behave as a long transient in the discrete space, preventing the manifold identification. To prevent this, the preimages of f should be considered as well in the construction of $\bar{P}_h$.

The process starts by verifying if a given distribution f is too concentrated. This is checked by the ratio between the distribution's indicator function support and the total volume of the phase-space window,

$$\operatorname{supp}(\bar{f}) \geq c_x \int_{\mathbb{X}} dx, \tag{3.11}$$

where $\bar{f} = f$ in the first iteration. If eq. (3.11) is true, then the attractor is not too concentrated in the discretized space. If it is false, then $\bar{f}$ is backpropagated through the Koopman operator, that is, $\bar{f} := \bar{f} K_h$, and eq. (3.11) is evaluated again. This process repeats until the condition is satisfied. Then, the j^{th} lines and columns of $\bar{P}_h$ corresponding to $\operatorname{supp}(\bar{f})$ are set to zero. All other entries of $\bar{P}_h$ are identical to P_h. The construction of $\bar{P}_h$ is summarized in Table 3.2.

Table 3.2 – Construction of open flow discrete transfer operator $\bar{P}_h^{(i)}$

0.	Take $\bar{f} = f^{(i)}$
1.	Evaluate eq. (3.11). If true, then go to 3, else continue
2	Backpropagate $\bar{f}$ through the Koopman operator, $\bar{f} := \bar{f} K_h^{(i)}$, and go to step 1
3.	Define $\bar{P}_h^{(i)} = P_h^{(i)}$. Then, set to zero its j^{th} lines and columns corresponding to $\operatorname{supp}(\bar{f})$

Next, the eigenvectors p and q are calculated by solving the eigenvalue problems (3.7) and (3.8) for the largest real part of μ. Finally, boxes b_j satisfying the inequalities

$$p_j \geq c_p, \tag{3.12}$$

$$q_j \geq c_p. \tag{3.13}$$

are selected for subdivision. Table 3.3 presents the refinement algorithm.

Table 3.3 – Modified refinement algorithm for box space

0.	Construct collection $\mathbb{S}_0$ and partition $\mathbb{B}_0$ of phase-space $\mathbb{X}$; set i = 0;
1.	Update $P_h^{(i)}$ or $F_h^{(i)}$ with the new collection $\mathbb{S}_i$ from partition $\mathbb{B}_i$;
2.	Obtain invariant distributions (attractors) $f^{(i)}$ solving the eigenvalue problem $f^{(i)}P_h^{(i)} = f^{(i)}$ or $f^{(i)}F_h^{(i)} = f^{(i)}$;
3.	Calculate basins of attraction $g^{(i)}$ of each distribution $f^{(i)}$;
4.	Construct $\overline{P}_h^{(i)}$ according to Table 3.2;
5.	Solve eq. (3.7) and eq. (3.8), then select the $p^{(i)}$ and $q^{(i)}$ eigenvectors with larger real part of eigenvalue μ;
6.	If $i = i_{\max}$ then finish, else continue;
7.	Identify additional sets for subdivision that obey eq. (3.12) and (3.13);
8.	Refine identified sets and construct new collection $\mathbb{S}_{i+1}$ and partition $\mathbb{B}_{i+1}$;
9.	Set i = i + 1 and go to step 1.

3.4.
Use of r-trees for phase-space subdivision

Here the efficiency of using r-trees to organize the phase-space subdivision instead of binary trees used in GAIO [43] is investigated. Consider a hyperdimensional phase-space, subdivided progressively from depth 0 (2^0 box) to the n depth (2^n boxes). Assume that the number of initial conditions in each box depends on the depth level, being $(n - i + 1)^d$ for a binary tree, where $0 \leq i \leq n$, and $(n - d\, i + 1)^d$ for a r-tree, where $0 \leq i \leq n/d$, and d is the phase-space dimension. The total number T of initial conditions in all phase-space at a given level is, for the binary tree, is given by

$$T_b = 2^i\left(n-i+1\right)^d \tag{3.14}$$

and is, for a r-tree,

$$T_n = 2^{di}\left(n-di+1\right)^d . \tag{3.15}$$

The cumulative number CT of initial conditions is, for the binary tree,

$$CT_b = \sum_{i=0}^{n} 2^i\left(n-i+1\right)^d , \tag{3.16}$$

and is, for a r-tree,

$$CT_n = \sum_{i=0}^{n/d} 2^{di}\left(n-di+1\right)^d . \tag{3.17}$$

By comparing eq. (3.16) and (3.17), the most advantageous procedure in terms of the total initial conditions can be quantified. For this, the expression CT_n/CT_b is plotted for various d values in Figure 3.2. All curves converge to a fixed ratio as the level depth increases. This stabilized ratio decreases as the phase-space dimension increases, indicating that the use of r-trees is more advantageous for larger dimensions and a complex phase-space structure.

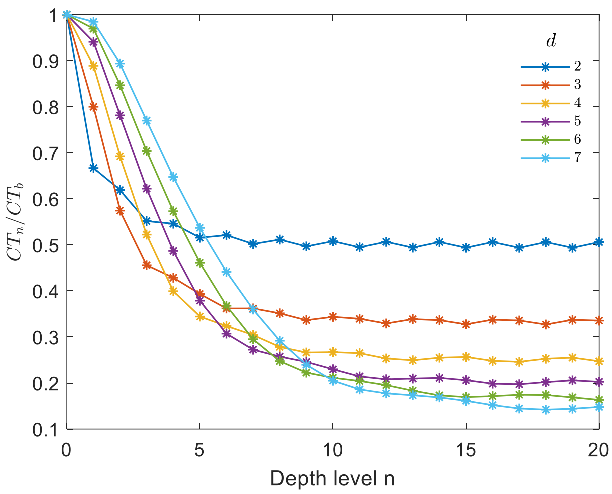

Figure 3.2 – Evolution of the ratio between cumulative initial conditions of a binary tree and a r-tree with the depth level, for various phase-space dimension values d

4 Archetypal oscillators

In this section, to understand the influence of noise and uncertainties on the global dynamics of multistable systems, the single-degree-of-freedom Duffing and Helmholtz oscillators are chosen. Despite their simplicity, Duffing and Helmholtz oscillators exhibit a rich dynamical behavior and have been used to describe the nonlinear dynamics of many real-world nonlinear systems for a wide range of frequency bands and amplitude of the excitation. Kovacic and Brennan [164] published a detailed historical review of the Duffing oscillator and its nonlinear dynamics, highlighting its application in engineering, physics, astronomy, mathematics, computer sciences, etc. The Helmholtz oscillator has been extensively used for the analysis of escape from a potential well (escape equation), with interesting applications ranging from ship capsize [189] to structures liable to asymmetric buckling [113, 190]. Also, Duffing and Helmholtz oscillators have been extensively used as a didactic tool for the phenomenological analysis of nonlinear dynamical systems [191–193] and to model the dynamics of structural systems liable to buckling since the presence of quadratic and cubic nonlinearities allows the description of the potential functions associated to the basic types of bifurcation [194]. The deterministic global dynamics and dynamic integrity of these two oscillators were previously explored in [63, 64, 76] and their results are here used as benchmarks. A proper probabilistic interpretation of the nondeterministic global dynamics, explored in Chapter 2, is adopted together with the concepts and numerical tools presented in Chapter 3. In this chapter, the algorithm shown in Table 3.1 is implemented to hierarchically discretizes the phase-space through a binary tree and obtain the attractors and basins' distributions. The computations are performed by an Intel Core i7-7700HQ with eight logical processors of 2.8GHz, and the total available RAM is 24GB. The algorithm performance is measured by the reduced number of phase-space boxes, which is the primary cost in the computations. Total time was not evaluated, since a parallel implementation with openMP (https://www.openmp.org/) was considered for the integration of the initial conditions.

4.1. Helmholtz oscillator with harmonic excitation

The first example consists of the standard dimensionless form of the damped harmonically excited Helmholtz oscillator,

$$\ddot{x} + \delta\dot{x} + (\alpha + \sigma\lambda)x + \beta x^2 = A\sin\Omega t + s\dot{W}. \tag{4.1}$$

where α is the mean linear stiffness value, the random variable λ is a truncated standard normal with density $f(\lambda;0,1,-3,3)$, σ is a scaling factor, $\dot{W}$ is a standard white noise process, and s is the noise standard deviation. Thus, the system is deterministic for $\sigma = 0$ and $s = 0$. For a normal distribution, the density decreases in a regular way with distance from the mean, most probable value. One drawback, however, is that it supplies a positive probability density to every value in $(-\infty, +\infty)$, although the actual probability of an extreme event will be very low. In most cases, based on design codes and experimental values, the range of a given parameter is bounded. A mathematical way to preserve the main features of the normal distribution while avoiding extreme values is achieved by adopting a truncated normal distribution, in which the range of definition is finite at one or both ends of the interval [195].

The Helmholtz oscillator has one potential well, with two different classes of oscillations, bounded periodic nonlinear oscillations within the well and unbounded nonperiodic solutions [63]. This is a useful archetypal model, presenting escape, basin erosion, and integrity loss, and may describe the behavior of various dynamical systems. See, for example, [10, 113, 189, 190]. The values in Table 4.1 are adopted, resulting in three possible outcomes, a small amplitude oscillation, a large amplitude oscillation, and escape solutions [63].

Table 4.1 – Helmholtz oscillator parameters

Parameter	Value
α	-1
λ	$f(\lambda; 0, 1, -3, 3)$
β	1
δ	0.1
Ω	0.81

Based on [63], the adopted phase-space window is $\mathbb{X} = \{-0.7, 1.8\} \otimes \{-1, 1\}$. The initial box partition is defined as a division of 2^5 in each dimension, totaling 32x32 = 1024 boxes of size {0.0781, 0.0625}, with one additional sink box that attracts the escape solutions. The procedure is conducted through 10 steps, with a final box size of {0.0024, 0.0020}. Also, the number of initial conditions per box depends on the box size, decreasing with refinement. The number of collocation points for each level is presented in Table 4.2. The usual Perron-Frobenius operator governs the phase-space distributions for the deterministic case, thus eq. (2.59) is considered. The fourth-order Runge-Kutta method is adopted for the construction of the flow φ_T, with time-step T/200, where $T = 2\pi/\Omega$ and Ω is the forcing frequency.

Table 4.2 – Discretization data for the Helmholtz oscillator

Depth level	Box-size	Points per dimension	Total collocation points
10	{0.0781, 0.0625}	12	144
11	{0.0391, 0.0625}	11	121
12	{0.0391, 0.0313}	10	100
13	{0.0195, 0.0313}	9	81
14	{0.0195, 0.0156}	8	64
15	{0.0098, 0.0156}	7	49
16	{0.0098, 0.0078}	6	36
17	{0.0049, 0.0078}	5	25
18	{0.0049, 0.0039}	4	16
19	{0.0024, 0.0039}	3	9
20	{0.0024, 0.0020}	2	4

The evolution of basins of attraction of the small and large amplitude solution as a function of the excitation magnitude $(A \in [0.05, 0.08])$ is shown in Figure 4.1 (nonresonant attractor) and Figure 4.2 (resonant attractor), respectively. The attractors are marked in red. The black region corresponds to attractors distinct from the one being displayed, including escape solutions. The color scale differentiates regions converging to the depicted attractor from probability zero to probability one. There is only one attractor for $A = 0.05$ (yellow basin). As expected for the deterministic case, the probability is either zero or one, with the exception of the folded fractal, see Figure 4.1(c, d) and Figure 4.2(c, d), where regions close to the boundaries have values between zero and one, since initial conditions in the same cell may, due to their finite size, converge to one of the two attractors or escape. After the emergence of the large amplitude attractor in the resonant region, the evolution of the basins' boundaries shows increasing competition. The loss of integrity of the basins with increasing load is clarified by the decreasing area. The algorithm has shown to be robust enough to discretize the boundaries in highly fractal and intertwined basins, as observed in Figure 4.1(d) and Figure 4.2(c). The set of initial conditions outside the two coexisting basins corresponds to solutions diverging to infinity [63].

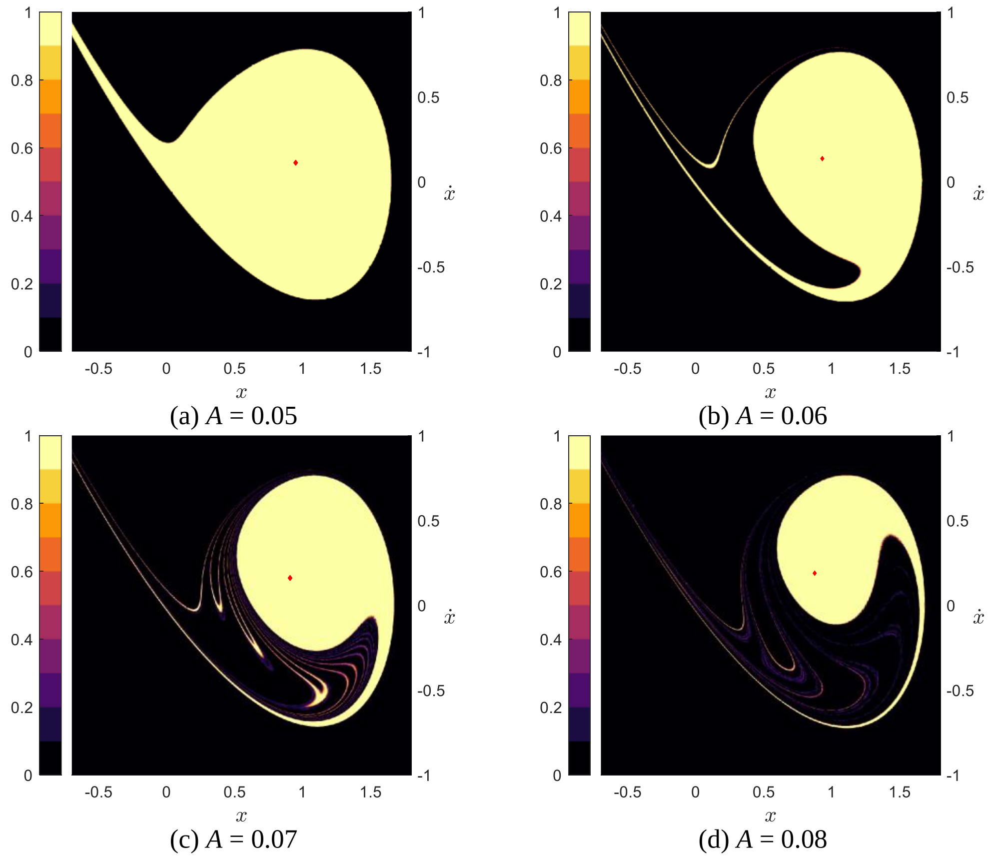

(a) $A = 0.05$ (b) $A = 0.06$

(c) $A = 0.07$ (d) $A = 0.08$

Figure 4.1 – Evolution of the Helmholtz oscillator small amplitude attractor's basin (color bar) with the forcing magnitude

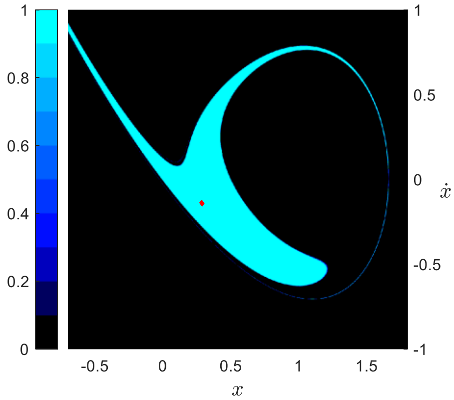

(a) A = 0.06

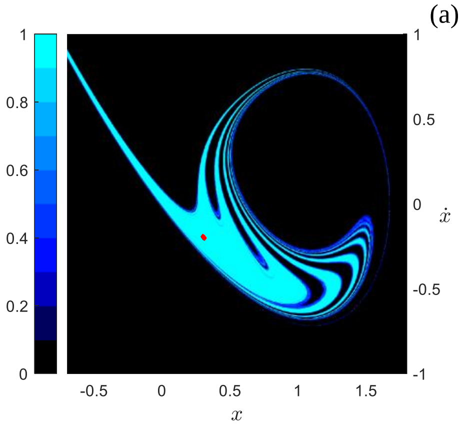

(b) A = 0.07

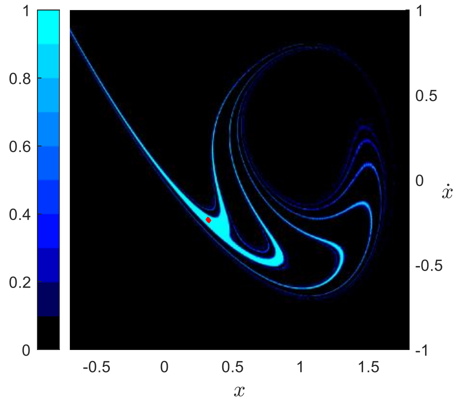

(c) A = 0.08

Figure 4.2 – Evolution of the Helmholtz oscillator large amplitude attractor's basin (color bar) with the forcing magnitude

Figure 4.3 presents the final box partition, $\mathbb{B}_{20}$, for an increasing excitation amplitude. It is evident that more boxes are needed to discretize the boundaries as the basin topology becomes more intricate. The partitions from level 10 up to 15 are depicted in Figure 4.4 for A = 0.06 to demonstrate the refinement procedure. Green boxes satisfy one of the conditions (3.2) and (3.3), being either boundary boxes or attractor boxes. Specifically, the distribution threshold of eq. (3.2) is adopted as $c_f = 10^{-10}$, while the boundary thresholds of eq. (3.3) are calculated as $c_g^{(1)} = \min g + 0.03\Delta g$ and $c_g^{(2)} = \max g - 0.01\Delta g$. This permits the boundary thresholds to be subdivided, allowing long transient solutions due to crude initial discretization to be refined as well. For example, in Figure 4.4, the thresholds for the escape basin and the nonresonant basin are (0.03; 0.99) for all levels, while the resonant basin has (0.0299; 0.9874) at level 10 and (0.0201; 0.6635) at level 11, only attaining the limits (0.03; 0.99) for higher levels of discretization. For discretization levels equal to or lower than 11, the eigenvalues of P_h show that the resonant solution behaves as a long transient solution. This could lead to the wrong assumption that there is no resonant solution unless the analysis proceeds to higher discretization levels.

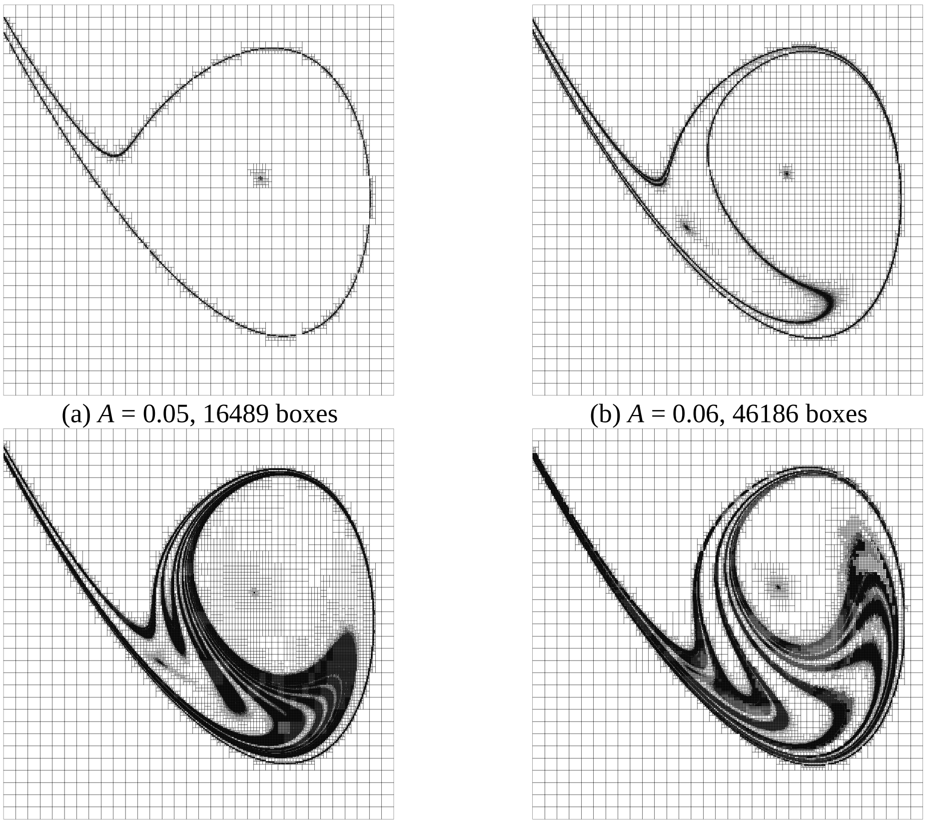

(a) A = 0.05, 16489 boxes (b) A = 0.06, 46186 boxes

(c) A = 0.07, 203564 boxes (d) A = 0.08, 202561 boxes

Figure 4.3 – Dependence of the final partition $\mathbb{B}_{20}$ of the Helmholtz oscillator as a function of the excitation magnitude A

In Figure 4.4, red boxes are preimages of the green boxes, recalculated in each subsequent step, as explained in Section 3.2. The partition refinement is conducted by subdividing green boxes, thus locally refining the phase-space near attractors and boundaries. As the algorithm progresses, the green boxes concentrate at the basins' boundary and the attractor, refining these regions in the phase-space, as desired. Finally, the total box count for each depth level and A = 0.06 is given in Table 4.3. A comparison of the current box count with a full discretization at a given level (maximum box count) is shown, with the last column representing the computational economy defined as the ratio between the maximum-to-current box count difference and the maximum box count. Lower economy values imply higher computational costs. This economy increases with the depth level, being over 90% from level 18 onwards.

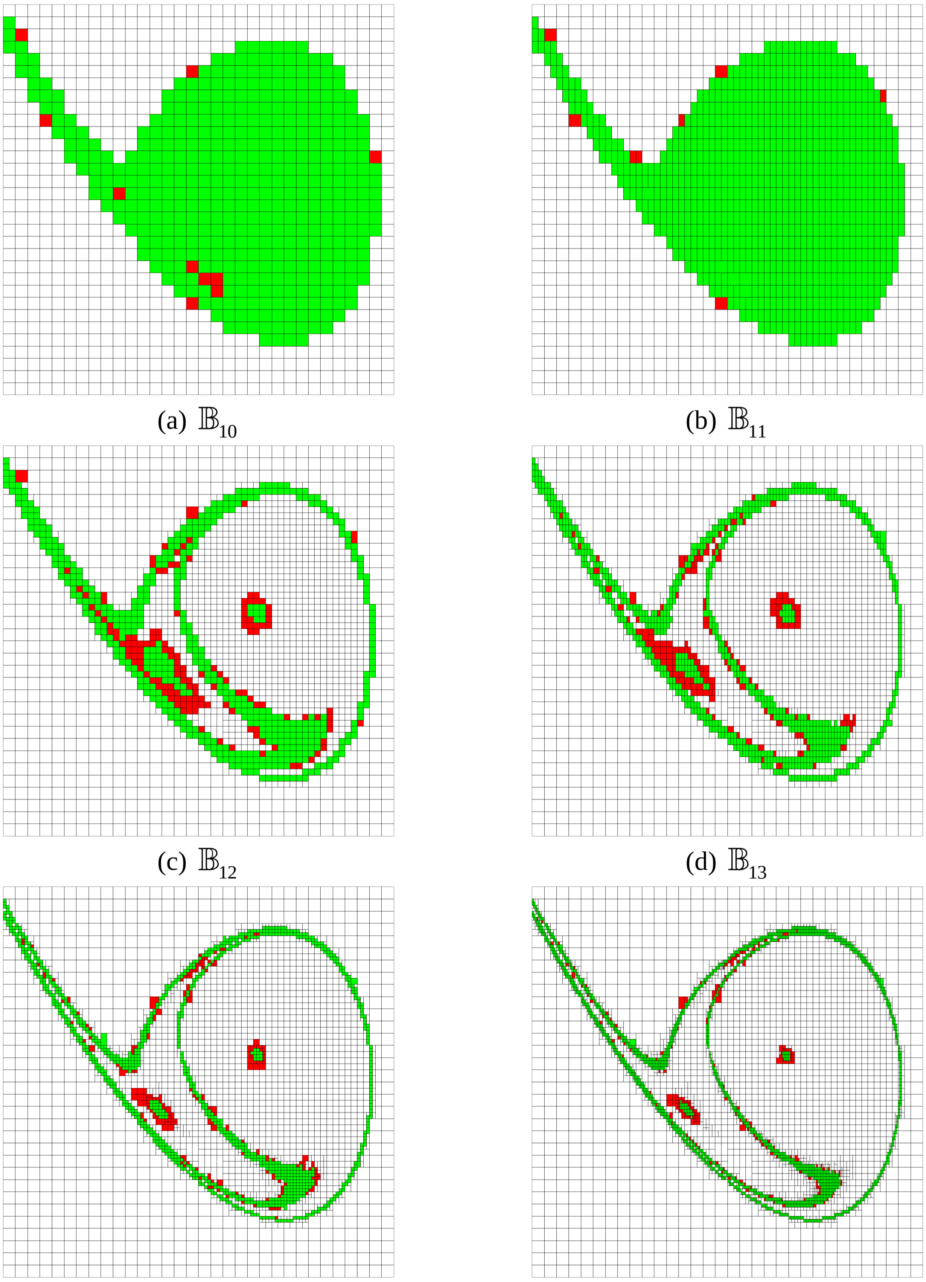

(a) $\mathbb{B}_{10}$ (b) $\mathbb{B}_{11}$

(c) $\mathbb{B}_{12}$ (d) $\mathbb{B}_{13}$

(e) $\mathbb{B}_{14}$ (f) $\mathbb{B}_{15}$

Figure 4.4 – Interactive partition evolution of the Helmholtz oscillator for A = 0.06. Green: cells for subdivision, red: cells for recalculation

Table 4.3 – Box count for the deterministic Helmholtz oscillator for A = 0.06

Depth level	Current box count	Maximum box count	Percentual	Economy
10	1024	1024	100.00%	0%
11	1906	2048	93.07%	6.93%
12	3596	4096	87.79%	12.21%
13	4756	8196	58.03%	41.97%
14	6426	16384	39.22%	60.78%
15	8712	32768	26.59%	73.41%
16	12104	65536	18.47%	81.53%
17	16940	131072	12.92%	87.53%
18	23816	262144	9.09%	90.91%
19	33322	524288	6.36%	93.64%
20	46186	1048576	4.40%	95.60%

4.1.1. Effects of parameter uncertainty

Before the influence of the parameter uncertainty is addressed, it is advantageous to understand the implications of considering an uncertain parameter near a bifurcation point. To this end, Figure 4.5 presents both the dependency of the stable responses on varying stiffness parameter α for the excitation magnitude A = 0.06 and the normalized probability distributions of $\alpha + \sigma\,\lambda$. There is a clear interval of α where the resonant and nonresonant responses coexist. Two saddle-node bifurcations limit the interval, with two possible jumps for a continuous change of α, forming a hysteretic cycle. Only one of the responses exists outside this region, the resonant for $\alpha < -1.1$ and the nonresonant for $\alpha > -0.92$. Three cases are chosen to investigate the influence of parameter uncertainty, varying the standard deviation σ. For $\sigma < 0.04$, the probability of $\alpha + \sigma\,\lambda$ being outside of the hysteresis cycle is negligible. However, for $\sigma \geq 0.04$, the uncertainty's effect on the results cannot be neglected. This is illustrated in Figure 4.6 where bifurcation diagram probability densities for varying values of the scaling parameter σ are shown. They are obtained through a Monte Carlo analysis of the Helmholtz oscillator considering 10000 initial conditions uniformly distributed over the phase-space $\mathbb{X}$ for A = 0.06 using the Poincaré section at t = 1000T. For comparison purposes the bifurcation path of the deterministic system is plotted in grey. For σ = 0.01 already a small region in the middle of the hysteretic cycle is affected by the uncertainty. As σ increases, the influence of uncertainty increases (see color bar), and at σ = 0.03 its influence is observed already beyond the hysteretic cycle, demonstrating the influence of the uncertainty on the two saddle-node bifurcations and consequently on the bifurcation values.

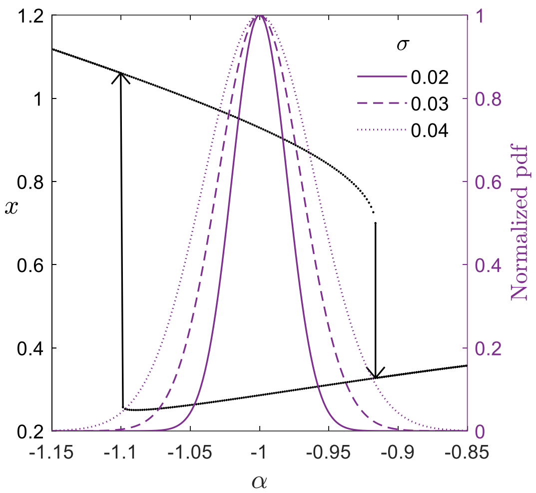

Figure 4.5 – Bifurcation diagram of the Helmholtz oscillator as a function of the stiffness parameter α and A = 0.06 and the normalized probability distributions of $\alpha + \sigma\lambda$ for selected values of the scaling parameter σ

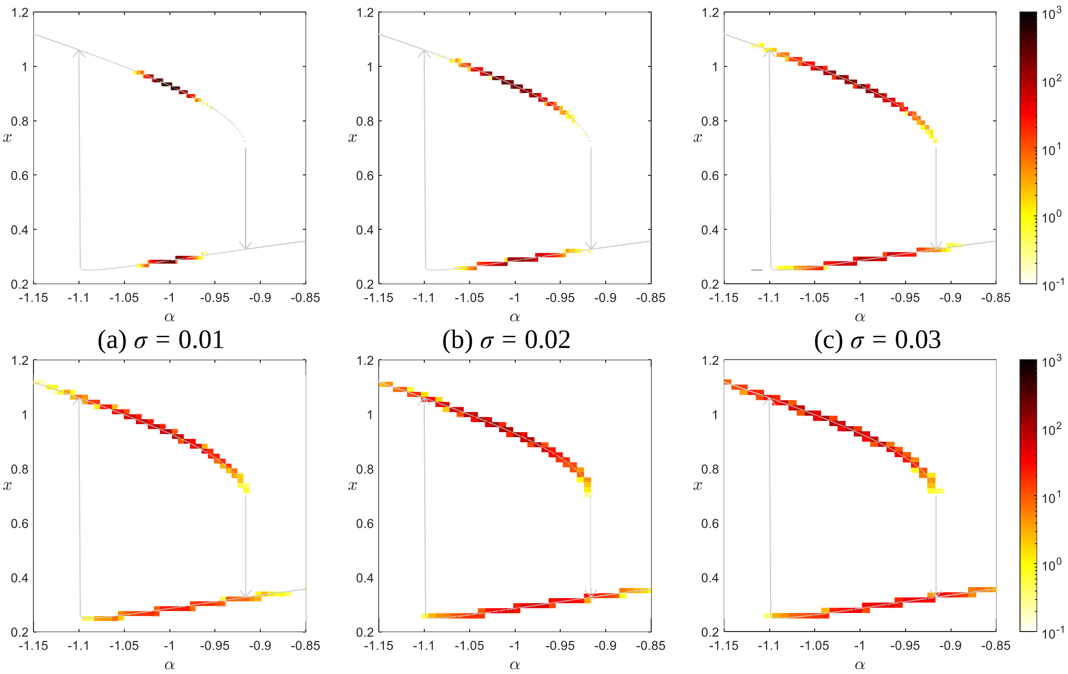

(a) σ = 0.01 (b) σ = 0.02 (c) σ = 0.03

(d) σ = 0.04 (e) σ = 0.05 (f) σ = 0.06

Figure 4.6 – Bifurcation diagram probability densities estimated from a Poincaré section at t = 1000T using 100000 trajectories of the Helmholtz oscillator uniformly distributed over $\mathbb{X}$ for A = 0.06 and varying values of the scaling parameter σ

The parametric analysis of the influence of parameter uncertainty on the global dynamics is conducted through partition levels 10 to 18 (see Table 4.2), alleviating the computational cost without compromising the quality of the result. The parameter space is discretized into 30 values, and the mean basins of attraction and mean attractors' densities are calculated through weighted sums, see Section 3.2. Since the system is deterministic for a fixed parameter value, the same time integrator of the previous analysis is considered, i.e., the fourth-order Runge-Kutta method with time-step $T/200$. This process is conducted in all the following analyses of systems with parametric uncertainty.

Figure 4.7 and Figure 4.8 presents the mean distributions (first color bar) and basins (second color bar) for increasing levels of the scaling parameter σ, demonstrating the effect of the probability distribution on the results. According to the adopted color scheme, the response for a set of initial conditions will converge to the expected attractor in the mean sense. The first and second columns refer to the small and large amplitude coexisting solutions, respectively. The effect of uncertainty is small for $\sigma = 0.01$, with only a slight spreading of both the attractors' distributions and their basins' boundaries. The latter concentrates near the saddle that is connected to the basin boundary. Furthermore, basins regions with a probability equal to one (yellow) almost coincide with the deterministic result. As the scaling parameter increases, the attractor distribution elongates (it is a one-dimensional structure embedded in the phase-space, an expected result according to the bifurcation diagram, Figure 4.5 and Figure 4.6) and approaches the boundary. The uncertain basin regions spread over the phase-space, and for $\sigma \geq 0.05$, there is no region with a probability equal to one to converge to the resonant attractor in the mean sense. The probability is lower than 0.8 for $\sigma = 0.06$. Also, the nonresonant basin with a probability equal to one decreases steadily, indicating a decrease in its dynamic integrity.

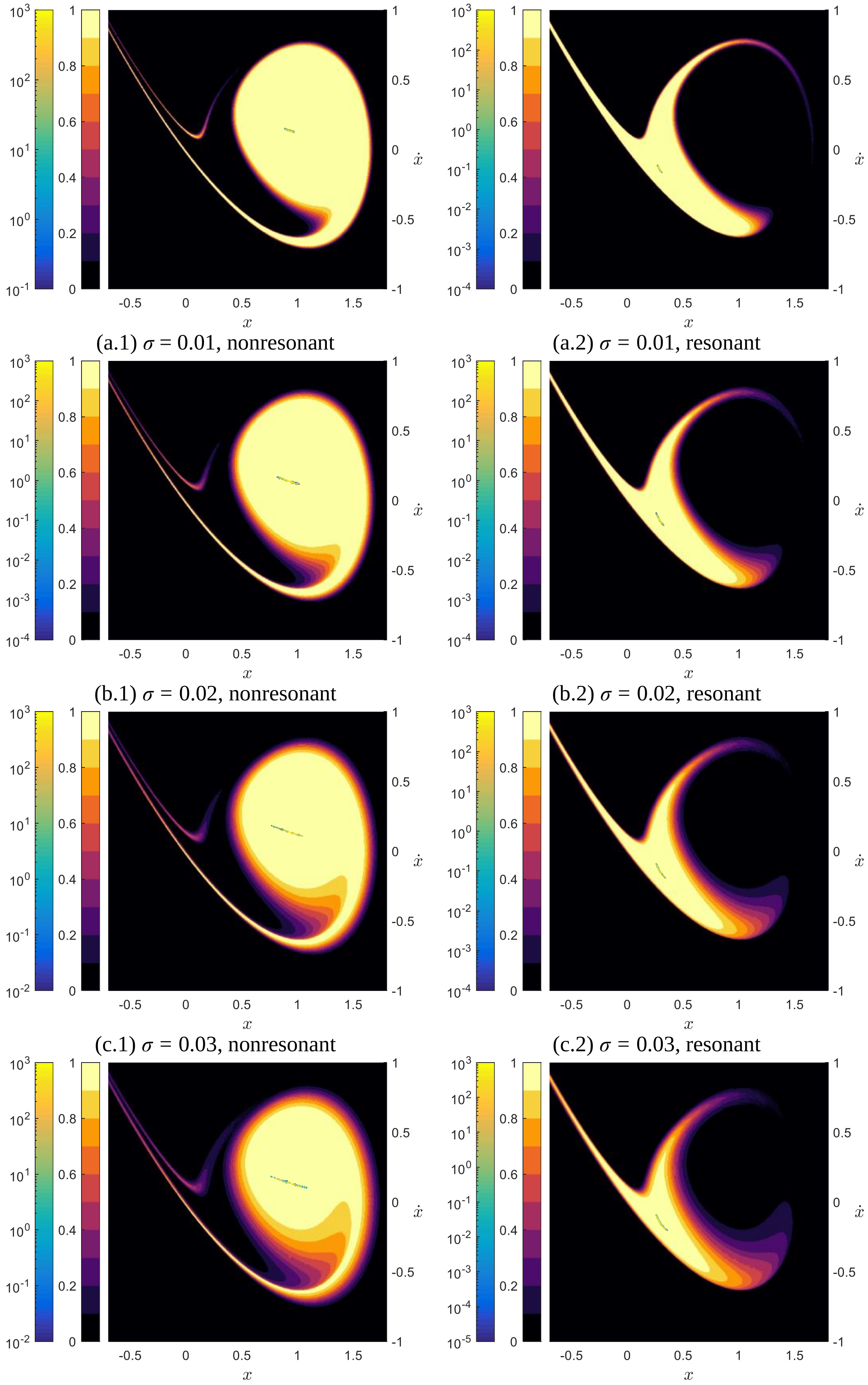

(a.1) σ = 0.01, nonresonant (a.2) σ = 0.01, resonant

(b.1) σ = 0.02, nonresonant (b.2) σ = 0.02, resonant

(c.1) σ = 0.03, nonresonant (c.2) σ = 0.03, resonant

(d.1) σ = 0.04, nonresonant (d.2) σ = 0.04, resonant

Figure 4.7 – Helmholtz oscillator mean attractor distributions (first color bar) and mean basins of attraction (second color bar) for A = 0.06 and small to moderate values of the scaling parameter σ

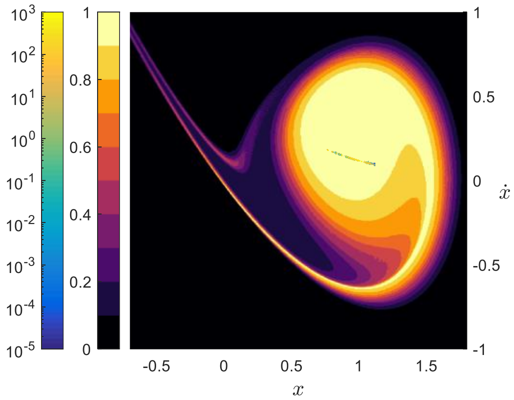

(a.1) σ = 0.05, nonresonant

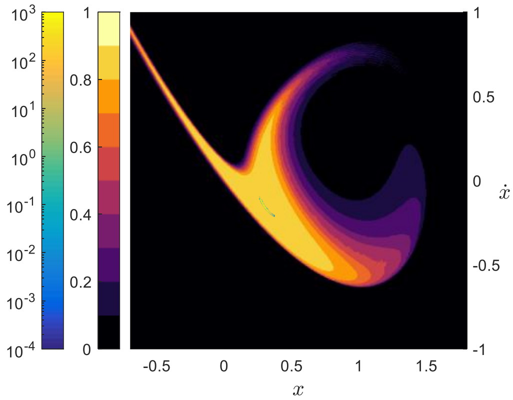

(a.2) σ = 0.05, resonant

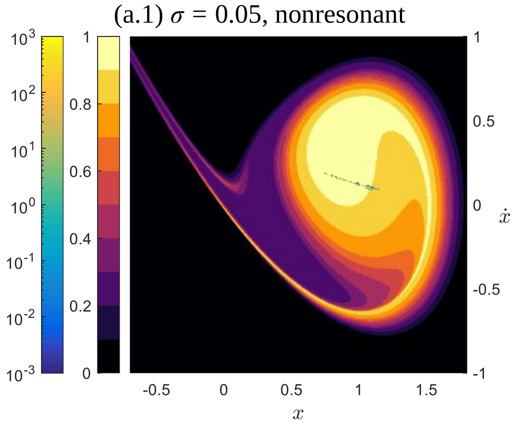

(b.1) σ = 0.06, nonresonant

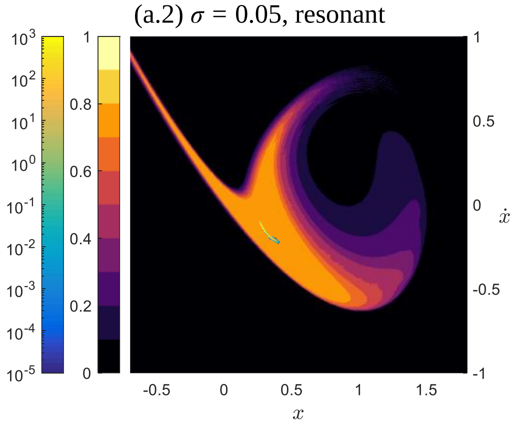

(b.2) σ = 0.06, resonant

Figure 4.8 – Helmholtz oscillator mean attractor distributions (first color bar) and mean basins of attraction (second color bar) for A = 0.06 and large values of the scaling parameter σ

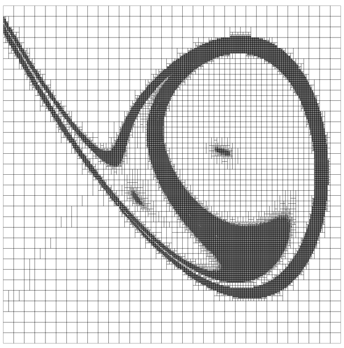
(a) σ = 0.01

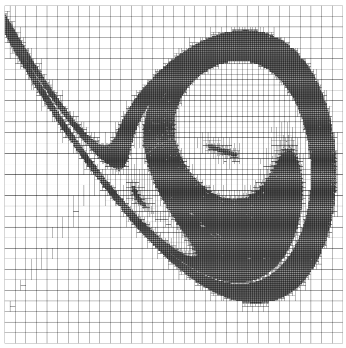
(b) σ = 0.02

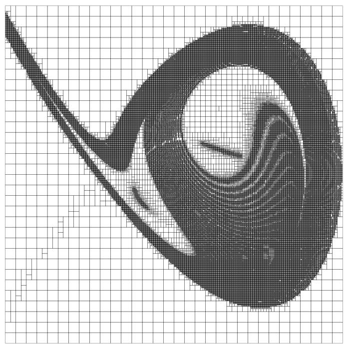
(c) σ = 0.03

Figure 4.9 – Dependence of the final partition $\mathbb{B}_{18}$ of the Helmholtz oscillator's mean fields as a function of the scaling parameter σ for A = 0.06

The final box set for the three initial scaling parameters is given in Figure 4.9, corresponding to the deepest level of all 30 λ-values for each σ-value. Table 4.4 presents a comparison of the total box count for all σ-values. As the uncertainty parameter increases, the discretization procedure results in an increasing number of boxes, implying that the computational cost also increases with σ, as confirmed by the final box-counting. For $\sigma \geq 0.03$, the final box counting does not change much since almost all potential well is discretized to the deepest level. The computational efficiency decreases, as expected, as σ increases, since higher σ-values result in larger basin areas with a probability smaller than one, which requires a more refined discretization. A significant economy would be observed if deeper levels were considered in such cases. However, the probability space should also be refined; otherwise, the results would not improve quality.

Table 4.4 – Box count for the Helmholtz oscillator with uncertainty at level 18 for A = 0.06

σ	Current box count	Maximum box count	Percentual	Economy
0.01	43666	262144	16.66%	83.34%
0.02	74299	262144	28.34%	71.66%
0.03	91422	262144	34.87%	65.13%
0.04	95003	262144	36.24%	63.76%
0.05	97649	262144	37.25%	62.75%
0.06	105205	262144	40.13%	59.87%

Figure 4.10 shows the variation of the Helmholtz oscillator normalized basins' areas as a function of the scaling parameter σ for $A = 0.06$ and selected probability thresholds, quantifying the integrity of the system with parameter uncertainty. The weighted normalized basins' areas are computed as

$$\frac{\int_{\mathbb{X}} \mathrm{id}_{[p,1]}(g)\, g\, dx}{\int_{\mathbb{X}} dx}, \tag{4.2}$$

where g is a stochastic basin of attraction, $\mathrm{id}_{[p,1]}(g)$ is an indicator function, which is equal to 1 if $g \in [p,1]$ and zero otherwise, and p is the probability threshold, between 0 and 1. In the deterministic limit (no uncertainty or noise and infinite resolution), the function g is an indicator function of the basin and eq. (4.2) reduces to the global integrity measure (GIM) [77]. This expression is a particular case of eq. (44) presented in [37], with $\rho_{pert}(x)$ as a uniform density over the phase-space window $\mathbb{X}$.

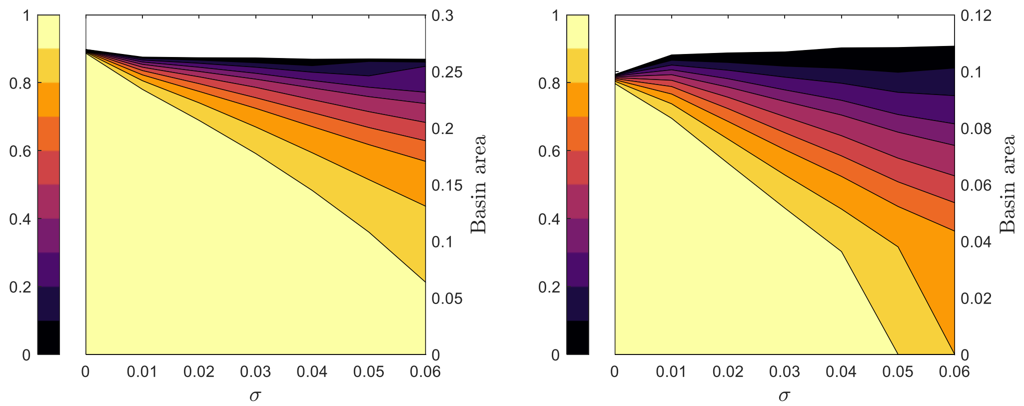

Figure 4.10 – Variation of the Helmholtz oscillator basins area as a function of the scaling parameter σ for A = 0.06, showing various probability thresholds (color bar)

A probability threshold close to 1 is a conservative selection in terms of evaluation of the actual integrity, while a threshold of 0 would provide the area of the entire phase-space $\mathbb{X}$. Of course, a probability threshold close to 1 actually corresponds to the maximal integrity only for vanishing parameter uncertainty ($\sigma = 0$), i.e., in the deterministic case. When the parameter uncertainty increases, the probability one conservative threshold provides notably reduced values of integrity, with the correspondingly higher ones being attained only with probability thresholds that are meaningfully lower (and thus not conservative). This result shows the importance of such analysis since real applications will almost-sure present a parametric variability.

Finally, Figure 4.11 presents a validation of the obtained results. Figure 4.11(a) shows the probability density estimated using a Monte Carlo experiment considering 100000 initial conditions uniformly distributed over the phase-space window with σ = 0.04. Each response is integrated up to t = 1000T, demonstrating the influence of the parameter uncertainty on the Poincaré sections of the two attractors. The results agree with the attractors' distributions, Figure 4.11(b), and the bifurcation diagram with respect to the support of the uncertainty parameter α, Figure 4.11(c), in terms of the attractor shape (plane curves), size, and probability distribution, thus matching the operator results and ratifying the present methodology.

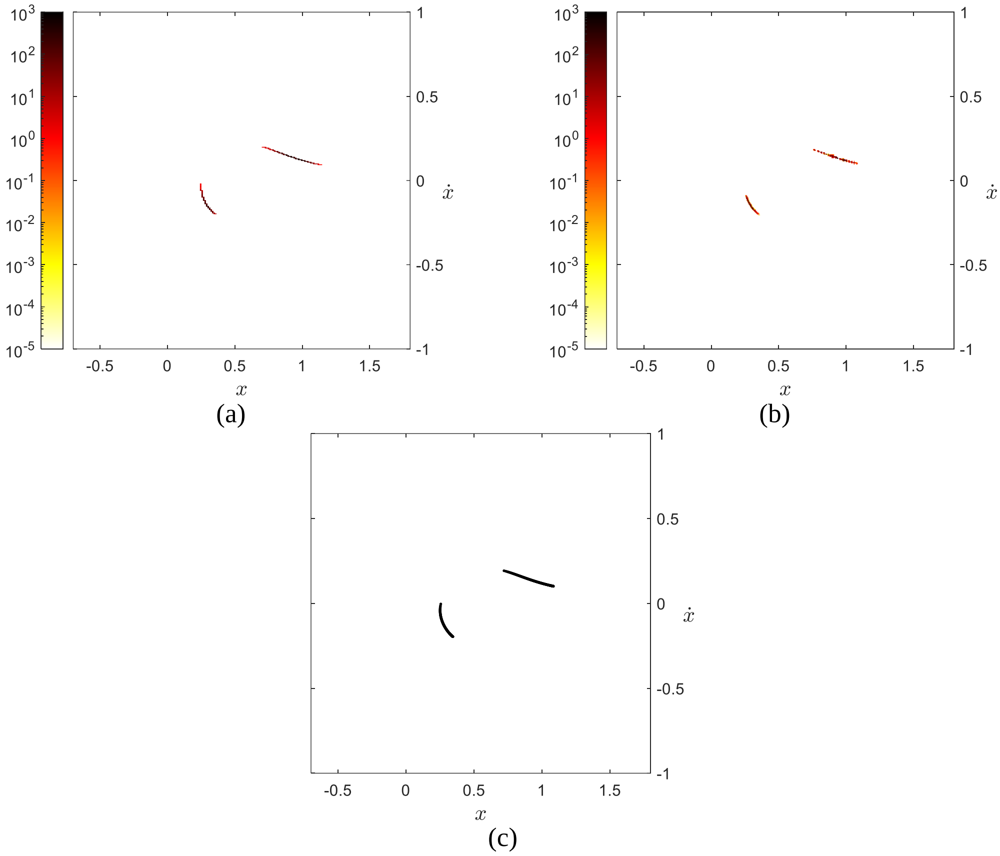

Figure 4.11 – (a) Probability density estimated from a Poincaré section at t = 1000T using 100000 trajectories of the Helmholtz oscillator initially uniformly distributed over $\mathbb{X}$, (b) attractors' mean distributions and (c) bifurcation diagram for A = 0.06 and σ = 0.04

4.1.2.
Effects of additive white noise

The noise-induced dynamics is now investigated. The same time-integration parameters are adopted. However, the noise requires specialized integrators, so a fourth-order Runge-Kutta with half stochastic order is adopted for the construction of the flow φ_T [96], with time-step T/200, where $T = 2\pi/\Omega$, and Ω is the forcing frequency. The transfer matrix of the noise-driven system is the Foias operator, and the projected operator is given by eq. (2.62). The probability integral in eq. (2.62) is solved by the Monte-Carlo method. Ten noise samples for each initial condition in each box are considered to calculate the discretized transfer operator F_h. Again, a sink box is defined to attract escape solutions.

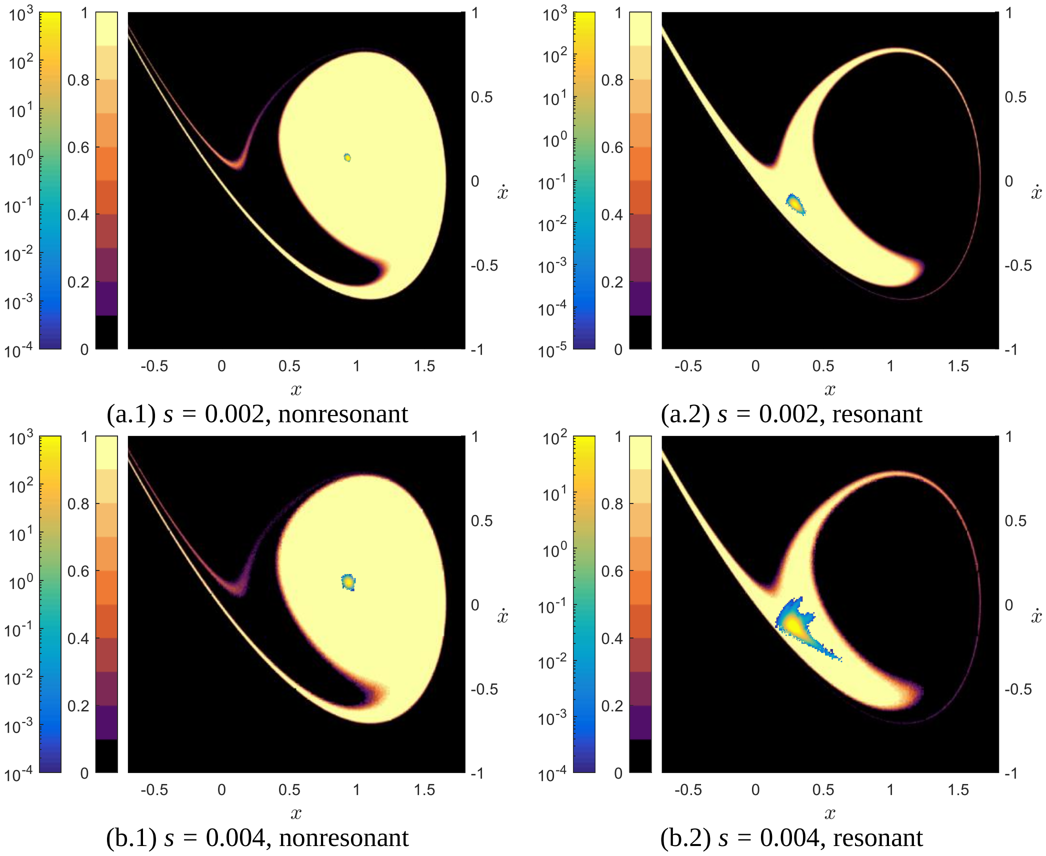

Figure 4.12 – Influence of increasing white noise standard deviation s on the stochastic basins of attraction (second color bar) and attractors distribution (first color bar) of the Helmholtz oscillator for A = 0.06. Nonresonant vs resonant

Figure 4.12 shows the results for the standard deviations s = 0.002 and s = 0.004. The influence of noise on the basin boundary is small. The basin structures present a pattern similar to the mean parameter results, with uncertainty associated with initial conditions only close to the boundaries. The crucial difference is the diffusion in the attractors' distributions over the phase space as the standard deviation increases. Again, the resonant solution is more affected than the nonresonant one, with the attractor spreading over a larger area and approaching the basin boundary, thus indicating a decrease in its dynamic integrity and possible disappearance of this attractor under increasing noise. For s = 0.006, the resonant solution is destroyed, see Figure 4.13(a), and only the nonresonant solution and basin remain, including all initial conditions occupied previously by the two coexisting basins, indicating a sudden but localized increase in its dynamic integrity. Indeed, as the noise intensity increases even further, see results for s = 0.010, initial conditions initially in the resonant region start to escape, as indicated by the gray area in Figure 4.13(b.2), which corresponds to the area with a probability lower than one in Figure 4.13(b.1). In Figure 4.12 and Figure 4.13, the steady spreading of the nonresonant attractor with the white noise standard deviation is observed.

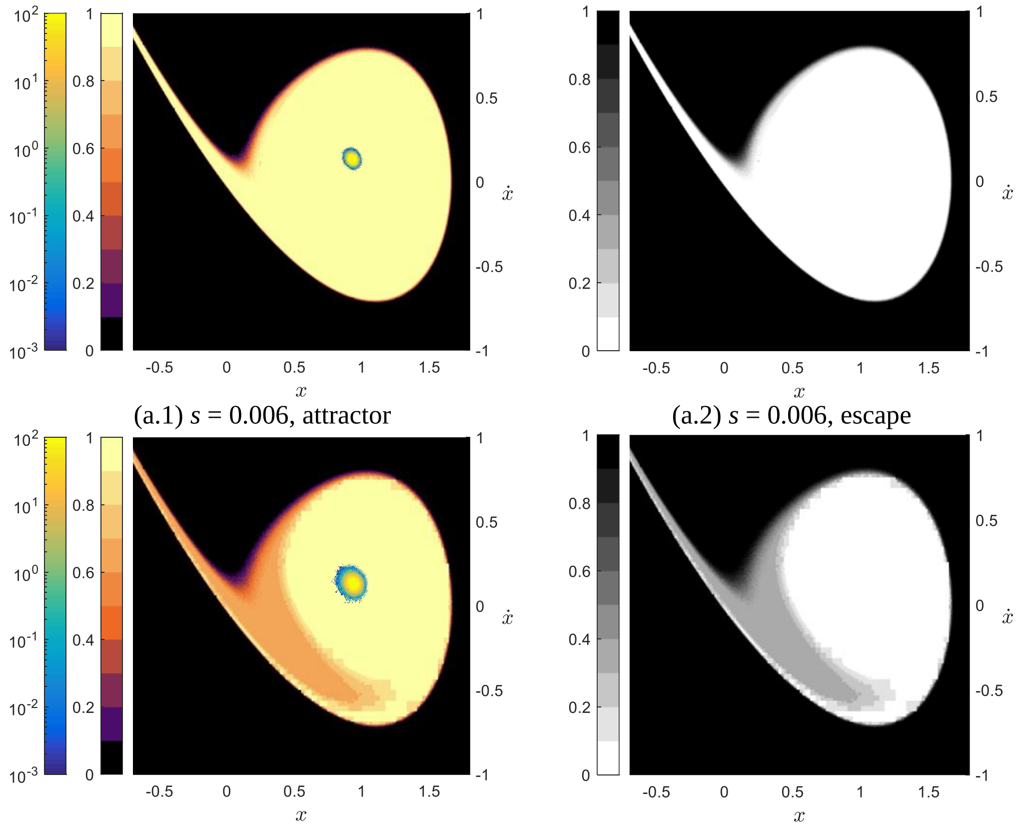

(a.1) *s* = 0.006, attractor (a.2) *s* = 0.006, escape

(b.1) *s* = 0.010, attractor (b.2) *s* = 0.010, escape

Figure 4.13 – Influence of increasing white noise standard deviation *s* on the stochastic basins of attraction (second color bar), attractors distribution (first color bar), and escape regions (third color bar) of the Helmholtz oscillator for *A* = 0.06. Bounded attractor vs escape

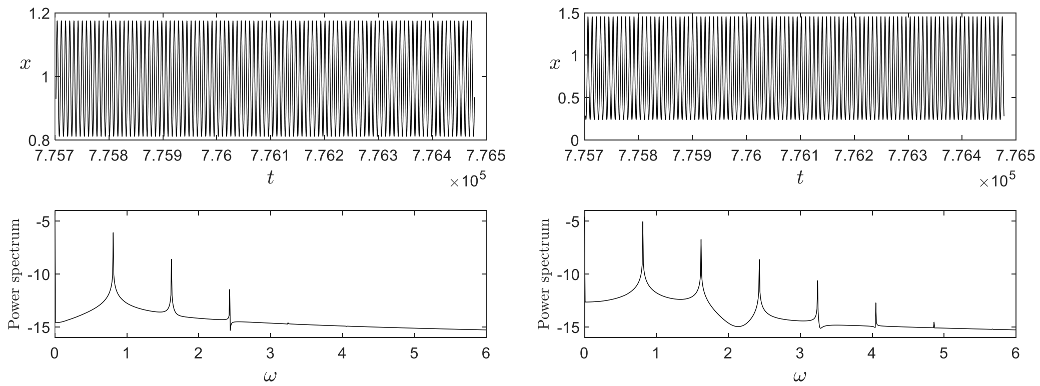

(a) nonresonant (b) resonant

Figure 4.14 – Time responses and power spectrum of the Helmholtz oscillator for *A* = 0.06 and *s* = 0. Nonresonant initial condition: (1.0; 0.13), resonant initial condition: (0.3; -0.13)

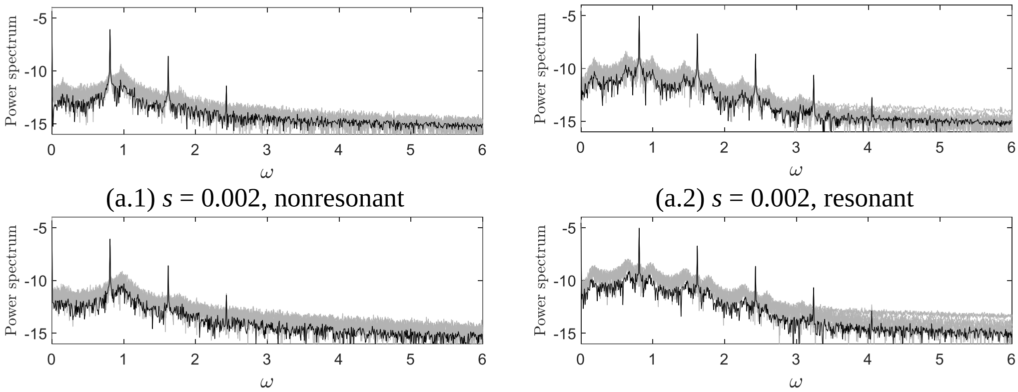

(a.1) s = 0.002, nonresonant (a.2) s = 0.002, resonant

(b.1) s = 0.004, nonresonant (b.2) s = 0.004, resonant

Figure 4.15 – Power spectrum of the Helmholtz oscillator for A = 0.06 and varying noise intensity. Light gray: 10 sample solutions; black: sample mean solution. Nonresonant initial condition: (1.0; 0.13), resonant initial condition: (0.3; -0.13)

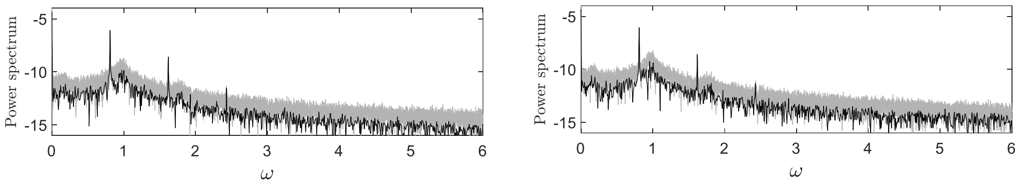

(a) s = 0.006, nonresonant (b) s = 0.010, nonresonant

Figure 4.16 – Power spectrum of the Helmholtz oscillator for A = 0.06 and increasing noise intensity. Light gray: 10 sample solutions; black: sample mean solution. Nonresonant initial condition: (1.0; 0.13)

The effect of noise on time responses and power spectrums is now addressed. For comparison, Figure 4.14 shows the deterministic case, with A = 0.06 and s = 0, for both attractors. Both power spectrums present peaks at the fundamental excitation frequency, ω = 0.81, and their super harmonics. The resonant solution, Figure 4.14(b), presents a richer spectrum with a higher number of excited harmonics. Figure 4.15 displays, for s = 0.002 and s = 0.004, the sample means, in black, and ten sampled time responses, in grey. The results show that the white noise masks the higher harmonics with a smaller power output of individual samples while they are still present, although with reduced power, in the sample means. The nonresonant results for s = 0.006 and s = 0.010 are displayed in Figure 4.16. The effect of increasing noise is observed, masking both the fundamental frequency and its harmonics. The resonant attractor for these cases is destroyed, as demonstrated by the basins of attraction in Figure 4.13, and, therefore, it does not have a stationary power spectrum.

The loss of stability of the resonant solution is identified by the eigenvalues of F_h slightly less than one. They correspond to long-transient solutions, that is, solutions that take a long time to converge to a given attractor. The influence of noise on the transient responses can be observed in Figure 4.17. For small noise intensity, s = 0.006, the resonant solution takes a rather long time to converge to the nonresonant solution, see Figure 4.17(a). This corresponds to an eigenvalue of F_h with a value of almost one. The obtained value for the corresponding case, Figure 4.13(a), is 0.999990835. For s = 0.010, the convergence time is reduced. However, the resonant attractor can converge to either the nonresonant solution, Figure 4.17(b), or escape, Figure 4.17(c), with different probabilities. Again, this result corresponds to the one observed in the basin analysis, Figure 4.13(b). The eigenvalue is smaller, with a value of 0.993246847, corroborating the observed convergence time reduction.

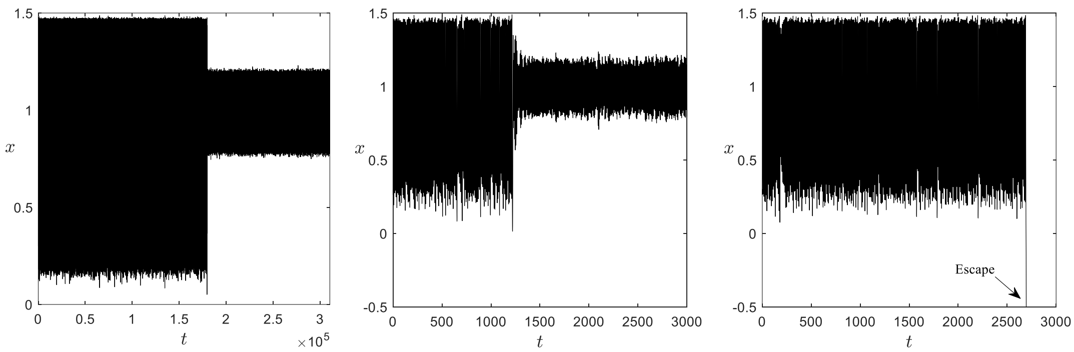

(a) s = 0.006, resonant to nonresonant | (b) s = 0.010, resonant to nonresonant | (c) s = 0.010, resonant to escape

Figure 4.17 – Helmholtz oscillator's resonant attractor long-time transient response due to high noise intensity for A = 0.06. Resonant initial condition: (0.3; -0.13)

As shown by the previous results, the noise leads to uncertainty along the basin boundary, where the probability is less than one. As in the deterministic case, the transient noisy response becomes longer as initial conditions are further away from the attractor. The time-dependency of the basins of attraction is demonstrated in Figure 4.18 for $A = 0.06$ and $s = 0.010$. Values of $\varepsilon \approx 1$ (respectively, $\varepsilon \approx 0$) correspond to a small (respectively, large) time-horizon, identifying regions where the time response converges in the mean sense to a given attractor after a small-time (respectively, large-time) interval. This corresponds to a small region surrounding the attractor, see Figure 4.18(a.1, a.1). As ε decreases, the time-horizon increases, and the obtained basin approaches its maximum size asymptotically. This is clear in Figure 4.18(a.2, a.3) and Figure 4.18(c.2, c.3), where the basin stabilizes at its final configuration. For this noise intensity, there is no resonant attractor in the classical sense, with solutions decaying to the nonresonant attractor or escaping. Figure 4.18(b) demonstrates what happens with the resonant region. Initially, solutions converge to the region where the resonant attractor exists for lower noise intensities, as demonstrated by the increase in basin area from Figure 4.18(b.1) to Figure 4.18(b.2). However, for large time-horizons, the supposed resonant basin decays to zero, see Figure 4.18(b.3). To obtain the asymptotic basin of attraction for this noise level with methods based on time integration, the number of periods of integration would be prohibitively large. Also, if time-horizons smaller than 1e4 (ε > 1e-4) are considered, the resonant region would mistakenly be considered as a basin, being, in fact, a set of initial conditions with a long transient.

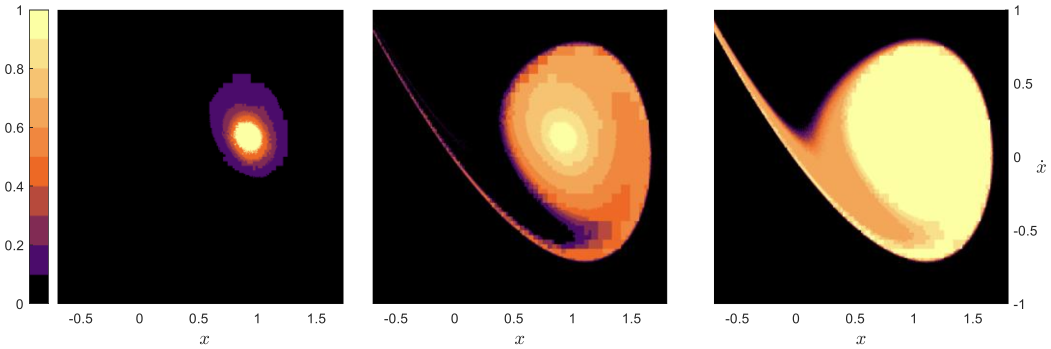

(a.1) ε = 0.5, attractor (a.2) ε = 0.1, attractor (a.3) ε = 1e-4, attractor

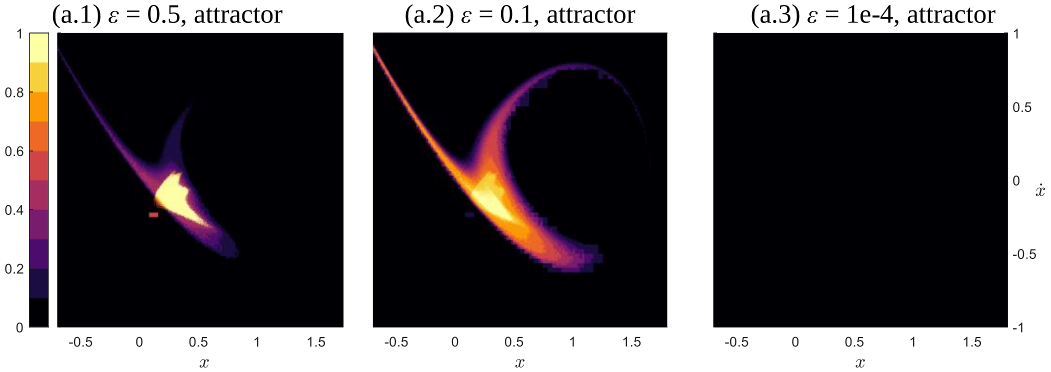

(b.1) ε = 0.5, resonant region (b.2) ε = 0.1, resonant region (b.3) ε = 1e-4, resonant region

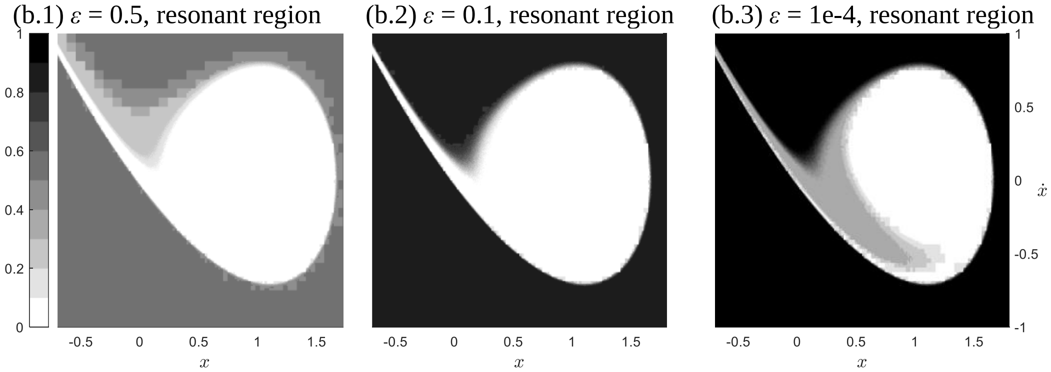

(c.1) ε = 0.5, escape (c.2) ε = 0.1, escape (c.3) ε = 1e-4, escape

Figure 4.18 – Dependency of the stochastic basin of attraction (color bars) on the final time-horizon $1/\varepsilon$ for A = 0.06, s = 0.010

Long transients lead to large computation time to obtain the asymptotic response by usual time integration techniques. However, the proposed phase-space subdivision procedure can identify and separate these solutions from the true asymptotic behavior. Figure 4.19 contains the corresponding eigenmeasure for the resonant solution, which, however, is not strictly a distribution but a long transient. This is shown in Figure 4.19(b), where negative (blue) and positive (red) regions, each with absolute value $|f| = 0.5$, are separated, the former representing regions where the solutions stay for a long time before decaying to the permanent nonresonant attractor, in red, or escape, as already observed in the basins of attraction, Figure 4.13(b) and in the time responses, Figure 4.17(b, c). Indeed, according to Dellnitz and Junge [33], there are two scenarios where almost invariant sets can be observed. The first case occurs when cyclic components of a periodic attractor collide. Specifically, the cyclic components' eigenvalues change from an absolute value of one to less than one. Only one attractor is involved in this process, changing its periodicity to an almost periodicity. The second case refers to the collision of two or more attractors, with at least one of them changing its eigenvalue from an absolute value of one to less than one. The attractor whose eigenvalue changes, loses stability, exhibiting a long transient solution. In this example, the resonant attractor loses stability by colliding with different probabilities (see Figure 4.18(a, c) for long time-horizons) with both the nonresonant attractor and the escape solution. A possible triple collision between the three distinct solutions, after which only two remain stable, may also occur for a very specific (i.e., coincident) probability value.

The proposed measure to quantify the system's integrity under various noise intensities is presented in Figure 4.20, for ε = 1e-8. Again, for each attractor, the measure is computed according to eq. (4.2). The nonresonant attractor resilience against the noise and the resonant attractor integrity loss for $s \geq 0.006$ are clearly observed. Therefore, the proposed procedure can be used to quantify the influence of noise on any integrity measure.

Figure 4.21 presents a comparison with a Monte Carlo experiment. The probability density estimated through 10000 initial conditions uniformly distributed over the phase-space window with $s = 0.004$ integrated up to t = 100000T is presented in Figure 4.21(a). The black areas represent high-density regions. They agree with the attractors' distribution, Figure 4.21(b), obtained from the proposed methodology, validating the present strategy.

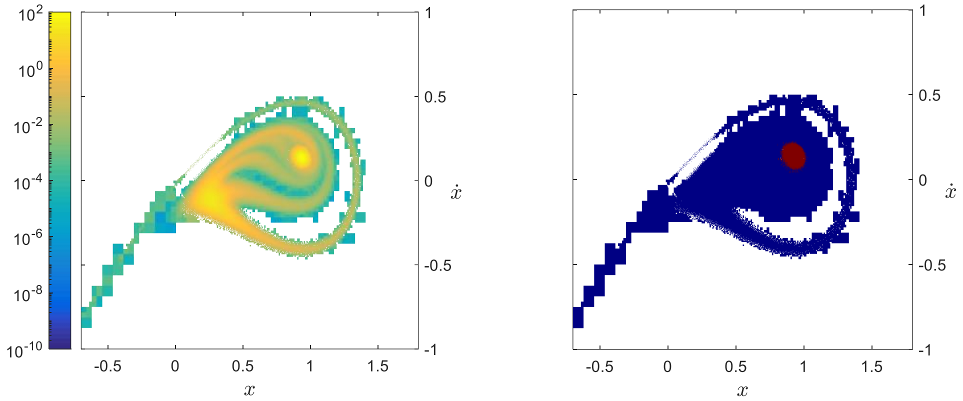

(a) absolute value

(b) negative (blue) and positive (red) distributions

Figure 4.19 – Helmholtz oscillator's almost permanent eigenmeasure for A = 0.06, s = 0.010

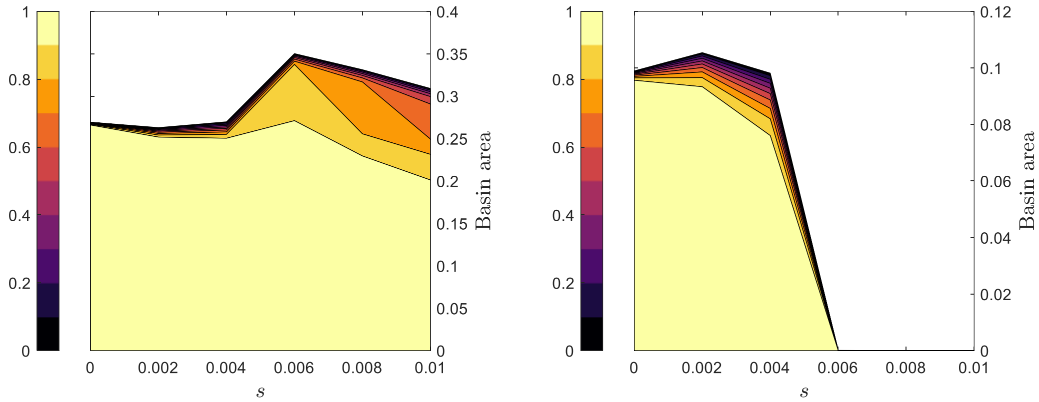

(a) nonresonant

(b) resonant

Figure 4.20 – Variation of the Helmholtz oscillator basins area as a function of the noise intensity s for A = 0.06, showing various probability thresholds (color bar). Time-horizon $1/\varepsilon$ = 1e8

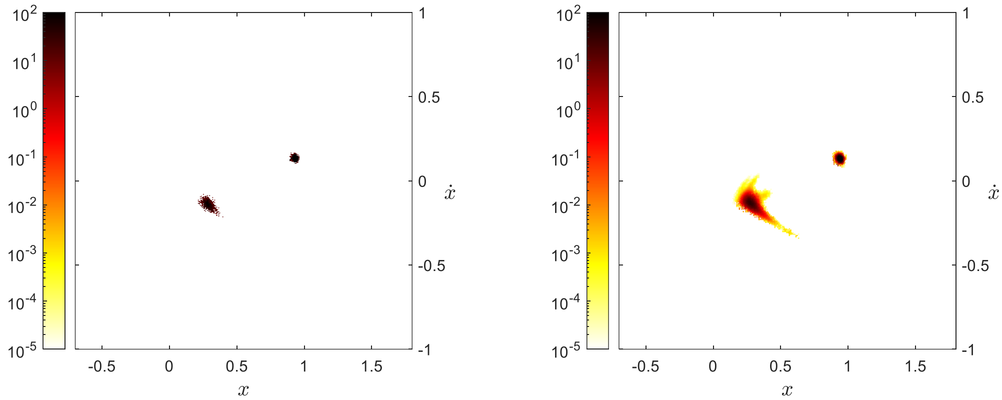

(a)

(b)

Figure 4.21 – (a) Probability density estimated from a Poincaré section at t = 100000T of 10000 trajectories of the Helmholtz oscillator initially uniformly distributed over $\mathbb{X}$, (b) attractors' mean distributions for A = 0.06 and s = 0.004

4.2.
Duffing oscillator with harmonic excitation

The second example consists of the standard dimensionless form of the damped harmonically excited Duffing oscillator,

$$\ddot{x}+\delta\dot{x}+\left(\alpha+\sigma\lambda\right)x+\beta x^{3}=A\cos\Omega t+s\dot{W}. \tag{4.3}$$

Depending on the values of α and β, the Duffing oscillator can display different potential functions, $\Pi(x)$, describing different classes of structural problems. For $\beta > 0$, a single-well potential is obtained for $\alpha > 0$ and a double-well potential for $\alpha < 0$. For $\beta < 0$ and $\alpha > 0$, there is a single-well and two maxima leading to escape, while for $\alpha, \beta < 0$, only escape solutions occur (unstable system). Thus, it is a good archetypal model, representing cases with competing potential wells, periodic to chaotic solutions, unbounded nonperiodic solutions, basin erosion, and loss of integrity. Initially, two cases are considered, Duffing with parameter uncertainty and noise. The adopted values for parameter uncertainty are obtained from [64] and summarized in Table 4.5. It represents a case with two potential wells and, depending on the forcing magnitude *A*, small and large amplitude solutions, multiple periodic solutions, chaotic solutions, and cross well oscillations can be obtained. The random variable λ is a truncated standard normal with density $f(\lambda;0,1,-3,3)$, and σ is a scaling parameter. Noise is also considered, where $\dot{W}$ is a standard white noise process, and *s* is the noise standard deviation. For $\sigma = 0$ and $s = 0$, the system is deterministic.

Table 4.5 – Duffing oscillator parameters for parameter uncertainty analysis

Parameter	Value
α	-0.5
λ	$f\left(\lambda;0,1,-3,3\right)$
β	0.5
δ	0.1
Ω	0.8

The investigated phase-space window is $\mathbb{X}=\left\{-2,2\right\}\otimes\left\{-1.1,1.1\right\}$. The initial box partition is defined as a division of 2^6x$2^5 = 2048$ boxes of size {0.0625, 0.0688}, at depth level 11. The procedure is conducted through 6 steps, with a final box of size {0.0078, 0.0086}. Table 4.6 presents the discretization data together with the total of collocation points at each level.

Table 4.6 – Discretization data for the Duffing oscillator

Depth level	Box-size	Points per dimension	Total collocation points
11	{0.0625, 0.0688}	11	121
12	{0.0625, 0.0344}	10	100
13	{0.0313, 0.0344}	9	81
14	{0.0313, 0.0172}	8	64
15	{0.0156, 0.0172}	7	49
16	{0.0156, 0.0086}	6	36
17	{0.0078, 0.0086}	5	25

The Perron-Frobenius operator governs the phase-space distribution. Thus eq (2.59) is used for the deterministic case. The influence of the forcing magnitude is illustrated in Figure 4.22 to Figure 4.24. For $A = 0.035$, Figure 4.22, only two solutions are observed (attractors identified by a red dot), one in each well, with the basins of attraction displaying smooth boundaries. The final phase-space subdivision demonstrates that indeed attractors and boundaries are refined. For $A = 0.060$, Figure 4.23, and $A = 0.065$, Figure 4.24, four attractors are identified, one resonant and one nonresonant attractor in each well. As the forcing magnitude increases and the new attractors appear, the basins become more convoluted with long thin tails with probabilities between 0 and 1 due to the discretization, suggesting that smaller boxes must be employed for the correct representation of the complex basin structure in these regions.

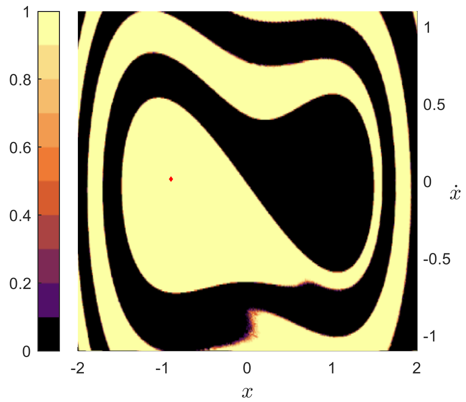

(a) left potential well

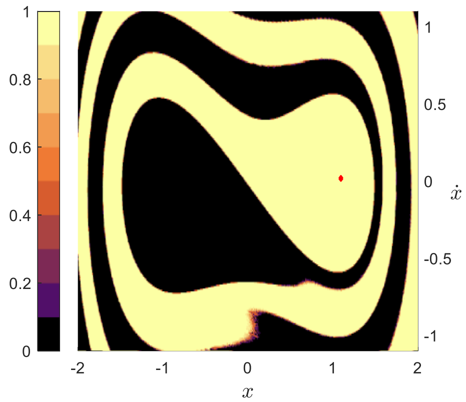

(b) right potential well

Figure 4.22 – Basins of attraction (color bar) of the deterministic Duffing oscillator for $A = 0.035$

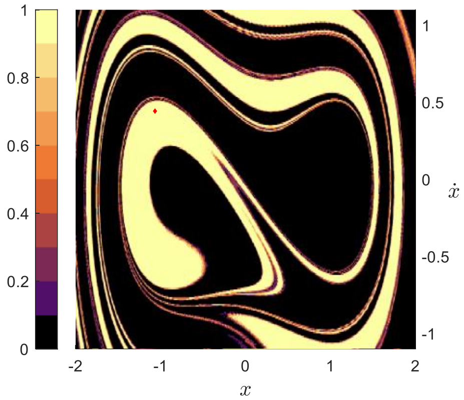

(a) left potential well, resonant attractor

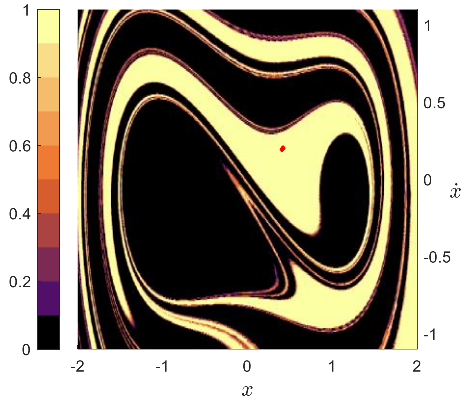

(b) right potential well, resonant attractor

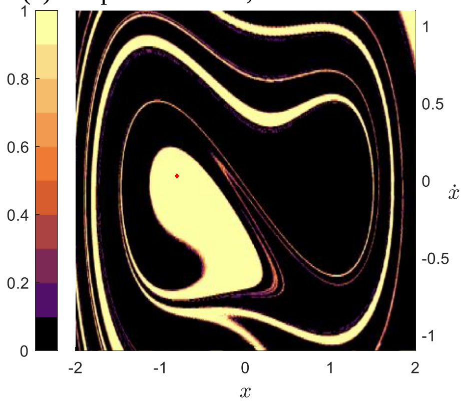

(c) left potential well, nonresonant attractor

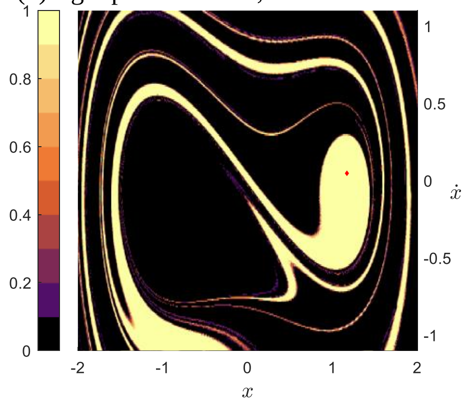

(d) right potential well, nonresonant attractor

Figure 4.23 – Basins of attraction (color bar) of the deterministic Duffing oscillator for A = 0.060

The dependency of the final partition $\mathbb{B}_{17}$ with A is demonstrated in Figure 4.25. It is evident that the procedure indeed refines the regions close to the basins' boundaries. However, cases where the boundaries are not localized still present a major computational difficulty. Figure 4.25(b) and Figure 4.25(c) are cases where basins become more convoluted due to the horseshoe effect with intertwined tongues. For these cases, large regions of the phase-space needed to be discretized, increasing the computational cost. A quantification of this cost is given in Table 4.7. Specifically, the last column shows the ratio between the maximum-to-current box count difference and the maximum box count. Lower values imply higher computational costs, as demonstrated by the last cases.

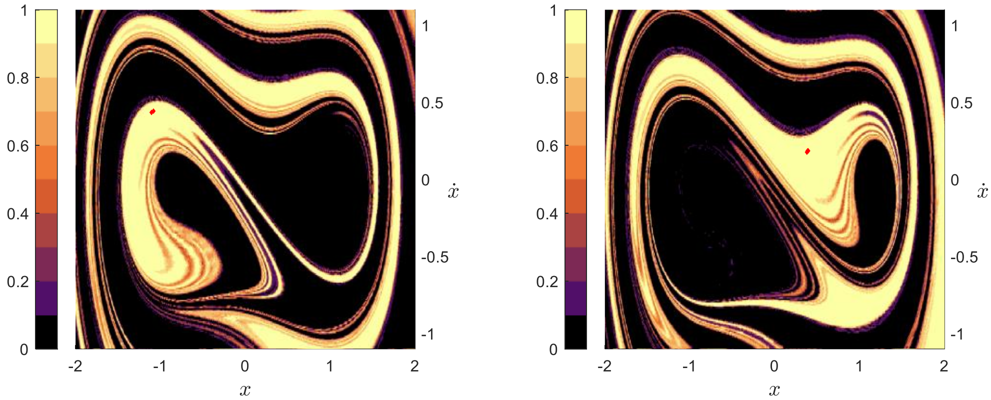

(a) left potential well, resonant attractor (b) right potential well, resonant attractor

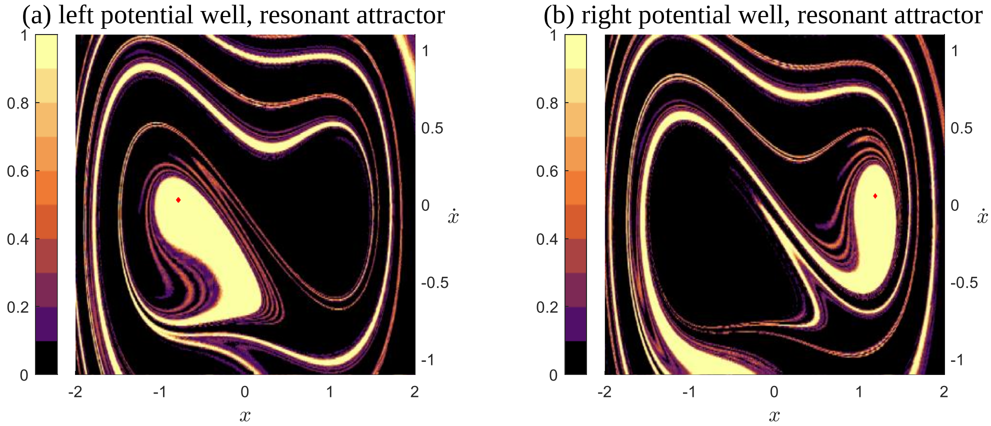

(c) left potential well, nonresonant attractor (d) right potential well, nonresonant attractor

Figure 4.24 – Basins of attraction (color bar) of the deterministic Duffing oscillator for A = 0.065

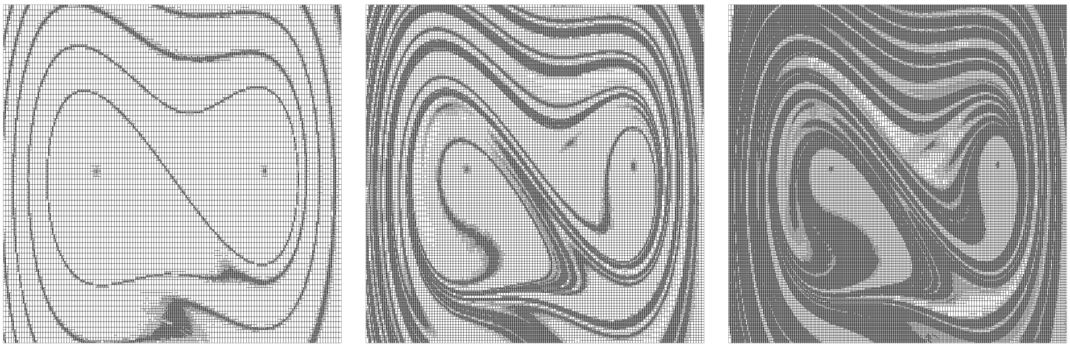

(a) A = 0.035 (b) A = 0.060 (c) A = 0.065

Figure 4.25 – Dependence of the final partition $\mathbb{B}_{17}$ of the deterministic Duffing oscillator as a function of the amplitude of excitation A

Table 4.7 – Box count for the deterministic Duffing oscillator at level 17

A	Current box count	Maximum box count	Percentual	Economy
0.035	19712	131072	15.04%	84.96%
0.060	57492	131072	43.86%	56.14%
0.065	96096	131072	73.32%	26.68%

4.2.1.
Effects of parameter uncertainty

Now the influence of uncertainty in the stiffness parameter of the Duffing oscillator is investigated. Figure 4.26 shows the bifurcation diagram as a function of the parameter α for $A = 0.06$ and the normalized probability distributions of $\alpha + \sigma\lambda$ for three values of σ. There are two pairs of attractors (in blue and red) corresponding to the solutions in each potential well. For $\alpha < -0.47$, four coexisting solutions exist (see Figure 4.23 for the basins at the mean value). At $\alpha = -0.47$, the nonresonant solutions disappear, and for $\alpha > -0.47$, only two resonant attractors remain, one in each potential well. Similar to what was observed for the Helmholtz oscillator, the scaling parameter σ changes the expected outcome considerably in the bifurcation region. Specifically, the $\alpha > -0.47$ region becomes statistically significant for $\sigma > 0.02$, as indicated by the superposition of the bifurcation diagrams and the normalized densities. Monte Carlo experiments of 10000 initial conditions uniformly distributed over the phase-space for varying σ-values demonstrate the influence of σ on the bifurcation diagram and bifurcation values, see Figure 4.27. The bifurcation diagram of the deterministic case is plotted in gray.

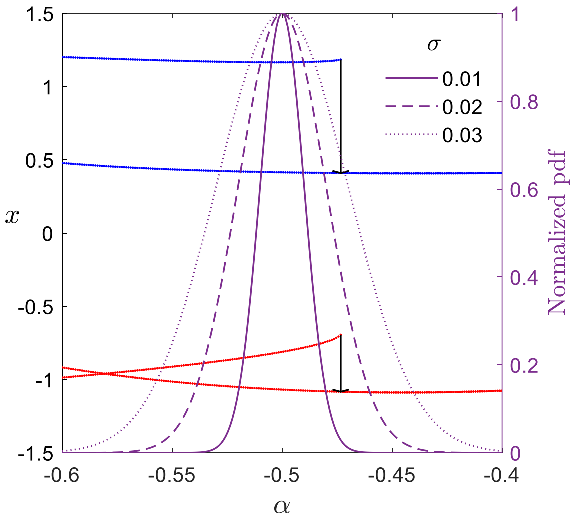

Figure 4.26 – Bifurcation diagram of the Duffing oscillator as a function of the stiffness parameter α for $A = 0.06$ and the normalized probability distributions of $\alpha + \sigma\lambda$ for selected values of the scaling parameter σ

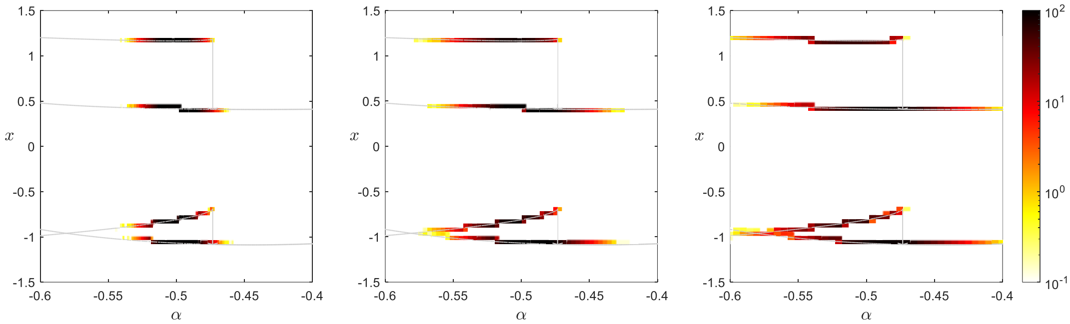

(a) σ = 0.01 (b) σ = 0.02 (c) σ = 0.03

Figure 4.27 – Bifurcation diagram probability densities estimated from a Poincaré section at t = 1000T using 100000 trajectories of the Duffing oscillator with initial conditions uniformly distributed over $\mathbb{X}$ for A = 0.06 and varying values of the scaling parameter σ

The analysis of the global dynamics considering the uncertain natural frequency is conducted through levels 11 to 17, the same levels used in the deterministic analysis. However, this resolution is not satisfactory for the analyzed attractors. To overcome this problem, an additional discretization of each attractor is performed: a local transfer matrix P_h of each attractor is computed and refined from levels 17 to 21, with 25 initial conditions per box for each level. Therefore, the basins boundaries have a maximum resolution corresponding to the 17$^{\text{th}}$ level, while the attractors have a maximum resolution corresponding to the 21$^{\text{th}}$ level. This is necessary to obtain a good representation of the attractors, for which the Poincaré sections are curves in the plane. Again, 30 parameter values are considered, and the mean basins of attraction and mean attractors' densities are obtained. Since the system is deterministic for a fixed parameter, the same integrator is considered, i.e., the fourth-order Runge-Kutta method with time-step T/200.

Initially, σ = 0.01 is adopted, see Figure 4.28. The parameter uncertainty diffuses the basins' boundaries, similar to what is observed for the Helmholtz oscillator, see Figure 4.5. The attractors' distributions also demonstrate the uncertainty effect. Due to a large number of coexisting attractors and the basins` competition, there is a significant diffusion of the boundaries, corroborating the influence of the parameter uncertainty in these regions.

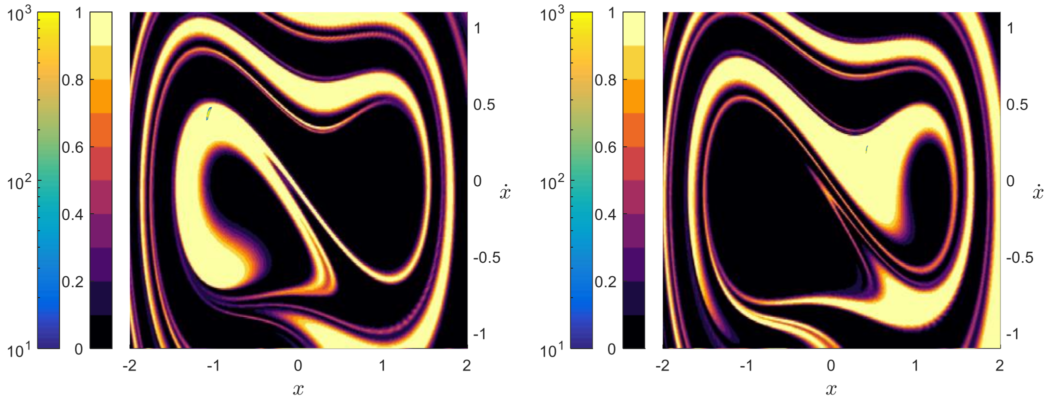

(a) left potential well, resonant attractor (b) right potential well, resonant attractor

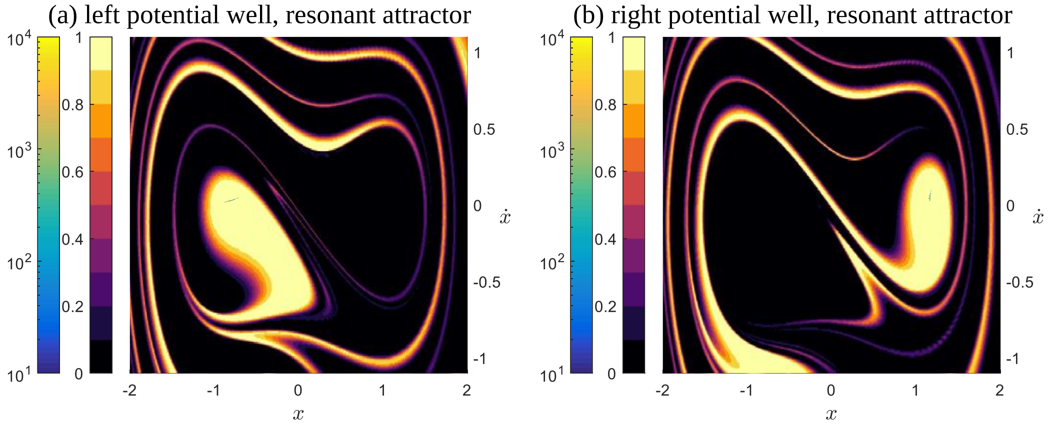

(c) left potential well, nonresonant attractor (d) right potential well, nonresonant attractor

Figure 4.28 – Mean basins of attraction (second color bar) and mean attractors distributions (first color bar) of the Duffing oscillator with A = 0.060 and σ = 0.01

Figure 4.29 displays the mean basins and mean distributions of the Duffing oscillator attractors for $\sigma = 0.02$. As σ increases, the diffusion along the basins' boundaries increases and spreads over larger regions of the phase-space, with the resonant region engulfing the nonresonant one, which is in agreement with Figure 4.26. The degradation of the nonresonant basins of attraction is observed by the decreasing regions with probability equal to one and large regions of phase-space where the outcome is uncertain. This pattern continues in the last considered case, Figure 4.30, for $\sigma = 0.03$. The degradation of the nonresonant basins is so intense that all intra-well initial conditions have a non-null probability to converge to the resonant solution.

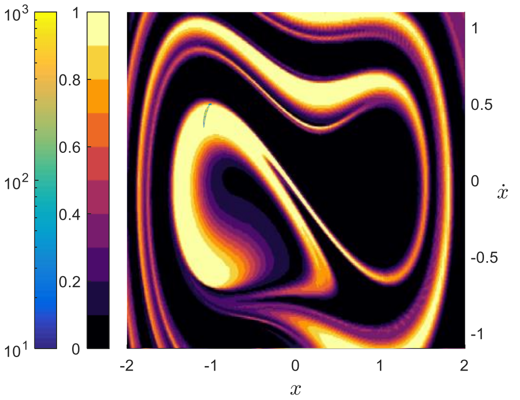

(a) left potential well, resonant attractor

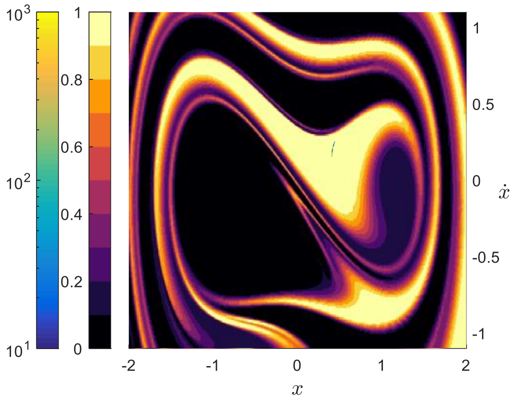

(b) right potential well, resonant attractor

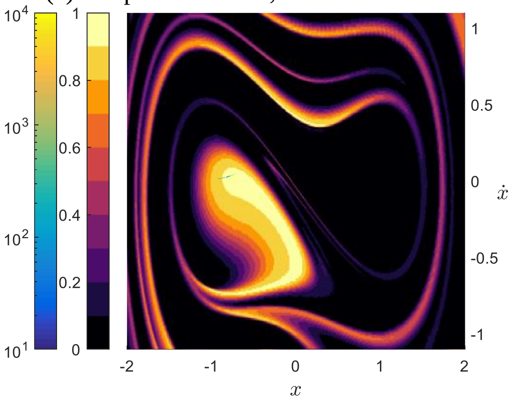

(c) left potential well, nonresonant attractor

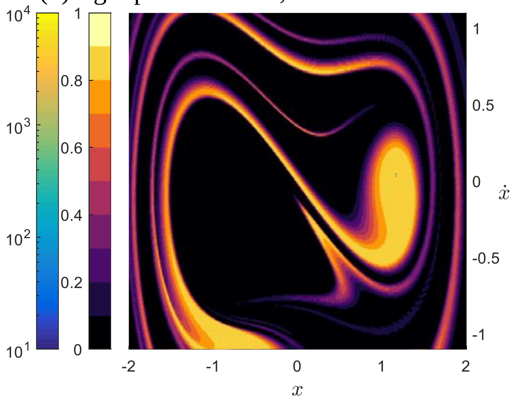

(d) right potential well, nonresonant attractor

Figure 4.29 – Mean basins of attraction (second color bar) and mean attractors distributions (first color bar) of the Duffing oscillator with A = 0.060 and σ = 0.02

Table 4.8 presents the dependency of the final partition, $\mathbb{B}_{17}$, with the scaling parameter, σ. As σ and the uncertainty of the outcome increases, the subdivision of most of the phase-space and a high degree of refinement becomes necessary, increasing the computational cost, with the computational cost approaching that of a computation without adaptative refinement but with a very refined, yet unknown, initial discretization. Thus, the proposed algorithm is computationally attractive when regions that must be refined are localized. This can be seen in the last two columns, where the current box count is almost equal to the maximum box count for the 17th level.

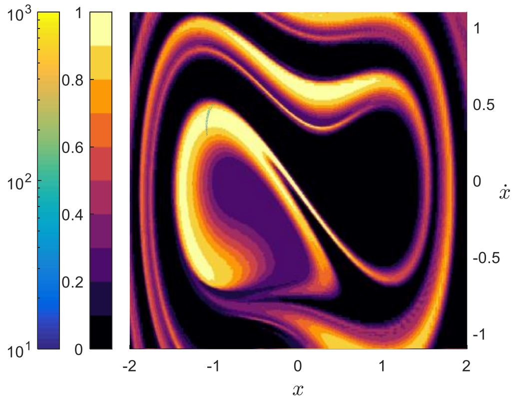

(a) left potential well, resonant attractor

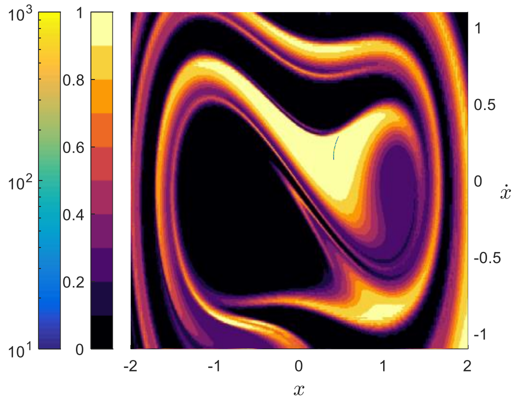

(b) right potential well, resonant attractor

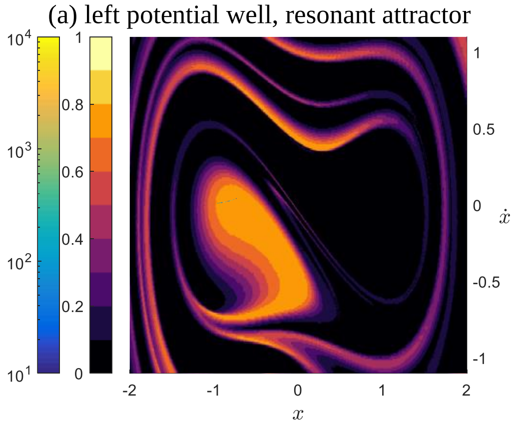

(c) left potential well, nonresonant attractor

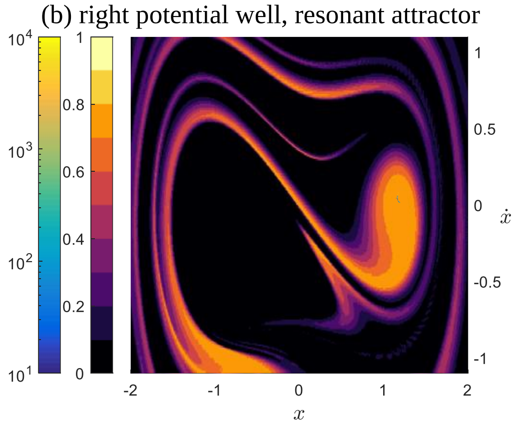

(d) right potential well, nonresonant attractor

Figure 4.30 – Mean basins of attraction (second color bar) and mean distributions (first color bar) of the Duffing oscillator with A = 0.060 and σ = 0.03

Table 4.8 – Box count for the uncertainty Duffing oscillator at level 17 for A = 0.060

σ	Current box count	Maximum box count	Percentual	Economy
0.01	113841	131072	86.85%	13.15%
0.02	124893	131072	95.29%	4.71%
0.03	125382	131072	95.66%	4.34%

Figure 4.31 shows the variation of the basins' area as a function of the scaling parameter σ for A = 0.060 and various probability thresholds, computed through eq. (4.2). Again, a probability threshold close to 1 is a conservative measure, giving smaller integrity values, while a threshold of exactly 0 would give the area of the entire phase-space $\mathbb{X}$. The parameter uncertainty decreases the integrity measure of all four attractors as the scale parameter increases. However, the two nonresonant attractors show faster integrity loss than their resonant companions, as already perceived in Figure 4.28, Figure 4.29, and Figure 4.30.

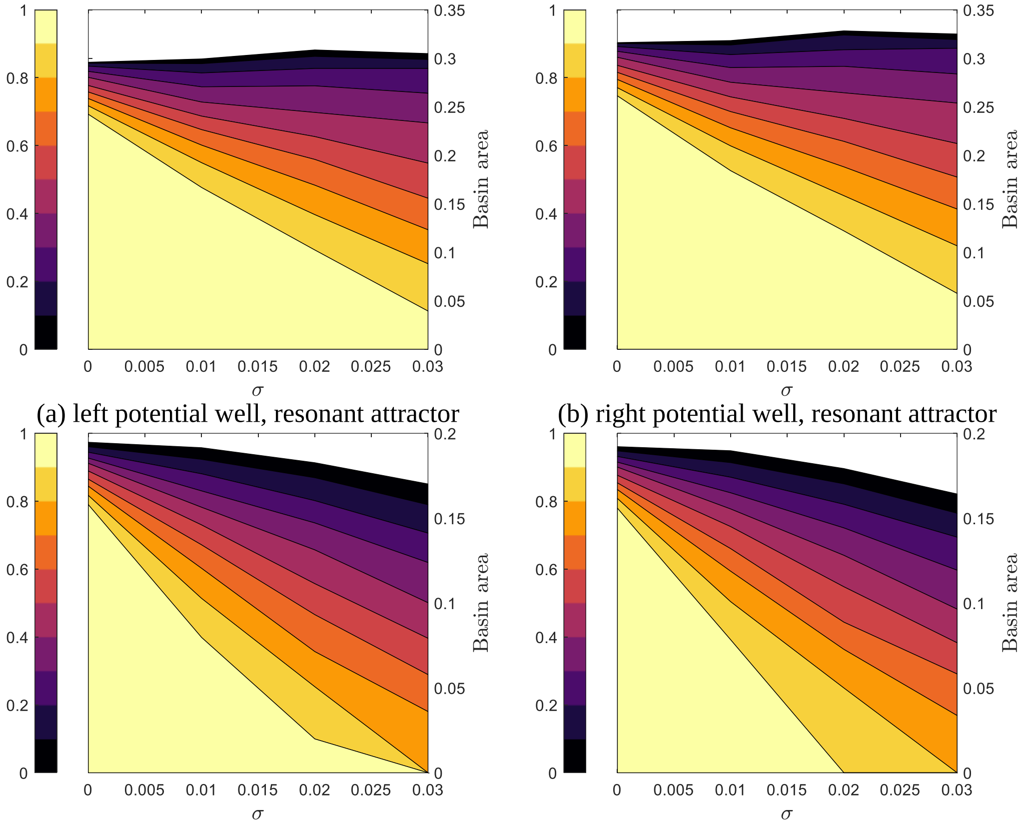

(a) left potential well, resonant attractor (b) right potential well, resonant attractor

(c) left potential well, nonresonant attractor (d) right potential well, nonresonant attractor

Figure 4.31 – Variation of the Duffing oscillator basins area as a function of the scaling parameter σ for A = 0.06, showing various probability thresholds (color bar)

Figure 4.32(a) presents the probability density estimated from a Monte Carlo experiment considering 100000 initial conditions uniformly distributed over the phase-space window with $\sigma = 0.03$. Each response is integrated up to t = 1000T, demonstrating the influence of the parameter uncertainty on the Poincaré sections of the four attractors. The results agree with the attractors' distribution, Figure 4.32(b), and the bifurcation diagram, Figure 4.32(c), in terms of the attractor shape (plane curves), size, and probability distribution, thus validating the operator results and endorsing the present methodology.

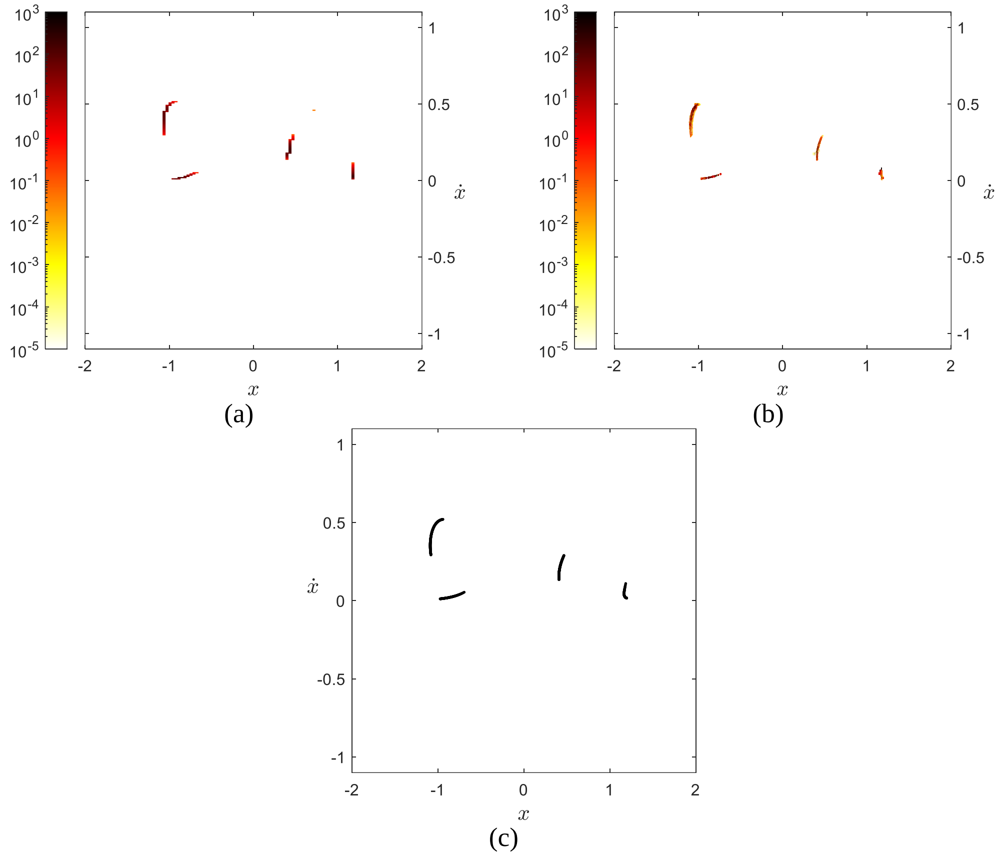

Figure 4.32 – (a) Probability density estimated from a Poincaré section at t = 1000T considering 100000 trajectories of the Duffing oscillator initially uniformly distributed over $\mathbb{X}$, (b) attractors' mean distributions, and (c) bifurcation diagram for A = 0.060 and σ = 0.03

4.2.2.
Chaotic attractor under white noise

The next example is the Duffing oscillator using the parameter values from [110], presented in Table 4.9. For these parameters, two attractors are obtained in the deterministic case: a period-1 attractor and a chaotic attractor. This example is used to demonstrate the capabilities of the proposed strategy to address not only periodic attractors but also nonperiodic attractors.

The global analysis is carried out considering the phase-space window $\mathbb{X} = \{-3.5, 3.5\} \otimes \{-3.5, 3.5\}$. The parameters of the subdivision procedure are summarized in Table 4.10. In the case of deterministic analysis, the Perron-Frobenius operator, eq. (2.59), is adopted, whereas for the stochastic analysis, the Foias operator, eq. (2.62), is adopted. In the latter case, each point in each box is integrated ten times to evaluate the effect of noise for each set of initial conditions.

Table 4.9 – Duffing oscillator parameters for additive white noise

Parameter	Value
α	-0.5
β	0.2
δ	0.085
Ω	0.71
A	0.204

Table 4.10 – Discretization data for the Duffing oscillator with a chaotic attractor

Depth level	Box-size	Points per dimension	Total collocation points
13	{0.0547, 0.1094}	9	81
14	{0.0547, 0.0547}	8	64
15	{0.0273, 0.0547}	7	49
16	{0.0273, 0.0273}	6	36
17	{0.0137, 0.0273}	5	25
18	{0.0137, 0.0137}	4	16

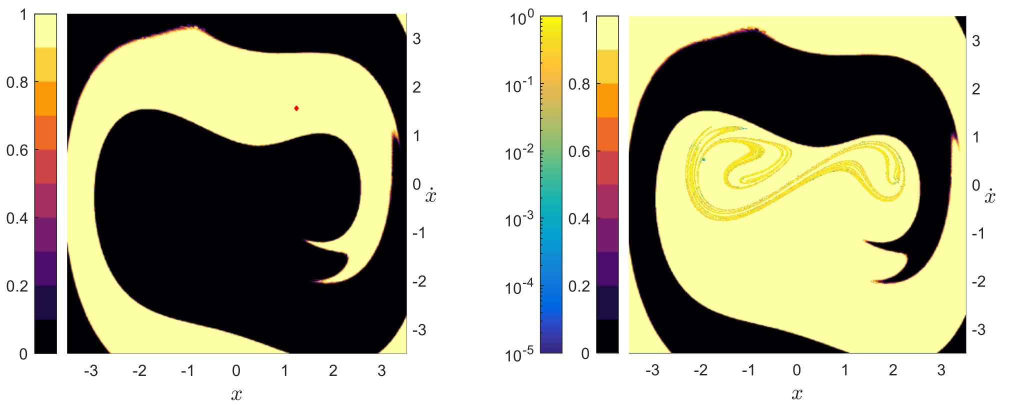

(a) 1-period attractor (b) chaotic attractor

Figure 4.33 – Basins of attraction and attractors' densities for the deterministic Duffing oscillator with a periodic and a chaotic attractor

The deterministic basins of the period-1 attractor and the chaotic attractor are shown in Figure 4.33. The influence of noise in such a case was previously studied in [96], where a box covering of the attractors was adopted instead of the present operator framework. Here a distinction between chaotic and nonchaotic solutions is observed in the attractors' distributions. Since chaotic solutions usually spread over the phase-space, they have an intrinsic distribution that is not a Dirac delta function. Nevertheless, the subdivision procedure is capable of identifying and refining this distribution. This is similar to previous results [31–33], where a subdivision procedure was adopted to cover attractors. Furthermore, the basins' boundaries are correctly identified, showing the capability of the proposed subdivision procedure.

The effect of additive white noise with increasing standard deviation is illustrated in Figure 4.34 for $s = 0.005$ and Figure 4.35 for $s = 0.008$. The attractors' distributions are more affected by noise in comparison with the basins' boundaries, diffusing over the phase-space as s increases. The boundaries remain localized to a certain degree, but a small diffusion is also observed. The proximity of the chaotic attractor to the boundary is an important characteristic of this system, which is already observed in the deterministic basin (Figure 4.33(b)) with the considered excitation amplitude A. Increasing A would indeed lead to a boundary crisis (see also [77]), with the chaotic basin being completely captured by the periodic one. When adding a low noise intensity, an attractor-saddle connection (here already observed for $s = 0.008$, Figure 4.35) also occurs with the considered excitation amplitude $A = 0.204$, highlighting how the stochasticity leads to the occurrence of the global bifurcation event. Note also that in Figure 4.35 the basins for a long time-horizon ($1/\varepsilon = 1e8$) are displayed. Actually, with the considered value of noise intensity ($s = 0.008$) as well as higher ones, regions with 100% certainty of staying at the chaotic attractor are actually inexistent, with all trajectories eventually converging to the period-1 attractor, as it will be shown later on. Therefore, the chaotic outcome for $s > 0.008$ only occurs as a long transient, with the final asymptotic attractor being periodic.

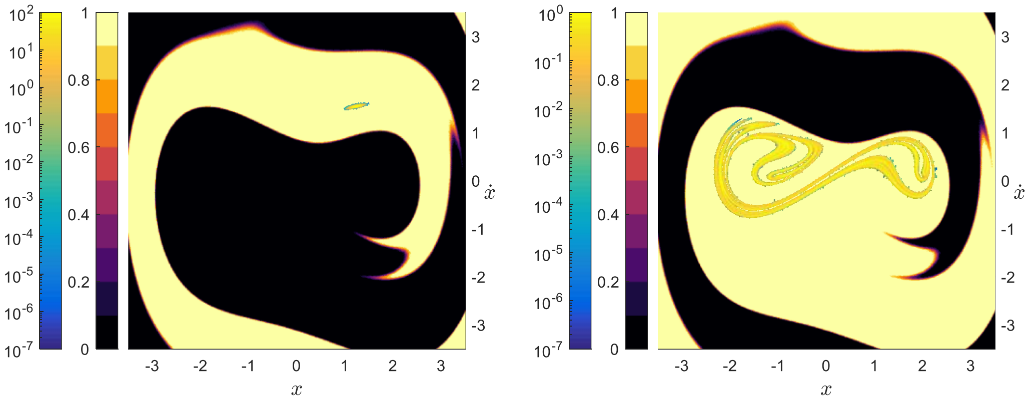

(a) 1-period attractor (b) chaotic attractor

Figure 4.34 – Stochastic basins of attraction (second color bar) and attractor's densities (first color bar) for the Duffing oscillator with a chaotic attractor and additive white noise $s = 0.005$. Time-horizon $1/\varepsilon = 1e8$

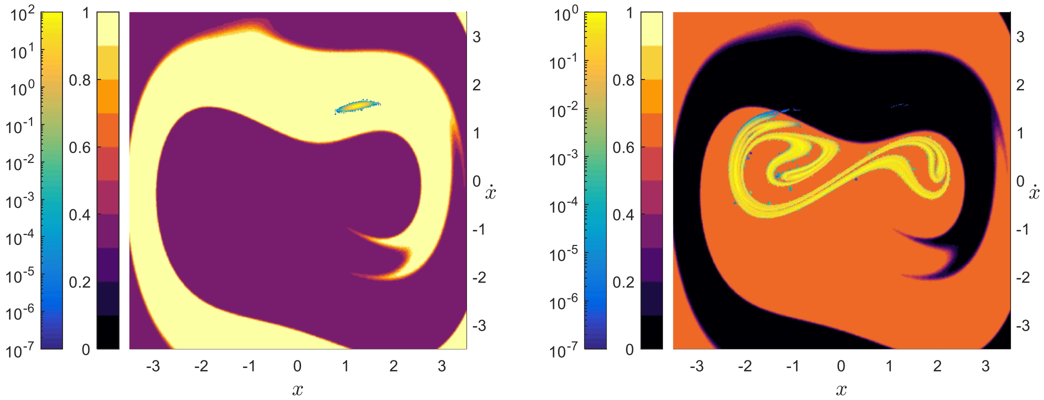

(a) 1-period attractor (b) chaotic quasi-attractor

Figure 4.35 – Stochastic basins of attraction (second color bar) and attractor’s densities (first color bar) for the Duffing oscillator with a chaotic attractor and additive white noise s = 0.008. Time-horizon $1/\varepsilon$ = 1e8

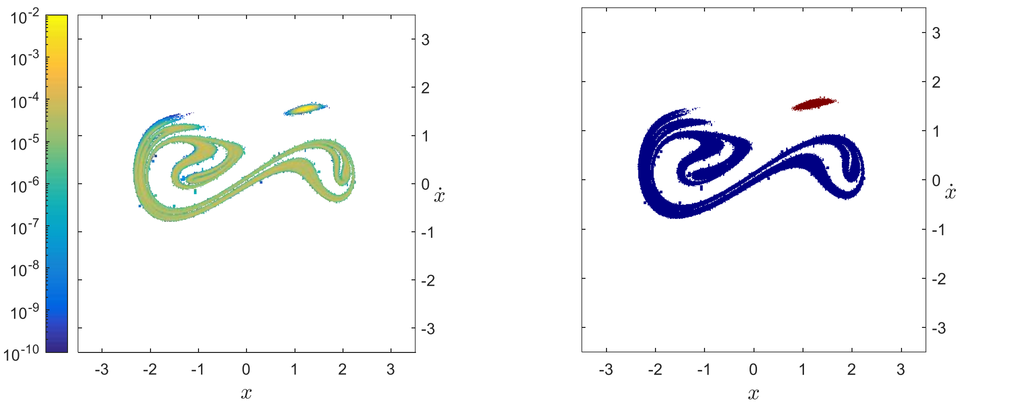

(a.1) s = 0.008, absolute value (a.2) s = 0.008, negative (blue) and positive (red) regions

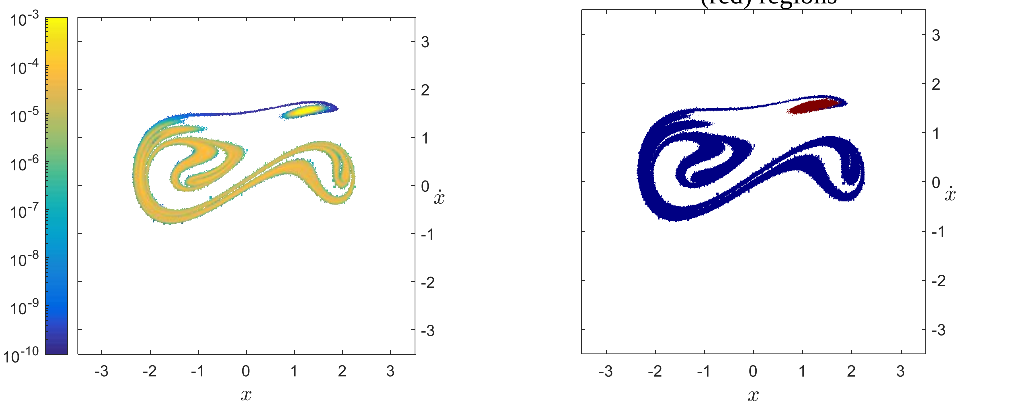

(b.1) s = 0.010, absolute value (b.2) s = 0.010, negative (blue) and positive (red) regions

Figure 4.36 – Duffing oscillator with chaotic attractor – almost permanent eigenmeasures for selected noise intensities

Figure 4.36 displays the corresponding eigenmeasure for selected values of the standard deviation. Similar to Figure 4.19, they are almost invariant, with eigenvalues equal to 0.999999995 for s = 0.008 and 0.999999882 for s = 0.01. In this case, two solutions collide, the period-1 and the chaotic attractor. The period-1 attractor remains stable, with eigenvalue 1. Trajectories stay in each region depicted in Figure 4.36(a.2, b.2) for a long time before decaying to an attractor. In this example, chaotic solutions decay to the period-1 solution, as observed in Figure 4.35.

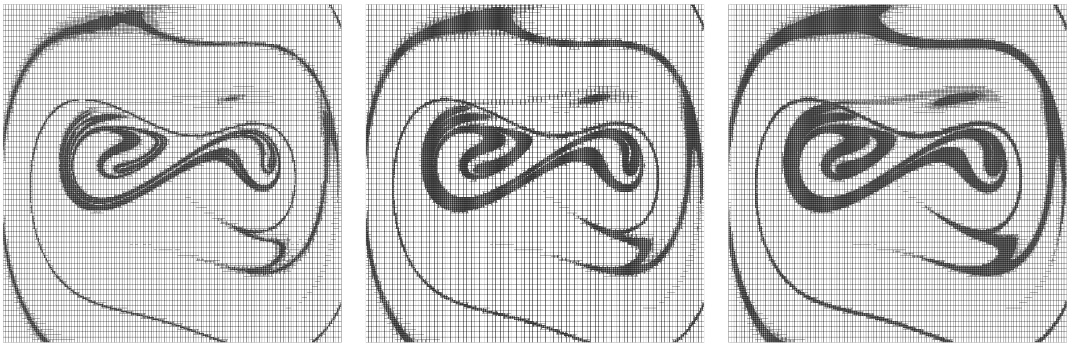

(a) s = 0.000 (b) s = 0.005 (c) s = 0.008

Figure 4.37 – Dependence of the final partition $\mathbb{B}_{18}$ of the chaotic Duffing oscillator's stochastic fields as a function of the standard deviation s

The final partition $\mathbb{B}_{18}$ is depicted in Figure 4.37 for increasing noise levels. The results confirm that the proposed subdivision procedure can identify and refine regions of higher diffusion, especially the attractors' densities, minimizing the numerical diffusion across the entire phase-space. Table 4.11 gives information on the total box count and the achieved economy. Since the basin boundaries are localized for all noise levels, the algorithm performs well, with economy values higher than 75%, for all cases.

Table 4.11 – Box count for the chaotic Duffing oscillator's stochastic field at level 18

s	Current box count	Maximum box count	Percentual	Economy
0.000	37061	262144	14.14%	85.86%
0.005	48772	262144	18.61%	81.39%
0.008	58250	262144	22.22%	77.78%

Figure 4.38 and Figure 4.39 illustrate the time-dependency of the basins of attraction for $s = 0.01$. Values of $\varepsilon \approx 1$ correspond to small time-horizons, identifying regions that converge to a given attractor after a small-time interval in the mean sense. As ε decreases, the time-horizon increases, approaching the asymptotic limit of all time responses, that is, the steady-state basin of attraction. Figure 4.38 shows the results for the period-1 attractor. Initially ($\varepsilon = 0.9$ and $\varepsilon = 0.5$), only a small region of initial conditions surrounding the attractor is obtained with a high probability of converging to the noisy attractor. For $\varepsilon = 0.1$, a

much larger region with varying probability is detected. For $\varepsilon = 1e\text{-}4$ (long transient), a large region with probability equal to one is obtained whose topology is rather similar to the basin of the period-1 attractor obtained in the deterministic case and for lower values of the standard deviation (see Figure 4.33 to Figure 4.35). Figure 4.39 shows that up to this time-horizon the two attractors are clearly distinct, see Figure 4.38(d) and Figure 4.39(d). For smaller values of ε (longer time-horizon), all solutions converge to the period-1 attractor, with its basin covering the whole phase-space. The chaotic attractor basin vanishes completely for this time-horizon, as shown in Figure 4.39(f). According to [110], jumps from the chaotic to the period-1 attractor were not expected for $s < 0.02$. This shows the importance of considering long transients in this kind of analysis, although this increases the computational effort. However, in many applications, transient basins are of importance [61, 112, 196], and the present results clearly demonstrate the impact of noise on them and how transient basins of noisy systems can be used to evaluate the system safety. Also, it can be used in control algorithms.

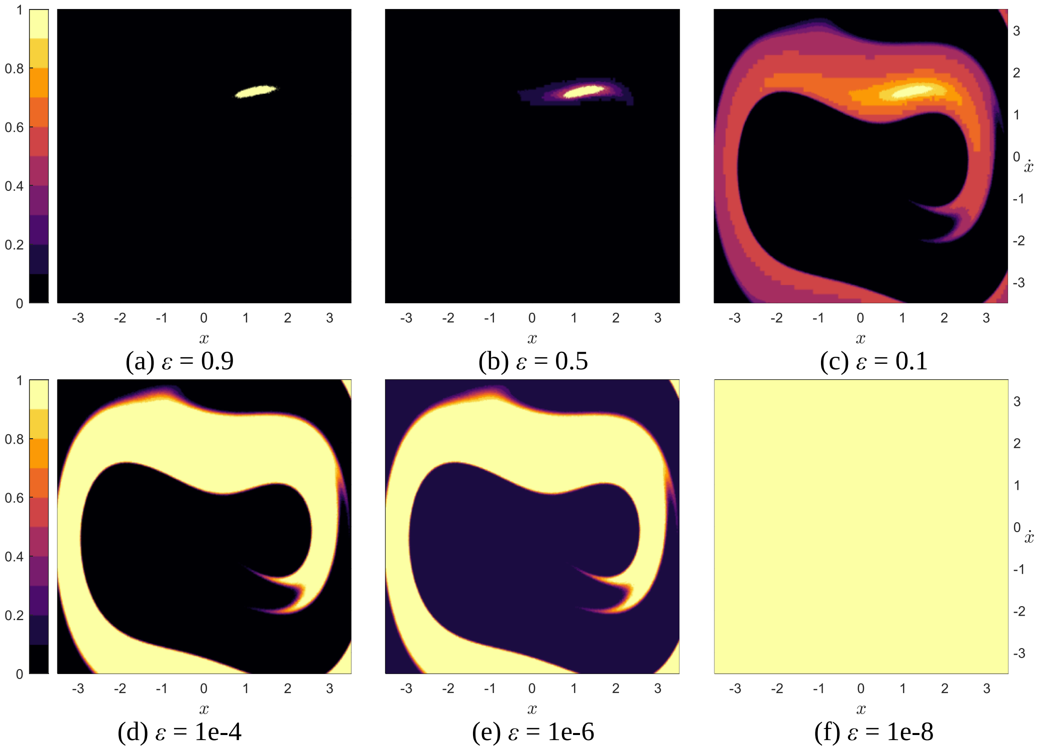

Figure 4.38 – Dependency of the stochastic basin of attraction for the period-1 attractor with additive white noise and s = 0.010 on the time-horizon $1/\varepsilon$

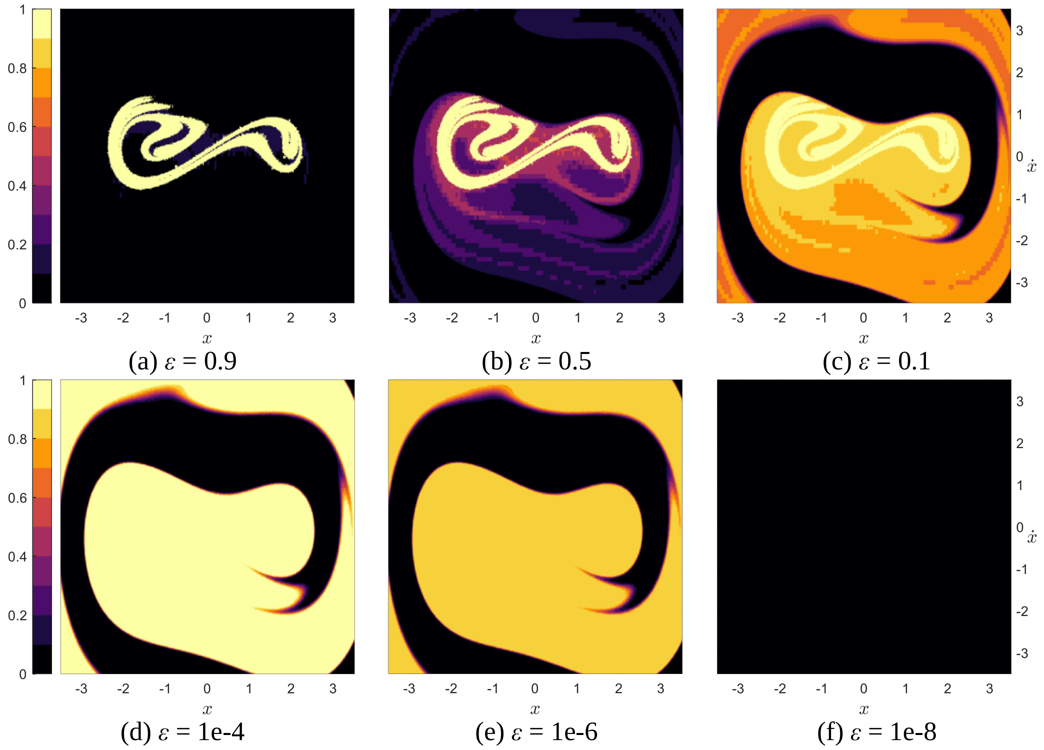

Figure 4.39 – Dependency of the stochastic basin of attraction for the chaotic attractor with additive white noise and s = 0.010 on the time-horizon $1/\varepsilon$

Figure 4.40 shows, for ε = 1e-8, the variation of the basins' area as a function of the scaling parameter σ for A = 0.060 and selected probability thresholds. Again, for each attractor, the integrity measure is computed employing eq. (4.2). The basin area of the period-1 attractor remains constant for small values of s up to s=0.050, being about 40% of the total area of the adopted window, while the remaining 60% belongs to the chaotic attractor. However, when s increases beyond this threshold, the period-1 attractor basin area increases steadily with the noise intensity s, converging to one at s = 0.01. In this range, the chaotic attractor displays an increasing loss of integrity with noise, as already illustrated by the analysis of its basin and distribution. This system represents a noise-sensitive case whose global effect is non-trivially enhanced also due to the relatively low amplitude value (A = 0.060) considered for the deterministic excitation, with one attractor suddenly vanishing in the asymptotic sense for a small parameter change.

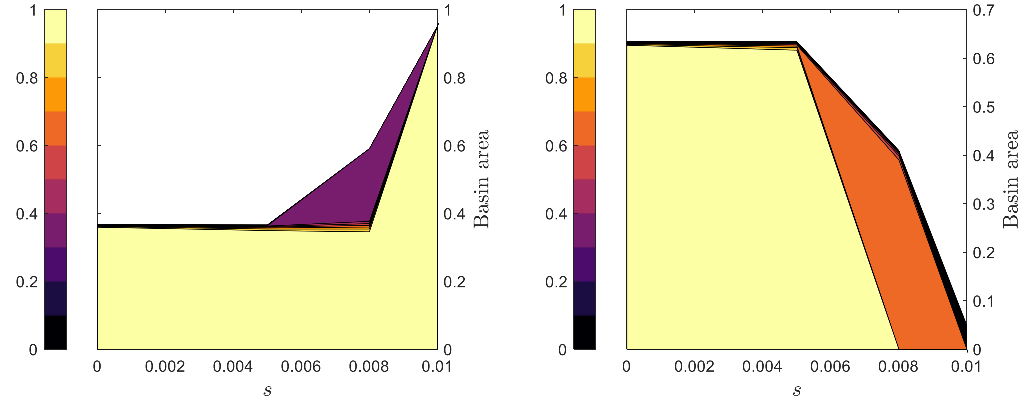

(a) 1-period attractor (b) chaotic attractor

Figure 4.40 – Variation of the Duffing oscillator basins area as a function of the noise intensity *s* for *A* = 0.06, showing various probability thresholds (color bar).
Time-horizon $1/\varepsilon$ = 1e8

A Monte-Carlo experiment was conducted to demonstrate the time-dependency of the attractors for *s* = 0.01 and the difference with the results presented in [110]. The initial condition $(x, \dot{x}) = (0, 0)$ at the center of the chaotic region was integrated 5000 times with the fourth-order stochastic Runge-Kutta. Figure 4.41 presents the histograms for three time-horizons, 1000*T*, 10000*T*, and the final value of 100000*T*. For 1000*T*, the results already indicate that some samples converge to the period-1 attractor, see Figure 4.41(a). The other histograms show that, as time progresses, an increasing number of samples converge to the period-1 region. This validates the previous results obtained through the proposed operator perspective, demonstrating the time-dependency of the responses and their respective basins.

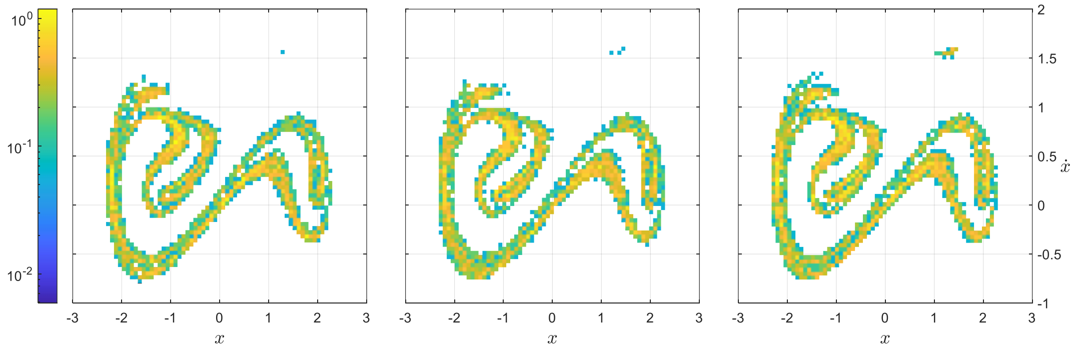

(a) $1/\varepsilon = 1000T$ (b) $1/\varepsilon = 10000T$ (c) $1/\varepsilon = 100000T$

Figure 4.41 – Histograms of 5000 samples with initial condition $(x, \dot{x}) = (0, 0)$ at selected time-horizons, for *s* = 0.010

4.3. Parametrically excited Duffing oscillator

This final example illustrates the behavior of a parametrically excited Duffing oscillator with noise, described by

$$\ddot{x}+\delta\dot{x}+\left(\alpha+A\cos\Omega t+s\dot{W}\right)x+\beta x^{3}=0. \tag{4.4}$$

The adopted parameters are summarized in Table 4.12. They represent a 2:1 parametric resonance, where the natural frequency is one, and the parametric excitation frequency is two. For these parameters, there is one potential well delimited by two saddles. This example is based on [197], where quasiperiodic oscillations of the vocal folds are investigated. The parameters of the subdivision procedure are summarized in Table 4.13. In the deterministic case, the Perron-Frobenius operator is adopted, eq. (2.59), whereas for the stochastic analysis, the Foias operator is adopted, eq. (2.62). For the latter case, each point in each box is integrated ten times to obtain the effect of noise for each set of initial conditions. The global analysis is carried out considering the phase-space window $\mathbb{X}=\{-1.99,2.01\}\otimes\{-1.09,1.11\}$. This particular window was chosen to avoid the attractors or repellors at $(x,\dot{x})=(0,0)$ to be at a box edge, helping the refinement convergence.

Table 4.12 – Parametrically excited Duffing oscillator parameters

Parameter	Value
α	1
β	-1
δ	0.1
Ω	2.0

The results of the deterministic global analysis for increasing values of *A* are shown in Figure 4.42. Initially, the free vibration results are obtained (*A* = 0.00), Figure 4.42(a). The yellow region corresponds to the equilibrium point at $(x,\dot{x})=(0,0)$, while black corresponds to escape. The yellow region for $A\geq 0.50$ is associated with the period-2 oscillations, characteristic of the main parametric resonance region at twice the natural frequency. This is indicated in the transfer operator P_h by a minus one eigenvalue. The Markovian nature of the transfer operators has a spectral radius of one, i.e., all eigenvalues are within the unit circle in the complex plane [37]. The cyclic behavior is identified through eigenvalues with an absolute value of one but a real part less than one. Specifically, the eigenvalues corresponding to an attractor are

$$\mu_{r,n} = e^{(n-1)2\pi I/r}, \tag{4.5}$$

where $r \geq 1$ is the periodicity of the attractor and $1 \leq n \leq r$. For r = 1, there is only one eigenvalue $\mu_{1,1}$ = 1; for r = 2, there are two, $\mu_{2,1}$ = 1, and $\mu_{2,2}$ = -1, and so on. For more details, refer to [33].

Table 4.13 – Discretization data for the parametrically excited Duffing oscillator

Depth level	Box-size	Points per dimension	Total collocation points
11	{0.0625, 0.0688}	12	144
12	{0.0625, 0.0344}	11	121
13	{0.0313, 0.0344}	10	100
14	{0.0313, 0.0172}	9	81
15	{0.0156, 0.0172}	8	64
16	{0.0156, 0.0086}	7	49
17	{0.0078, 0.0086}	6	36
18	{0.0078, 0.0043}	5	25
19	{0.0039, 0.0043}	4	16

As the forcing amplitude increases, the safe basin area decreases, with increasing incursive tongues from the escape region eroding the original stable basin, a mechanism common to all periodically driven nonlinear damped oscillators with the ability to escape from a potential well [198]. Due to a global bifurcation, shortly after the Melnikov tangency, large incursive fractal fingers start to penetrate into the yellow parametrically resonant basin. The basins for the last three amplitude values, A = {0.75, 0.80, 0.85}, Figure 4.42(f, g, h), show a central region with increasing fractality, resulting in a rapid rate of erosion of the safe area.

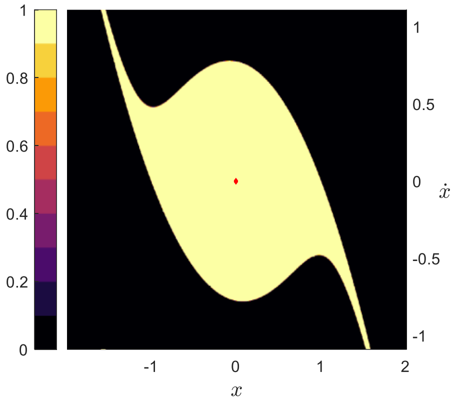

(a) A = 0.00

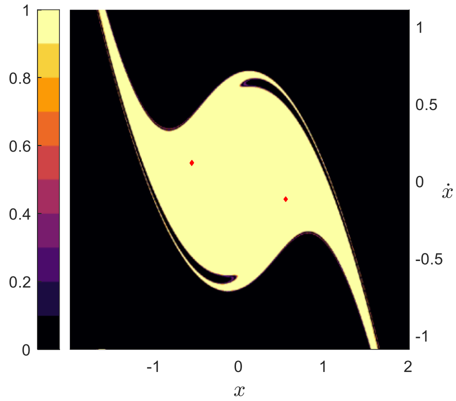

(b) A = 0.50

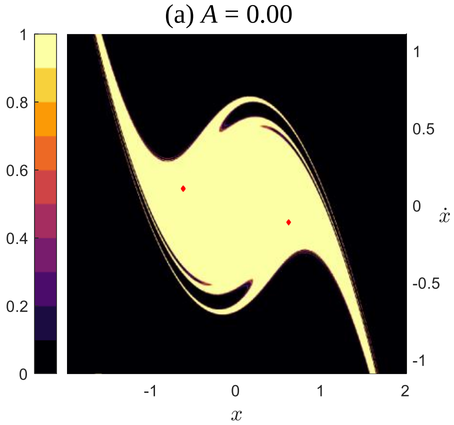

(c6) A = 0.60

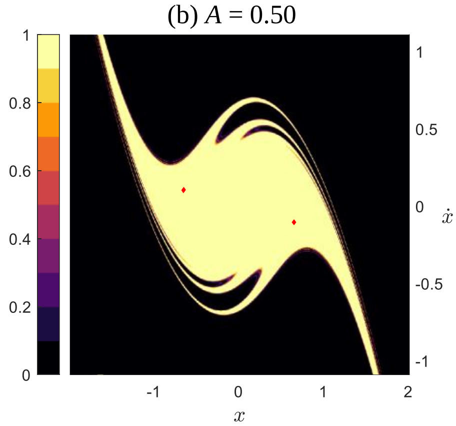

(d) A = 0.65

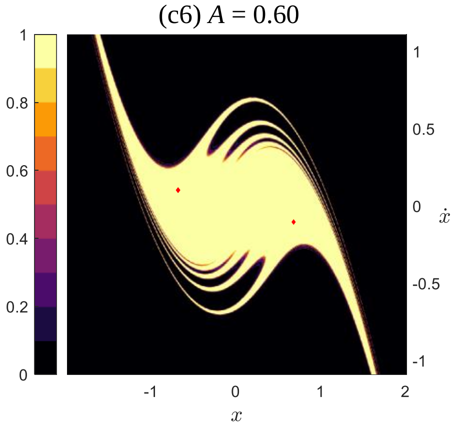

(e) A = 0.70

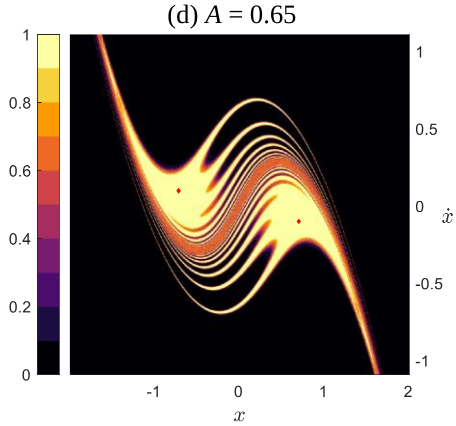

(f) A = 0.75

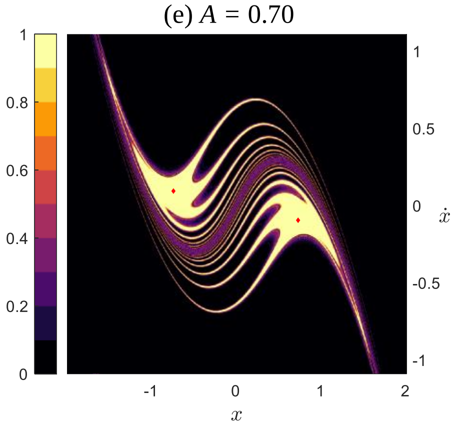

(g) A = 0.80

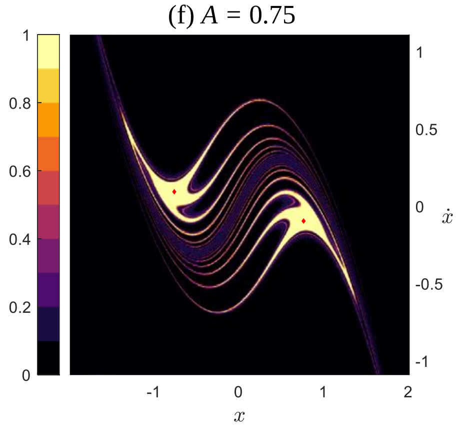

(h) A = 0.85

Figure 4.42 – Basins of attraction (color bar) and attractors of the parametrically excited deterministic Duffing oscillator as a function of the excitation magnitude A

4.3.1. Effects of parametric white noise

The noise-induced dynamics are considered next. An amplitude of A = 0.6 with varying noise intensity s is adopted. The transfer matrix of the noise-driven system is the Foias operator, F_h. The probability integral in eq. (2.62) is solved by the Monte-Carlo method. Ten noise samples for each set of initial conditions in each box are considered to calculate the discretized transfer operator F_h.

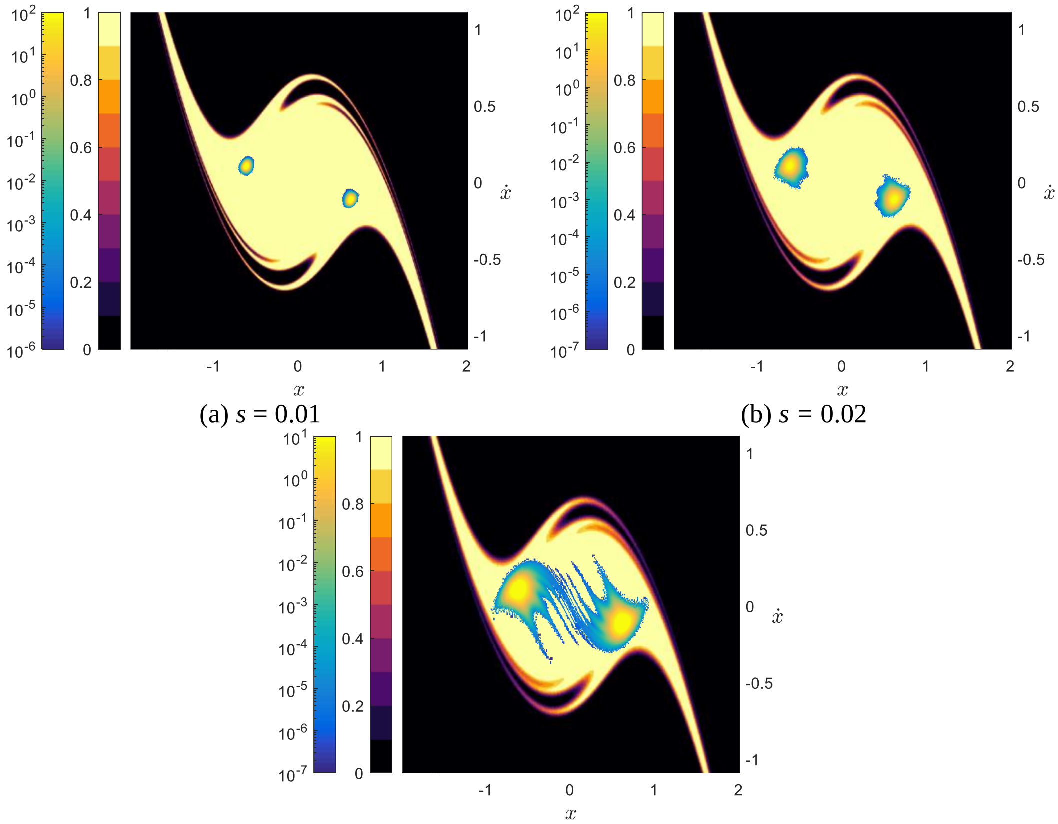

(a) s = 0.01 (b) s = 0.02

(c) s = 0.03

Figure 4.43 – Stochastic basins of attraction (second color bar) and the period-2 attractor's density (first color bar) of the parametrically excited Duffing oscillator for A = 0.6 as a function of the noise intensity s

Figure 4.43 presents the results for the three noise levels, s = 0.01, 0.02, and 0.03. The effect of noise on the probability density of this periodic attractor is clearly demonstrated by its swift diffusion over the phase-space. The basins' boundaries are also affected by noise, becoming blurred as noise increases. The case with s = 0.03, Figure 4.43(c), is interesting because the periodic counterpart is an almost invariant eigenmeasure, with eigenvalue equal to -0.999999973. The depicted eigenmeasure corresponds only to the permanent eigenvalue, λ = 1. This is an almost cyclic behavior, that is, a collection of frequently cyclically permuted sets as the dynamical system evolves [33]. These sets are depicted for the selected values of s in Figure 4.44. The two colors identify the two distinct cyclic sets. This behavior corresponds to the first scenario described by Dellnitz and Junge [33], where cyclic components lose stability.

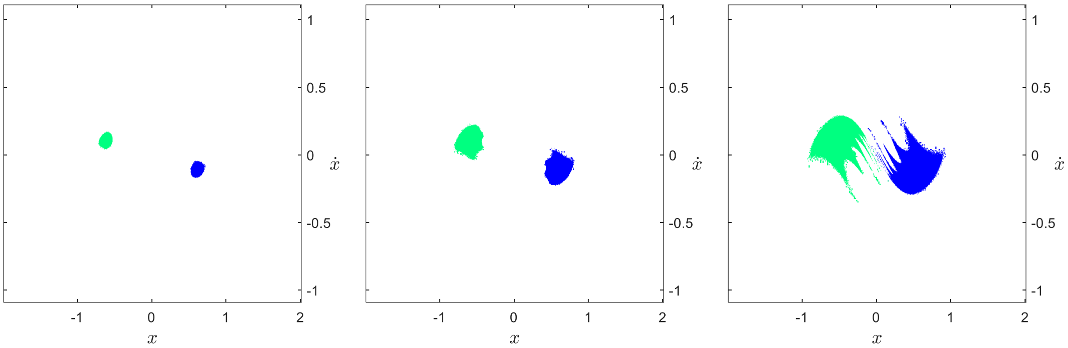

(a) cyclic sets, s = 0.01 (b) cyclic sets, s = 0.02 (c) almost cyclic sets, s = 0.03

Figure 4.44 – Stochastic (almost) cyclic behavior of the parametrically excited Duffing oscillator for A = 0.6 and increasing noise intensity s

For the next noise level, $s = 0.04$, there is no attractor in the asymptotic sense. The previous attractors are long transient solutions, decreasing the probability density as time evolves. The eigenvalues of the transfer matrix F_h demonstrate this, with a value of 0.999999719. This long transient behavior is depicted in Figure 4.45, where the variation of the areas that converge to the initial attractors as a function of the time-horizon $1/\varepsilon$ is depicted. For $1/\varepsilon \geq 1e6$, Figure 4.45 (e, f), the basin loses stability, with zero probability of converging to the initially stable attractor. The opposite is observed when the sink cell is treated as an attractor, Figure 4.46. The escape region remains almost identical to the previous case until $1/\varepsilon$ = 1e4. For the last cases with $1/\varepsilon \geq 1e6$, Figure 4.46 (e, f), the basin set is absorbed by the escape basin (see the long-time instability of the period-2 attractor in Figure 4.47.

The proposed measure to quantify the system's integrity is presented in Figure 4.48, for ε = 1e-8. The product between the period-2 attractor probabilities and its normalized basin area for each threshold, eq. (4.2), is depicted with its noise dependence. As before, the attractor loses stability at s = 0.04, accompanied by a fast decrease in safe area. It is again shown that the results can be used to quantify the effect of noise on the dynamic integrity measures.

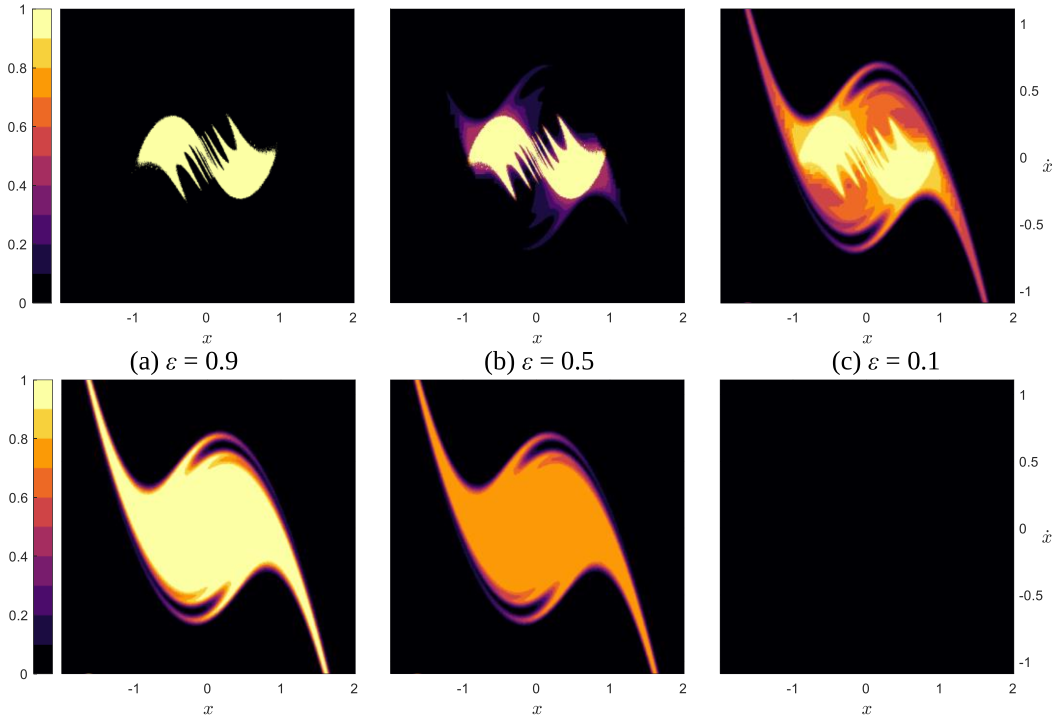

(a) ε = 0.9 (b) ε = 0.5 (c) ε = 0.1

(d) ε = 1e-4 (e) ε = 1e-6 (f) ε = 1e-8

Figure 4.45 – Dependency of the stochastic basin of attraction for the period-2 attractor with white noise on the time-horizon $1/\varepsilon$. s = 0.04

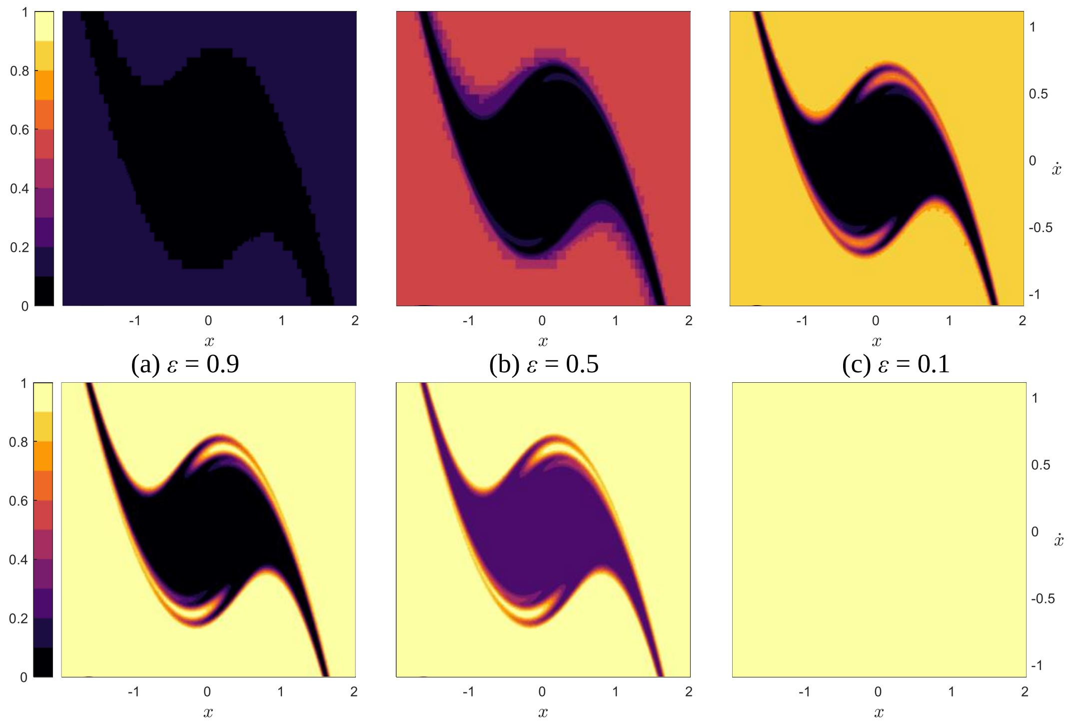

(a) ε = 0.9 (b) ε = 0.5 (c) ε = 0.1

(d) ε = 1e-4 (e) ε = 1e-6 (f) ε = 1e-8

Figure 4.46 – Dependency of the stochastic basin of attraction for the escape solution with white noise on the time-horizon $1/\varepsilon$. s = 0.04

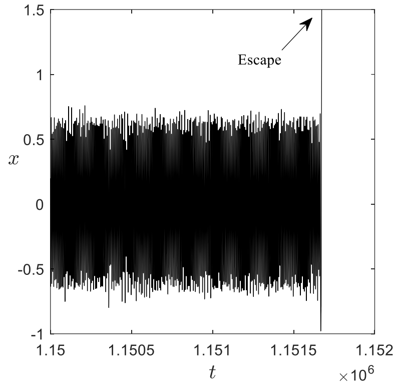

Figure 4.47 – Parametrically excited Duffing oscillator's long-time instability due to high noise intensity for A = 0.60 and s = 0.04

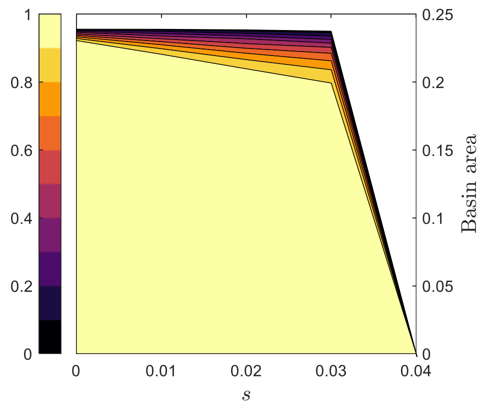

Figure 4.48 – Parametrically excited Duffing oscillator – period-2 basin area versus the noise intensity s for various probability thresholds (color bar). Time-horizon $1/\varepsilon$ = 1e8

5
Nonlinear response of an imperfect microcantilever static and dynamically actuated considering uncertainties and noise

A theoretical investigation is conducted on an imperfect MEMS device constituted of an imperfect clamped-free microbeam electrostatically and electrodynamically actuated with added noise. Using Hamilton's principle, the nonlinear equation of motion is derived by considering the nonlinear electric load, the geometric nonlinearities up to the third order, and the geometric imperfections. Additive white noise is considered to model forcing uncertainties, and the Galerkin modal discretization method is employed to generate stochastic differential equations of Itô type, which are solved by the stochastic Runge-Kutta method. Finally, the global dynamics are investigated by the generalized cell mapping [19, 22, 23], through which the appropriate transfer operators are constructed. The effects of additive noise on resonant and non-resonant solutions are observed, changing the probability measures and basins of attraction. Special attention is given to the effect of imperfections and noise on the pull-in instability. The computations are performed by an Intel Core i7-7700HQ with eight logical processors of 2.8GHz, and the total available RAM is 24GB.

5.1.
Nonlinear Rayleigh microcantilever electrically actuated

The planar flexural imperfect Rayleigh beam equation is derived based on the 3D formulation presented in Appendix A, where Euler-Bernoulli beams are modeled, and the effect of rotary inertia is also considered. Assuming only planar motions, nonplanar displacements and the Euler angles ψ and ψ_0 become zero, see the trigonometric relations (A21) and (A23). Three coordinate systems are considered for the beam's kinematic definitions, which are the reference system (X, Z), the undeformed coordinates of the imperfect beam configuration (ξ_0, ζ_0), and the deformed configuration, (ξ, ζ). The reference and undeformed systems are Lagrangian frames of reference, with the former corresponding to the perfect model. The deformed axes define an Eulerian reference frame. The undeformed axes represent the imperfect model in a stress-free configuration. The undeformed arclength is identified by s, while the deformed arclength is identified by $\tilde{s}$. The resulting undeformed and deformed coordinate systems with respect to the reference system are given in Figure 5.1. The actuation plate is also depicted at a distance d. The axial and transversal displacements are denoted by u and w, respectively, and $w_0(x)$ is the initial geometric imperfection. An elastic isotropic linear material is considered.

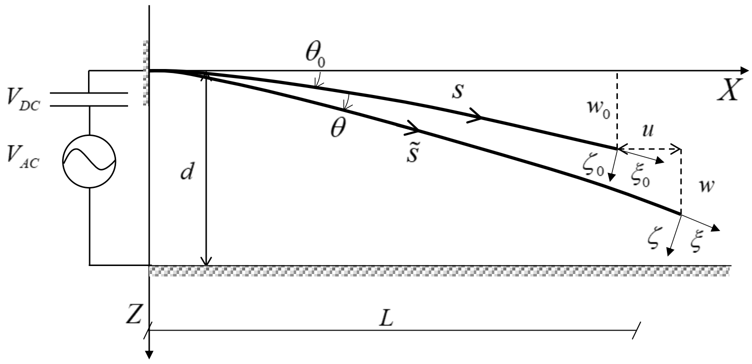

Figure 5.1 – Imperfect undeformed and deformed beam and coordinate systems

Trigonometric relations for the Euler angles θ and θ_0 restricted to the plane X-Z are obtained by setting to zero the displacements v and imperfections v_0 in eqs. (A22) and (A24), resulting in

$$\sin\bar{\theta} = \frac{-\bar{w}'}{\sqrt{\left(\sqrt{1-w_0'^2}+u'\right)^2+\bar{w}'^2}},$$
$$\cos\bar{\theta} = \frac{\sqrt{1-w_0'^2}+u'}{\sqrt{\left(\sqrt{1-w_0'^2}+u'\right)^2+\bar{w}'^2}}, \tag{5.1}$$

$$\sin\theta_0 = w_0',$$
$$\cos\theta_0 = \sqrt{1+w_0'^2}. \tag{5.2}$$

Similarly, the axial elongation in the plane X-Z is defined as

$$\Delta_e = \sqrt{\left(\sqrt{1-w_0'^2}+u'\right)^2+\bar{w}'^2}-1. \tag{5.3}$$

The final equations of motion are given by

$$G_u' = \left[A_\theta \frac{\partial\theta}{\partial u'} - \lambda \frac{u'+\sqrt{1+w_0'^2}}{2\left(1+\Delta_e\right)}\right]' = \frac{d}{dt}\left(\frac{\partial \ell}{\partial \dot{u}}\right) - Q_u^{nc}, \tag{5.4}$$

$$G_w' = \left[A_\theta \frac{\partial\theta}{\partial w'} - \lambda \frac{\bar{w}'}{2\left(1+\Delta_e\right)}\right]' = \frac{d}{dt}\left(\frac{\partial \ell}{\partial \dot{w}}\right) - Q_w^{nc}, \tag{5.5}$$

with A_θ given by eq. (A54), and the Lagrangian kernel ℓ by

$$\ell = \frac{1}{2}\left(m\dot{u}^2 + m\dot{w}^2 + J_\eta \dot{\theta}^2\right) - \frac{D_\eta}{2}\theta'^2 + \frac{\lambda}{2}\Delta_e. \tag{5.6}$$

The eqs. (5.4) and (5.5) are exact within the adopted theory. Approximate equations are obtained by expanding then in Taylor series of the displacements w and imperfection w_0 up to the third order and axial displacement u up to the second order since $u<<w$. Thus, the equations of motion with polynomial nonlinearities are given by

$$m\ddot{u} = \left\{D_\eta \bar{w}' w''' - J_\eta \bar{w}' \ddot{w}' + \frac{\lambda}{2}\left(\frac{\bar{w}'^2}{2} - 1\right)\right\}', \tag{5.7}$$

$$\begin{aligned} m\ddot{w} + c_w\dot{w} - Q_w = \Big\{ &-D_\eta \Big[\bar{w}' w''\left(\bar{w}'' + w_0''\right) + w' w_0''^2 + \\ &w' w_0'''\left(w_0' + \frac{w'}{2}\right) + w'''\Big] + J_\eta\left(\bar{w}'\dot{w}'^2 + \ddot{w}'\right) - \frac{\lambda}{2}\bar{w}'\Big\}', \end{aligned} \tag{5.8}$$

where the relation (A46) is assumed and axial loads Q_u* are neglected.

The axial displacement is obtained from eq. (5.3), resulting in

$$u = -\frac{1}{2}\int_0^s w'^2 + 2w'w_0' ds, \tag{5.9}$$

By substituting eq. (5.9) into eq. (5.7), the Lagrange multiplier can be written as

$$\lambda = 2D_\eta \bar{w}' w''' - 2J_\eta \bar{w}' \ddot{w}' + 2m \int_L^s \int_0^s \dot{w}'^2 + \bar{w}' \ddot{w}' ds ds. \tag{5.10}$$

Finally, the equation of motion is obtained by substituting the Lagrange multiplier, eq. (5.10), into eq. (5.8), resulting in the following integro-differential equation of motion

$$\begin{aligned} m\ddot{w} + c_w \dot{w} - Q_w = \Bigg\{ & -D_\eta \left[\bar{w}' w'' \left(\bar{w}'' + w_0'' \right) + w' w_0''^2 + w' w_0''' \left(w_0' + \frac{w'}{2} \right) + \right. \\ & \left. \left(\bar{w}'^2 + 1 \right) w''' \right] + J_\eta \left[\bar{w}' \dot{w}'^2 + \left(\bar{w}'^2 + 1 \right) \ddot{w}' \right] - \\ & m\bar{w}' \int_L^s \int_0^s \dot{w}'^2 + \bar{w}' \ddot{w}' ds ds \Bigg\}' . \end{aligned} \tag{5.11}$$

which is the same equation used in [96] obtained through a simplified bidimensional formulation.

The associated boundary conditions of the clamped-free beam are given by,

$$\begin{aligned} & w(0,t) = w'(0,t) = 0, \\ & w''(L,t) = D_\eta w'''(L,t) - J_\eta \ddot{w}'(L,t) = 0. \end{aligned} \tag{5.12}$$

Considering a parallel plate capacitor with a rectangular cross-section, the electrostatic force Q_w can be written as [116]

$$Q_w = \frac{b\varepsilon V^2}{2\left(d - \bar{w}\right)^2}, \tag{5.13}$$

where b is the beam width, d is the initial gap for a perfect beam, ε is the free space permittivity, and V is the applied voltage.

Equation (5.11) is then nondimensionalized considering the following parameters

$$\begin{aligned} & s^* = s/L, \qquad t^* = t\sqrt{D_\eta / \left(mL^4\right)}, \\ & w^* = w/d, \qquad w_0^* = w_0/d, \qquad Q_w^{\ *} = Q_w L^3 / D_\eta, \\ & J_\eta^* = J_\eta / \left(mL^2\right), \qquad c_w^* = c_w L^2 / \sqrt{mD_\eta}, \\ & \varepsilon^* = \varepsilon L^2 / D_\eta, \qquad d^* = d/L, \qquad b^* = b/L, \end{aligned} \tag{5.14}$$

resulting in

$$\ddot{w}+c_w\dot{w}-\frac{Q_w}{d}=\Bigg\{-d^2\left[\bar{w}'w''\left(\bar{w}''+w_0''\right)+w'w_0''^2+w'w_0'''\left(w_0'+\frac{w'}{2}\right)+\right.$$
$$\left.\left(\bar{w}'^2+\frac{1}{d^2}\right)w'''\right]+d^2J_\eta\left[\bar{w}'\dot{w}'^2+\left(\bar{w}'^2+\frac{1}{d^2}\right)\ddot{w}'\right]- \tag{5.15}$$
$$d^2\bar{w}'\int_1^s\int_0^s\left(\bar{w}'\dot{w}'\right)^\bullet ds ds\Bigg\}'.$$

where * is dropped for brevity. The nondimensional boundary conditions are

$$\begin{aligned} &w(0,t)=w'(0,t)=0,\\ &w''(1,t)=w'''(1,t)-J_\eta\ddot{w}'(1,t)=0, \end{aligned} \tag{5.16}$$

and the nondimensional electrostatic load is given by

$$Q_w^{\ *}=\frac{b\varepsilon V^2}{2d^2\left(1-\bar{w}\right)^2}, \tag{5.17}$$

with the singularity now at $\bar{w}=1$.

The total applied voltage is the sum of the direct current (V_{dc}) and the time-dependent alternate current (V_{ac}), i.e.:

$$V(t)=V_{dc}+V_{ac}(t). \tag{5.18}$$

The displacement is, therefore, decomposed into its dynamic and static parts as,

$$w(t,x)=w_d(t,x)+w_s(x). \tag{5.19}$$

Considering only the DC voltage in eq. (5.15), substituting eqs. (5.18) and (5.19) into eqs. (5.15) and (5.17) and setting to zero all terms with time derivatives, the static displacement component w_s is obtained from the following nonlinear equilibrium equation

$$\frac{b\varepsilon V_{dc}^{\ 2}}{2d^3\left(1-\bar{w}_s\right)^2}=d^2\Bigg\{\bar{w}_s'w_s''\left(\bar{w}_s''+w_0''\right)+w_s'w_0''^2+$$
$$w_s'w_0'''\left(w_0'+\frac{w_s'}{2}\right)+\left(\bar{w}_s'^2+\frac{1}{d^2}\right)w_s'''\Bigg\}', \tag{5.20}$$

where $\bar{w}_s=w_s+w_0$.

The additional dynamic displacement $w_d\left(t,x\right)$ is assumed as a perturbation of the static equilibrium position, and the resulting equation of motion is obtained by substituting eqs. (5.18) and (5.19) into eqs. (5.15) and (5.17) and expanding in Taylor series of w_d up to the third order, resulting in

$$\begin{aligned}&\ddot{w}_d + c_w\dot{w}_d - \frac{b\varepsilon}{d^3}\left[\frac{2w_d{}^3V_{dc}{}^2}{\left(1-\bar{w}_s\right)^5} + \frac{w_d{}^2\left(3V_{dc}{}^2 - 2V_{dc}V_{ac}\right)}{2\left(1-\bar{w}_s\right)^4} + \frac{w_d\left(V_{ac}+V_{dc}\right)^2}{\left(1-\bar{w}_s\right)^3} + \right.\\ &\left.\frac{2V_{dc}V_{ac}+V_{ac}{}^2}{2\left(1-\bar{w}_s\right)^2}\right] = \left\{-d^2\left[\left(\bar{w}'^2 + \frac{1}{d^2}\right)w_d'''' + w_d'\bar{w}_s''^2 + \right.\right.\\ &\left.\frac{1}{2}w_d'\left(\bar{w}'+\bar{w}_s'\right)\left(\bar{w}_s'''+w_s'''\right) + \bar{w}'w_d''\left(\bar{w}''+\bar{w}_s''\right)\right] + \\ &\left.d^2J_\eta\left[\bar{w}'\dot{w}_d'^2 + \left(\bar{w}'^2+\frac{1}{d^2}\right)\ddot{w}_d'\right] - d^2\bar{w}'\int_1^s\int_0^s \dot{w}_d'^2 + \bar{w}'\ddot{w}_d' ds ds\right\}',\end{aligned} \tag{5.21}$$

where $\bar{w}_s = w_s + w_0$ and $\bar{w} = w_d + w_s + w_0$. The sum of zeroth-order terms is equal to zero since they correspond to the static equilibrium position, eq. (5.20).

The geometric imperfection shape and the static and dynamic displacement fields are expanded in terms of the linear vibration modes. The Galerkin method is employed to discretize the equation of motion using as interpolation functions the linear vibration modes. The assumed mode expansion is derived from the boundary value problem considering the undamped linearized equation of motion. The linear vibration modes are the solution of the linearized equation of motion

$$\ddot{w} - J_\eta\ddot{w}'' + w^{iv} = 0, \tag{5.22}$$

with boundary conditions (5.16). Equation (5.22) corresponds to a Rayleigh beam, where the rotational inertia is considered [199]. The solution of eq. (5.22) is

$$w\left(s,t\right) = \sum_{i=1}^{\infty} w^{(i)}\left(t\right)F_i\left(s\right) \tag{5.23}$$

where $w^{(i)}$ is the ith modal amplitude and F_i is the ith natural mode of vibration. The natural modes are, for boundary conditions (5.16) [199],

$$F_i(s) = C_i \left\{ \cosh(b_i s) - \cos(a_i s) - \frac{a_i^2 \cos(A_i) + b_i^2 \cosh(b_i)}{a_i b_i \sin(A_i) + b_i^2 \sinh(b_i)} \left[\sinh(b_i s) - \frac{b_i}{a_i} \sin(a_i s) \right] \right\}, \tag{5.24}$$

where

$$a_i = \sqrt{\frac{J_\eta}{2}\omega_i^2 + \sqrt{\frac{J_\eta^2}{4}\omega_i^4 + \omega_i^2}}, \quad b_i = \sqrt{-\frac{J_\eta}{2}\omega_i^2 + \sqrt{\frac{J_\eta^2}{4}\omega_i^4 + \omega_i^2}}, \tag{5.25}$$

C_i are normalization constants with respect to the orthogonality condition of eq. (5.22), which is given by [199]

$$C_i = \frac{1}{\int_0^1 F_i^2 + J_\eta F_i' F_i' \, ds}, \tag{5.26}$$

and the natural frequencies are the roots of the nonlinear transcendental equation

$$\left(b_i^4 + a_i^4\right)\cos(a_i)\cosh(b_i) + \left(b_i^2 - a_i^2\right) a_i b_i \sin(a_i)\sinh(b_i) + 2a_i^2 b_i^2 = 0. \tag{5.27}$$

In most of the present chapter, a first mode expansion is adopted for both the geometric imperfection w_0, the static deflection w_s, and the dynamic deflection w_d, leading to a sdof reduced-order model, a usual procedure in the literature. Regarding geometric imperfection and static deflection, the first mode is the dominant one. As for the dynamic deflection, the excitation frequency is adopted close to the first natural frequency. In the rest of the text, the symbols for the modal amplitudes will be adopted as the same as those adopted for the state variables, namely w_0, w_s, and w_d, simplifying the notation.

5.2. Nonlinear equilibrium and deterministic local dynamics

The nondimensional constants adopted here are the same employed in [124] and [131]. They are summarized in Table 5.1.

Table 5.1 – Microbeam geometric and material nondimensional parameters

Parameters	Symbol	Values
Width	b^*	0.25
Initial gap	d^*	0.0046
Free space permittivity (V^{-2})	ε^*	2.9446 e-10
Damping	c_w^*	0.05
Rotational inertia	J_η^*	6.76875e-7

5.2.1. Static actuation

The discretized equilibrium equation is obtained by multiplying eq. (5.20) by the denominator $(1-\bar{w}_s)^2$ and then applying the Galerkin method considering the linear vibration modes as interpolating functions. The nonlinear equilibrium paths are obtained through a pseudo arc-length continuation procedure together with the Newton-Raphson method [200, 201]. The stability of the static solution is verified using the minimum potential energy criterion. Initially, the static response results are compared with the experimental results from [140]. Figure 5.2 show the results for the perfect beam and two imperfection levels, w_0, clarifying the influence of the imperfection uncertainties on the results. The displacement w_s is evaluated at s = 1, considering only the first linear vibration mode in the Galerkin approximation. Additionally, analytical results considering a modal expansion with three linear modes and w_0=-0.05 is displayed for comparison. A good agreement between the experimental results and analytical results is observed up to pull-in. Specifically, the perfect system static pull-in load is 65.34, while the experimental result is 68.5. The resulting ratio is 0.953, showing the validity of the formulation for loads in the vicinity of the pull-in limit. It should be observed that the imperfection level in the experiment is not mentioned in [140], but from the results, it is concluded to be small.

Figure 5.3(a) shows the nonlinear response of the beam under DC actuation for selected levels of geometric imperfection. Here continuous lines correspond to stable solutions while dashed lines correspond to unstable solutions. Figure 5.3(b) shows the typical cusp catastrophe surface by introducing the imperfection magnitude as a second control parameter.

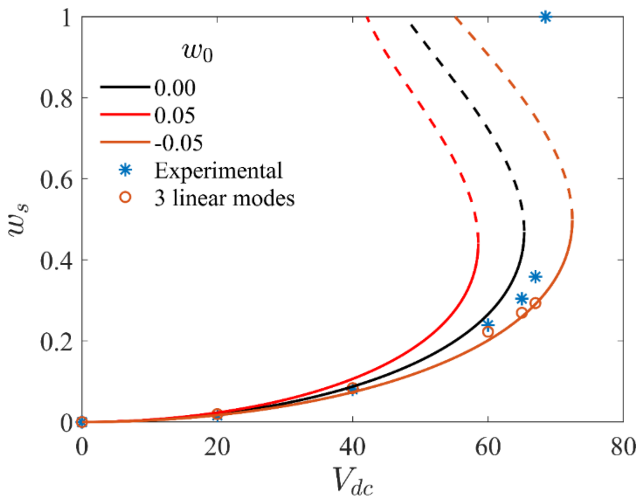

Figure 5.2 – Comparison of the static response at s = 1 of the microbeam under DC actuation for selected levels of geometric imperfection

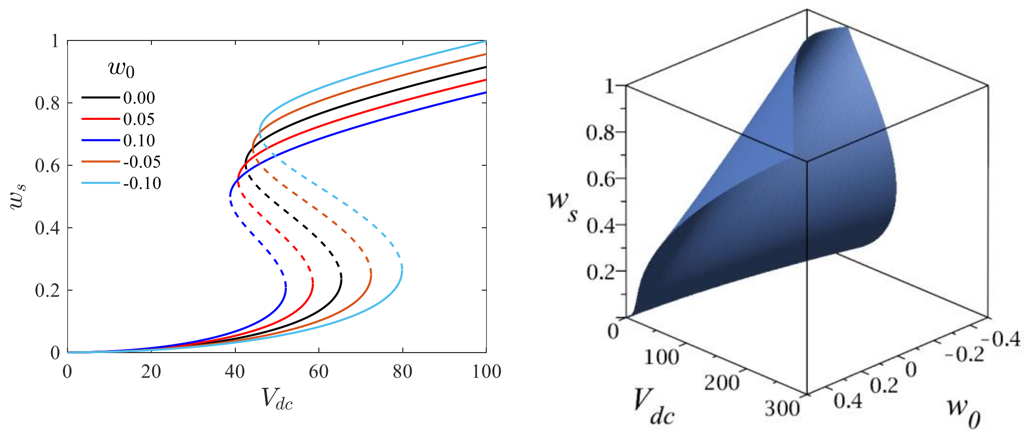

(a) (b)

Figure 5.3 – Static response of the microbeam under DC actuation for selected levels of geometric imperfection: (a) nonlinear equilibrium paths (b) cusp catastrophe surface

The pull-in instability is observed in all cases, being the pull-in voltage particularly sensitive to the imperfection level and sign. The perfect system obtained pull-in voltage is 65.341V, being in good agreement with the formula presented in [116], where the pull-in voltage is 67.443V for the constants adopted in [124] and [131]. The imperfection changes the pull-in voltage band; for $w_0 > 0$, the gap between the beam and the actuator plate decreases, resulting in lower pull-in voltages and a system more susceptible to this type of instability. On the other hand, the pull-in load and consequently the stability increases for $w_0 < 0$, since the distance between the beam and the plate increases. This dependency is illustrated in Figure 5.4.

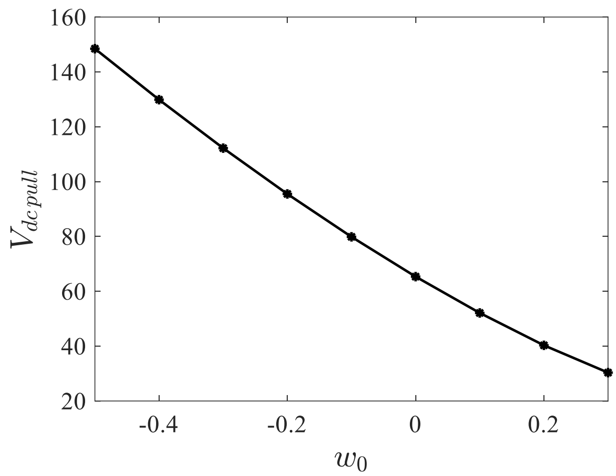

Figure 5.4 – Dependency of the static pull-in voltage on the magnitude and sign of the geometric imperfection

The dependency of the natural frequency of vibration on the DC voltage is well known for microelectromechanical beams [116]. In order to investigate the combined influence of the DC voltage and geometric imperfection magnitude on the natural frequencies, eq. (5.21) is linearized, and the damping coefficient and AC voltage are set to zero, resulting in

$$\begin{aligned}\ddot{w}_d - \frac{b\varepsilon w_d\left(V_{dc}\right)^2}{d^3\left(1-\bar{w}_s\right)^3} = \Bigg\{ & -d^2\left[\left(\bar{w}_s'^2 + \frac{1}{d^2}\right)w_d'''' + \left(w_d'\bar{w}_s'\bar{w}_s''\right)' + \right. \\ & \left. \bar{w}_s'\left(w_d''\bar{w}_s'' + w_d'w_s'''\right)\right] + \\ & d^2 J_\eta \ddot{w}_d'\left(\bar{w}_s'^2 + \frac{1}{d^2}\right) - d^2\bar{w}_s'\int_1^s\int_0^s \bar{w}_s'\ddot{w}_d' ds ds\Bigg\}'.\end{aligned} \tag{5.28}$$

where the influence of the imperfection and DC voltage can be observed.

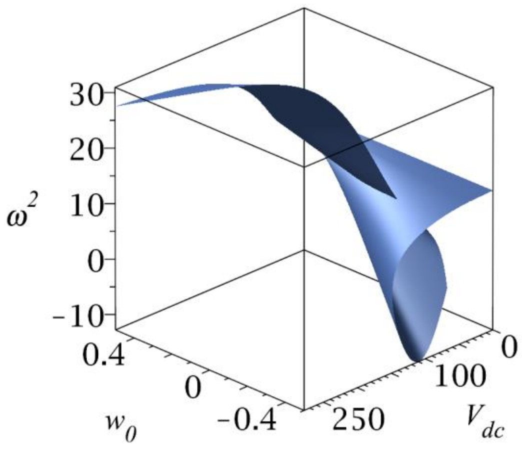

Figure 5.5 – Natural frequency of vibration dependency against DC voltage and imperfection w_0

Figure 5.5 shows the influence of the imperfection magnitude w_0 and DC voltage on the lowest natural frequency. As expected, the imperfection significantly affects the natural frequency of vibration. Also, in the region of the cusp catastrophe in Figure 5.3(b), the system shows three distinct frequencies, two with real values ($\omega^2 > 0$) and one with imaginary value ($\omega^2 < 0$). The real frequencies correspond to stable solutions, while the imaginary frequency corresponds to the unstable solution. Also, for a threshold of approximately $w_0 > 0.3$, only one frequency persists for all DC voltages, corroborating the result presented in Figure 5.4.

5.2.2.
Dynamic actuation

For the dynamic analysis, a direct current voltage $V_{dc} = 45V$ is adopted (see Figure 5.1). The periodic alternate voltage between the beam and the substrate is given by

$$V_{ac} \equiv \bar{V}_{ac} \cos(\Omega t), \tag{5.29}$$

where $\bar{V}_{ac}$ is the forcing magnitude and Ω the forcing frequency.

The values of static deflection w_s depend on the imperfection magnitude, as shown in the static analysis. The static deflection for the six selected levels of imperfection, varying from 0 to 0.05, is shown in Table 5.2.

Table 5.2 – Static deflection as a function of the imperfection magnitude for V_{dc} = 45V

w_0	w_s
0	0.057977
0.01	0.060345
0.02	0.062895
0.03	0.065648
0.04	0.068636
0.05	0.071892

Five different equations of motion are obtained from eq. (5.21) by applying the first mode Galerkin expansion for values of V_{dc}, w_0, and w_s given in Table 5.2. For the calculations, the fourth order Runge-Kutta method is employed, with a time-step $\Delta t = T / 4000$, where T is the period of excitation, $T = 2\pi/\Omega$. Resonance curves are obtained through a pseudo arc-length continuation of periodic orbits [200, 201] for three values of the forcing magnitude, namely $\bar{V}_{ac} = 1$, 5, 10. The stability of each solution is verified through the analysis of Floquet multipliers (eigenvalues of the monodromy matrix), which also allow the characterization of the bifurcation type.

Figure 5.6 displays the resonance curves of the microbeam for selected values of AC actuation and increasing imperfection level w_0 and V_{dc} = 45. As in the static case, continuous lines denote stable solutions and dashed lines unstable solutions. According to [133], the nonlinear response could be either softening or hardening, depending on which nonlinearity prevails, load or geometric. The expected response for the initial gap d presented in Table 5.1, chosen to match an experiment [140], is of softening type, with the load nonlinearity stronger than the geometric nonlinearity [133]. Therefore, the presented results agree with the previously obtained results, displaying softening nonlinear response for all values of w_0 and $\bar{V}_{ac}$.

As $\bar{V}_{ac}$ increases, a pull-in bandwidth develops, thus making the system more susceptible to dynamic pull-in instability. The imperfection decreases the values of $\bar{V}_{ac}$ for which the pull-in band appears and increases the pull-in bandwidth, as illustrated in Figure 5.7 for $\bar{V}_{ac}$ = 10. Also, of notice is, in all cases, the resonant peak at a forcing frequency equal to half of the natural frequency where a second pull-in band is observed for $w_0 \geq 0.03$. As the imperfection level increases, the resonant peak at a third of the natural frequency also increases, leading to an additional resonance region that may influence the microbeam dynamic response.

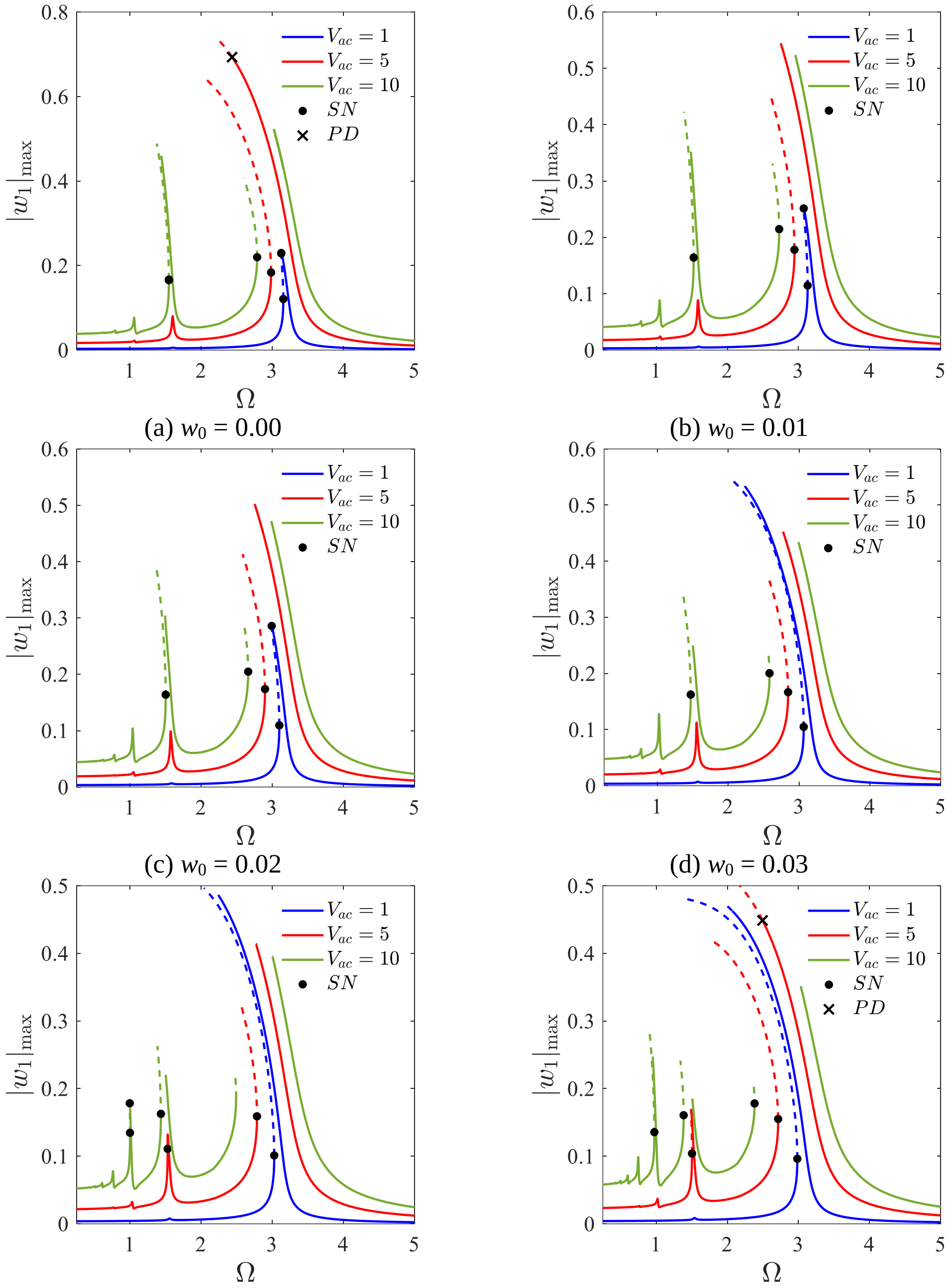

(a) w_0 = 0.00 (b) w_0 = 0.01

(c) w_0 = 0.02 (d) w_0 = 0.03

(e) w_0 = 0.04 (f) w_0 = 0.05

Figure 5.6 – Frequency-response curves for selected values of AC actuation, with V_{dc} = 45. SN – saddle-node bifurcation, PD – period-doubling bifurcation

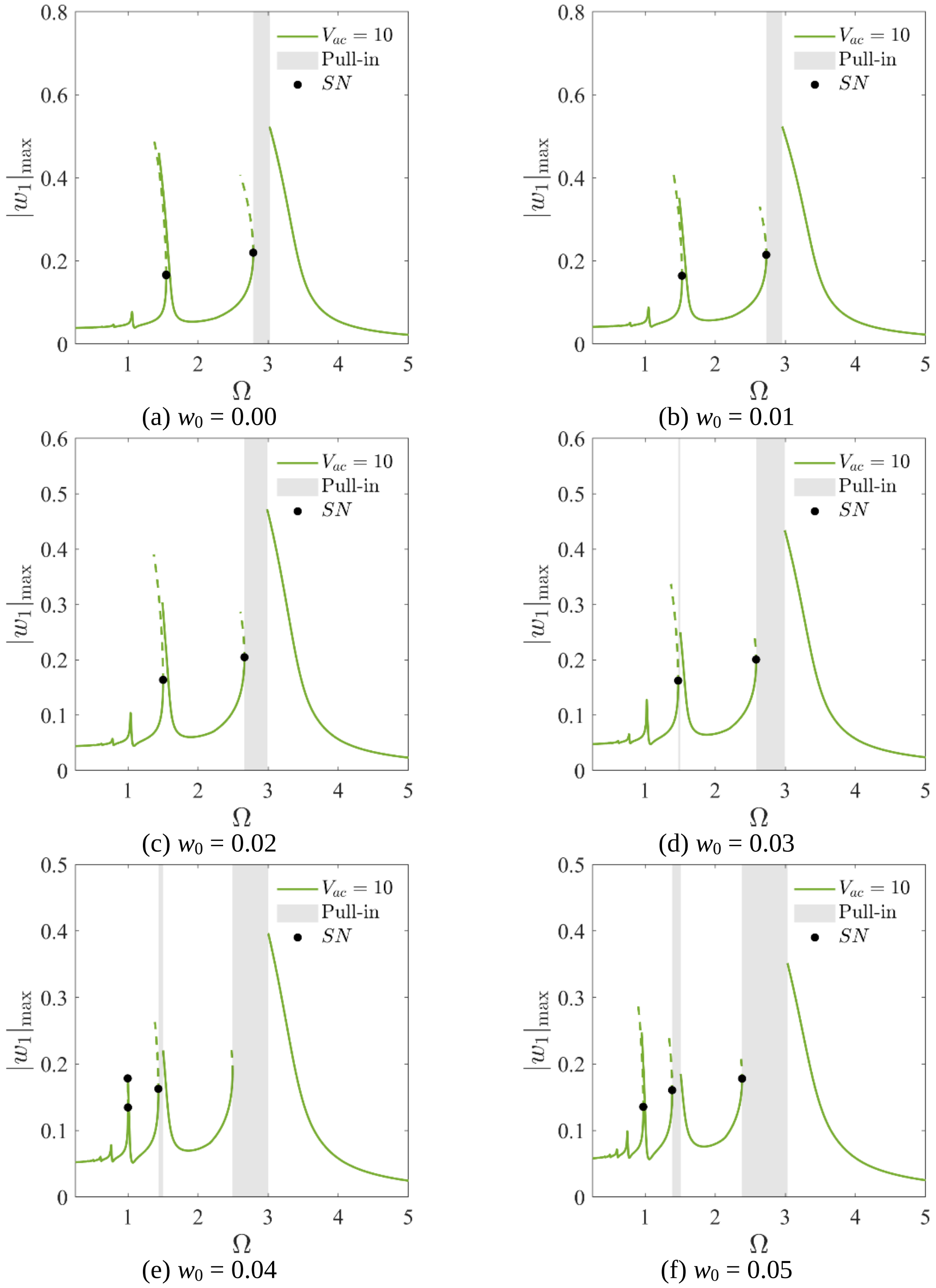

Figure 5.7 – Frequency-response curves for V_{dc} = 45 and V_{ac} = 10. Pull-in bandwidth as a function of the imperfection magnitude. SN – saddle-node bifurcation

5.3. The deterministic and stochastic global dynamics

The global analysis of the electrostatically actuated microbeam is initially investigated considering the phase-space $\mathbb{X} = [-3,3]^2$, with the boundaries assumed as of the absorbing type. This region is discretized with 300x300 boxes, with 5x5 initial conditions uniformly distributed within each cell. The same equations of motion used in the local dynamic analysis are considered, with parameters given in Table 5.1 and Table 5.2. Moreover, an additive stochastic excitation $\sigma\dot{W}$ is also considered, resulting in stochastic differential equations of Itô type. A stochastic Runge-Kutta method of fourth order in drift and half order in diffusion is employed, with a time-step $\Delta t = T / 4000$, where $T = 2\pi/\Omega$ is the period of excitation. For the stochastic cases ($\sigma \neq 0$), each initial condition is integrated 100 times, resulting in 2500 trajectories for each cell. The time interval of integration corresponds to one excitation period in all cases, resulting in a one-period stochastic transition matrix p_{ij}, that is, a Perron-Frobenius discretized operator for the deterministic case, eq. (2.59), or the Foias discretized operator for the stochastic case, eq. (2.62). Probability density distributions and (stochastic) basins of attraction are then obtained through the classical Ulam method, following Section 3.1.

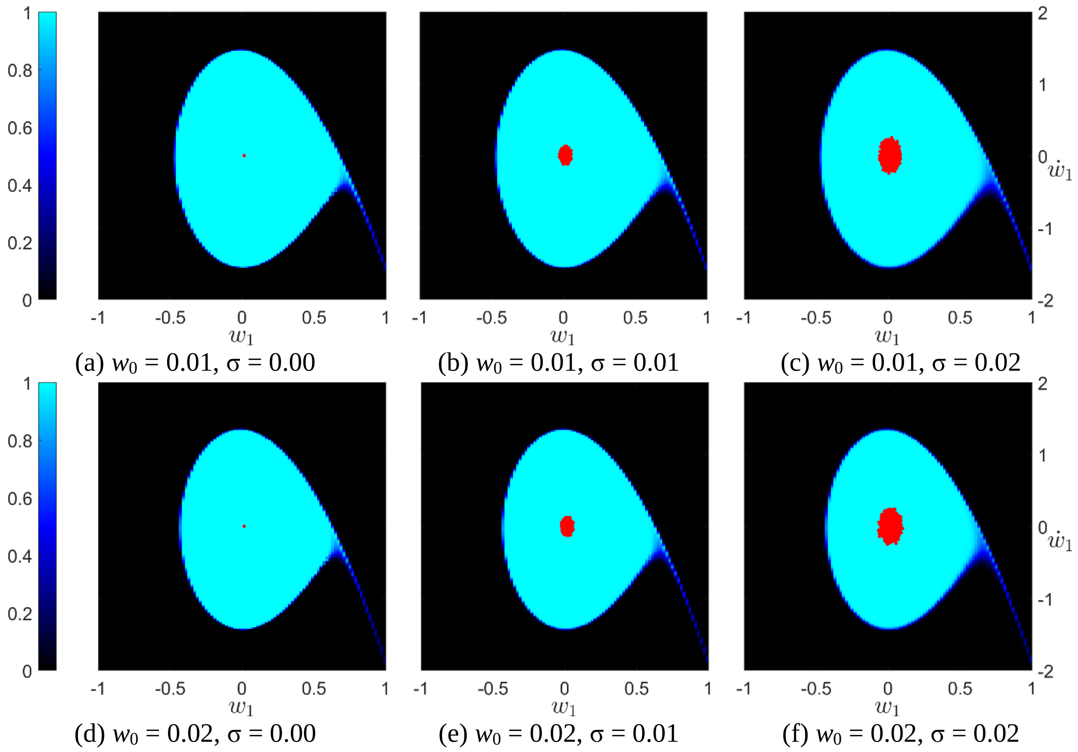

(a) w_0 = 0.01, σ = 0.00 (b) w_0 = 0.01, σ = 0.01 (c) w_0 = 0.01, σ = 0.02

(d) w_0 = 0.02, σ = 0.00 (e) w_0 = 0.02, σ = 0.01 (f) w_0 = 0.02, σ = 0.02

Figure 5.8 – Microbeam stochastic basin of attraction for V_{dc} = 45, $\bar{V}_{ac}$ = 1, Ω = 2.8, low imperfection and noise levels. Light blue: non-resonant attractor, black: pull-in

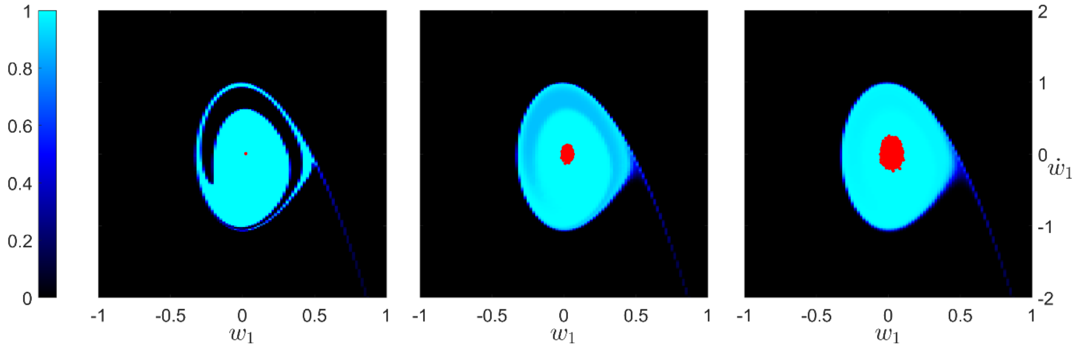

(a) σ = 0.00 (b) σ = 0.01 (c) σ = 0.02

Figure 5.9 – Microbeam stochastic basin of attraction for the non-resonant attractor, with V_{dc} = 45, $\bar{V}_{ac}$ = 1, Ω = 2.8, w_0 = 0.05

First, numerical simulations have been carried out for the nonlinear system with V_{dc} = 45, $\bar{V}_{ac}$ = 1, and Ω = 2.8. Six combinations of the parameters w_0 and σ are considered with w_0 = 0.01, 0.02, and σ = 0, 0.01, 0.02. For these six cases, only one attractor exists, as observed in Figure 5.6(a, b). The stochastic basins of attraction are depicted for the selected values of w_0 and σ in Figure 5.8, where the light blue region corresponds to the periodic 1T non-resonant attractor and black to pull-in, i.e., zero probability of converging to the non-resonant attractor. This basin persists for all noise levels, with minor changes near the saddle region, suggesting that the attractor is resilient to noise for small imperfection levels and noise magnitudes. The noise effect is more evident in the attractor's distribution. As the noise increases, the Poincaré section of the attractor spreads to larger regions in phase-space, as indicated by the red region in Figure 5.8.

The next example demonstrates the effect of higher imperfection levels on the results. As shown in Figure 5.6, the softening nonlinearity increases with the imperfection magnitude. Considering again V_{dc} = 45, $\bar{V}_{ac}$ = 1, Ω = 2.8 but w_0 = 0.05, the deterministic microbeam has a non-resonant and a resonant attractor, as shown in Figure 5.6(f). Figure 5.9 shows the stochastic basin of attraction of the non-resonant periodic attractor for $\sigma = 0$, $\sigma = 0.01$, and $\sigma = 0.02$, while Figure 5.10 shows the results for the resonant attractor, and Figure 5.11 depicts the set of initial conditions leading to pull-in. The non-resonant attractor's overall size decreases in comparison with the previous case, Figure 5.8. For $\sigma = 0.00$, the basin boundary is well defined, as shown in Figure 5.9(a), Figure 5.10(a, b), and Figure 5.11(a), with the black regions corresponding to initial conditions leading to pull-in, demonstrating the destabilizing effect of the geometric imperfections. As the noise increases, the probability of the noisy response converging to the resonant attractor decreases, and its basin shrinks with only 10~20% of solutions asymptotically converging to this region for $\sigma = 0.01$, as observed in Figure 5.10(c, d). In contrast, as shown in Figure 5.9(b), most trials converge to the non-resonant attractor. The pull-in region remains practically unaltered except for a small region near the saddle. For $\sigma = 0.02$, only the non-resonant solution remains, comprising the regions initially occupied by the non-resonant and resonant basins. The probability density distribution evolution with the noise level clarifies this, Figure 5.14, showing the collapse of the resonant solution and the spread of the noisy non-resonant attractor. For $\sigma = 0.00$, two well-defined peaks are observed, while for $\sigma = 0.01$, the noisy resonant attractor spreads to a large region with low probability and approaches the noisy non-resonant attractor. Finally, for $\sigma = 0.02$, the resonant attractor completely disappears, while the remaining attractor spreads over a larger region of the phase plane, see Figure 5.9(c). Still, the pull-in region remains largely unaffected by noise.

The results presented in Figure 5.9 and Figure 5.10 distinguish themselves from previous noise considerations from Orlando et al. [112], Silva and Gonçalves [113], and Silva et al. [179]. In these previous works, a given state is marked as unbounded if the noise leads at least once to unbounded oscillations during the Monte Carlo analysis. Here, on the other hand, the probability of an initial condition leading to unbounded oscillations is calculated for each cell. Although the computational demand is significantly higher, the exact probability quantification allows addressing the effect of uncertainties more precisely. Also, the decrease in the probability of a given region directly influences its dynamic integrity [67, 77]. This effect must be taken into account in systems with noise.

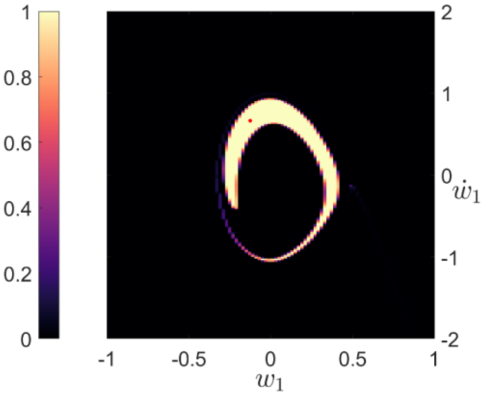

(a) σ = 0.00, 2D view

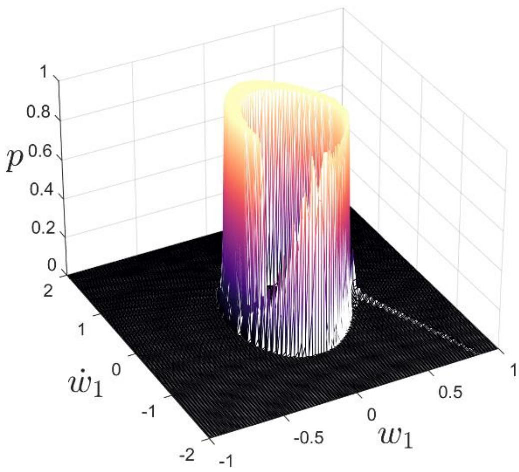

(b) σ = 0.00, 3D view

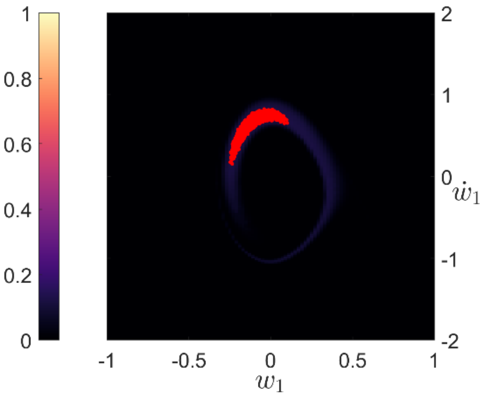

(c) σ = 0.01, 2D view

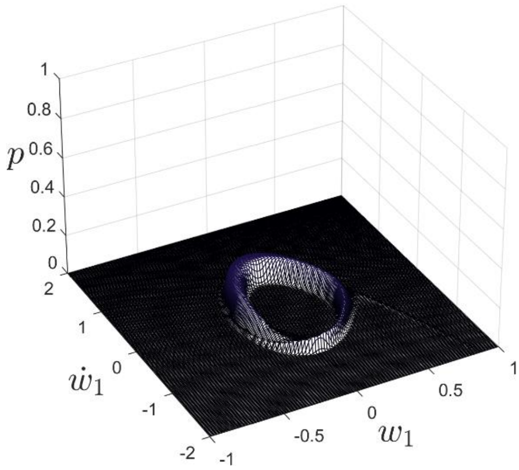

(d) σ = 0.01, 3D view

Figure 5.10 – Microbeam stochastic basin of attraction for the resonant attractor, with $V_{\mathrm{dc}} = 45$, $\bar{V}_{ac} = 1$, $\Omega = 2.8$, $w_0 = 0.05$

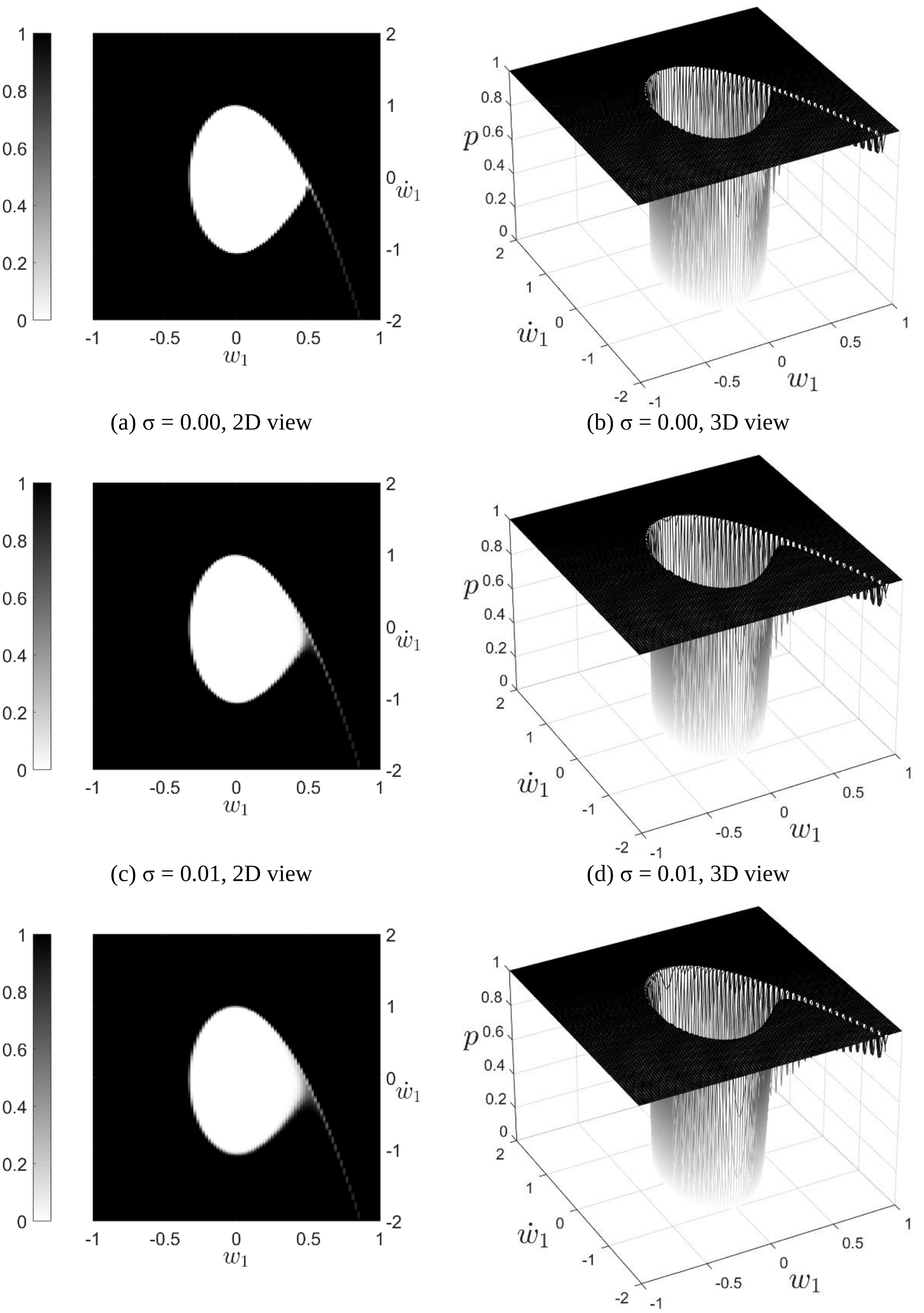

(a) σ = 0.00, 2D view

(b) σ = 0.00, 3D view

(c) σ = 0.01, 2D view

(d) σ = 0.01, 3D view

(e) σ = 0.02, 2D view

(f) σ = 0.02, 3D view

Figure 5.11 – Set of initial conditions leading to pull-in, with V_{dc} = 45, $\overline{V}_{ac}$ = 1, Ω = 2.8, w_0 = 0.05

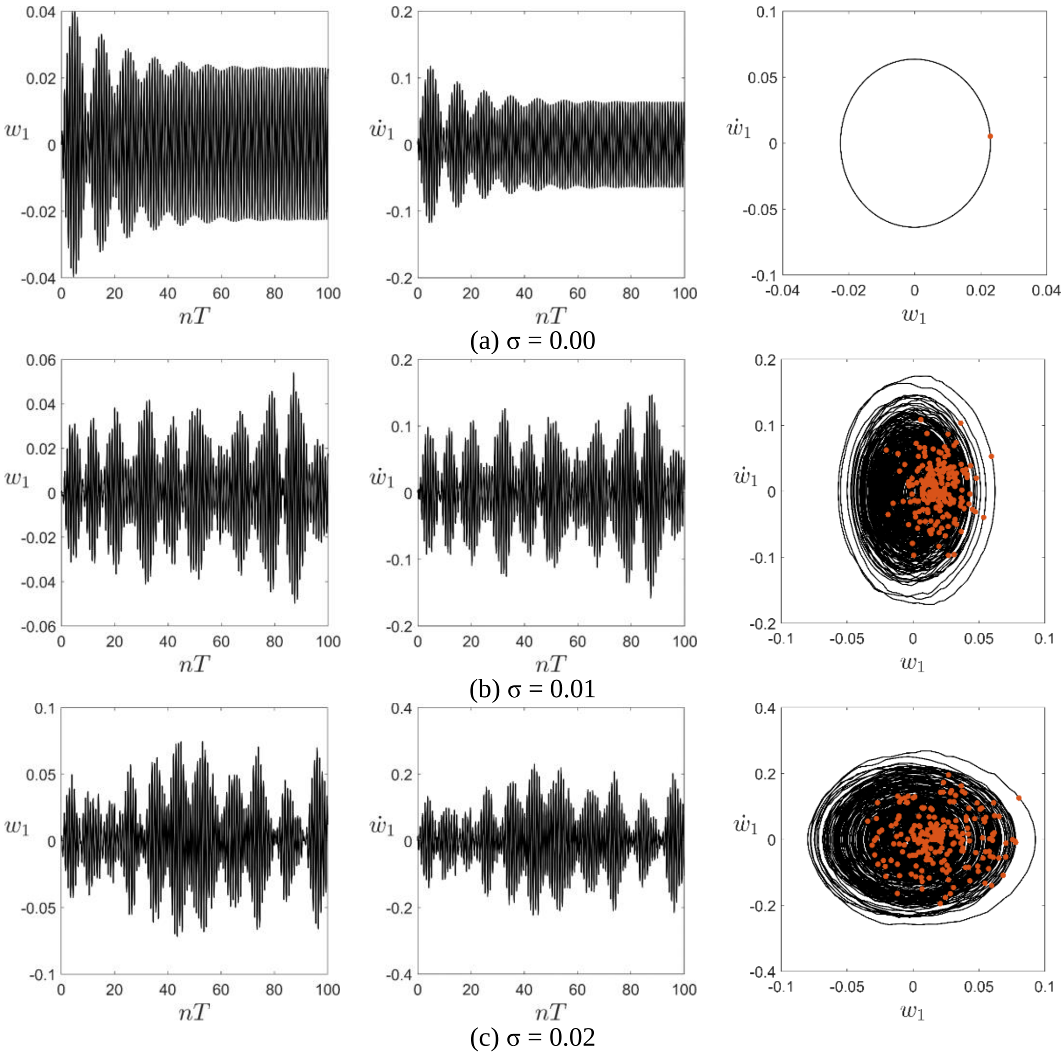

Figure 5.12 – Microbeam time histories with V_{dc} = 45, $\overline{V}_{ac}$ = 1, Ω = 2.8, w_0 = 0.05, and non-resonant initial condition $(w_1, \dot{w}_1) = (0,0)$

Figure 5.12 and Figure 5.13 show the effect of noise on the time histories. The initial condition in the non-resonant region, Figure 5.12, reveals increasing irregularity as noise increases, whereas solutions with the initial condition in the resonant region, Figure 5.13, lose stability and converge to the non-resonant attractor as noise increases, Figure 5.13(c). The probability density distribution evolution with the noise illustrates this, Figure 5.14, showing the collapse of the resonant solution. As verification, Monte Carlo experiments were conducted, where each initial condition was integrated for 10000 periods, generating 5000 samples. The final time histograms for σ = 0.01 and σ = 0.015 are shown in Figure 5.15. For σ = 0.015, the paths starting in the resonant initial condition almost entirely end in the non-resonant region, as correctly addressed by the probability density distributions in Figure 5.14. The differences between the Monte Carlo experiments, Figure 5.15, and the probability density distributions, Figure 5.14, is due to the limited phase-space discretization adopted in the Ulam method, where the quality of the results depends on discretization, requiring a refinement analysis to check the convergence. The other constraint is choosing one starting point for the Monte Carlo experiment since the Ulam method gives mean values of the solutions starting in all the phase-space. Nevertheless, the results are in qualitative agreement, showing the potentiality of the present strategy. Also, the present results demonstrate that the decrease of the probability of a given region directly influences its dynamic integrity measures [65, 187], and this must be taken into account in systems with noise.

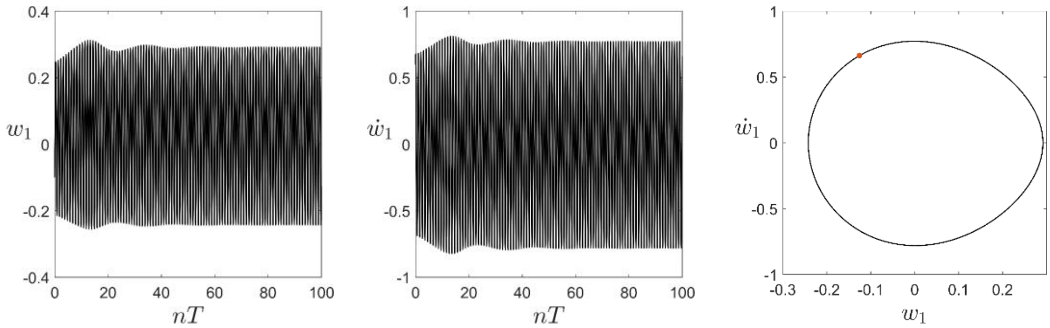

(a) σ = 0.00

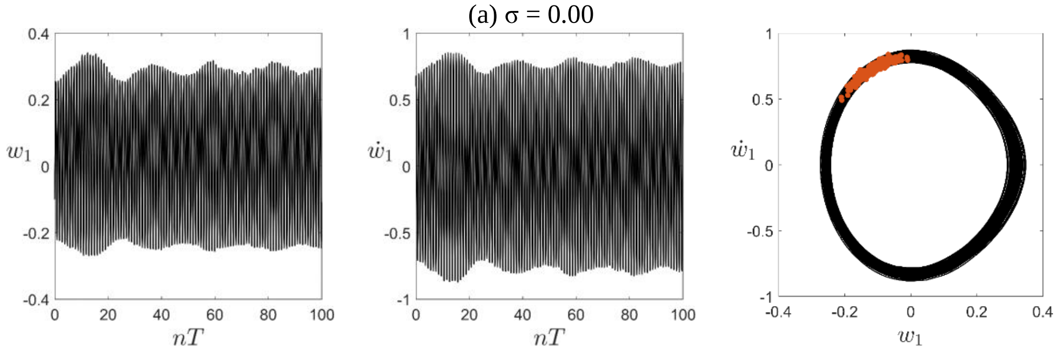

(b) σ = 0.01

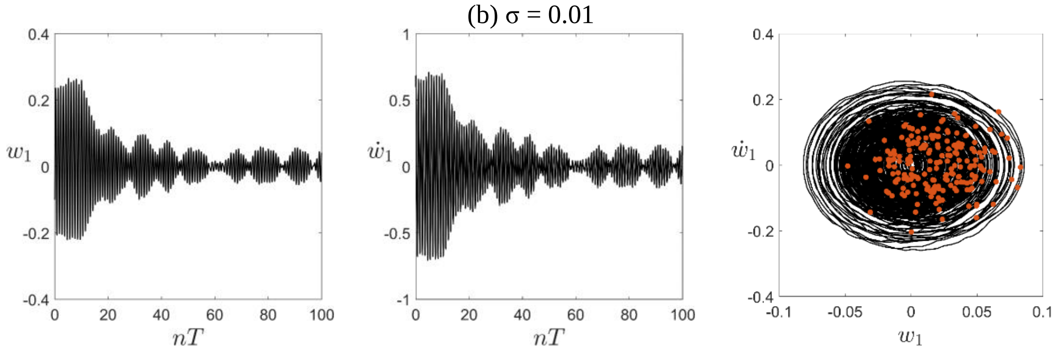

(c) σ = 0.02

Figure 5.13 – Microbeam time histories with V_{dc} = 45, $\overline{V}_{ac}$ = 1, Ω = 2.8, w_0 = 0.05, and resonant initial condition $(w_1, \dot{w}_1) = (-0.1, 0.6)$

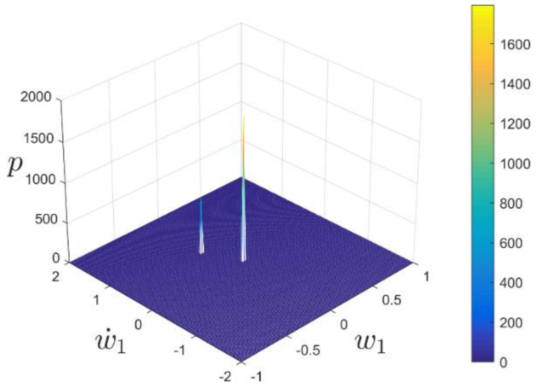

(a) σ = 0.00

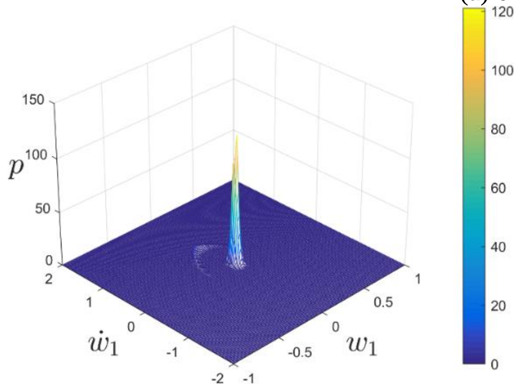

(b) σ = 0.01

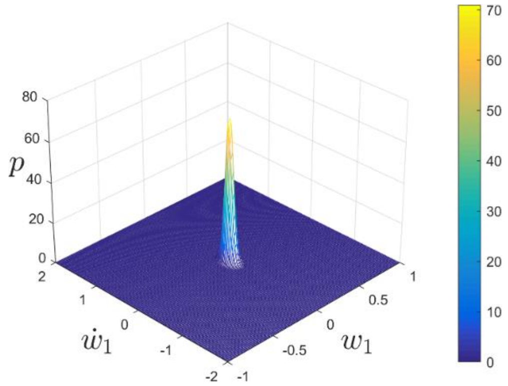

(c) σ = 0.02

Figure 5.14 – Microbeam attractor's probability density distribution for V_{dc} = 45, $\overline{V}_{ac}$ = 1, Ω = 2.8, high imperfection: w_0 = 0.05

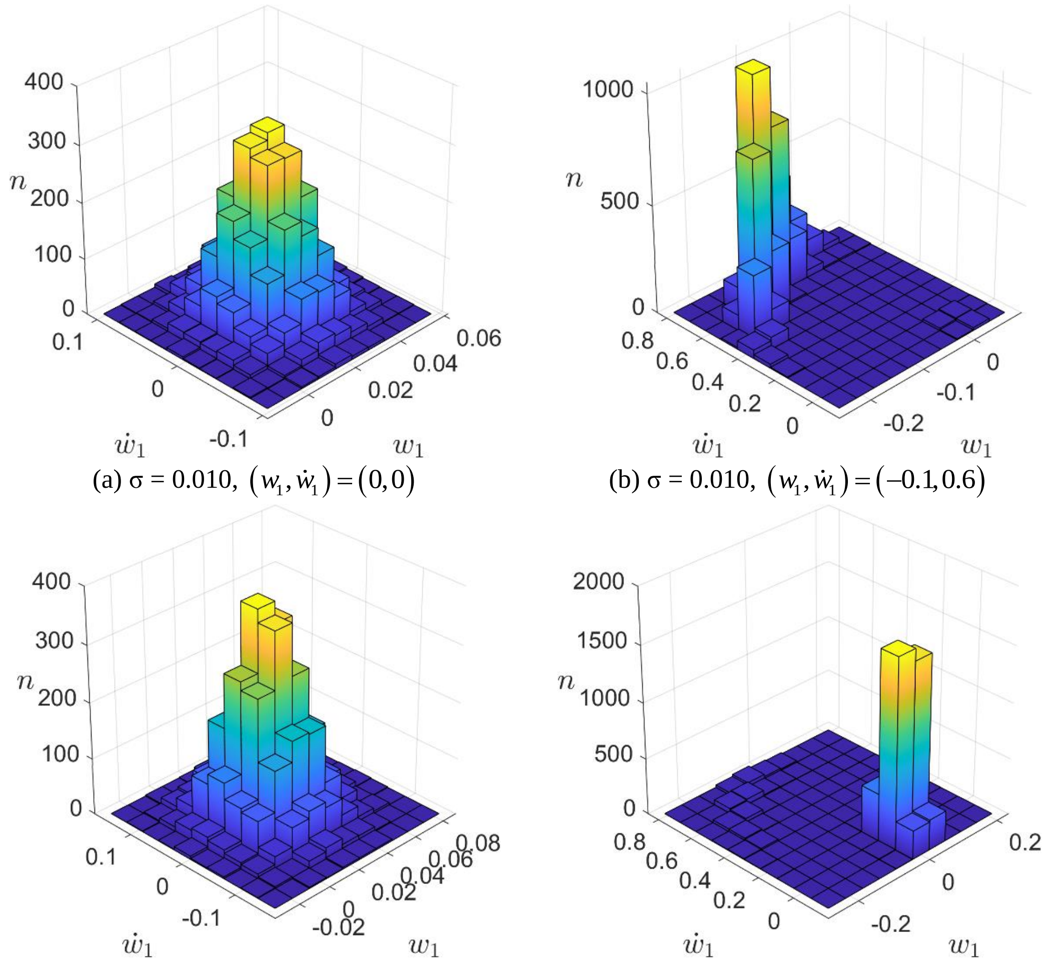

(a) σ = 0.010, $(w_1, \dot{w}_1) = (0,0)$ (b) σ = 0.010, $(w_1, \dot{w}_1) = (-0.1, 0.6)$

(c) σ = 0.015, $(w_1, \dot{w}_1) = (0,0)$ (d) σ = 0.015, $(w_1, \dot{w}_1) = (-0.1, 0.6)$

Figure 5.15 – Microbeam's histograms for two initial conditions at time t = 10000T integrated 5000 times for V_{dc} = 45, $\overline{V}_{ac}$ = 1, Ω = 2.8, w_0 = 0.05. (a, c) non-resonant initial condition, (b, d) resonant initial condition

A system with a medium level of AC actuation, $\overline{V}_{ac}$ = 5 and w_0 = 0, is now considered to demonstrate the noise impact in more detail. Again, there are two coexisting periodic attractors due to a region of hysteresis (see Figure 5.6). Figure 5.16 shows the non-resonant stochastic basin of attraction for $0 \leq \sigma \leq 0.014$. There are little or no qualitative changes observed in the basin area for these noise levels, displaying the same behavior observed for $\overline{V}_{ac}$ = 1, apart from spreading the Poincaré section, with the low probability region restricted to the long tail. However, the resonant stochastic basin, Figure 5.17, changes significantly, with finger-like regions leading to pull-in (see Figure 5.18) eroding the basin. These finger-like regions are similar to those observed in the escape equation due to a homoclinic tangle [57, 62]. The probability of the resonant solution along the boundaries of these finger-like regions decreases with the noise level, as shown by the color scale, diffusing from the boundary to the compact region. Also, a significant spread of the attractor is observed, approaching the basin boundary as the noise level increases. This also affects the probability of pull-in, as shown in Figure 5.18. The color scheme is the same as in the previous figures for $\overline{V}_{ac}$ = 1.

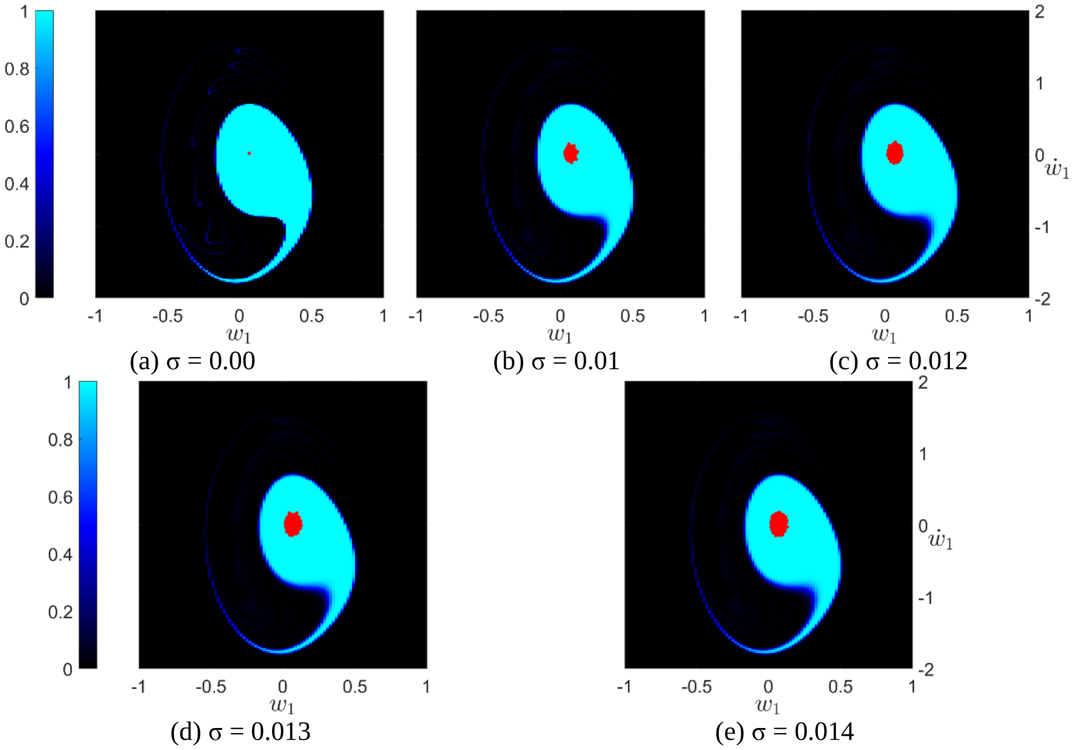

(a) σ = 0.00 (b) σ = 0.01 (c) σ = 0.012

(d) σ = 0.013 (e) σ = 0.014

Figure 5.16 – Evolution of the microbeam non-resonant stochastic basin of attraction as a function of the noise level V_{dc} = 45, $\overline{V}_{ac}$ = 5, Ω = 2.8, w_0 = 0, low noise level

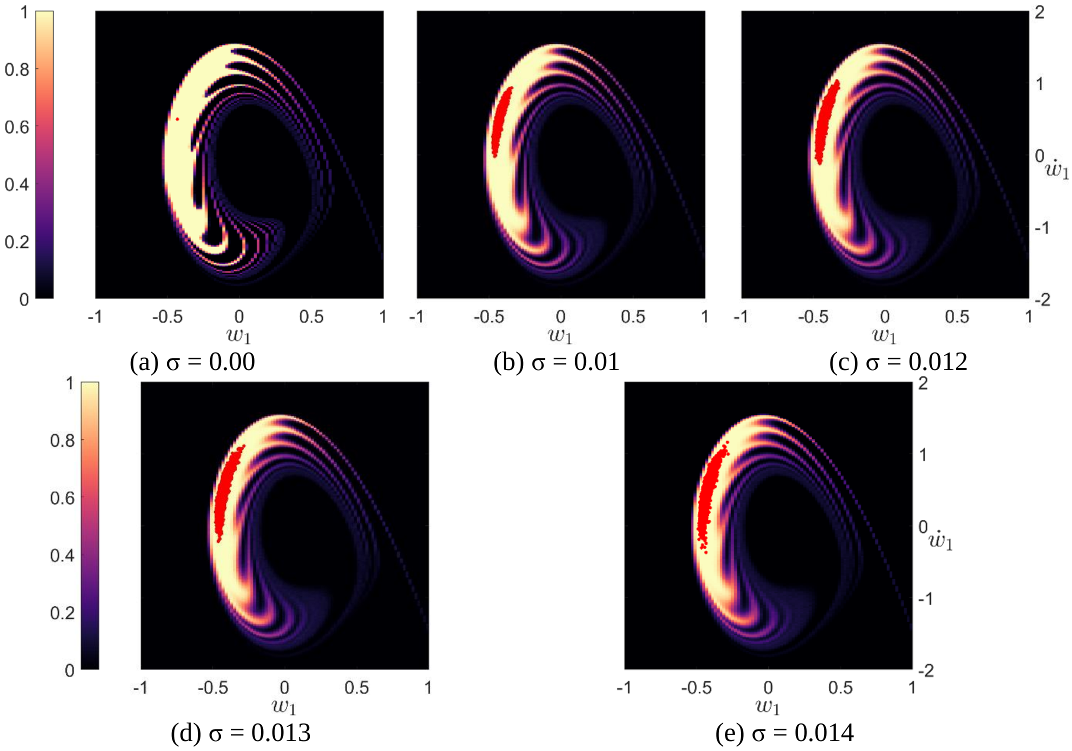

(a) σ = 0.00 (b) σ = 0.01 (c) σ = 0.012

(d) σ = 0.013 (e) σ = 0.014

Figure 5.17 – Evolution of the microbeam resonant stochastic basin of attraction as a function of the noise level for V_{dc} = 45, $\overline{V}_{ac}$ = 5, Ω = 2.8, w_0 = 0, low noise level

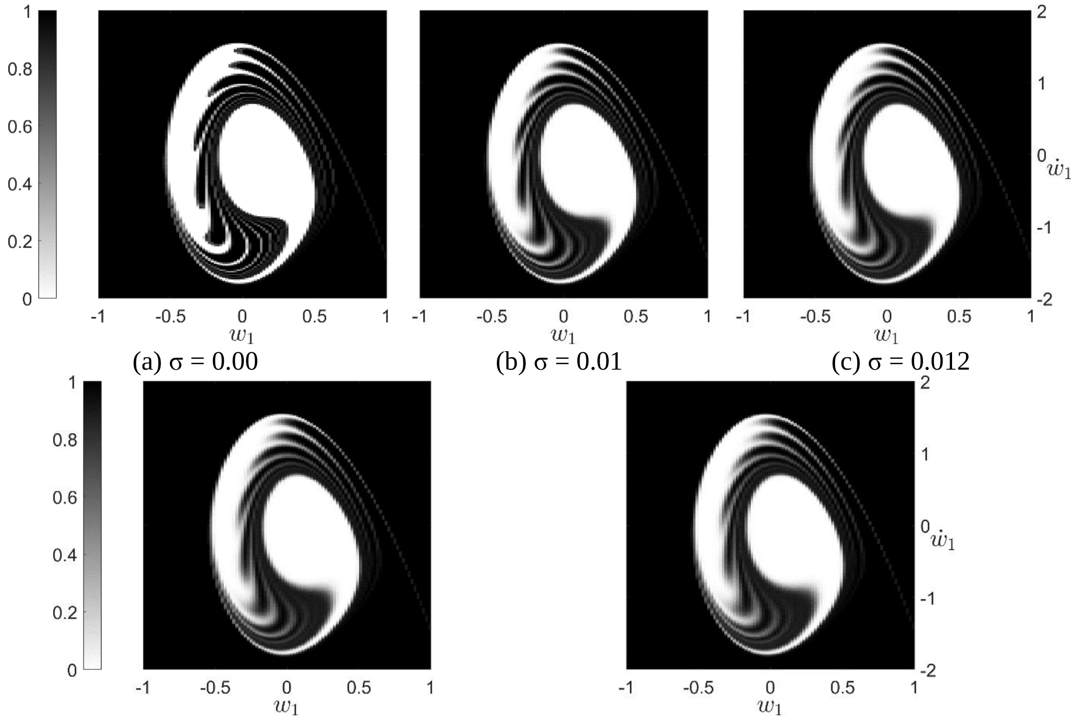

(a) σ = 0.00 (b) σ = 0.01 (c) σ = 0.012

(d) σ = 0.013 (e) σ = 0.014

Figure 5.18 – Set of initial conditions leading to pull-in as a function of the noise level for $V_{\text{dc}} = 45$, $\overline{V}_{ac} = 5$, $\Omega = 2.8$, $w_0 = 0$, low noise level

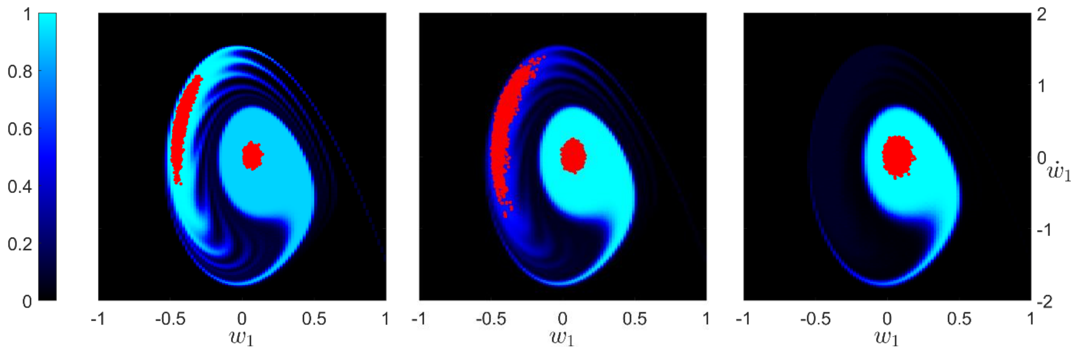

(a) σ = 0.015 (b) σ = 0.02 (c) σ = 0.025

Figure 5.19 – Evolution of the microbeam stochastic basin of attraction as a function of the noise level for $V_{\text{dc}} = 45$, $\overline{V}_{ac} = 5$, $\Omega = 2.8$, $w_0 = 0$

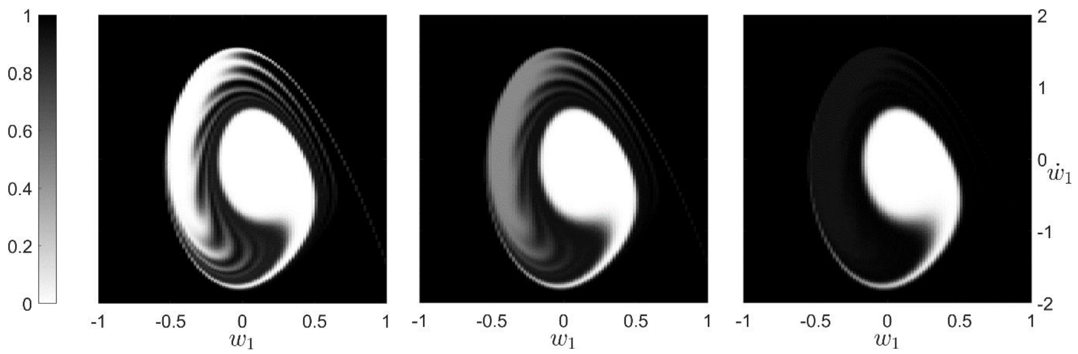

(a) σ = 0.015 (b) σ = 0.02 (c) σ = 0.025

Figure 5.20 – Set of initial conditions leading to pull-in as a function of the noise level for $V_{\text{dc}} = 45$, $\overline{V}_{ac} = 5$, $\Omega = 2.8$, $w_0 = 0$

A drastic change occurs for σ = 0.015, see Figure 5.19(a) and Figure 5.20(a). For this noise level, the two basins of attraction cannot be distinguished from each other, which indicates that jumps can happen between the possible three outcomes. As the noise increases even further (σ = 0.02), no initial condition has more than a 50% probability of converging to the resonant region, Figure 5.19(b). For the last noise level (σ = 0.025), the resonant solution no longer exists, merging with the pull-in region, see Figure 5.20(c), with only the non-resonant attractor remaining. Time series solutions for initial conditions in the non-resonant and resonant regions are shown in Figure 5.21 and Figure 5.22 to complement the analysis. As expected, the pull-in occurs for σ = 0.025 and an initial condition in the resonant region.

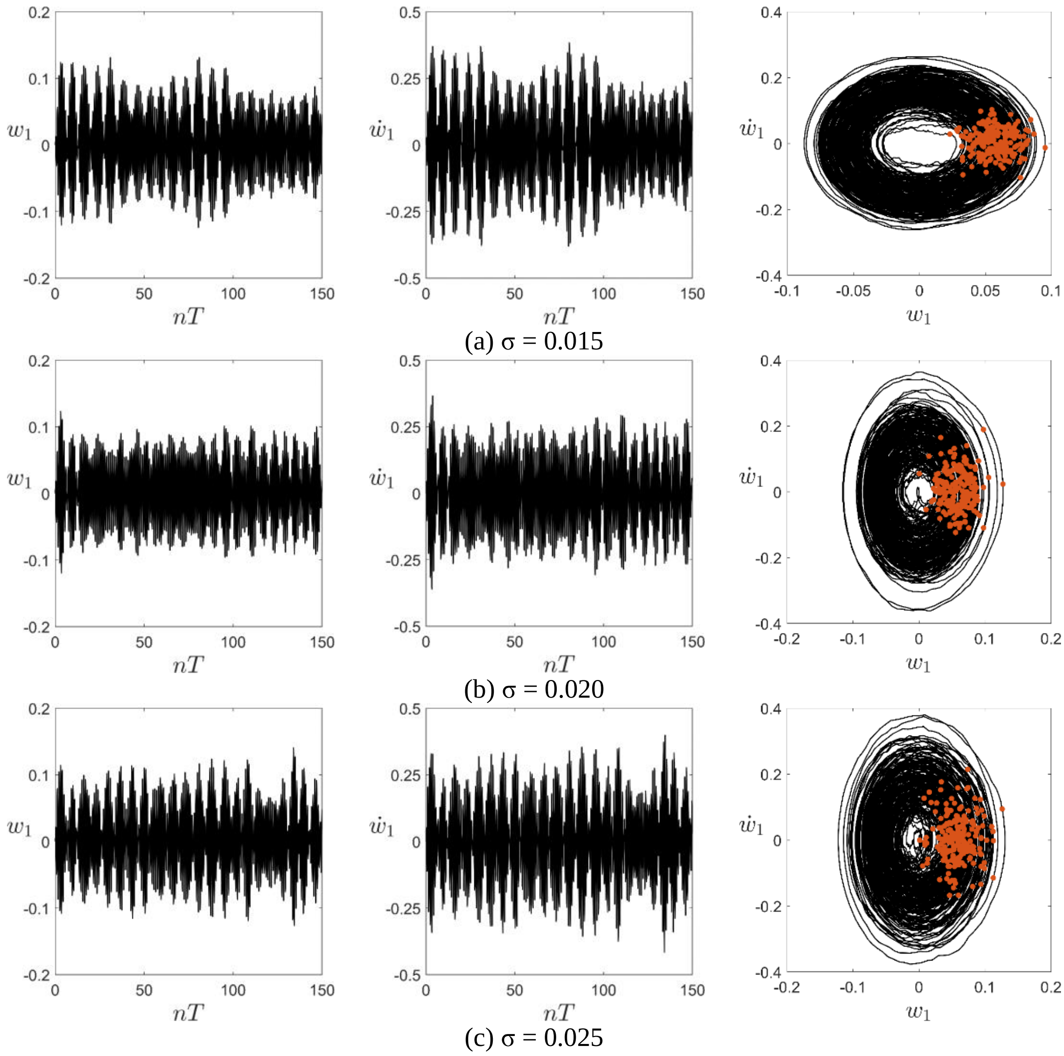

Figure 5.21 – Microbeam time histories for V_{dc} = 45, $\overline{V}_{ac}$ = 5, Ω = 2.8, w_0 = 0, and non-resonant initial condition $(w_1, \dot{w}_1) = (0,0)$

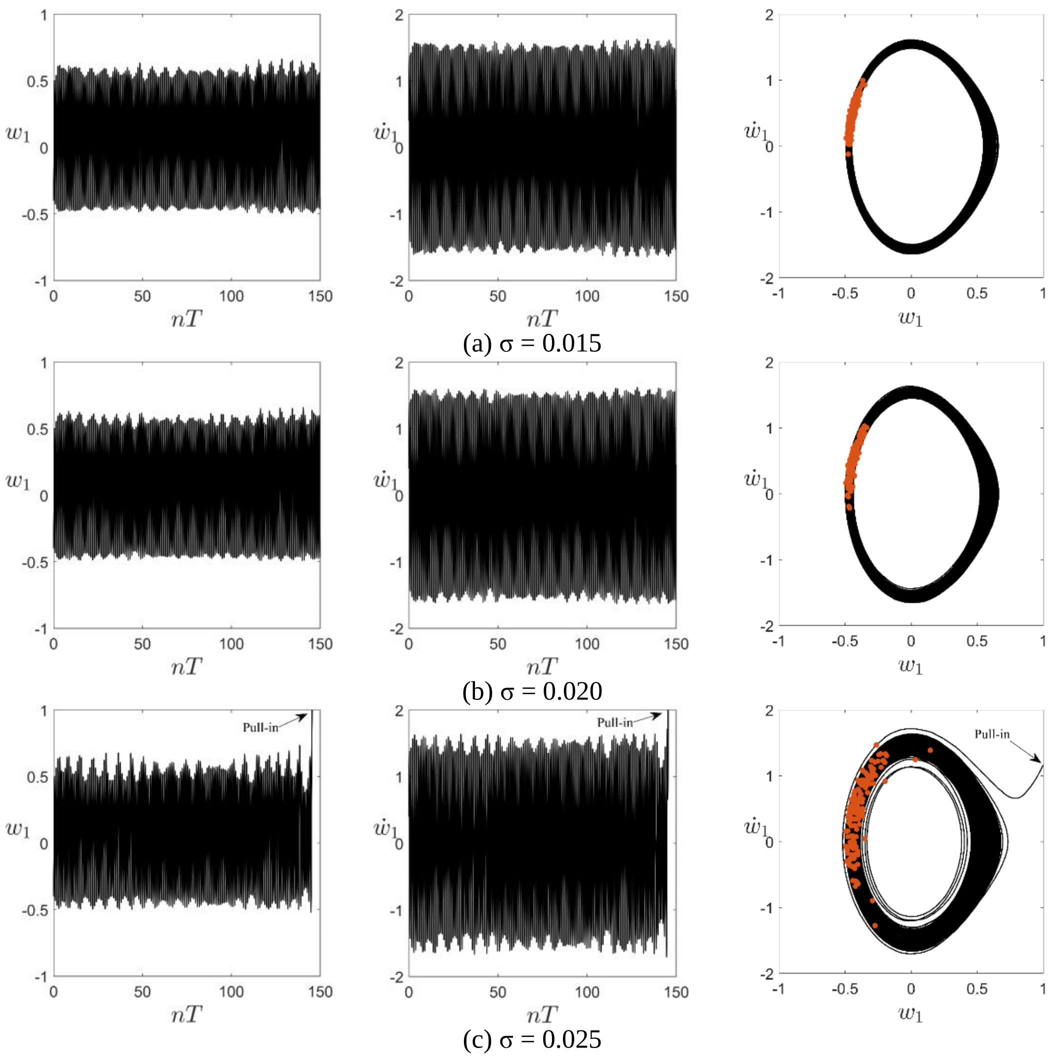

Figure 5.22 – Microbeam time histories for V_{dc} = 45, $\bar{V}_{ac}$ = 5, Ω = 2.8, w_0 = 0, and resonant initial condition $(w_1, \dot{w}_1) = (-0.4, 0.4)$

The evolution of the probability density distribution is depicted in Figure 5.23. The first notorious change happens between the deterministic case, Figure 5.23(a), and the first stochastic case, Figure 5.23(b). The deterministic case has well-defined attractors. This is expected for deterministic systems, where Poincaré sections of periodic attractors possess Dirac delta distributions. As the noise level increases, the resonant solution's sensibility to noise is clearly observed, spreading the attractor over the phase-space. The last cases, Figure 5.23(g, h), show the vanishing of the resonant solution due to the high noise level. Monte Carlo experiments were conducted for verification, where each initial condition was integrated for 10000 periods, generating 5000 samples, see Figure 5.24. As expected, the non-resonant attractor is stable for all three noise levels, see Figure 5.24(a, c, e), agreeing with the Ulam method results. The resonant attractor loses stability for the last noise case, Figure 5.24(f), with even some solutions converging to the nonresonant attractor. Escaped solutions are not depicted in the histogram because they are not located in a limited-size phase-space. Still, the percentage of escaped solutions is 81.78%, and only 11.54% of these sample paths are in the resonant region at time t = 10000T, qualitatively agreeing with the Ulam method.

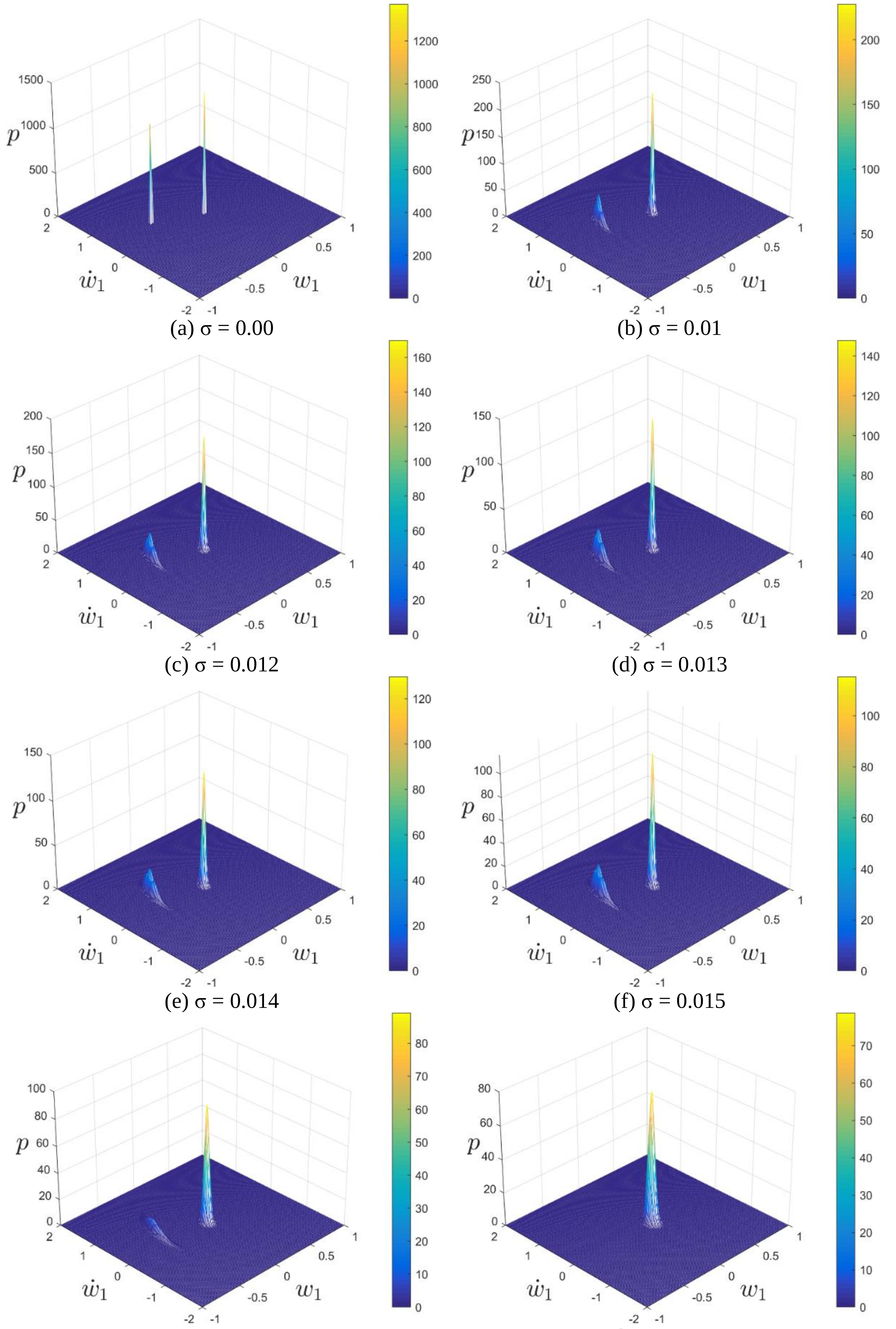

(a) σ = 0.00 (b) σ = 0.01

(c) σ = 0.012 (d) σ = 0.013

(e) σ = 0.014 (f) σ = 0.015

(g) σ = 0.02 (h) σ = 0.025

Figure 5.23 – Microbeam attractor’s probability density distribution as a function of the noise levels for $V_{\mathrm{dc}} = 45$, $\bar{V}_{ac} = 5$, $\Omega = 2.8$, $w_0 = 0$

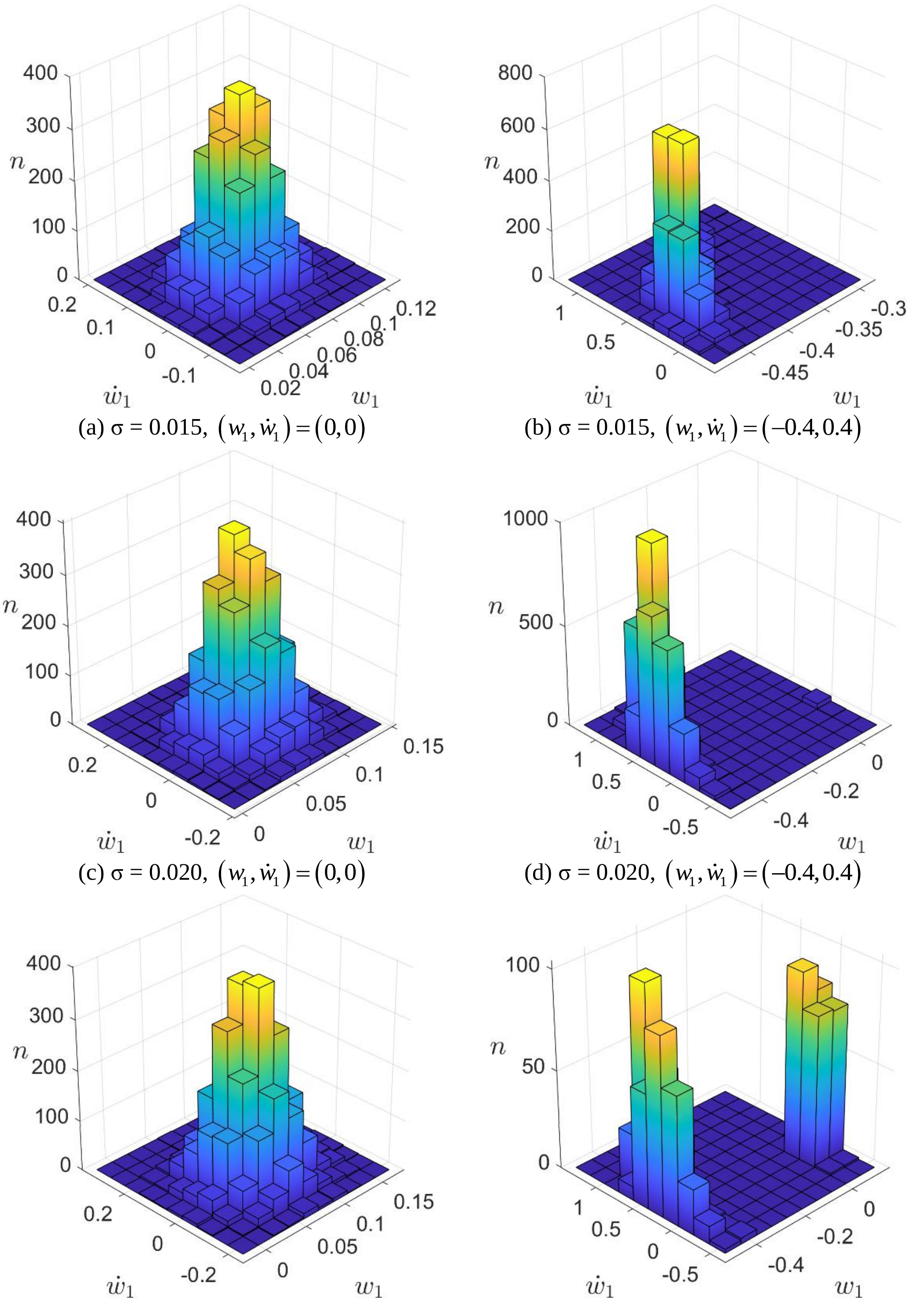

(a) σ = 0.015, $(w_1, \dot{w}_1) = (0,0)$ (b) σ = 0.015, $(w_1, \dot{w}_1) = (-0.4, 0.4)$

(c) σ = 0.020, $(w_1, \dot{w}_1) = (0,0)$ (d) σ = 0.020, $(w_1, \dot{w}_1) = (-0.4, 0.4)$

(e) σ = 0.025, $(w_1, \dot{w}_1) = (0,0)$ (f) σ = 0.025, $(w_1, \dot{w}_1) = (-0.4, 0.4)$

Figure 5.24 – Microbeam’s histograms of two initial conditions at time t = 10000T integrated 5000 times for V_{dc} = 45, $\overline{V}_{ac}$ = 5, Ω = 2.8, w_0 = 0. (a, c, e) non-resonant initial condition, (b, d, f) resonant initial condition

5.4.
The refinement procedure applied to the microcantilever

Now the influence of the proposed refinement procedure, where the phase-space is hierarchically subdivided, on the results is investigated. The phase-space window $\mathbb{X} = [-1,1] \otimes [-2,2]$ is adopted, and the boundaries are assumed as of the absorbing type. The phase-space is initially at level 10, with 32 boxes in each dimension, increasing up to level 18 via the refinement algorithm, Table 3.1. The discretization data is given in Table 5.3

Table 5.3 – Discretization data for the microcantilever

Depth level	Box-size	Points per dimension	Total collocation points
10	{0.0625, 0.125}	12	144
11	{0.0312, 0.125}	11	121
12	{0.0312, 0.0625}	10	100
13	{0.0156, 0.0625}	9	81
14	{0.0156, 0.0312}	8	64
15	{0.0078, 0.0312}	7	49
16	{0.0078, 0.0156}	6	36
17	{0.0039, 0.0156}	5	25
18	{0.0039, 0.0078}	4	16

The time integration scheme is the same adopted in the previous analysis, with time-step $\Delta t = T/4000$. For the stochastic cases, each initial condition is integrated ten times. At each level, a transition matrix is constructed, that is, a discretization of the Perron-Frobenius operator when the system is deterministic, eq. (2.59), or discretization of the Foias operator when the system is stochastic, eq. (2.62). Probability density distributions and (stochastic) basins of attraction are then obtained through the classical Ulam method, following Section 3.1. Finally, the phase-space is subdivided following the algorithm in Table 3.1, and the process is repeated until the final level.

The results for small imperfections and different noise levels are presented in Figure 5.25. The refinement algorithm reveals the basin boundaries in more detail, reducing the numerical diffusion due to discretization observed in Figure 5.8(a, b, c). Additionally, the localized discretization of the attractor allows its density to be correctly depicted for stochastic cases, see Figure 5.25(b, c), with its diffusion being properly quantified. These results provide new insights into the previous analysis, demonstrating the capabilities of the proposed subdivision strategy.

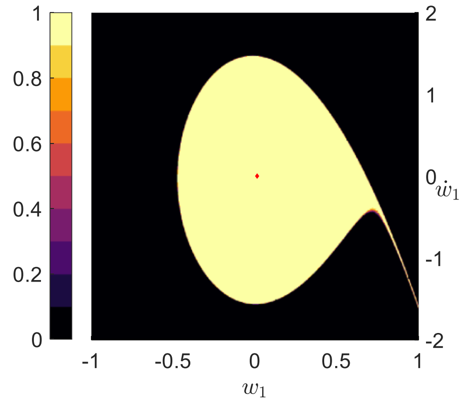

(a) w_0 = 0.01, σ = 0.00

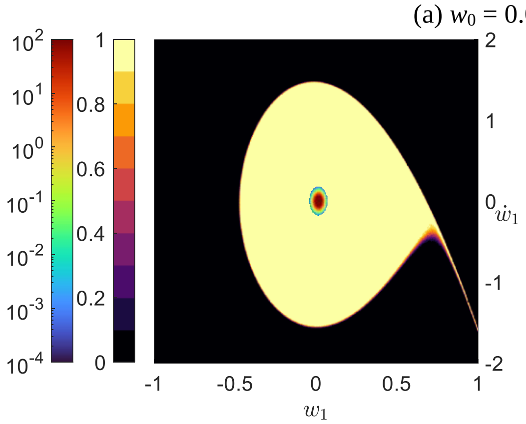

(b) w_0 = 0.01, σ = 0.01

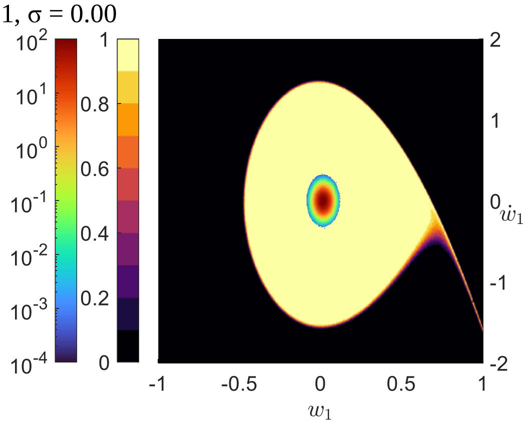

(c) w_0 = 0.01, σ = 0.02

Figure 5.25 – Microbeam global dynamics obtained after the application of the refinement algorithm for V_{dc} = 45, $\overline{V}_{ac}$ = 1, Ω = 2.8, low imperfection and noise levels. Outer color bar: attractor's density, inner color bar: stochastic basin of attraction

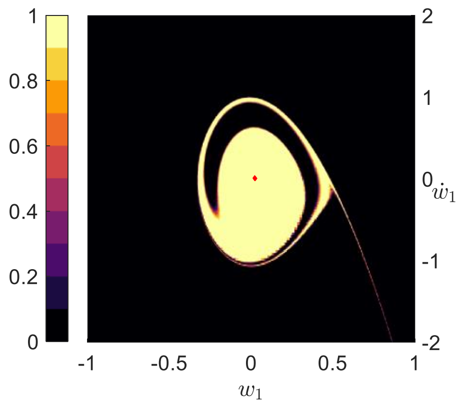

(a) nonresonant attractor

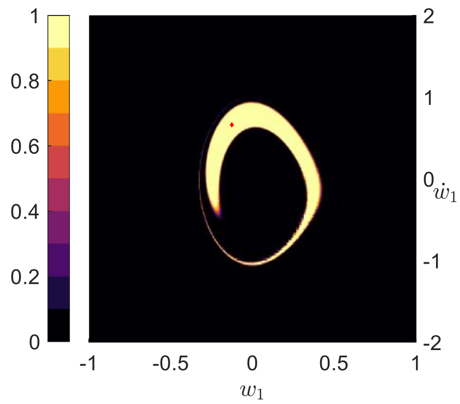

(b) resonant attractor

Figure 5.26 – Microcantilever deterministic global dynamics obtained after the application of the refinement algorithm for V_{dc} = 45, $\overline{V}_{ac}$ = 1, Ω = 2.8, w_0 = 0.05. Attractors marked in red. Color bar: basin of attraction

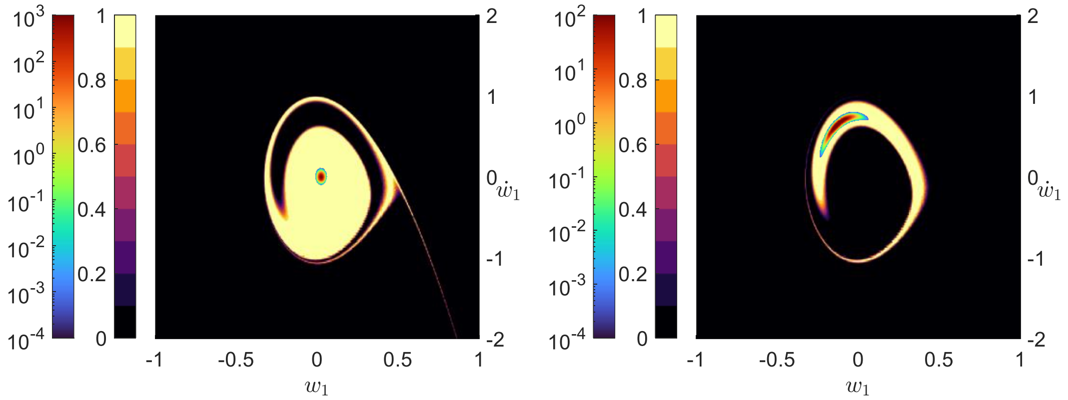

(a) nonresonant attractor (b) resonant attractor

Figure 5.27 – Microcantilever global dynamics obtained after the application of the refinement algorithm for $V_{\mathrm{dc}} = 45$, $\overline{V}_{ac} = 1$, $\Omega = 2.8$, $w_0 = 0.05$, $\sigma = 0.005$. First color bar: stochastic basin of attraction, second color bar: attractors' densities

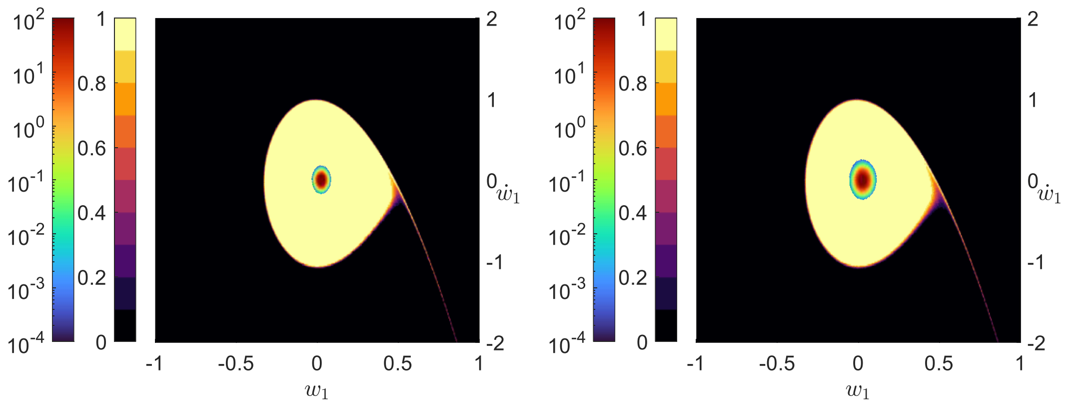

(a) $\sigma = 0.010$ (b) $\sigma = 0.015$

Figure 5.28 – Microcantilever nonresonant attractor global dynamics obtained after the application of the refinement algorithm for $V_{\mathrm{dc}} = 45$, $\overline{V}_{ac} = 1$, $\Omega = 2.8$, $w_0 = 0.05$. First color bar: stochastic basin of attraction, second color bar: attractor's density

The results for a larger imperfection value, $w_0 = 0.05$, are now obtained. The deterministic case is presented in Figure 5.26. Compared with the previous results, Figure 5.9(a) and Figure 5.10(a, b), it is observed that the refinement strategy shows the basins' boundaries in much more detail, as expected. Regions with probability values between 0 and 1 are small, showing that the numerical diffusion is indeed mitigated. Figure 5.27 shows the results for the stochastic case with $\sigma = 0.005$. The diffusion of the attractors' distributions is demonstrated, with the resonant attractor being more affected by it. The basins' boundaries diffusion is not large, being localized to specific regions in phase-space. Higher noise intensity is depicted in Figure 5.28. For $\sigma \geq 0.01$, only the nonresonant attractor remains for sufficient large time-horizons. Increasing the noise intensity past $\sigma \geq 0.01$ only increases the spreading of the nonresonant attractor over the phase-space, as observed in the distributions. This result could be thought of as in contradiction with the Monte-Carlo experiment in Figure 5.15(a, b). However, the Monte-Carlo was conducted only until $t = 10000T$, and here the expected outcome for larger time-horizons is observed. This will be made clear in the following transient analysis.

The transient analysis is demonstrated in Figure 5.29 and Figure 5.30, for $\sigma = 0.01$, and in Figure 5.31 and Figure 5.32, for $\sigma = 0.015$. For the first noise case, $\sigma = 0.01$, it is observed that for time-horizons $1/\varepsilon \leq 10000T$, the usual basin is obtained, see Figure 5.29(a, b, c) and Figure 5.30(a, b, c). The vanishing of the resonant region is only observed for larger time-horizons, which is completely absent for $1/\varepsilon = 1e7T$. This result confirms the Monte-Carlo experiment in Figure 5.15(a, b), which was conducted only until $t = 10000T$, a time for which a separation between the basins is still observed. For the second noise case, $\sigma = 0.015$, the degradation of the resonant region occurs much earlier, as observed in Figure 5.31(c) and Figure 5.32(c) for $1/\varepsilon = 1e3T$. The case for $1/\varepsilon = 1e4T$ again is validated by the Monte-Carlo experiment in Figure 5.15(c, d), with only a small probability for initial conditions in the resonant region to converge to the resonant solution and the majority decaying to the nonresonant solution. The transient basin analysis is only possible because the separation between the basins is very refined. The adoption of a crude refinement in these regions could result in wrong time-horizon values of basin decay since the numerical diffusion is not sufficiently mitigated in such cases, therefore justifying the adoption of the proposed algorithm.

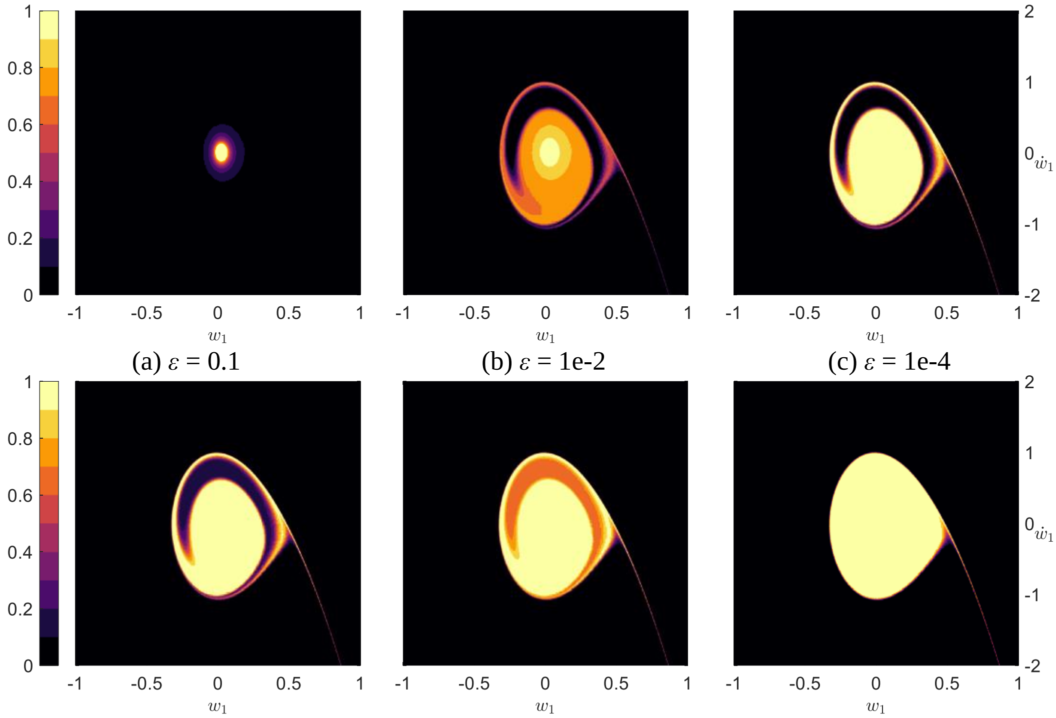

(a) ε = 0.1 (b) ε = 1e-2 (c) ε = 1e-4

(d) ε = 1e-5 (e) ε = 1e-6 (f) ε = 1e-7

Figure 5.29 – Dependency of the stochastic nonresonant basin of attraction (color bars) on the final time-horizon $1/\varepsilon$ for V_{dc} = 45, $\bar{V}_{ac}$ = 1, Ω = 2.8, w_0 = 0.05, σ = 0.010

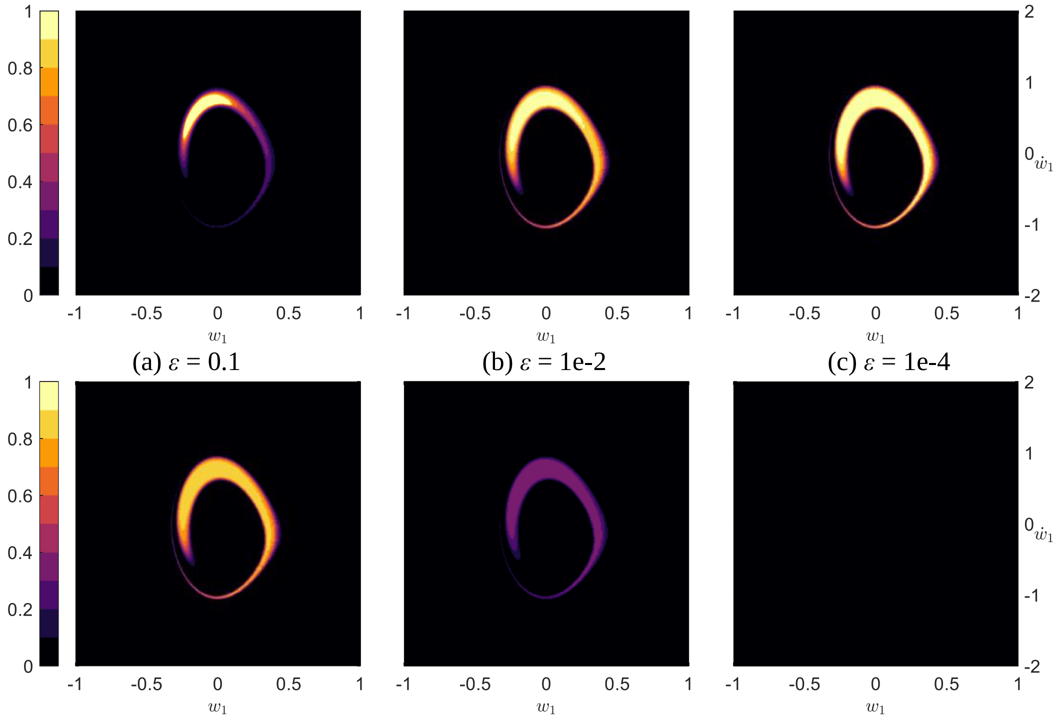

(a) ε = 0.1 (b) ε = 1e-2 (c) ε = 1e-4

(d) ε = 1e-5 (e) ε = 1e-6 (f) ε = 1e-7

Figure 5.30 – Dependency of the stochastic resonant region (color bars) on the final time-horizon $1/\varepsilon$ for V_{dc} = 45, $\bar{V}_{ac}$ = 1, Ω = 2.8, w_0 = 0.05, σ = 0.010

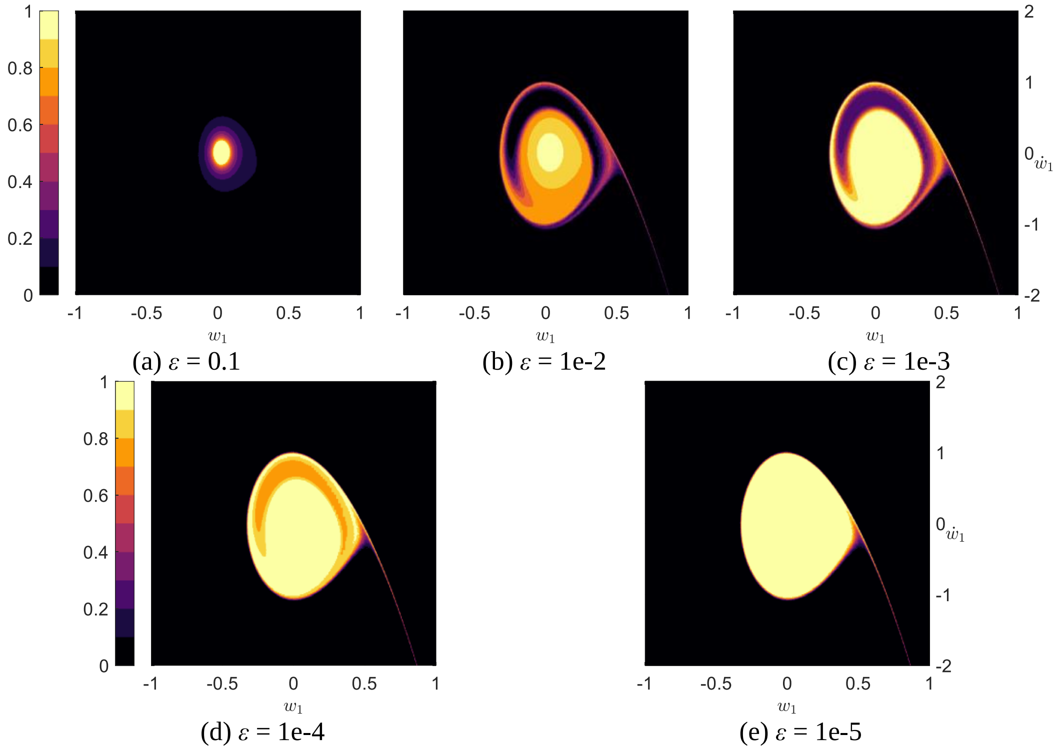

(a) ε = 0.1 (b) ε = 1e-2 (c) ε = 1e-3

(d) ε = 1e-4 (e) ε = 1e-5

Figure 5.31 – Dependency of the stochastic nonresonant basin of attraction (color bars) on the final time-horizon 1/ε for V_{dc} = 45, $\overline{V}_{ac}$ = 1, Ω = 2.8, w_0 = 0.05, σ = 0.015

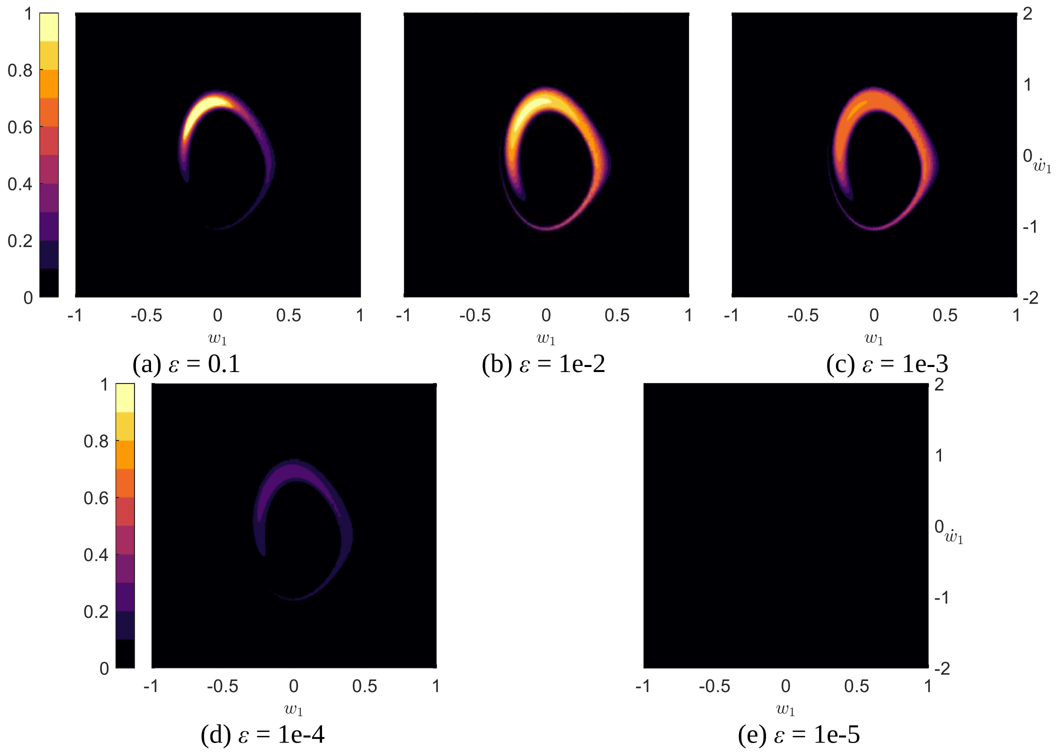

(a) ε = 0.1 (b) ε = 1e-2 (c) ε = 1e-3

(d) ε = 1e-4 (e) ε = 1e-5

Figure 5.32 – Dependency of the stochastic resonant region (color bars) on the final time-horizon 1/ε for V_{dc} = 45, $\overline{V}_{ac}$ = 1, Ω = 2.8, w_0 = 0.05, σ = 0.015

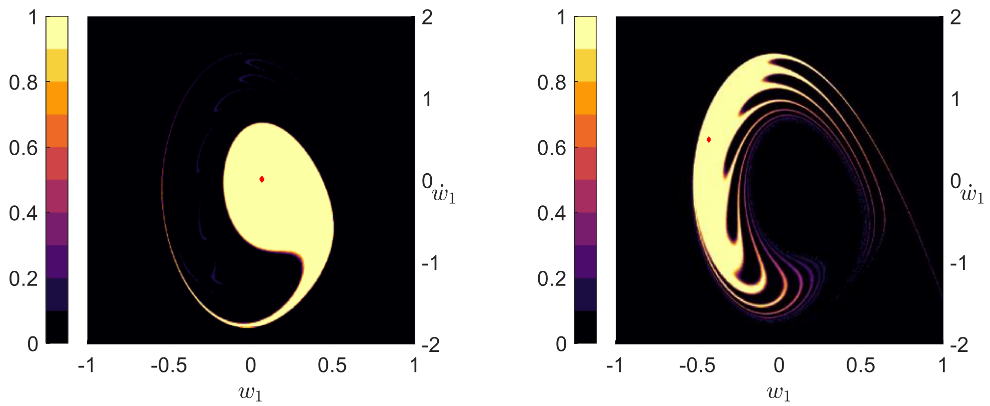

(a) nonresonant attractor (b) resonant attractor

Figure 5.33 – Microcantilever global dynamics obtained after the application of the refinement algorithm for V_{dc} = 45, $\bar{V}_{ac}$ = 5, Ω = 2.8, w_0 = 0, σ = 0.000. Attractors marked in red. Color bar: basin of attraction

The last analyzed case is a perfect microcantilever, $w_0 = 0$, with nonresonant and resonant solutions. Figure 5.33 displays for the deterministic case the basins' boundaries in much more detail, if compared to the initial investigation, Figure 5.16(a), Figure 5.17(a), and Figure 5.18(a), as expected. Stochastic cases are presented in Figure 5.34, for the nonresonant attractor, and in Figure 5.35, for the resonant attractor. In both cases, the attractors' distributions spread over the phase-space as noise increases. A different outcome is observed for the analysis with phase-space hierarchical subdivision: for noise intensity $\sigma \geq 0.013$, the resonant solution vanishes for long time-horizons. In the initial investigation, this was only observed for $\sigma \geq 0.015$, see Figure 5.19 and Figure 5.20. Also, the resonant and nonresonant regions could not be separated from each other, whereas the subdivision strategy is capable of differentiating each outcome. Also, in the last nonresonant basin, Figure 5.34(f), the color bar is shown as continuous to illustrate that there is a small probability that initial conditions in the resonant region converge to the nonresonant attractor, as observed in the Monte-Carlo experiment, Figure 5.24(f).

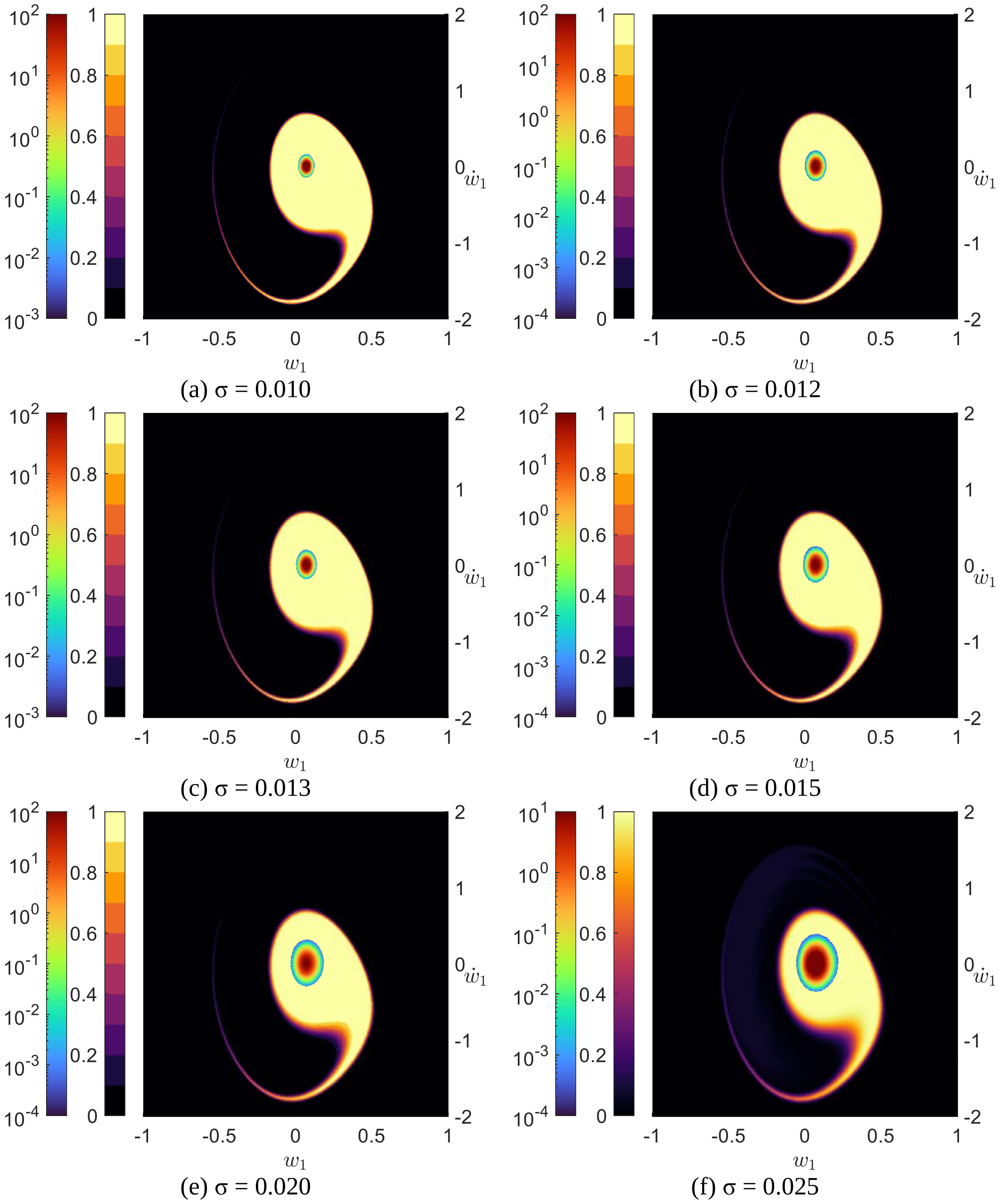

Figure 5.34 – Microcantilever nonresonant attractor global dynamics after the use of the refinement algorithm for V_{dc} = 45, $\overline{V}_{ac}$ = 5, Ω = 2.8, w_0 = 0. First color bar: stochastic basin of attraction, second color bar: attractor’s density

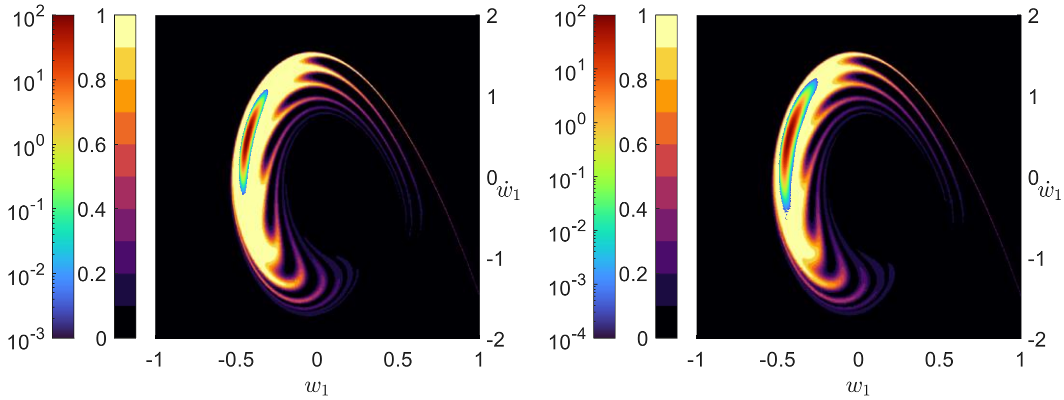

(a) σ = 0.010 (b) σ = 0.012

Figure 5.35 –Microcantilever resonant attractor global dynamics for V_{dc} = 45, $\overline{V}_{ac}$ = 5, Ω = 2.8, w_0 = 0 after the use of the refinement algorithm. First color bar: stochastic basin of attraction, second color bar: attractor's density

The transient analysis for σ = 0.013 and σ = 0.025 are detailed in Figure 5.36 and Figure 5.39, for the nonresonant attractor, in Figure 5.37 and Figure 5.40 for the resonant region, and in Figure 5.38 and Figure 5.41 for the escape region. For the lower noise intensity, σ = 0.013, the resonant region only vanishes after a long period of time. That is, the transient feature of this solution is made clear only for time-horizons 1/ε > 1e10*T*. The Monte-Carlo experiments were conducted only up until 1e4*T*, missing the long-transient characteristic of this solution in Figure 5.24(b, d). Once again, this is only possible if the resonant and nonresonant regions are properly separated, which would demand a very refined phase-space, whereas the subdivision strategy can do so without increasing the computational cost. The case with σ = 0.025 shows that the resonant region vanishes much earlier, with 1/ε = 1e4*T*, also with some solutions leading to the nonresonant attractor, see Figure 5.39(d), while the majority leads to escape, see Figure 5.41(f). This is in agreement with the Monte-Carlo experiment, Figure 5.24(e, f), where this same outcome is observed.

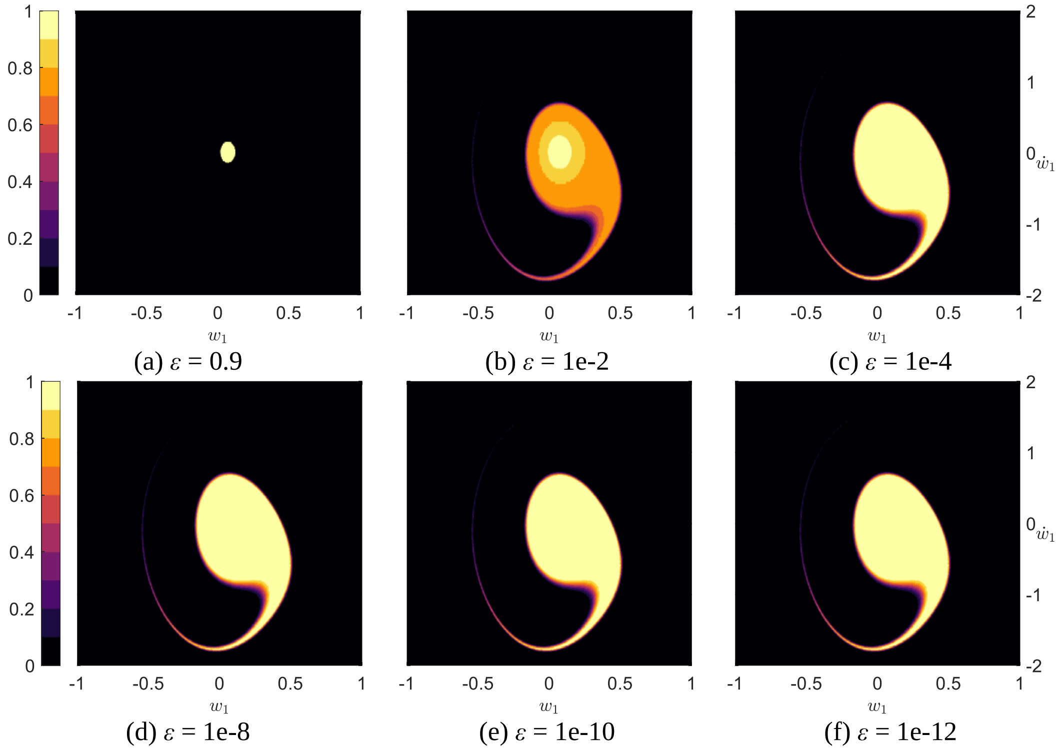

Figure 5.36 – Dependency of the stochastic nonresonant basin of attraction (color bars) on the final time-horizon $1/\varepsilon$ for V_{dc} = 45, $\overline{V}_{ac}$ = 5, Ω = 2.8, w_0 = 0, σ = 0.013

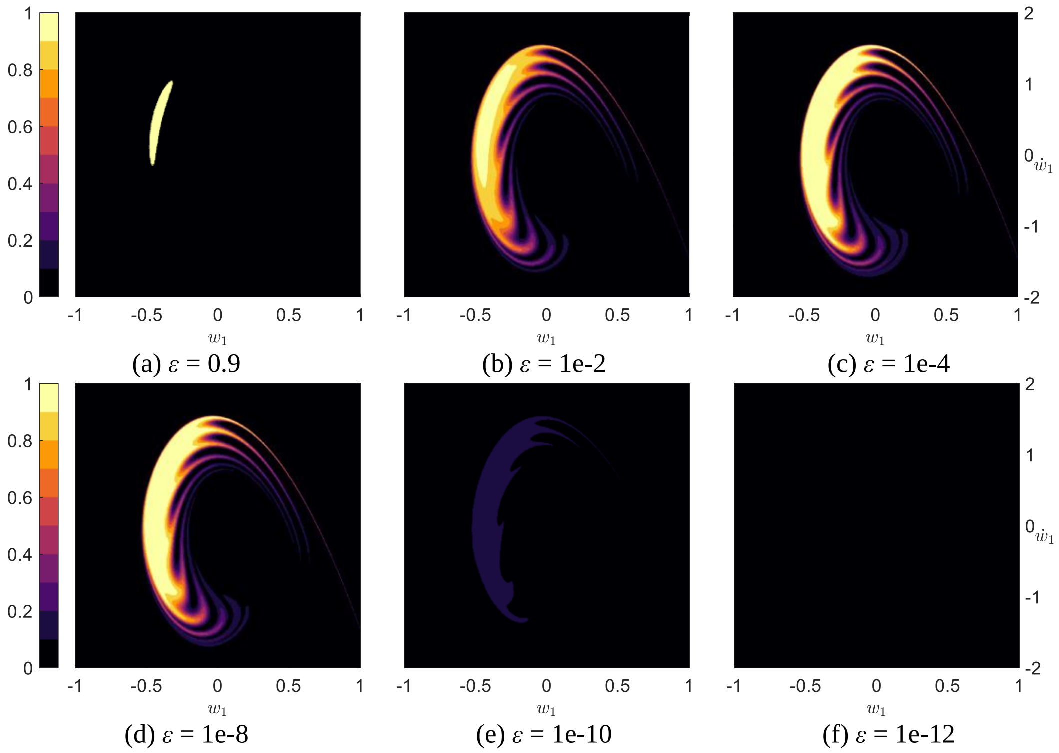

Figure 5.37 – Dependency of the stochastic resonant basin of attraction (color bars) on the final time-horizon $1/\varepsilon$ for V_{dc} = 45, $\overline{V}_{ac}$ = 5, Ω = 2.8, w_0 = 0, σ = 0.013

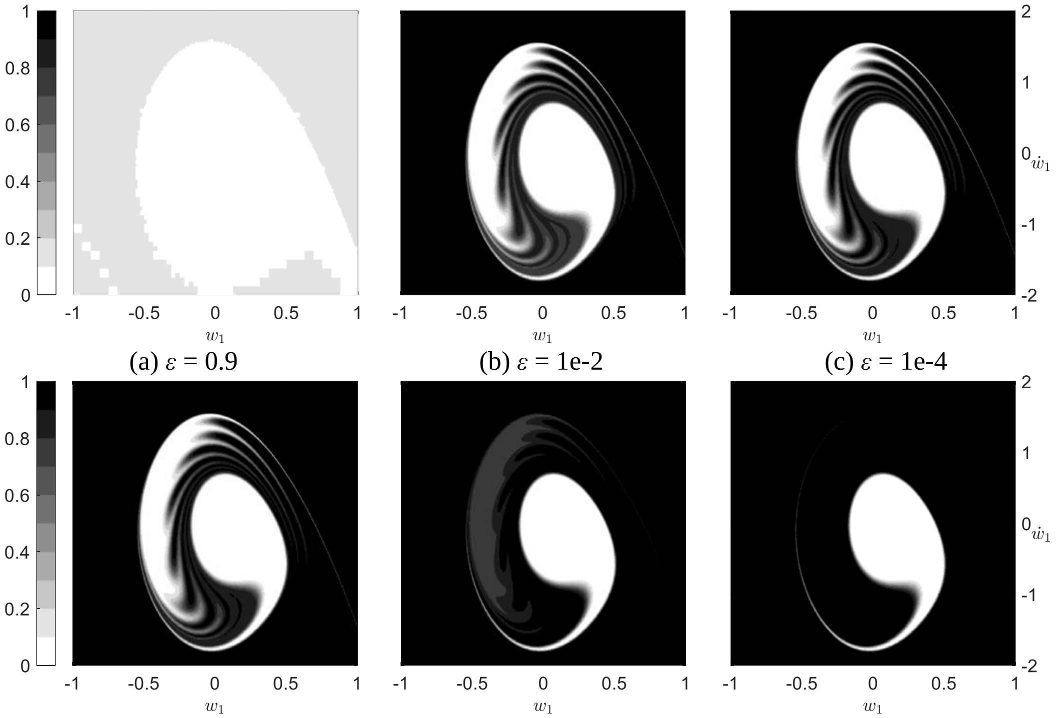

(a) ε = 0.9 (b) ε = 1e-2 (c) ε = 1e-4

(d) ε = 1e-8 (e) ε = 1e-10 (f) ε = 1e-12

Figure 5.38 – Dependency of the stochastic escape region (color bars) on the final time-horizon $1/\varepsilon$ for V_{dc} = 45, $\overline{V}_{ac}$ = 5, Ω = 2.8, w_0 = 0, σ = 0.013

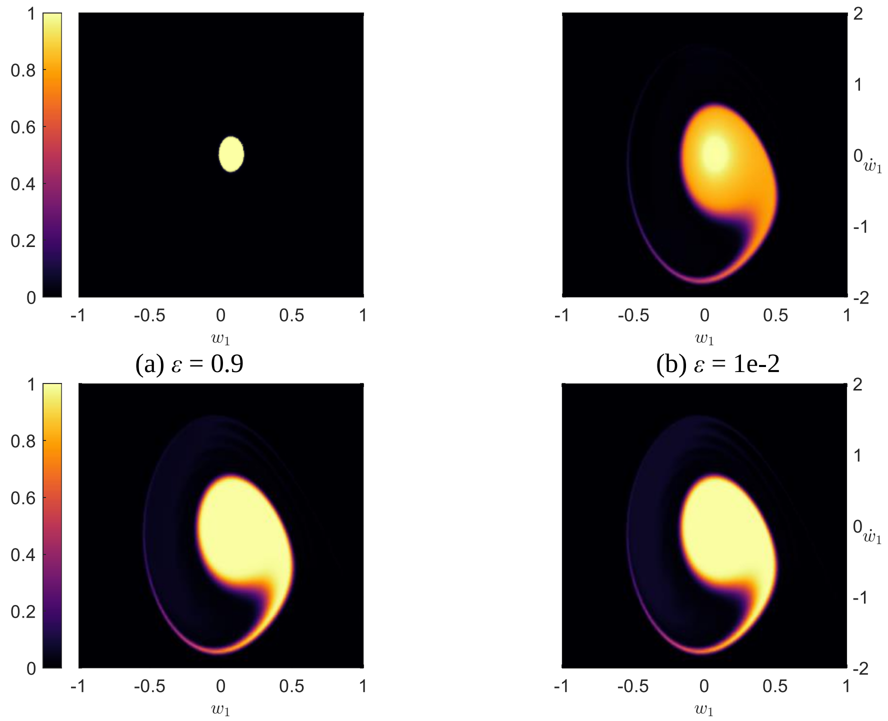

(a) ε = 0.9 (b) ε = 1e-2

(c) ε = 1e-4 (d) ε = 1e-6

Figure 5.39 – Dependency of the stochastic nonresonant basin of attraction (color bars) on the final time-horizon $1/\varepsilon$ for V_{dc} = 45, $\overline{V}_{ac}$ = 5, Ω = 2.8, w_0 = 0, σ = 0.025

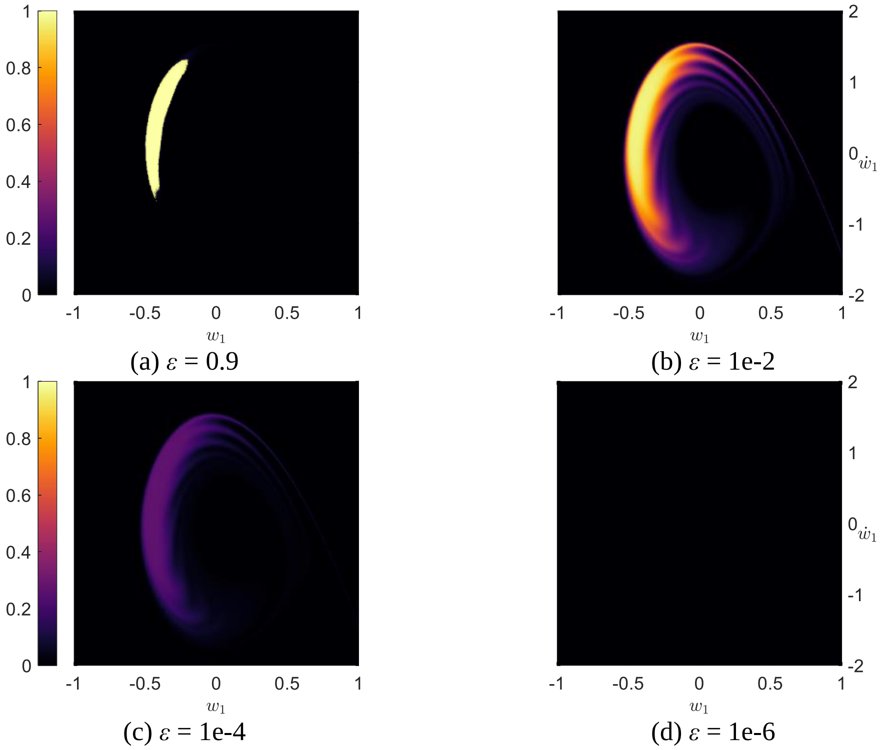

Figure 5.40 – Dependency of the stochastic resonant basin of attraction (color bars) on the final time-horizon $1/\varepsilon$ for $V_{dc} = 45$, $\bar{V}_{ac} = 5$, $\Omega = 2.8$, $w_0 = 0$, $\sigma = 0.025$

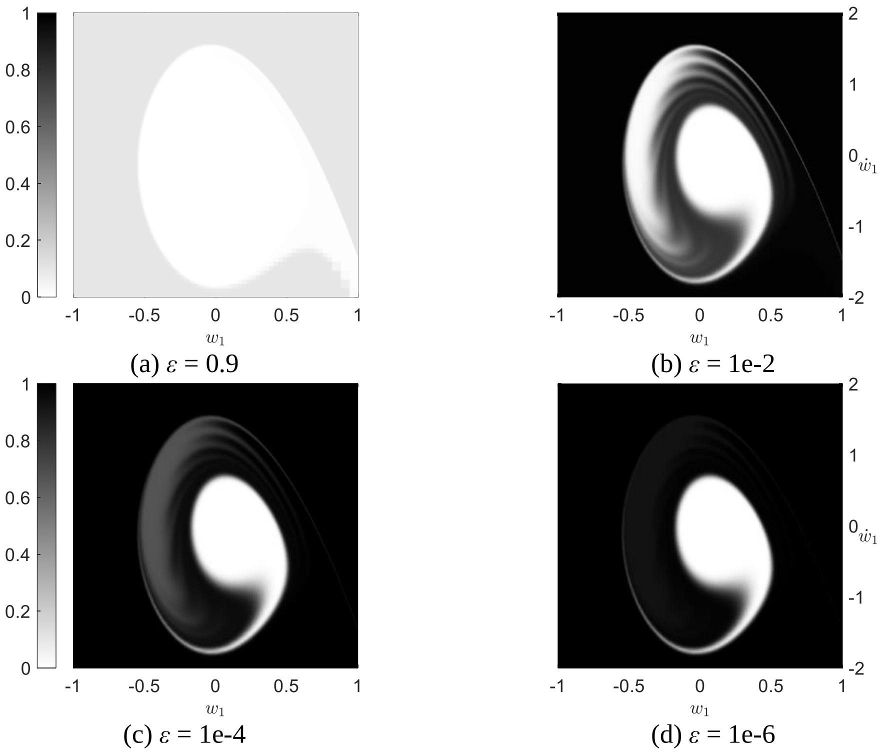

Figure 5.41 – Dependency of the stochastic escape region (see color bars) on the final time-horizon $1/\varepsilon$ for $V_{dc} = 45$, $\bar{V}_{ac} = 5$, $\Omega = 2.8$, $w_0 = 0$, $\sigma = 0.025$

Figure 5.42 shows, for ε = 1e-8, the variation of the basins' area as a function of the noise intensity σ for the perfect case, $w_0 = 0$, and an imperfect case, $w_0 = 0.05$, for selected probability thresholds. For each attractor, the measure is computed employing eq. (4.2). The basin area of the nonresonant attractor demonstrates resilience against noise. For the perfect case, the area is almost constant with only a small increase due to the erosion of the resonant basin as σ increases. The diffusion of the basins' boundaries can be observed in the perfect case in Figure 5.42(a). As noise increases, a divergence of the various probability thresholds is observed. For the imperfect case, the vanishing of the resonant basin results in an increase in the basin area of the nonresonant attractor, jumping from 10% of the window area to almost 15% of the total area, for all probability levels. The sensitivity to noise of the resonant responses is correctly depicted in both cases, showing that this measure can be considered for the quantification of dynamic integrity of systems under noise.

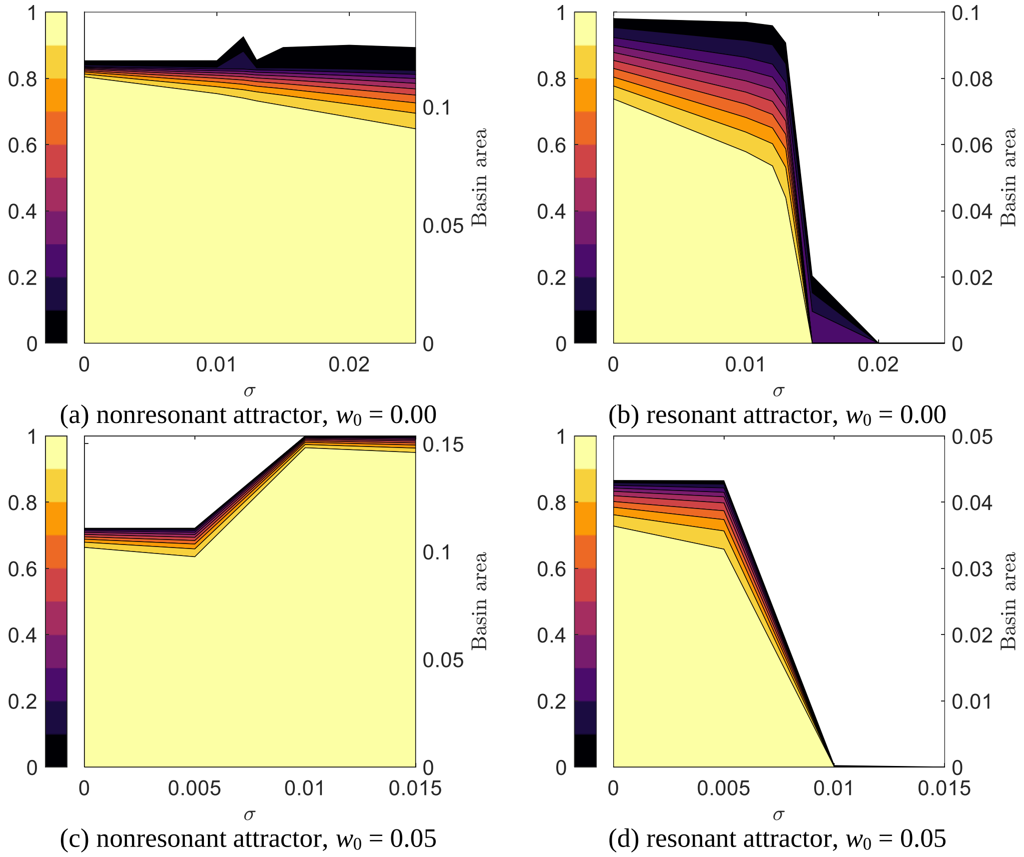

(a) nonresonant attractor, $w_0 = 0.00$ (b) resonant attractor, $w_0 = 0.00$

(c) nonresonant attractor, $w_0 = 0.05$ (d) resonant attractor, $w_0 = 0.05$

Figure 5.42 – Variation of the microcantilever basins area as a function of the noise intensity σ for $V_{dc} = 45$, $\Omega = 2.8$, (a, b) $\overline{V}_{ac} = 5$, (c, d) $\overline{V}_{ac} = 1$, showing various probability thresholds (color bar)

6
Parameter uncertainty and noise effects on the global dynamics of an electrically actuated microarch

An investigation of parameter uncertainty and noise effects on the nonlinear oscillations of a planar microarch electrically actuated is conducted. Extensional effects are considered, resulting primarily from an axial load. An initial geometric imperfection is also considered. A reduced order model is derived from a 2-mode expansion following [202], allowing the analysis to be performed in a bidimensional phase-space. The modified subdivision algorithm developed in Sections 3.3 and 3.4, given in Table 3.3, is adopted. The phase-space is hierarchically discretized into a quadtree, and stable and unstable manifolds are obtained. The effect of additive white noise and parametric uncertainty in the damping coefficient are investigated. The computations are performed by an Intel Core i7-7700HQ with eight logical processors of 2.8GHz, and the total available RAM is 24GB. The algorithm performance is measured by the reduced number of phase-space boxes and initial conditions, which represent the primary cost in the computations. Total time was not evaluated since a parallel implementation with openMP (https://www.openmp.org/) was considered for the integration of the initial conditions.

6.1.
Nonlinear Euler-Bernoulli microarch electrically actuated

A Microelectromechanical System (MEMS) model is derived based on the experimental and numerical analyses in [123]. The microstructure is simulated as a fixed-fixed imperfect microbeam, with length L and a constant rectangular cross-section of width b and thickness h. The initial geometric imperfection is described by a function $w_0(s)$. As in [123], residual stresses are represented by a constant axial load P, which produces the axial displacement u_B at the right end of the beam. Assuming only planar motions, the Euler angles ψ and ψ_0 become zero, see the trigonometric relations (A21) and (A23). Furthermore, this formulation assumes zero torsional displacements, with the Euler angles ϕ and ϕ_0 set to zero. The resulting undeformed and deformed coordinate systems with respect to the reference system are given in Figure 6.1. The actuation plate is also depicted at a positive distance d in the adopted reference system.

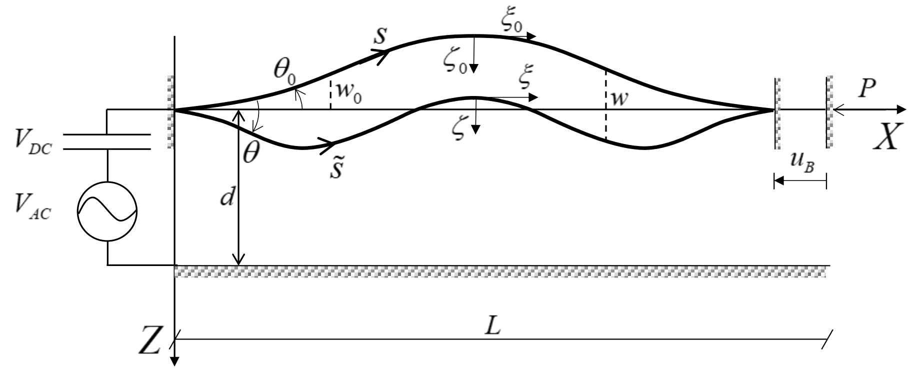

Figure 6.1 – Orientation of imperfect undeformed and deformed coordinate systems of the microarch with respect to the reference system

Considering the full nonlinear planar equations of motion (5.4) and (5.5) and the Lagrangian multiplier definition in eq. (A53) to account for the axial deformation, the extensional equations of motion take the form

$$G_u' = \left[A_\theta \frac{\partial \theta}{\partial u'} + \frac{D_u \Delta_e}{\left(1+\Delta_e\right)} \left(u' + \sqrt{1 + w_0'^2} \right) \right]' = \frac{d}{dt}\left(\frac{\partial \ell}{\partial \dot{u}} \right) - Q_u^{nc}, \tag{6.1}$$

$$G_w' = \left[A_\theta \frac{\partial \theta}{\partial w'} + \frac{D_u \Delta_e}{\left(1+\Delta_e\right)} \bar{w}' \right]' = \frac{d}{dt}\left(\frac{\partial \ell}{\partial \dot{w}} \right) - Q_w^{nc}, \tag{6.2}$$

with A_θ given by eq. (A54), Δ_e given by eq. (5.3), and the Lagrangian kernel ℓ defined as

$$\ell = \frac{1}{2}\left(m\dot{u}^2 + m\dot{w}^2 \right) - \frac{D_\eta}{2}\theta'^2 - \frac{D_u}{2}\Delta_e^{\,2}. \tag{6.3}$$

The rotary inertia $J\eta$ is order of magnitudes smaller than the other constants. Thus, the angular velocity is not considered in eq. (6.3), simplifying the development even further.

Finally, eqs. (6.1) and (6.2) are expanded up to the third order in the state variables w and u and in the geometric imperfection w_0. The axial displacement u is, in this formulation, assumed to be of the first order. The expanded equations are

$$m\ddot{u}+c_u\dot{u}-Q_u=\left\{D_u\left(u'+w'w_0'+\frac{w'^2}{2}\right)+D_\eta\bar{w}'w'''\right\}', \tag{6.4}$$

$$\begin{aligned} m\ddot{w}+c_w\dot{w}-Q_w=&\left\{D_u\bar{w}'\left(u'+w'w_0'+\frac{w'^2}{2}\right)+D_\eta\left[\left(w_0'''w'+2\left(\bar{w}'w''\right)'\right)\bar{w}'-\right.\right.\\ &\left.\left.w'''\left(w_0'^2+1\right)+w'w_0''\left(\bar{w}''+w''\right)+u'w'''+\left(u'\bar{w}'\right)''\right]\right\}'. \end{aligned} \tag{6.5}$$

The impact of the extensional assumption is evident, with the axial displacement present in both equations.

The microarch analyzed by Ruzziconi et al. [123] accounts for an initial axial displacement as a boundary condition in $s=L$. The axial boundary conditions are written as

$$u\left(0,t\right)=0,\ u\left(L,t\right)=-u_B, \tag{6.6}$$

Assuming u to be time-independent and the axial distributed load Q_u to be zero in eq. (6.4) and integrating the result two times with respect to s, the axial displacement is obtained as

$$u=-\int_0^s w'\left(\frac{w'}{2}+w_0'\right)+\frac{D_\eta}{D_u}\bar{w}'w'''ds+C_1s+C_2. \tag{6.7}$$

By applying the boundary conditions (6.6), the constants C_i in (6.7) are obtained, resulting in

$$\begin{aligned} u=&\frac{s}{L}\int_0^L w'\left(\frac{w'}{2}+w_0'\right)+\frac{D_\eta}{D_u}\bar{w}'w'''ds-\frac{s}{L}u_B\\ &-\int_0^s w'\left(\frac{w'}{2}+w_0'\right)+\frac{D_\eta}{D_u}\bar{w}'w'''ds. \end{aligned} \tag{6.8}$$

It is important to mention that only the initial displacement w_0 is stress-free. The boundary condition u_B imposes an initial deformation that is not in equilibrium. Thus, the corresponding w must be calculated.

The condensed flexural equation of motion is obtained by substituting the axial displacement, eq. (6.8), into eq. (6.5), leading to

$$
\begin{aligned}
& m\ddot{w}+c_w\dot{w}+D_\eta w^{\mathrm{iv}}+\frac{D_u}{L}\bar{w}''\left(u_B-\int_0^L \frac{w'^2}{2}+w'w_0'\,ds\right)-Q_w= \\
& \qquad \left[\frac{D_\eta}{L}\bar{w}''+\frac{D_\eta{}^2}{D_u L}\left(w^{\mathrm{iv}}+\bar{w}^{\mathrm{iv}}\right)\right]\int_0^L \bar{w}'w'''\,ds- \\
& \qquad \frac{D_\eta}{L}\left(w^{\mathrm{iv}}+\bar{w}^{\mathrm{iv}}\right)\left(u_B-\int_0^L \frac{w'^2}{2}+w'w_0'\,ds\right)- \\
& \qquad \left\{D_\eta\left[w'\left(\frac{w'w_0'''}{2}+w_0''^2+\left(w_0'w_0''\right)'\right)+\bar{w}'\left(w''w_0''+\left(w''\bar{w}'\right)'\right)\right]+\right. \\
& \qquad \left.\frac{D_\eta{}^2}{D_u}\left[\left(\bar{w}'^2 w'''\right)''-\bar{w}'w'''^2\right]\right\}'.
\end{aligned}
\tag{6.9}
$$

The left side of Eq. (6.9) is identical to the equation obtained by Ruzziconi et al. [123], where it is equated to zero. The difference between the models is due to the nonlinearities in eqs. (6.4) and (6.5) that are considered here. Finally, clamped boundary conditions are considered at both ends after the imposed axial displacement. Thus

$$
\begin{aligned}
& w(0,t)=w'(0,t)=0, \\
& w(L,t)=w'(L,t)=0.
\end{aligned}
\tag{6.10}
$$

A parallel plate capacitor with a rectangular cross-section is assumed, with the electrostatic force Q_w written as [116]

$$
Q_w=\frac{b\varepsilon V^2}{2\left(d-\bar{w}\right)^2},
\tag{6.11}
$$

where b is the beam width, d is the initial gap for a perfect system, ε is the free space permittivity, and V is the applied voltage.

Eq. (6.9) is nondimensionalized considering the following parameters

$$
\begin{aligned}
&s^* = s/L, \qquad t^* = t\sqrt{D_\eta/(mL^4)}, \\
&w^* = w/d, \qquad w_0^* = w_0/d, \qquad u_B^* = u_B/L, \\
&Q_w^{\ *} = Q_w L^3/D_\eta, \qquad \beta_u = D_u L^2/D_\eta \\
&c_w^* = c_w L^2/\sqrt{mD_\eta}, \qquad \varepsilon^* = \varepsilon L^2/D_\eta, \\
&d^* = d/L, \qquad b^* = b/L,
\end{aligned}
\tag{6.12}
$$

resulting in

$$
\begin{aligned}
&\ddot{w} + c_w\dot{w} + w^{\text{iv}} + \beta_u \bar{w}''\left(u_B - d^2\int_0^1 \frac{w'^2}{2} + w'w_0' ds\right) - \frac{Q_w}{d} = \\
&\quad \left[\bar{w}'' + \frac{d^2}{\beta_u}\left(w^{\text{iv}} + \bar{w}^{\text{iv}}\right)\right]\int_0^1 \bar{w}'w''' ds - \\
&\quad \left(w^{\text{iv}} + \bar{w}^{\text{iv}}\right)\left(u_B - d^2\int_0^1 \frac{w'^2}{2} + w'w_0' ds\right) - \\
&\quad \left\{d^2\left[w'\left(\frac{w'w_0'''}{2} + w_0''^2 + \left(w_0'w_0''\right)'\right) + \bar{w}'\left(w''w_0'' + \left(w''\bar{w}'\right)'\right)\right] + \right. \\
&\quad \left.\frac{d^2}{\beta_u}\left[\left(\bar{w}'^2 w'''\right)'' - \bar{w}'w'''^2\right]\right\}'.
\end{aligned}
\tag{6.13}
$$

where * is dropped for brevity. The nondimensional electrostatic load is given by [116]

$$
Q_w^{\ *} = \frac{b\varepsilon V^2}{2d^2\left(1-\bar{w}\right)^2},
\tag{6.14}
$$

with the singularity now at $\bar{w} = 1$.

The total applied voltage is the sum of the direct current (V_{dc}) and the time-dependent alternate current (V_{ac}), i.e.:

$$
V(t) = V_{dc} + V_{ac}(t).
\tag{6.15}
$$

The displacement is, therefore, decomposed into its dynamic and static parts,

$$
w(t,x) = w_d(t,x) + w_s(x).
\tag{6.16}
$$

The static displacement component w_s is obtained by substituting eqs. (6.15) and (6.16) into eq. (6.13) and setting to zero all terms with derivatives with respect to time. The resulting nonlinear equilibrium equation is

$$
\begin{aligned}
& w_s^{\mathrm{iv}} + \beta_u \bar{w}_s'' \left(u_B - d^2 \int_0^1 \frac{w_s'^2}{2} + w_s' w_0' \, ds \right) - \frac{b\varepsilon V_{dc}{}^2}{2d^3 \left(1-\bar{w}_s\right)^2}, = \\
& \quad \left[\bar{w}_s'' + \frac{d^2}{\beta_u} \left(w_s^{\mathrm{iv}} + \bar{w}_s^{\mathrm{iv}} \right) \right] \int_0^1 \bar{w}_s' w_s''' ds - \\
& \quad \left(w_s^{\mathrm{iv}} + \bar{w}_s^{\mathrm{iv}} \right) \left(u_B - d^2 \int_0^1 \frac{w_s'^2}{2} + w_s' w_0' \, ds \right) - \\
& \quad \left\{ d^2 \left[w_s' \left(\frac{w_s' w_0'''}{2} + w_0''^2 + \left(w_0' w_0'' \right)' \right) + \bar{w}_s' \left(w_s'' w_0'' + \left(w_s'' \bar{w}_s' \right)' \right) \right] + \right. \\
& \quad \left. \frac{d^2}{\beta_u} \left[\left(\bar{w}_s'^2 w_s''' \right)'' - \bar{w}_s' w_s'''^2 \right] \right\}' .
\end{aligned}
\tag{6.17}
$$

where $\bar{w}_s = w_s + w_0$.

The static and dynamic displacement fields are expanded in terms of the linear vibration modes, and the Galerkin method is employed to discretize the equation of motion. The linear vibration modes are solutions of

$$
\ddot{w} + w^{iv} = 0, \tag{6.18}
$$

subjected to boundary conditions (6.10). Equation (6.18) corresponds to the classic linear Euler-Bernoulli beam [199]. Its solution is

$$
w(s,t) = \sum_{i=1}^{\infty} w_i(t) F_i(s) \tag{6.19}
$$

where w_i is the ith modal amplitude and F_i is the ith natural mode of vibration, which, for the clamped-clamped boundary conditions (6.10), are given by [199],

$$
\begin{aligned}
F_i(s) = C_i & \left\{ \cosh\left(\sqrt{\omega} s\right) - \cos\left(\sqrt{\omega} s\right) + \right. \\
& \left. \frac{\sin\sqrt{\omega} + \sinh\sqrt{\omega}}{\cos\sqrt{\omega} - \cosh\sqrt{\omega}} \left[\sinh\left(\sqrt{\omega} s\right) - \sin\left(\sqrt{\omega} s\right) \right] \right\},
\end{aligned}
\tag{6.20}
$$

where C_i are the modal amplitudes normalized using the orthogonality condition [199]

$$C_i = \frac{1}{\int_0^1 F_i^2 ds}. \tag{6.21}$$

The natural frequencies are the nontrivial solutions of the characteristic equation

$$\cos\sqrt{\omega}\cosh\sqrt{\omega} = 1. \tag{6.22}$$

The initial displacement field w_0 is assumed in the form of the clamped-clamped beam buckling mode, given by

$$w_0 = \frac{y_0}{2}\left(1-\cos\left(\frac{2\pi s}{L}\right)\right), \tag{6.23}$$

which is rewritten in nondimensional form as

$$w_0^* = \frac{y_0^*}{2}\left(1-\cos\left(2\pi s\right)\right), \tag{6.24}$$

with $y_0^* = y_0/d$. The magnitude y_0 is the maximum initial rise of the imperfect beam in $s^* = 0.5$.

The present formulation is valid for shallow arches under small to moderate displacements. Also, the capacitor assumption [116] dictates that the system behaves as parallel plates. The parameters of Ruzziconi et al. [123] consider these constraints and therefore are adopted in this study. They are summarized in Table 6.1.

Table 6.1 – Microarch geometric and material parameters

Parameters	Symbol	Values
Width	b^*	0.1268
Nominal gap	d^*	0.0016
Free space permittivity (V^{-2})	ε^*	3.4273e-7
Axial stiffness	β_u	668643.74
Initial transversal displacement at $s^* = 0.5$	y_0^*	-1.9243
Initial axial displacement at $s^* = 1$	u_B	6.7288e-5

The minus sign of y_0^* implies that the total initial gap is larger than the nominal gap. In dimensional form, the maximum initial gap is $y_0 + d = 2.047\text{e-}6$. The nondimensionalization in [123] of the displacement fields is with respect to a nominal micrometer, while here, the nominal gap is adopted. Thus, the pull-in position becomes w = 1. Hereafter the symbol * is dropped for brevity unless stated otherwise. The only exception is the actuation load V and its static V_{dc} and dynamic V_{ac} components, which are in units of Volt (V).

6.2.
Nonlinear equilibrium at static actuation

The static response of the microarch is now investigated. Initially, the modal equations are obtained. Following a classical procedure [116], eq. (6.17) is multiplied by its denominator, and then a Galerkin projection using the linear modes is conducted, resulting in the system of equations

$$\begin{aligned} & w_i\left[\mathrm{B}_{in} - w_j \mathrm{B}_{ijn} + w_j w_k \mathrm{B}_{ijkn}\right] + \beta_u\left(\mathbf{C}_n + w_i \mathbf{C}_{in} + w_i w_j \mathbf{C}_{ijn} + \right. \\ & \qquad \left. w_i w_j w_k \mathbf{C}_{ijkn} + w_i w_j w_k w_l \mathbf{C}_{ijkln} + w_i w_j w_k w_l w_m \mathbf{C}_{ijklmn}\right) = \\ & \qquad \mathbf{D}_n + w_i \mathbf{D}_{in} + w_i w_j \mathbf{D}_{ijn} + w_i w_j w_k \mathbf{D}_{ijkn} + w_i w_j w_k w_l \mathbf{D}_{ijkln} + \\ & \qquad w_i w_j w_k w_l w_m \mathbf{D}_{ijklmn} + \frac{b\varepsilon V_{dc}^{\ 2}}{2d^3}\int_0^1 F_n \, ds, \end{aligned} \tag{6.25}$$

where w_i are static modal amplitudes, the tensor constants are given in Appendix B, and the Einstein summation convention is adopted. Eq. (6.25) presents nonlinearities up to the fifth order with coupling between all linear modes. The nonlinear equilibrium paths are obtained through a pseudo arc-length continuation procedure together with the Newton-Raphson method [191, 192], and their stability is verified through the maximum eigenvalue of the Jacobian matrix.

The static equilibrium responses for various imperfection levels are displayed in Figure 6.2, considering an increasing number of modes, namely, the first, third and fifth linear modes (symmetric modes). The vertical axis corresponds to the total static displacement $\bar{w}_s$ at the middle of the microarch span, s = 0.5, with respect to the perfect reference system. That is, it accounts for the displacement due to the static actuation V_{dc}, the initial imperfection y_0, and the initial axial displacement u_b. Recalling the nondimensional relations in (6.12), the displacement $\bar{w}_s^*\left(0.5\right)=1$ corresponds to the pull-in, and results for $\bar{w}_s^*\left(0.5\right)>1$ are not physically admissible.

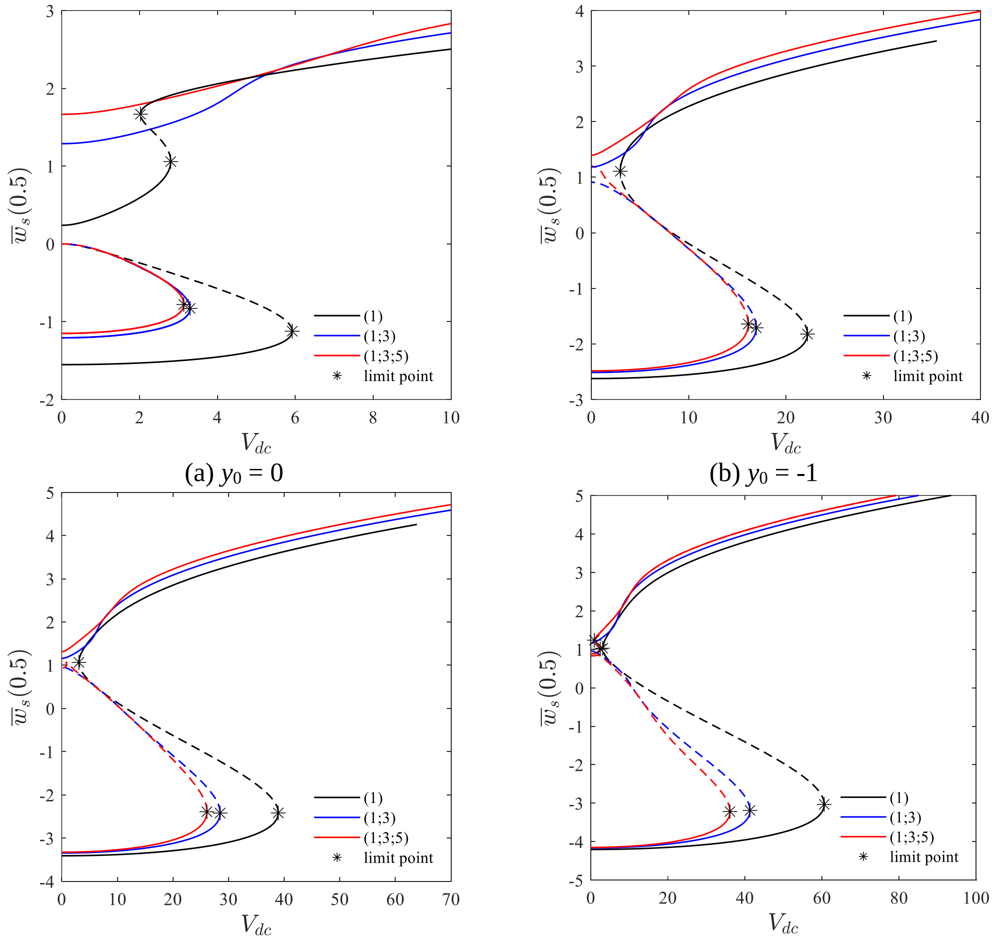

(a) y_0 = 0 (b) y_0 = -1

(c) y_0 = -2 (d) y_0 = -3

Figure 6.2 – Comparison of the microarch static response for different modal expansions and levels of initial imperfection. – stable, -- unstable

At least the first two symmetric modes are necessary to predict with precision the nonlinear response before pull-in occurs for all imperfection levels and, consequently, the associated potential energy function and the ensuing global dynamics. Specifically, the absolute error of the limit point load using the 1-mode expansion is much higher in comparison with that obtained with the 2-mode expansion, see Figure 6.3. For $y_0 \geq -2$, the 2-mode expansion absolute error with respect to the 3-mode expansion is one order of magnitude less than that of the 1-mode expansion. This indicates the viability of the 2-mode expansion for shallow arches, being a good compromise between quality of results and difficulty of analysis. Notice that, although the imperfection magnitude y_0 is a multiple of the nominal gap d, it is still very small in comparison to the nominal microarch span L [123]. The maximum absolute displacement corresponds to 0.477% of the microarch span, therefore, the displacements are still very small. Finally, symmetry-breaking bifurcations are not considered, so asymmetric modes are not investigated.

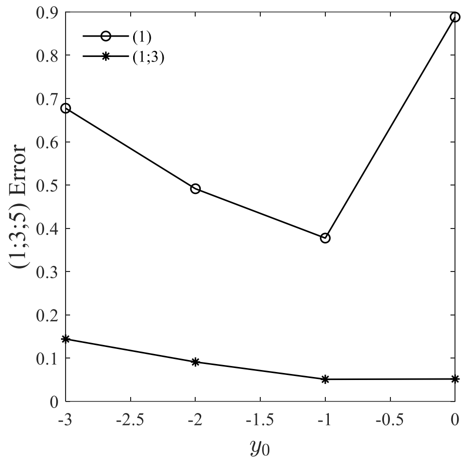

Figure 6.3 – First limit-point load absolute error of the 1 and 2 modes expansions with respect to the three modes expansion

6.3.
Formulation of the reduced order model

Here the concept of normal nonlinear modes is used to derive a reliable sdof ROM for the microarch [83]. The usual procedure to obtain the modal equations of motion is to define the displacement *w* as a sum of static and dynamic components, expand the dynamic part in Taylor series and then apply a Galerkin projection onto the linear modes, eq. (6.20) [116]. This procedure was considered in the dynamic analysis of the microcantilever in Section 5.2. The resulting system represents a dynamic perturbation of the static position. Depending on the excitation frequency and the expected displacement amplitude, several linear modes are necessary to describe the original continuous problem correctly [202]. This is a problem for global dynamic analysis since the phase-space dimension increases with the number of modal equations n (dimension 2^n), and discretizations of multidimensional spaces are computationally prohibitive, especially when noise and uncertainties are considered.

To address this issue, a reduced order model of eq. (6.13) is here derived. By multiplying eq. (6.13) by its denominator and then applying the Galerkin projection without separating static and dynamic displacement components, the n-th modal equation takes the form

$$
\begin{aligned}
&\left(\ddot{w}_i + c_w \dot{w}_i\right)\left[\mathbf{A}_{in} - w_j \mathbf{A}_{ijn} + w_j w_k \mathbf{A}_{ijkn}\right] + w_i\left[\mathrm{B}_{in} - w_j \mathrm{B}_{ijn} + w_j w_k \mathrm{B}_{ijkn}\right] + \\
&\quad \beta_u \left(\mathbf{C}_n + w_i \mathbf{C}_{in} + w_i w_j \mathbf{C}_{ijn} + w_i w_j w_k \mathbf{C}_{ijkn} + w_i w_j w_k w_l \mathbf{C}_{ijkln} + \right. \\
&\quad \left. w_i w_j w_k w_l w_m \mathbf{C}_{ijklmn}\right) = \mathbf{D}_n + w_i \mathbf{D}_{in} + w_i w_j \mathbf{D}_{ijn} + w_i w_j w_k \mathbf{D}_{ijkn} + \\
&\quad w_i w_j w_k w_l \mathbf{D}_{ijkln} + w_i w_j w_k w_l w_m \mathbf{D}_{ijklmn} + \frac{b\varepsilon}{2d^3}\left(V_{dc} + V_{ac}\right)^2 \int_0^1 F_n \, ds,
\end{aligned} \tag{6.26}
$$

where the Einstein summation convention is adopted, and the constant tensors are given in Appendix B. The electrostatic load V is separated into static and dynamic contributions due to the direct current voltage V_{dc} and alternating current voltage V_{ac}. This is a strongly nonlinear equation, with second-order nonlinearities in the inertia and damping terms and up to fifth-order nonlinear stiffness terms. Modal systems obtained from eq. (6.26) are highly coupled, complicating the analysis.

Following the results from the static analysis, the symmetric 2-mode expansion system is adopted. However, the adoption of the 2-mode expansion results in a 4-dimensional phase-space, which is still complicated to analyze. An alternative is to restrict the analysis to solutions embedded in a lower dimensional invariant manifold [83], following the definition of nonlinear normal modes of Shaw and Pierre [202].

To construct the ROM, the symmetric 2-mode system is expanded using Taylor series around a static equilibrium position $\left(w_s^{(1)}, w_s^{(2)}, V_{dc}\right)$ given by the solution of the symmetric 2-mode expansion of eq. (6.25) up to fifth order. The resulting first-order differential system is

$$
\begin{aligned}
&\frac{d}{dt} w_1 = \dot{w}_1, \\
&\frac{d}{dt} \dot{w}_1 = F_1\left(w_s^{(1)}, w_s^{(2)}, V_{dc}, \dot{w}_1, \dot{w}_2, w_1, w_2, V_{ac}\right),
\end{aligned} \tag{6.27}
$$

$$
\begin{aligned}
&\frac{d}{dt} w_2 = \dot{w}_2, \\
&\frac{d}{dt} \dot{w}_2 = F_2\left(w_s^{(1)}, w_s^{(2)}, V_{dc}, \dot{w}_1, \dot{w}_2, w_1, w_2, V_{ac}\right).
\end{aligned} \tag{6.28}
$$

For the following numerical analysis, the static position is calculated assuming V_{dc} = 0.7V, as in [123], with parameters from Table 6.1, and $w_s^{(1)} = -0.8382$, $w_s^{(2)} = 0.0200$. Then, the procedure described in [202] is applied.

One of the modal amplitudes is taken as the independent manifold variable (master pair), while the others are assumed as dependent variables (slave coordinates). Here the first modal amplitude and the corresponding velocity are adopted as governing or master coordinates, and the second modal amplitude and velocity as slave coordinates. Expanding w_2 up to the fifth order results in

$$w_2 = a_0 + \sum_{n=1}^{5}\sum_{i=0}^{n} a_{i,n} w_1^{n-i} \dot{w}_1^{i}, \tag{6.29}$$

$$\dot{w}_2 = b_0 + \sum_{n=1}^{5}\sum_{i=0}^{n} b_{i,n} w_1^{n-i} \dot{w}_1^{i}. \tag{6.30}$$

The constants are obtained by substituting eq. (6.29) and (6.30) into the first and second of eqs. (6.28), respectively, and setting damping and forcing terms to zero. Applying the second equation in (6.27) to eliminate the acceleration terms, and retaining terms up to fifth power of w_1 and $\dot{w}_1$, results in

$$C_{1;0} + \sum_{n=1}^{5}\sum_{i=0}^{n} C_{1;i,n} w_1^{n-i} \dot{w}_1^{i} = C_{2;0} + \sum_{n=1}^{5}\sum_{i=0}^{n} C_{2;i,n} w_1^{n-i} \dot{w}_1^{i}, \tag{6.31}$$

$$C_{3;0} + \sum_{n=1}^{5}\sum_{i=0}^{n} C_{3;i,n} w_1^{n-i} \dot{w}_1^{i} = C_{4;0} + \sum_{n=1}^{5}\sum_{i=0}^{n} C_{4;i,n} w_1^{n-i} \dot{w}_1^{i}, \tag{6.32}$$

which are dependent of the constants $a_{i,n}$ and $b_{i,n}$ in eqs. (6.29) and (6.30). The nonlinear polynomial system

$$\begin{aligned}
&C_{1;0} - C_{2;0} = 0, \\
&C_{3;0} - C_{4;0} = 0, \\
&C_{1;i,n} - C_{2;i,n} = 0, \qquad \forall i,n, \\
&C_{3;i,n} - C_{4;i,n} = 0, \qquad \forall i,n,
\end{aligned} \tag{6.33}$$

governs the coefficients $a_{i,n}$ and $b_{i,n}$ of eq. (6.29) and (6.30). In this case, there are forty-two equations up to the fifth power in $a_{i,n}$ and $b_{i,n}$. Solving this problem results in the nonlinear normal mode governed by

$$\frac{d}{dt}w_1 = \dot{w}_1,$$
$$\frac{d}{dt}\dot{w}_1 = 5.0854w_1^5 + 14.3037w_1^4 + 0.0035\dot{w}_1^2 - 2.4554\text{E}-6\dot{w}_1^4 - \left(121.6181 + 0.0224\dot{w}_1^2\right)w_1^3 + \left(762.4990 - 0.0114\dot{w}_1^2\right)w_1^2 - \left(1385.5761 - 0.0172\dot{w}_1^2 + 1.5913\text{E}-5\dot{w}_1^4\right)w_1. \tag{6.34}$$

Figure 6.4 illustrates the two-dimensional manifold of the nonlinear normal mode given by eq. (6.34). This manifold is tangent to the plane corresponding to the linear normal mode at the origin.

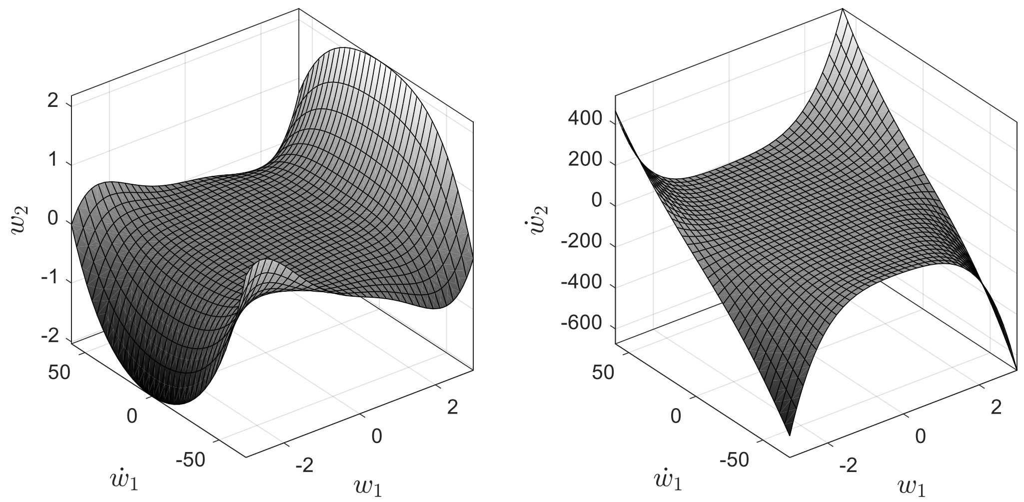

Figure 6.4 – Two-dimensional invariant manifold of the reduced order model

By substituting eq. (6.29) and eq. (6.30) into eq.(6.27), the first-order nonlinear equations of the forced and damped system are given by

$$
\begin{aligned}
&\frac{d}{dt}w_1 = \dot{w}_1, \\
&\frac{d}{dt}\dot{w}_1 = 5.0854w_1^5 + 14.3037w_1^4 + 0.0035\dot{w}_1^2 - 2.4554\text{E}-6\dot{w}_1^4 - \\
&\qquad \left(121.6181 + 0.0224\dot{w}_1^2\right)w_1^3 + \left(762.4990 - 0.0114\dot{w}_1^2\right)w_1^2 - \\
&\qquad \left(1385.5761 - 0.0172\dot{w}_1^2 + 1.5913\text{E}-5\dot{w}_1^4\right)w_1 - c_w^{(1)}\dot{w}_1 + \\
&\qquad \left(c_w^{(1)} - c_w^{(2)}\right)\Big[\left(0.0351w_1^4 + 1.0034\text{E}-5w_1^2\dot{w}_1^2\right)\dot{w}_1 + \\
&\qquad \left(0.0164w_1^2 + 6.5676\text{E}-7\dot{w}_1^2\right)w_1\dot{w}_1 - \\
&\qquad \left(0.0193w_1^2 - 5.2796\text{E}-6\dot{w}_1^2\right)\dot{w}_1 - 0.0104w_1\dot{w}_1 - 0.1449\dot{w}\Big] + \\
&\qquad V_{ac}\Big[1.0091\text{E}-5w_1^2\dot{w}_1^2 + 0.0399w_1^4 + 7.2601\text{E}-6w_1\dot{w}_1^2 + \\
&\qquad 0.0980w_1^3 + 1.0335\text{E}-6\dot{w}_1^2 + 0.2257w_1^2 + 0.4405w_1 + 0.6280\Big] + \\
&\qquad V_{ac}^2\Big[0.0700w_1^3 + 5.1858\text{E}-6w_1\dot{w}_1^2 + 0.1612w_1^2 + \\
&\qquad 7.3821\text{E}-7\dot{w}_1^2 + 0.3146w_1 + 0.4486\Big],
\end{aligned}
\tag{6.35}
$$

which is a reduced order model for vibrations in the pre-buckling potential well, with $\left(w_1, \dot{w}_1\right) = \left(0, 0\right)$ as the energy minimum.

If $c_w^{(1)} = c_w^{(2)}$, the damping is significantly simplified, which is the case adopted in [123]. Here, the damping ratio ξ is the same for the two modes, leading to distinct values for $c_w^{(1)}$ and $c_w^{(2)}$, and also to nonlinear damping terms in eq. (6.35).

6.4. Frequency response under dynamic actuation

The dynamic actuation is given by the periodic voltage,

$$
V_{ac} = A\cos\left(\Omega t\right), \tag{6.36}
$$

where A is the forcing magnitude, and Ω is the forcing frequency. The damping coefficients are given in terms of the damping ratio, ξ, as

$$c_w^{(1)} = 2\xi\omega_1,$$
$$c_w^{(2)} = 2\xi\omega_2, \qquad (6.37)$$

where ω_1 and ω_2 are the first and second natural frequencies. The natural frequencies are a function of the static voltage V_{dc}, the initial axial displacement u_B, and the initial imperfection y_0. For the parameters in Table 6.1 and V_{dc} = 0.7V, the natural frequencies are ω_1 = 37.6699 and ω_2 = 116.7780.

The analysis is conducted with the software Continuation Core and Toolboxes (COCO) [203]. Initially, the free vibrations of the 2 dof model, described by the 2-mode expansion, eq. (6.26), and the conservative reduced order model, eq. (6.34), are compared. The backbone curves are shown in Figure 6.5 in terms of the transversal displacement $\overline{w}$ at s = 0.5, with respect to the reference frame, and in Figure 6.6 in terms of the modal amplitudes w_1 and w_2. A softening behavior is observed, which is the expected behavior of a shallow arch. The two models agree qualitatively well in terms of the transversal displacement $\overline{w}$ and the first modal amplitude w_1, even for large displacements. The two models diverge in the second modal amplitude w_2 for frequencies lower than 35, as observed in Figure 6.6(b). However, w_2 is much smaller in comparison to w_1, in this range which minimizes the impact of the difference between the models, as shown by the resonance curves in Figure 6.7. These results demonstrate the quality of the reduced order model as a lower dimensional substitute for the original modal expansion when excitation frequencies concentrate around the first natural frequency.

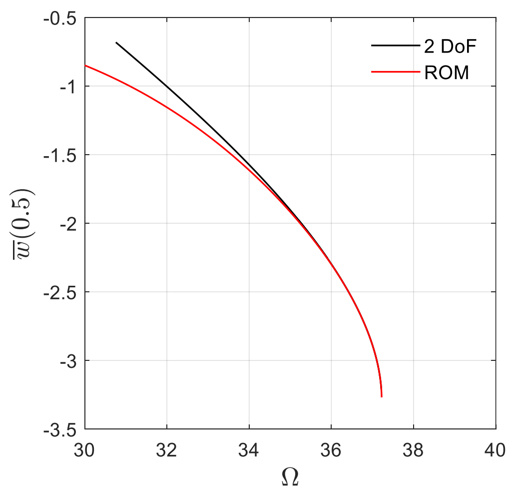

Figure 6.5 – Backbone curves for the first mode natural frequency of the total displacement $\overline{w}$ at s = 0.5

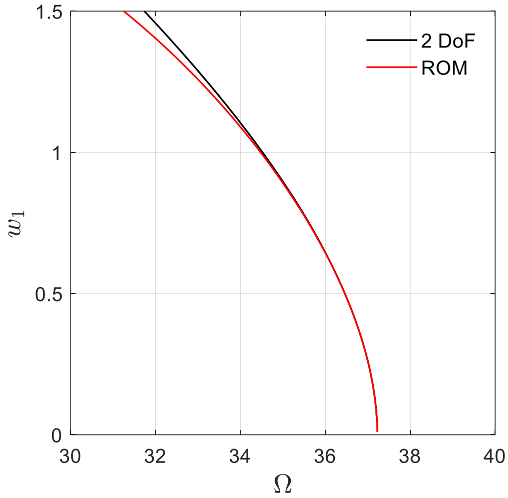

(a)

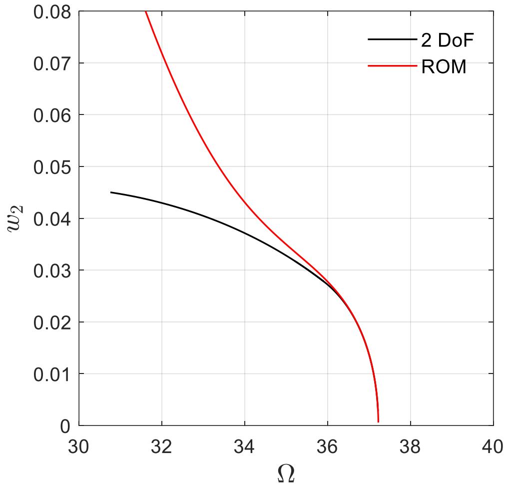

(b)

Figure 6.6 – Backbone curves for the first natural frequency in the modal amplitudes (a) w_1 and (b) w_2

The resonance curves for both models are compared in Figure 6.7 for $A = 17$V, $\xi = 0.05$, and $\xi = 0.03$. Two resonance regions are observed, one at $\Omega = 37.2$ and other at $\Omega = 18.6$. The former corresponds to the first mode natural frequency, while the latter is a subharmonic resonance. The subharmonic resonance is due to the term V_{ac}^2 in both the reduced model, eq. (6.35), and the 2 dof model, eq. (6.26). Specifically, the subharmonic resonance is more prominent, with larger displacement values. Markers identify the bifurcation points: saddle-node bifurcation points in green and period-doubling bifurcation points in red. Stable and unstable solutions are identified by respectively continuous and dashed lines. The reduced order model agrees well with the 2 dof model, again showing its capability, including the point where the saddle-node bifurcation occurs. Finally, the impact of increasing forcing amplitude is demonstrated in Figure 6.8, for $\xi = 0.05$, in Figure 6.9, for $\xi = 0.03$, and in Figure 6.10, for $\xi = 0.01$. The main resonant region exhibits small amplitude vibrations for the two former cases, while the subharmonic region presents much larger vibration amplitudes. For smaller damping ratios, $\xi = 0.01$, Figure 6.10, a more complex response is observed, with the main resonant region exhibiting large amplitude vibrations. This shows the importance of the damping parameter on the results. Thus, the influence of damping uncertainty will be explored later in this chapter.

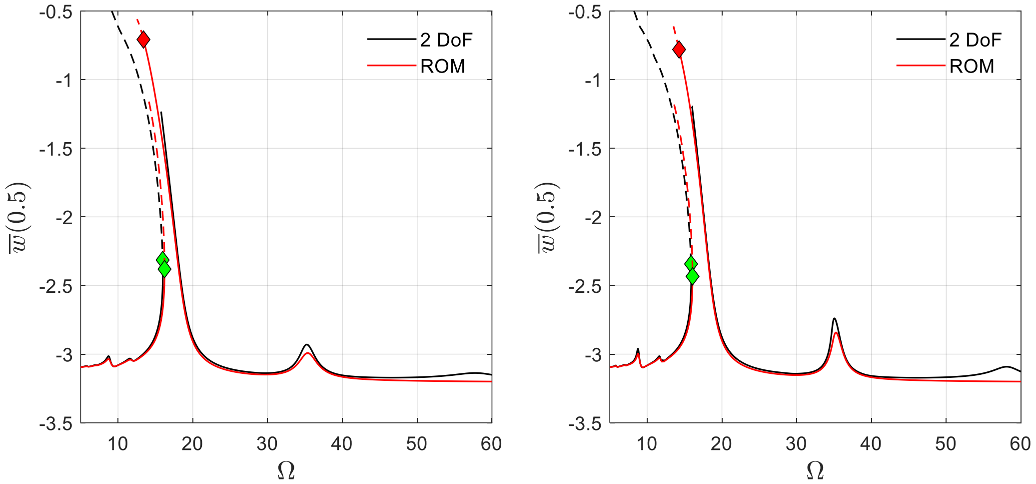

(a) ξ = 0.05 (b) ξ = 0.03

Figure 6.7 – Resonance response curves for A = 17V and varying ξ. Saddle-nodes in green, period-doubling points in red. – stable, -- unstable

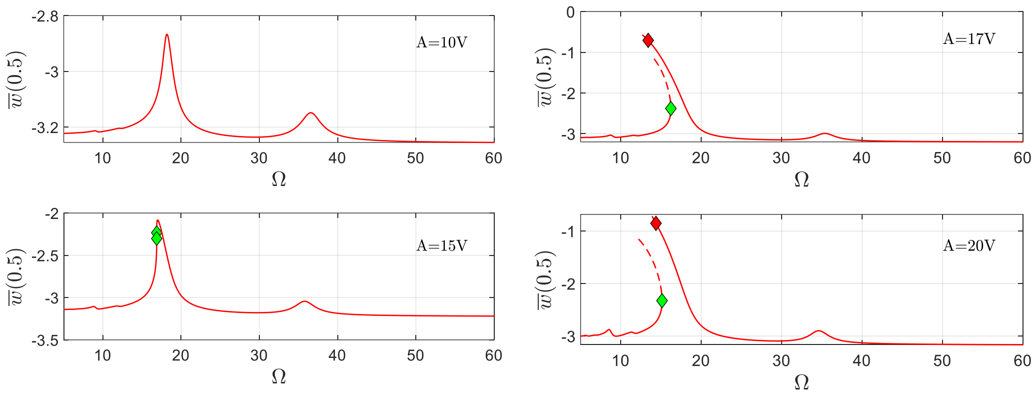

Figure 6.8 – Resonance response curves of the reduced order model for ξ = 0.05 and varying amplitude A. Saddle-nodes in green, period-doubling points in red. – stable, -- unstable

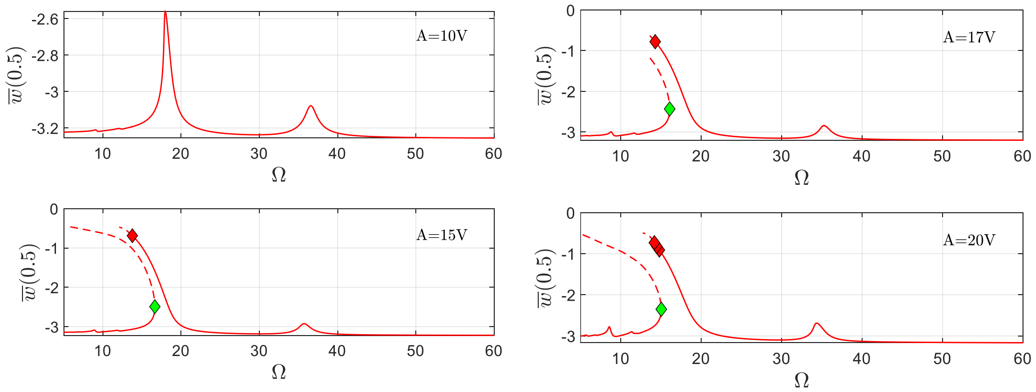

Figure 6.9 – Resonance response curves of the reduced order model for ξ = 0.03 and varying amplitude A. Saddle-nodes in green, period-doubling points in red. – stable, -- unstable

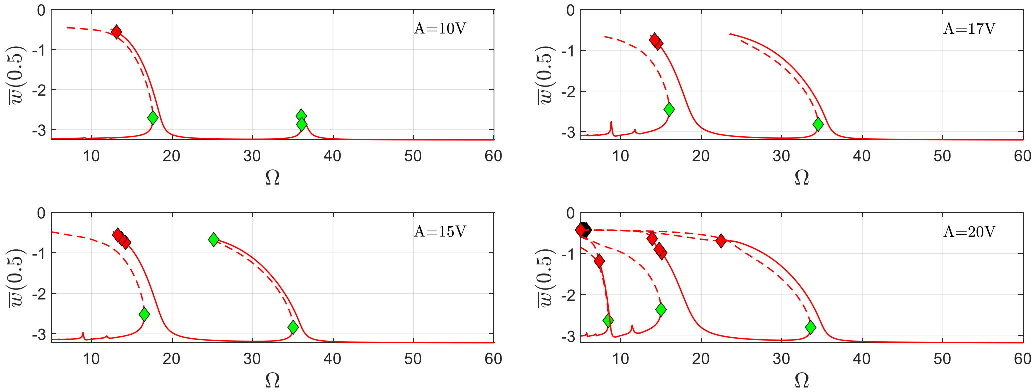

Figure 6.10 – Resonance response curves of the reduced order model for ξ = 0.01 and varying amplitude *A*. Saddle-nodes in green, period-doubling points in red. – stable, -- unstable

6.5. Global dynamic analysis

6.5.1. Deterministic results

The deterministic global dynamics of the arch are now discussed. The subharmonic resonance region is investigated, considering a forcing frequency $\Omega = 15$. The amplitude of excitation is A = 17V for all cases. The fourth order Runge-Kutta integrator is adopted for the construction of the flow φ_T, with time-step T/2000.

The analyzed phase-space window is $\mathbb{X} = \{-2, 3\} \otimes \{-70, 60\}$, which contains the relevant attractors. The initial box partition is defined as a division of 2^5 in each dimension, totaling 32x32 = 1024 boxes of size {0.1562, 4.0625}. The procedure is conducted through four steps, with a final box size of {0.0098, 0.2539}, box subdivision is accomplished using the quadtree procedure. The number of initial conditions per box depends on the box size, decreasing with refinement. Table 6.2 presents the number of collocation points for each depth level.

The changes in the basins of attraction topology in the subharmonic resonance region with the damping ratio ξ are shown in Figure 6.11. For $\xi = 0.05$, the two basins are robust, with well-defined smooth boundaries. As the damping ratio decreases, both basins' integrity degrades, with escape tongues gradually eroding them, with the resonant basin more affected than the nonresonant one. This is also evident in Figure 6.12, where the increase of the escape region with the damping ratio is presented. Also, the resonant and the nonresonant basins become more intertwined as ξ decreases.

Table 6.2 – Discretization data for the Reduced order model

Depth level	Box-size	Points per dimension	Total collocation points
10	{0.1562, 4.0625}	11	121
12	{0.0781, 2.0312}	9	81
14	{0.0391, 1.0156}	7	49
16	{0.0195, 0.5078}	5	25
18	{0.0098, 0.2539}	3	9

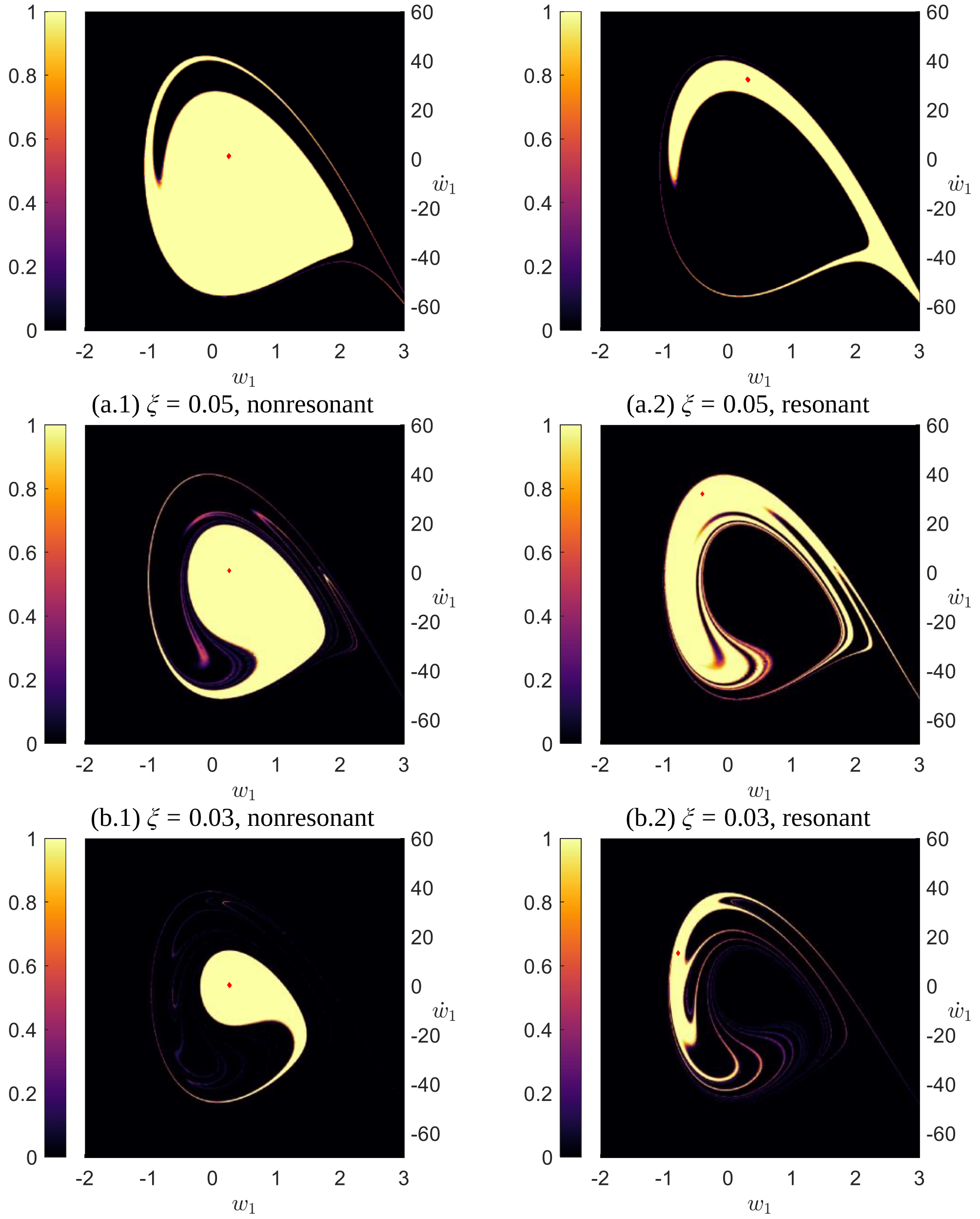

Figure 6.11 – Basins' distributions (color bar) dependency with the critical damping ratio ξ, for A = 17V and Ω = 15. Attractors marked in red

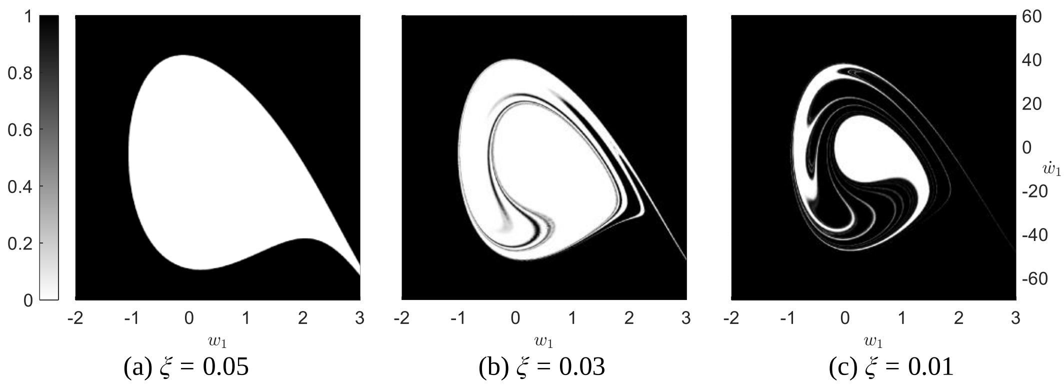

Figure 6.12 – Escape regions' distributions (color bar) dependency with the critical damping ratio ξ, for A = 17V and Ω = 15

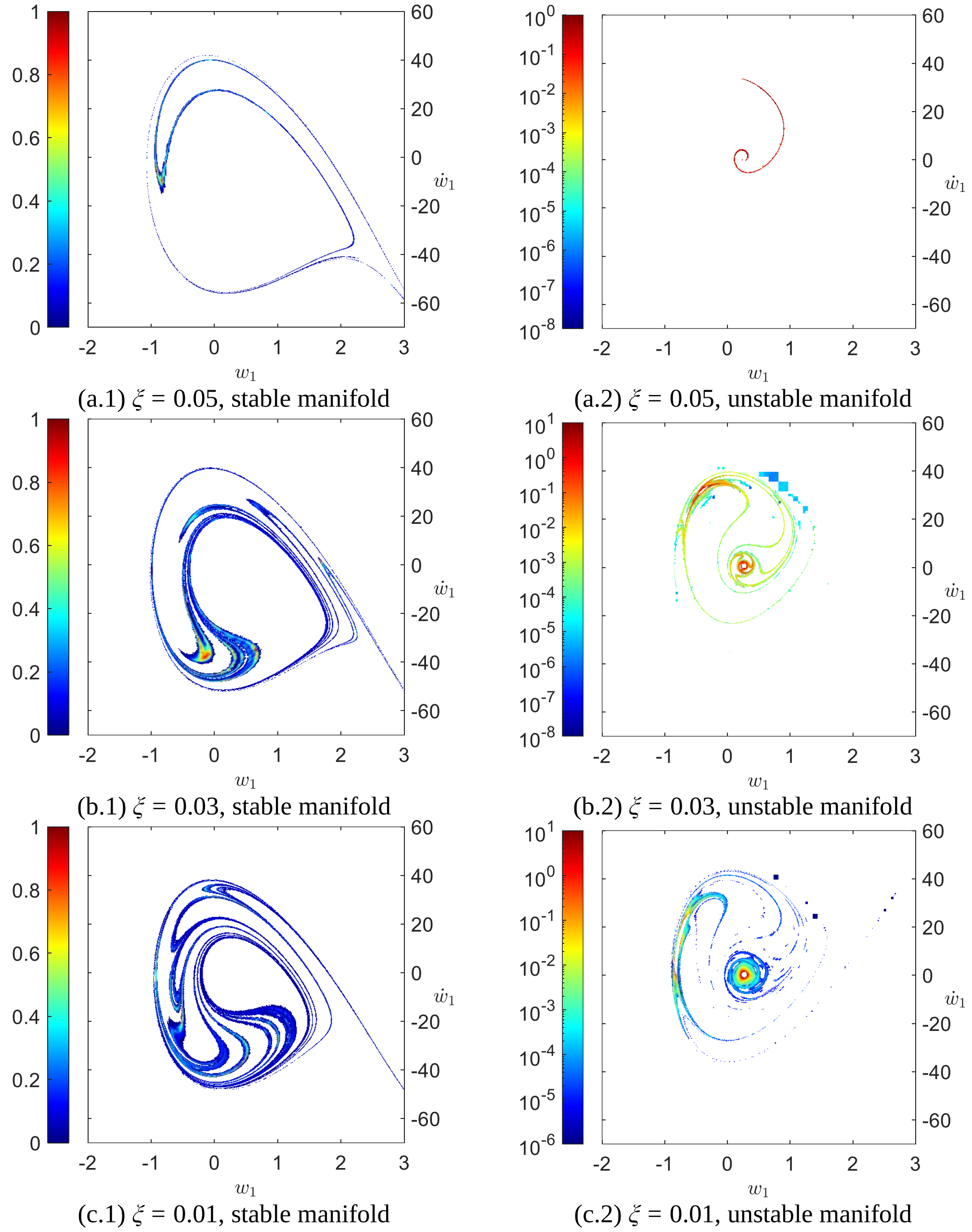

Figure 6.13 – Dependency of the stable and unstable manifolds distributions (color bar) with the critical damping ratio ξ. A = 17V, Ω = 15

Complementary to the basins analysis, Figure 6.13 presents the evolution of the stable and unstable manifolds of the saddle lying along the basin boundary in the subharmonic resonance region with the damping ratio. The stable and unstable manifolds for $\xi = 0.05$, Figure 6.13(a), are the simplest ones, in agreement with the smooth boundaries observed in Figure 6.11(a). The structures become more complex for lower damping ratios, as shown in Figure 6.13(b, c). Figure 6.13(a.1, b.1, c.1) illustrates the geometry of the stable manifolds and the increasing stretching and folding process as damping decreases, which increases the basin fractality and sensitivity to initial conditions near the basins' boundaries, which are expected to increase with the addition of noise. The unstable manifolds converging to the two attractors also exhibit an increasingly complex structure as damping decreases, Figure 6.13(a.2, b.2, c.2). Figure 6.14 shows the superposition of the stable manifold (in green) and the unstable manifold (in blue). Numerous transverse intersections (in red) are observed for low damping ratios, implying the existence of a topological horseshoe. These observations show that the damping coefficient significantly influences the microarch global dynamics.

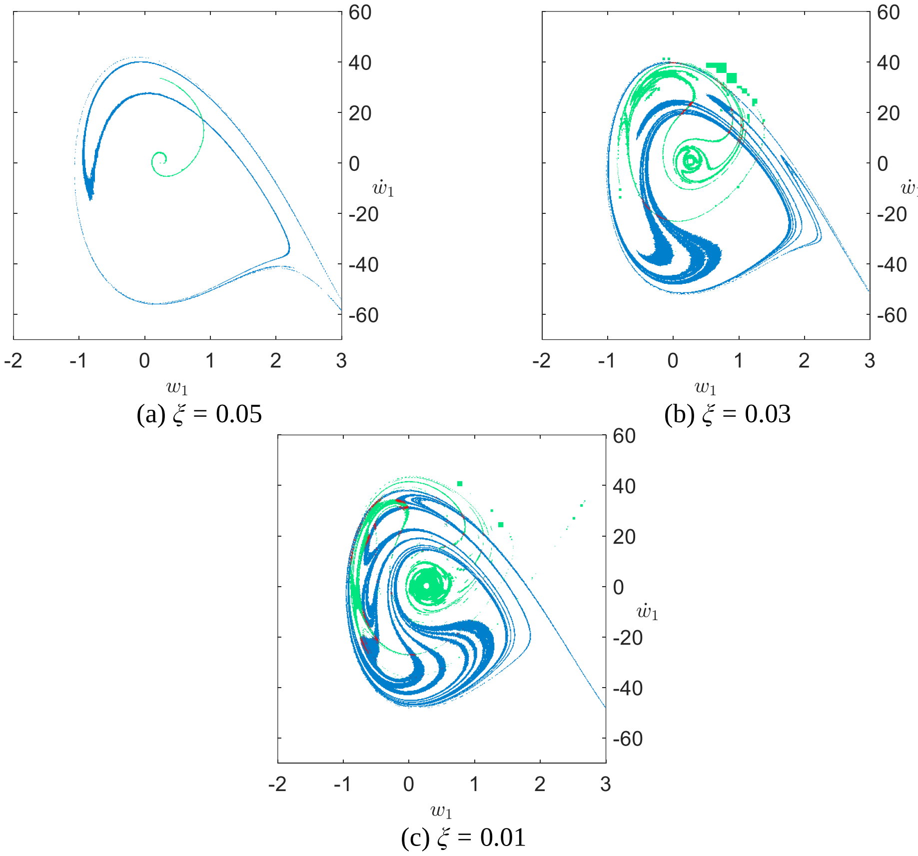

Figure 6.14 – Stable (blue), and unstable (green) manifolds superposition (in red) for different damping ratio ξ. A = 17V, Ω = 15

Figure 6.15 demonstrates how the final partition $\mathbb{B}_{18}$ changes with the damping ratio. As expected, the most refined regions correspond to the attractors' stable and unstable manifold regions. Regarding the algorithm efficiency, Figure 6.16 displays the total box and initial conditions count, while Figure 6.17 compare the discretization values with an equivalent full discretization of the phase-space for a given depth level. As expected, the case with the most complex structures, ξ = 0.01, led to the largest box and initial conditions count for all levels. The ratios in Figure 6.17 demonstrate the capability of the proposed procedure in comparison with a full discretized phase-space. With ratios respectively lower than 40% and 70%, the method could fully depict the dynamical system attractors, basins, and complex stable and unstable manifolds. The lower box and initial conditions count were observed for the case with simple phase-space structures, which is again an expected outcome.

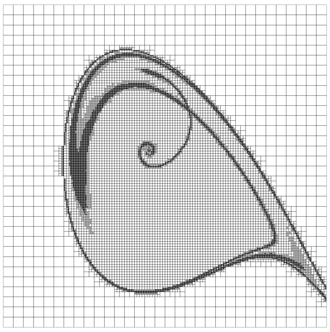

(a) ξ = 0.05

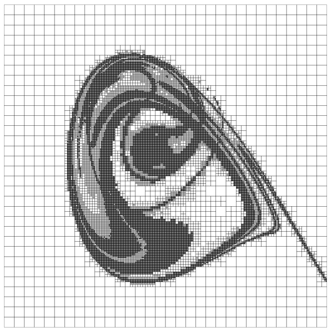

(b) ξ = 0.03

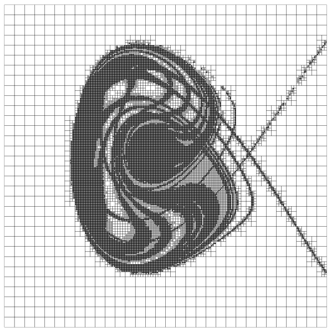

(c) ξ = 0.01

Figure 6.15 – Dependency of the last partition $\mathbb{B}_{18}$ with the critical damping ratio ξ, for A = 17V and Ω = 15

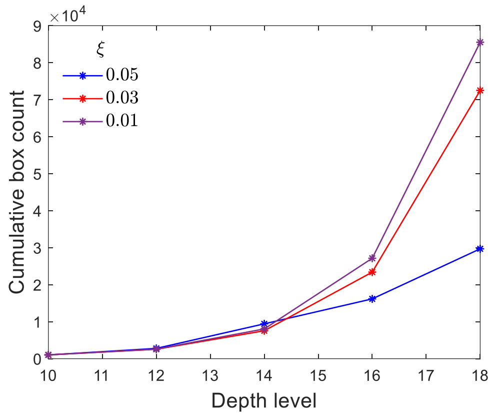

(a)

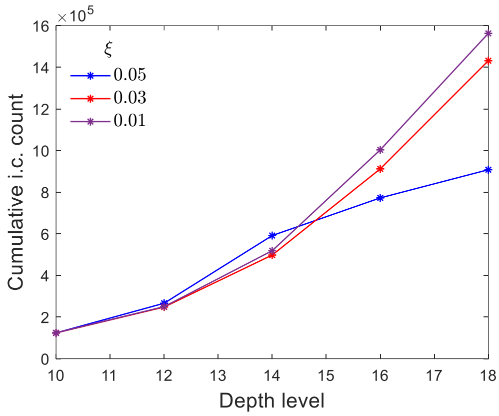

(b)

Figure 6.16 – Evolution of the (a) cumulative box count and (b) cumulative initial conditions count with the critical damping ratio ξ, for A = 17 and Ω = 15

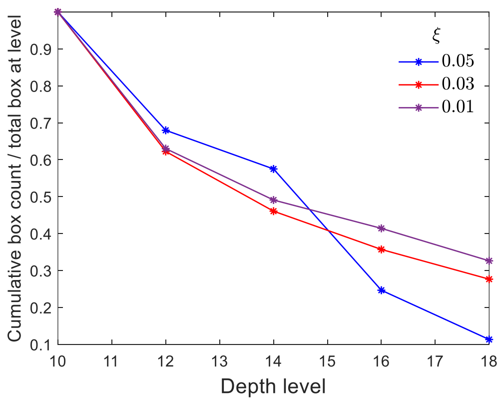

(a)

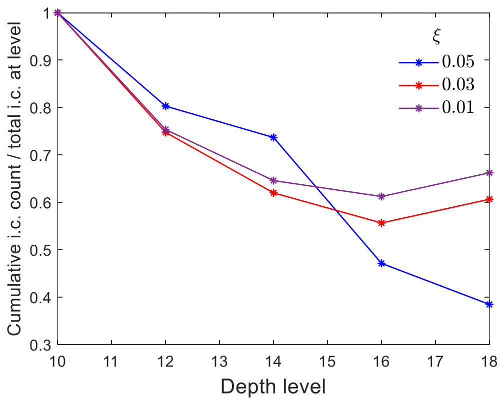

(b)

Figure 6.17 – Ratio between the localized refinement and full discretization of the (a) cumulative box count and (b) cumulative initial conditions count for A = 17V, Ω = 15

6.5.2.
Effects of additive white noise

On one hand, almost all theoretical and most numerical studies of nonlinear dynamics are performed for idealized noise-free systems; on the other hand, in experiments, and real-life noise is ubiquitous. Adding a stochastic excitation $\sigma\dot{W}$ to the second equation of the reduced order model (6.35), results in a stochastic differential system, which is here interpreted as of Itô type. The sampling numerical integration of this system is obtained by a stochastic Runge-Kutta method of fourth order in drift and half order in diffusion, with the same time-step of the deterministic case, $T/2000$. Ten samples for each set of initial conditions are integrated for the construction of the discretized Foias operator F_h in eq. (2.62); see Section 2.5. The number of collocation points for each depth level is shown in Table 6.3. The higher number of collocation points compared to the deterministic case is to better represent the changes in global dynamics due to the stochastic excitation.

Table 6.3 – Discretization data for the stochastic Reduced order model

Depth level	Box-size	Points per dimension	Total collocation points
10	{0.1562, 4.0625}	12	144
12	{0.0781, 2.0312}	10	100
14	{0.0391, 1.0156}	8	64
16	{0.0195, 0.5078}	6	36
18	{0.0098, 0.2539}	4	16

Initially, the effect of noise on the attractors and basins is investigated, and the results are displayed in Figure 6.18, for the nonresonant attractor, and in Figure 6.19, for the resonant attractor. A damping ratio $\xi = 0.03$ is adopted in this section. As Lindner and Hellmann [37] discussed, the generalization of stochastic basins of attraction for noisy dynamical systems, which assigns to each phase-space region a probability of converging to a specific attractor, given a fixed time-horizon, is adopted. In all cases, the time-horizon for the stochastic basin computation in eq. (3.1) is $1/\varepsilon = 1e9$, giving the expected outcome. For $\sigma = 0.5$, a mild diffusion of both attractors is observed, see Figure 6.18(a) and Figure 6.19(a). The basins boundaries maintain the same structure as in the determinist case, but a slight diffusion is already evident, with regions with a probability between 0 and 1 appearing. These regions are here referred to as nondeterministic. Also, the noise results in the spreading of both attractors over the phase-space, with the resonant attractor seemingly more sensitive to it. As noise increases up to $\sigma = 1.4$, these effects increase, the attractors spreading over larger regions of phase-space and basin boundaries becoming more diffused, Figure 6.18(d) and Figure 6.19(d). The distance between the resonant attractor and its basin's boundary decreases considerably, indicating a loss of dynamic integrity for this system. For $\sigma \geq 1.6$, only the nonresonant attractor is observed. The previous resonant basin becomes nondeterministic, being partially absorbed by the nonresonant basin: initial conditions in this region have a probability between 40% and 50% to converge to the nonresonant attractor after 1e9 periods of excitation, and the complementary probability corresponds to escape. The stochastic basin's change for $\sigma \geq 1.6$ is akin to a global bifurcation, drastically changing the outcome for this system.

The nonautonomous character of stochastic dynamical systems suggests that stochastic basins are time dependent. An investigation of the transient behavior is desirable for $\sigma \geq 1.6$, when the resonant attractor disappears. To this end, the transient behavior for $\sigma = 1.6$ is addressed. Increasing values of the time-horizon $1/\varepsilon$ are considered in eq. (3.1), with the initial condition id_f marking the nonresonant and resonant attractor, and escape solution. The results for $\sigma = 1.6$ are summarized in Figure 6.20, for the nonresonant attractor, in Figure 6.21, for the resonant attractor, and in Figure 6.22, for the escape solution. Similar results are obtained for sigma $\sigma = 1.8$ and $\sigma = 2.0$. The first three time-horizons, with $\varepsilon = 0.5$, $\varepsilon = 1e\text{-}1$, and $\varepsilon = 1e\text{-}2$, show the transient stochastic basin spreading in phase space but already with regions of probability lower than one, see Figure 6.20(a, b, c), Figure 6.21(a, b, c), and Figure 6.22(a, b, c). The resonant basin starts to decrease for $\varepsilon \leq 1e\text{-}7$, that is, after 1e7 periods of excitation. This is demonstrated in Figure 6.21(d, e), for $\varepsilon = 1e\text{-}7$ and $\varepsilon = 1e\text{-}8$. For $\varepsilon = 1e\text{-}9$, Figure 6.21(f), the resonant basin completely disappears, with initial conditions in this region either converging to the nonresonant basin or the escape region. These results stress the time dependency of basins in stochastic systems. Due to computational limitations, the system is assumed ergodic for $1/\varepsilon \geq 1e9$, that is, it has converged to the steady-state response after 1e9 periods of excitation.

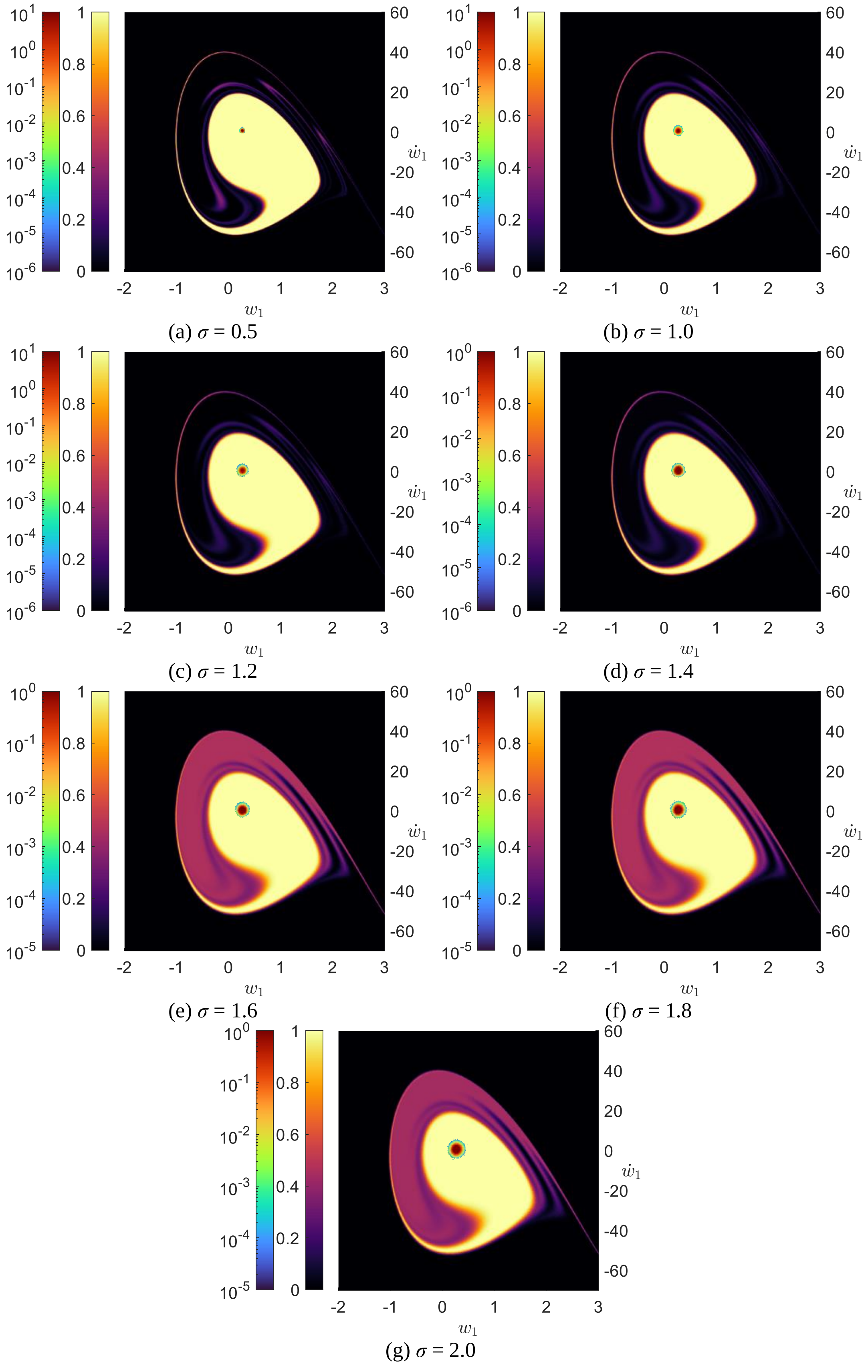

Figure 6.18 – Stochastic nonresonant attractors' distributions (first color bar) and basins' distributions (second color bar) for varying noise intensity. A = 17V, Ω = 15, ξ = 0.03

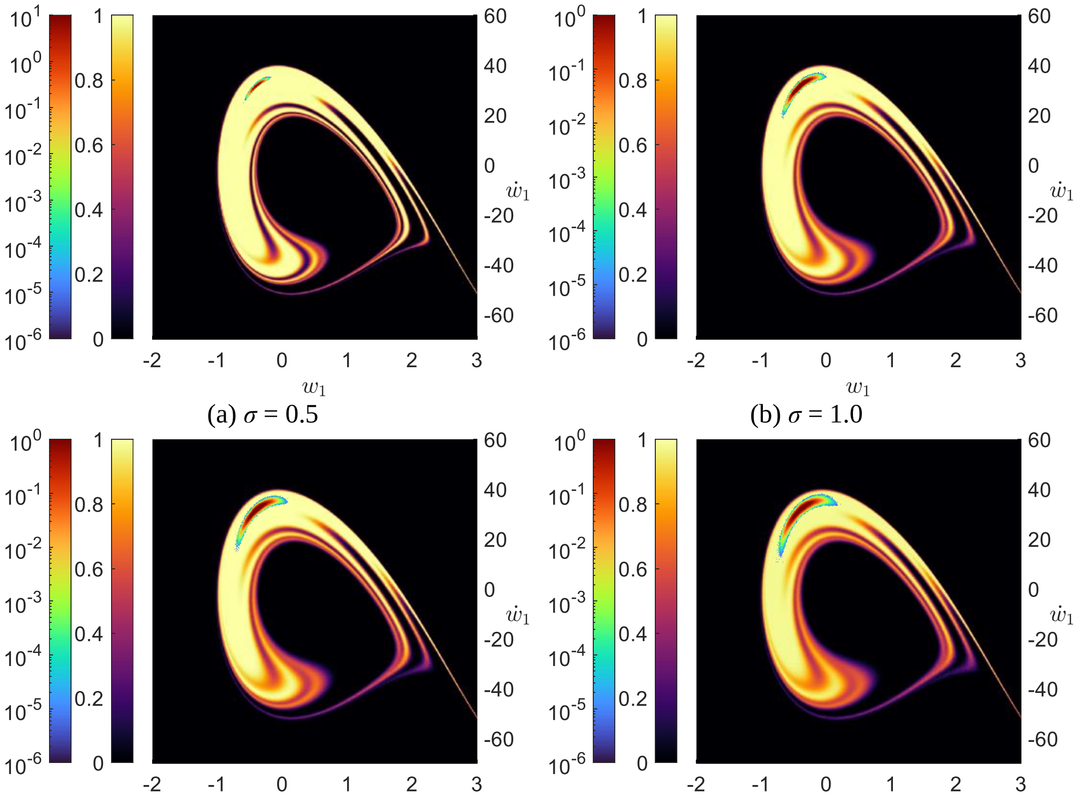

(a) σ = 0.5 (b) σ = 1.0

(c) σ = 1.2 (d) σ = 1.4

Figure 6.19 – Stochastic resonant attractors' distributions (first color bar) and basins' distributions (second color bar) for varying noise intensity. A = 17V, Ω = 15, ξ = 0.03

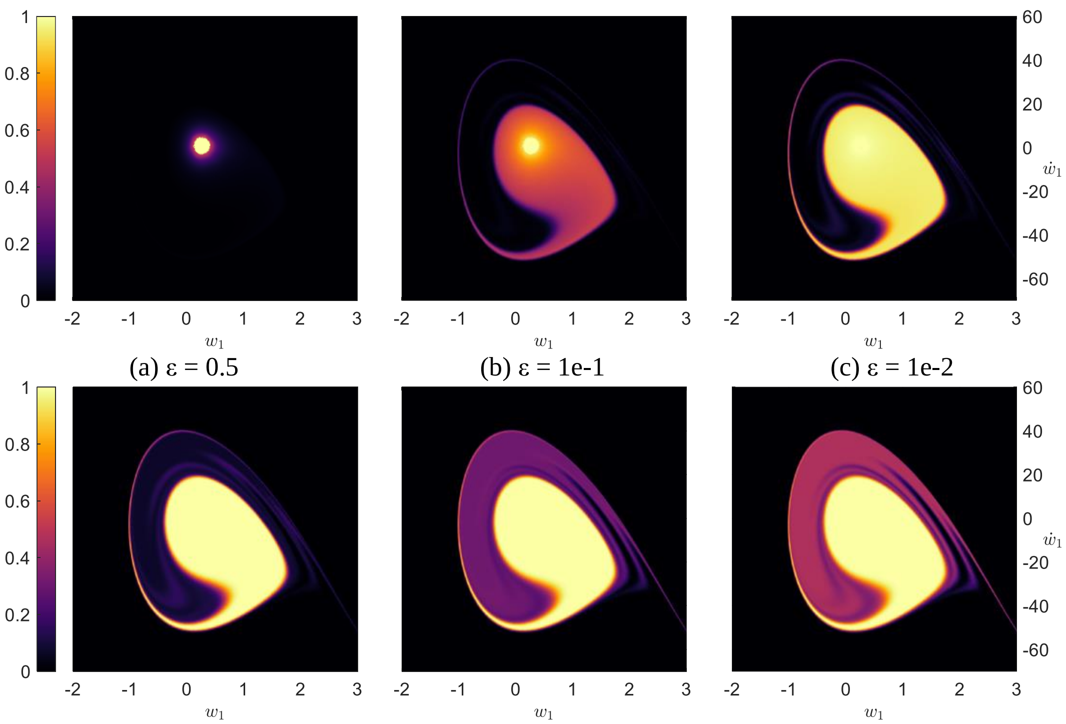

(a) ε = 0.5 (b) ε = 1e-1 (c) ε = 1e-2

(d) ε = 1e-7 (e) ε = 1e-8 (f) ε = 1e-9

Figure 6.20 – Dependency of the nonresonant basin's distributions (color bar) with the time-horizon 1/ε. A = 17V, Ω = 15, ξ = 0.03, σ = 1.6

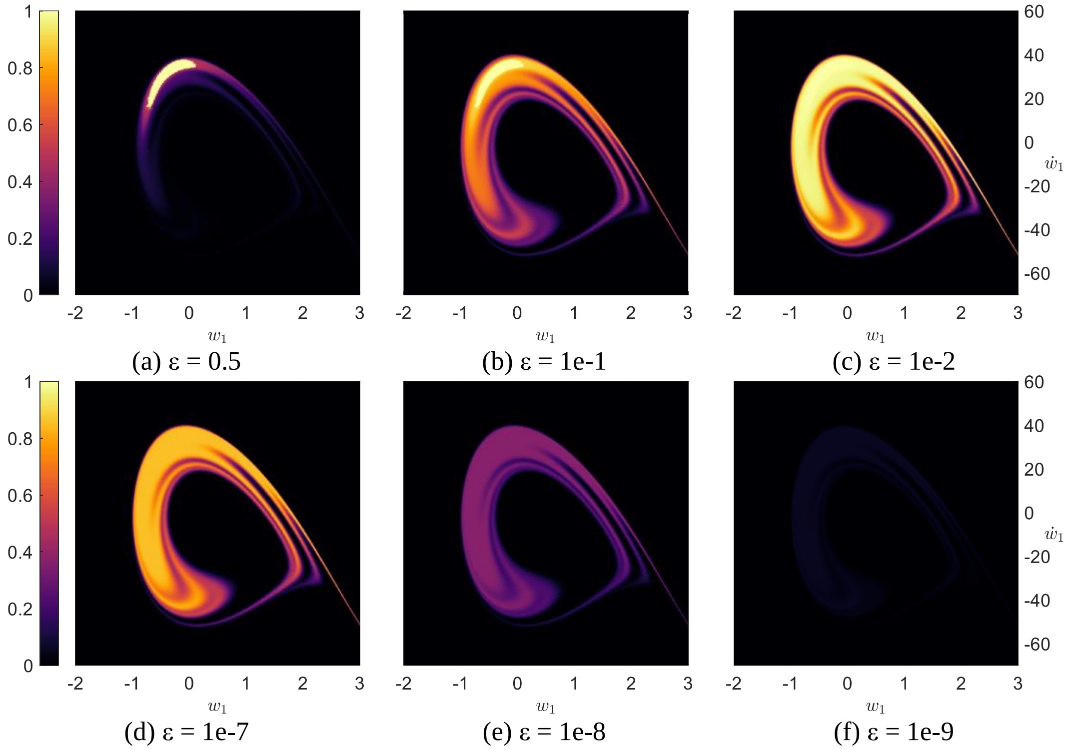

Figure 6.21 – Dependency of the resonant region's distribution (color bar) with the time-horizon 1/ε. A = 17V, Ω = 15, ξ = 0.03, σ = 1.6

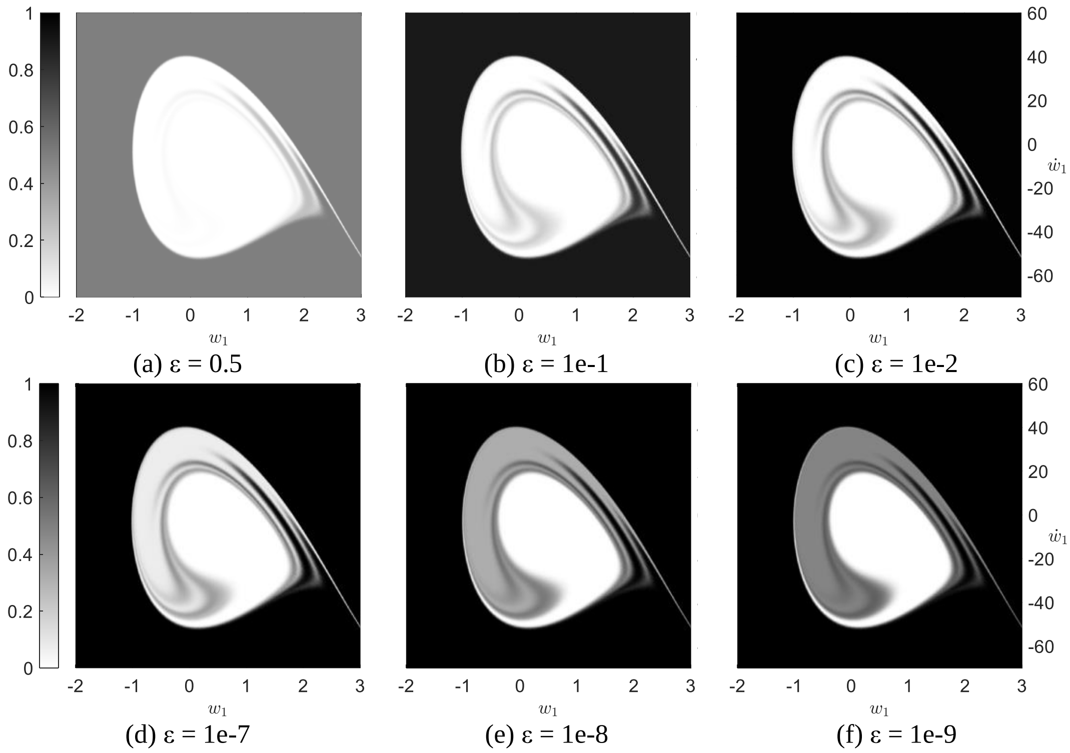

Figure 6.22 – Dependency of the escape region's distributions (color bar) with the time-horizon 1/ε. A = 17V, Ω = 15, ξ = 0.03, σ = 1.6

The integrity measure proposed in eq. (4.2) is now applied to quantify the noise influence on the system's dynamic integrity. Figure 6.23 shows the result for $0 \leq \sigma \leq 2$ and 1/ε = 1e9. The nonresonant attractor dynamic integrity, Figure

6.23(a), corroborates its resilience to noisy perturbations, with its basin area being practically constant for $\sigma < 1.6$. Also, the probability is practically equal to one for all initial conditions. For $\sigma > 1.6$, the integrity measure increases, but the results show a more marked variation of the probability with large regions with $p < 0.5$. However, the basin area with probability $p = 1.0$ remains practically constant. The resonant attractor dynamic integrity measure, Figure 6.23(b), shows a steady decline, with an abrupt Dover cliff integrity loss at $\sigma = 1.6$, as already observed in Figure 6.19. If a conservative p-value is required, for example, $p \geq 0.8$, then the constant decline of the basin area can be viewed as a warning for $\sigma < 1.6$.

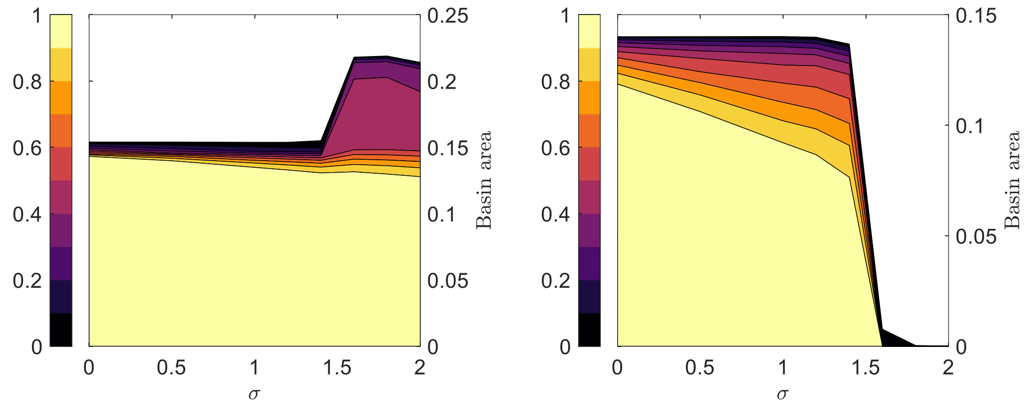

(a) nonresonant (b) resonant

Figure 6.23 – Integrity profile of the weighted basins area as a function of the noise intensity σ for A = 17V, Ω = 15, ξ = 0.03. Color scale corresponds to the probability threshold p. Time-horizon $1/\varepsilon$ = 1e9

Continuing the discussion of the dynamic integrity, its dependency on the adopted time-horizon is illustrated in Figure 6.24, where the variation of the basin area is plotted for increasing values of the time-horizon $1/\varepsilon$ for selected probability thresholds p. Initially, the basin area increases up to a plateau, as expected for short transients, and between 10^2 and 10^6 periods of excitation, the integrity of both attractors remains practically unchanged, however, the resonant attractor shows a significant probability variation, indicating its high sensitivity to noise. The basin area only changes after 10^6 periods of excitation, with the resonant basin vanishing completely after 10^9 periods. Classical methods, which rely on the time integration of each initial condition up to the time-horizon, would be too expensive to represent the permanent state of this system. Therefore, the approximation of the flow structure in phase-space becomes advantageous, considerably diminishing the computational cost.

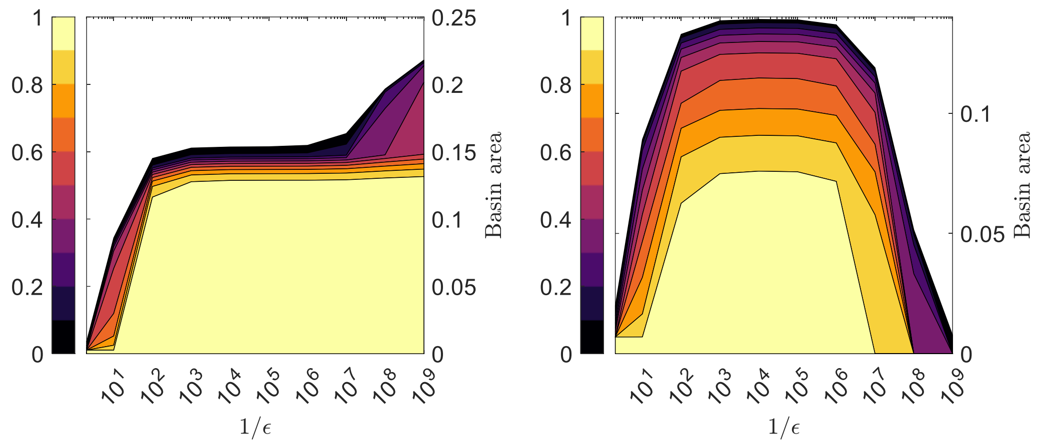

Figure 6.24 – Integrity profile of the weighted basins area as a function of the time-horizon $1/\varepsilon$ for A = 17V, Ω = 15, ξ = 0.03, σ = 1.6. Color scale corresponds to the probability threshold p

The final analysis consists in investigating the noise effects on the stable and unstable manifolds and the flow structures in phase-space. Figure 6.25 and Figure 6.26 show the stable and unstable manifolds for noise levels before and after the stochastic bifurcation, respectively. In addition, Figure 6.27 shows the superposition of the stable and unstable manifolds. These results show that the diffusive nature of the noise also affects the flow structures. Stable and unstable manifolds spread over the phase-space with decreasing densities and increasing intersections. The stable manifold is particularly important, with the tongues observed in the deterministic case (Figure 6.13(b.1)) spreading to the point of not being distinguishable from each other, Figure 6.25(d.1). The results after the stochastic bifurcation, Figure 6.26, depict a drastic change. The stable manifolds, Figure 6.26(a.1, b.1, c.1), coalesce and occupy the whole resonant region. This is in agreement with the transient basins observed in Figure 6.21. Also, the saddle-attractor paths in Figure 6.26(a.2, b.2, c.2) spreads even more. These results suggest that this stochastic bifurcation implies a change of the permanent basin to a transient one due to the stable manifold accretion. These results are important because it allows one to develop a fundamental understanding of this complex phenomenon.

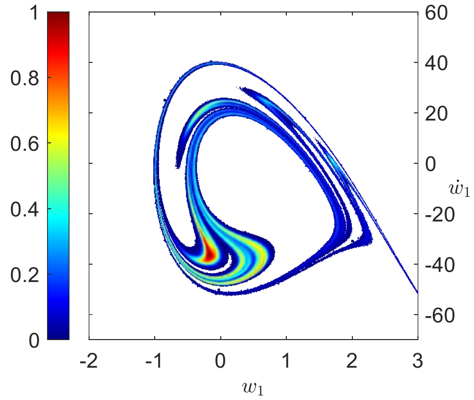

(a.1) σ = 0.5, stable manifold

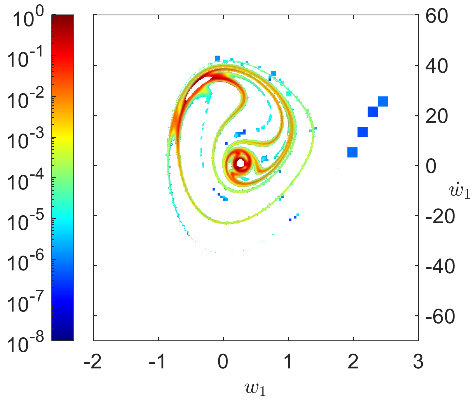

(a.2) σ = 0.5, unstable manifold

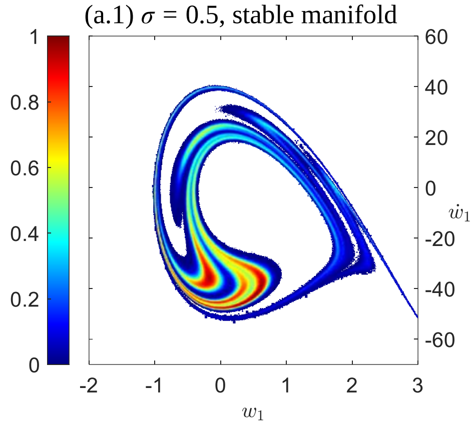

(b.1) σ = 1.0, stable manifold

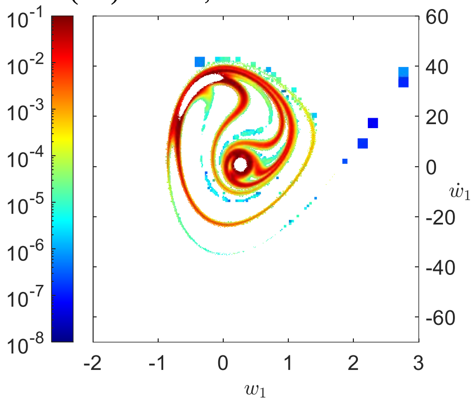

(b.2) σ = 1.0, unstable manifold

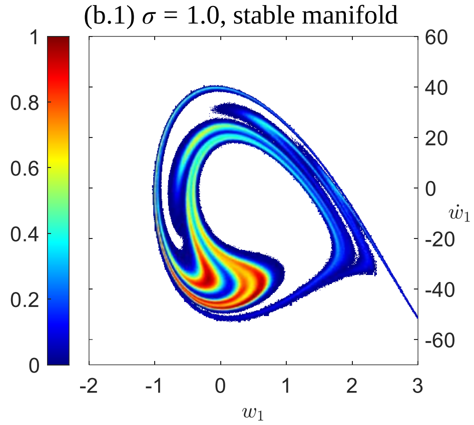

(c.1) σ = 1.2, stable manifold

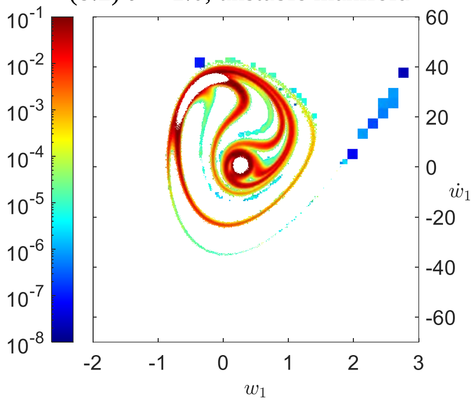

(c.2) σ = 1.2, unstable manifold

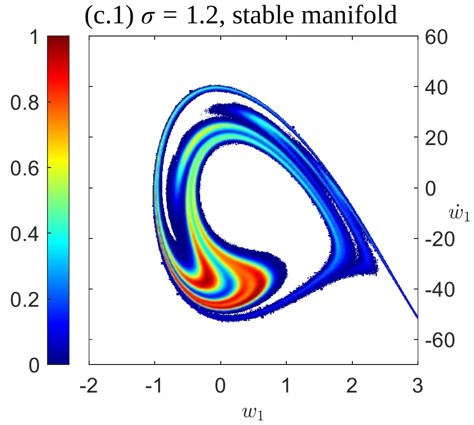

(d.1) σ = 1.4, stable manifold

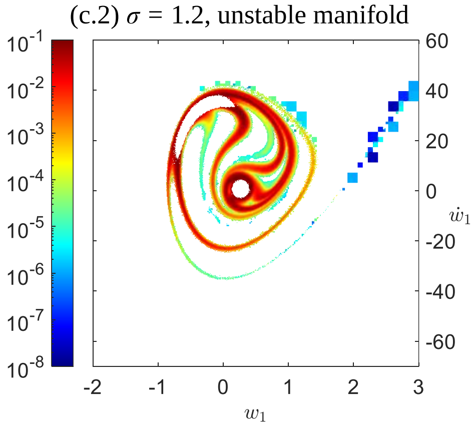

(d.2) σ = 1.4, unstable manifold

Figure 6.25 – Dependency of the stable and unstable manifolds' distributions (color bar) with the noise intensity σ before the stochastic bifurcation. A = 17V, Ω = 15, ξ = 0.03

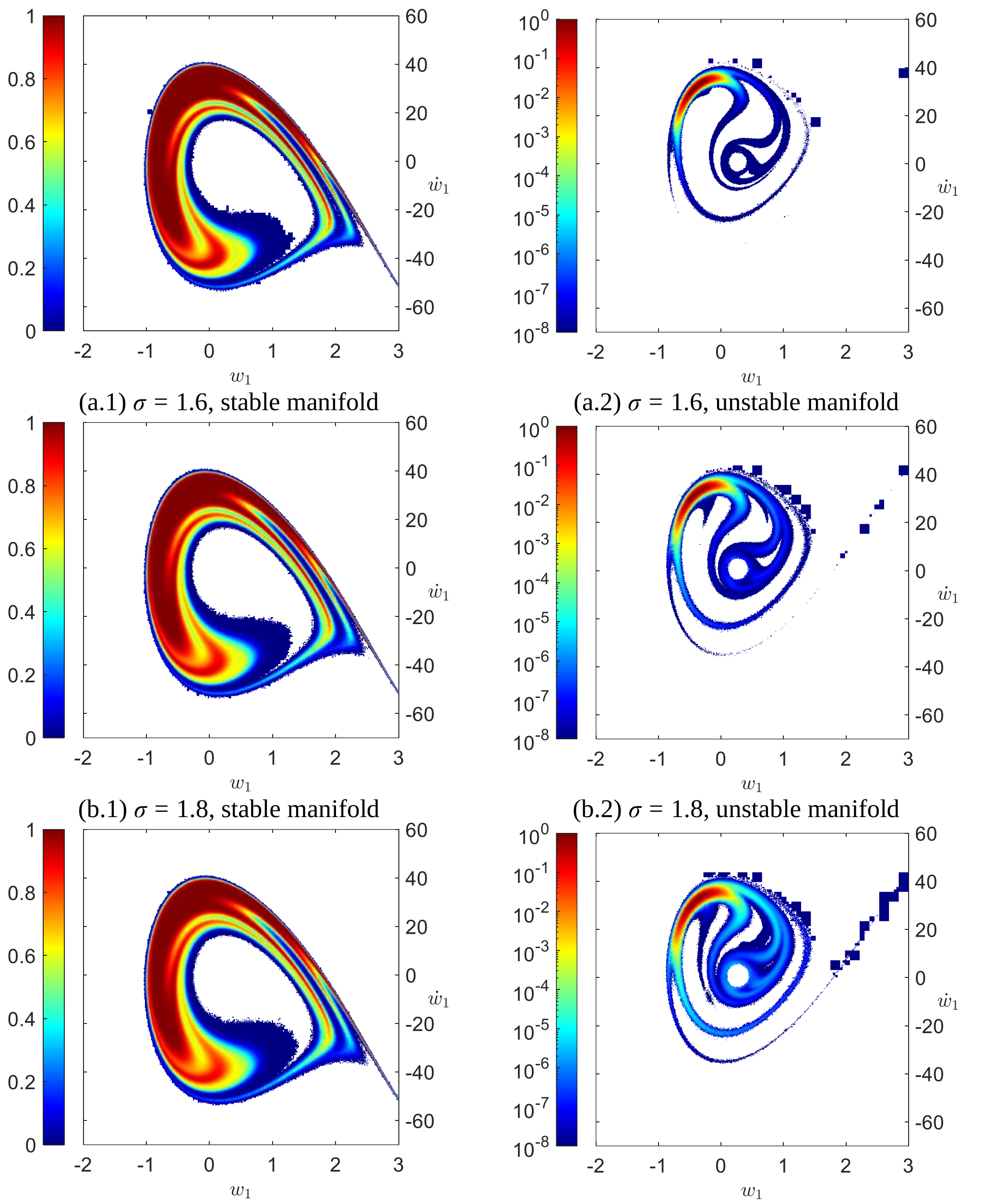

(a.1) σ = 1.6, stable manifold (a.2) σ = 1.6, unstable manifold

(b.1) σ = 1.8, stable manifold (b.2) σ = 1.8, unstable manifold

(c.1) σ = 2.0, stable manifold (c.2) σ = 2.0, unstable manifold

Figure 6.26 – Dependency of the stable and unstable manifolds' distributions (color bar) with the noise intensity σ after the stochastic bifurcation. A = 17V, Ω = 15, ξ = 0.03

The results also illustrate how noise affects the features of the attractors, changing the structure of the unstable and stable manifolds and the homoclinic tangencies (HTs), a topic rarely investigated in the technical literature [204], and that deserves further attention. The trajectory is driven out of the neighborhood of the attractor by noise over a certain number of iterates which causes considerable local deformation of the attractor (formation of "tails").

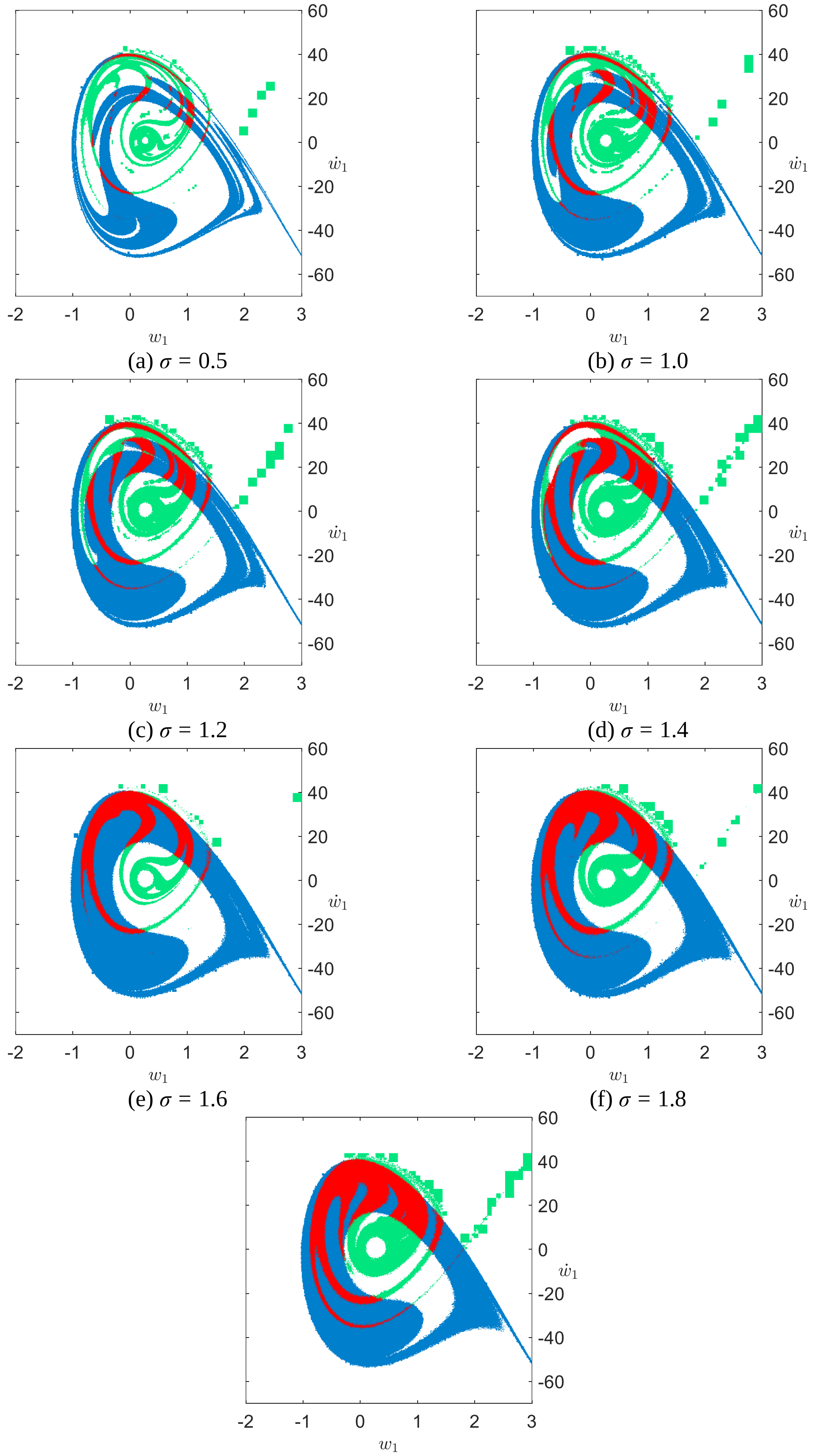

(a) σ = 0.5 (b) σ = 1.0 (c) σ = 1.2 (d) σ = 1.4 (e) σ = 1.6 (f) σ = 1.8 (g) σ = 2.0

Figure 6.27 – Stable (blue), and unstable (green) manifolds superposition (in red) for different noise intensity σ. A = 17V, Ω = 15, ξ = 0.03

A comparison of the cumulative number of integrated initial conditions against a hypothetical complete subdivision at level 18 with 16 initial conditions per box is given in Figure 6.28, for increasing noise magnitude σ. The computational advantage of the proposed algorithm in Table 3.3 is evident, with ratios of 0.7 even for the highest noise amplitude. From the binary – r-tree comparison in Figure 3.2, it is concluded that a binary tree refinement of the phase-space would result in a larger number of integrated initial conditions. Therefore, the r-tree refinement procedure is computationally advantageous and should be considered instead of the binary tree.

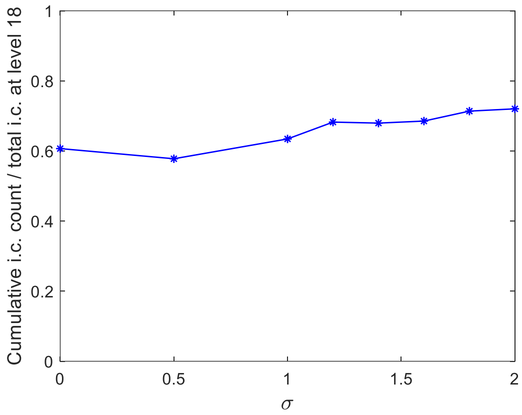

Figure 6.28 – Dependency of the cumulative integrated initial conditions ratio with the noise amplitude σ. A = 17V, Ω = 15, ξ = 0.03

6.5.3. Effects of parametric uncertainty of the critical damping ratio

As shown in the previous sections, damping has a critical influence on the global dynamics of the microarch. However, damping is usually difficult to model or measure since it stems from different sources. Thus, it is important to investigate the influence of damping uncertainty on global dynamics. The variation of the frequency responses in Figure 6.8 to Figure 6.10 demonstrates how the subharmonic oscillations vary with the damping ratio ξ. However, as an estimated parameter, it is usually associated with a distribution, defined as a random parameter of a given probability space. To better understand how this uncertainty affects the global dynamics, the effects of this assumption on the subharmonic global dynamics of the microarch, with $A = 17$V and $\Omega = 15$, is investigated. Here, the modified refinement algorithm, Table 3.3, is applied in conjunction with a probability space discretization, explained in Section 3.2, to obtain mean global structures.

The damping ratio is assumed as uniformly distributed over the real continuous interval $[a, b]$, that is, $\xi \sim \mathrm{U}(a, b)$. The computation of the mean structures is accomplished through the Gauss-Legendre quadrature, a common choice for treating uniform random variables through spectral expansion [172]. Taking ξ_{std} as a standard random variable uniformly distributed over [-1, 1], $\xi_{\text{std}} \sim \mathrm{U}(-1, 1)$, the damping ratio can be defined as

$$\xi\left(\xi_{\text{std}}\right) = \frac{(b-a)}{2}\xi_{\text{std}} + \frac{(b+a)}{2}. \tag{6.38}$$

It is clear that $\xi(-1) = a$ and $\xi(1) = b$. The probability $\mathbb{P}_{\xi}\left[\xi \le X\right]$ is given by

$$\int_a^{X(x)} \xi f\left(\xi\right) d\xi = \frac{1}{2}\int_{-1}^{x} \frac{(b-a)}{2}\xi_{\text{std}} + \frac{(b+a)}{2} d\xi_{\text{std}}, \tag{6.39}$$

where $f(\xi)$ is the probability density of ξ. Differentiating both sides of eq. (6.39) with respect to x and applying eq. (6.38) by taking $\xi = X$ and $\xi_{\text{std}} = x$, one obtains

$$f\left(\xi\right) = \begin{cases} \dfrac{1}{b-a} & \forall \xi \in [a,b], \\ 0 & \forall \xi \notin [a,b]. \end{cases} \tag{6.40}$$

Therefore, the damping ration $\xi \sim \mathrm{U}(a, b)$ can be represented by eq. (6.38). This allows the Gauss-Legendre quadrature in [172] to be applied for ξ_{std} and the original ξ is obtained through eq. (6.38). In the following application, ten collocation points are adopted, discretizing the probability space into 10 points.

Four cases are considered adopting a = 0.04, 0.03, 0.02, 0.01, and b = 0.05. The interval $[a, b]$ = [0.04, 0.05] represents a low uncertainty case, and the interval $[a, b]$ = [0.01, 0.05] represents a high uncertainty case. Figure 6.29 shows the mean basins and attractor's distributions for the four cases, showing how these structures change as uncertainty increases. In the first case with $\xi \sim \mathrm{U}(0.04,0.05)$, Figure 6.29(a), the effect of uncertainty is already evident in the mean basins, diffusing their boundaries. That is, regions with probabilities different from 0 and

1 to converge to either attractor start to appear. Again, these regions are referred to as nondeterministic. The uncertainty already affects the resonant attractor, with its mean distribution forming a curve in the phase-space. The nonresonant attractor, however, stays localized. This pattern is observed for all uncertainty cases, with the resonant attractor mean distribution spreading over a curve in phase-space as uncertainty increases. Also, the nonresonant mean basin diffusion depicts increasing regions with probability lower than one. In the last case, Figure 6.29(d), large nondeterministic regions are observed for both attractors, and the deterministic region of the resonant attractor is confined to a small area in phase-space. This suggests that the resonant attractor is sensitive to uncertainty in the damping ratio.

Figure 6.30 shows how the escape region is affected by the uncertainty in the damping ratio. As the uncertainty increases, nondeterministic escape zones inside the original deterministic basins of attraction regions appear. The last case, Figure 6.30(d), demonstrates how large uncertainties deteriorate the classical basin of attraction, with large nondeterministic regions. Finally, the results are time-independent since the parametric uncertainty of ξ does not depend on time. Therefore, there is no influence of time-horizons on the stochastic basins. Classical global analysis methods, such as the Grid of starts, could be considered with low time-horizons, with the uncertainty addressed, for example, through a Monte-Carlo method. However, this would still be computationally expensive since such a method demand that initial conditions are integrated until the time-horizon is reached, whereas the Ulam method/Generalized cell-mapping approximates the phase-space flow through only one period of integration for each set of initial conditions.

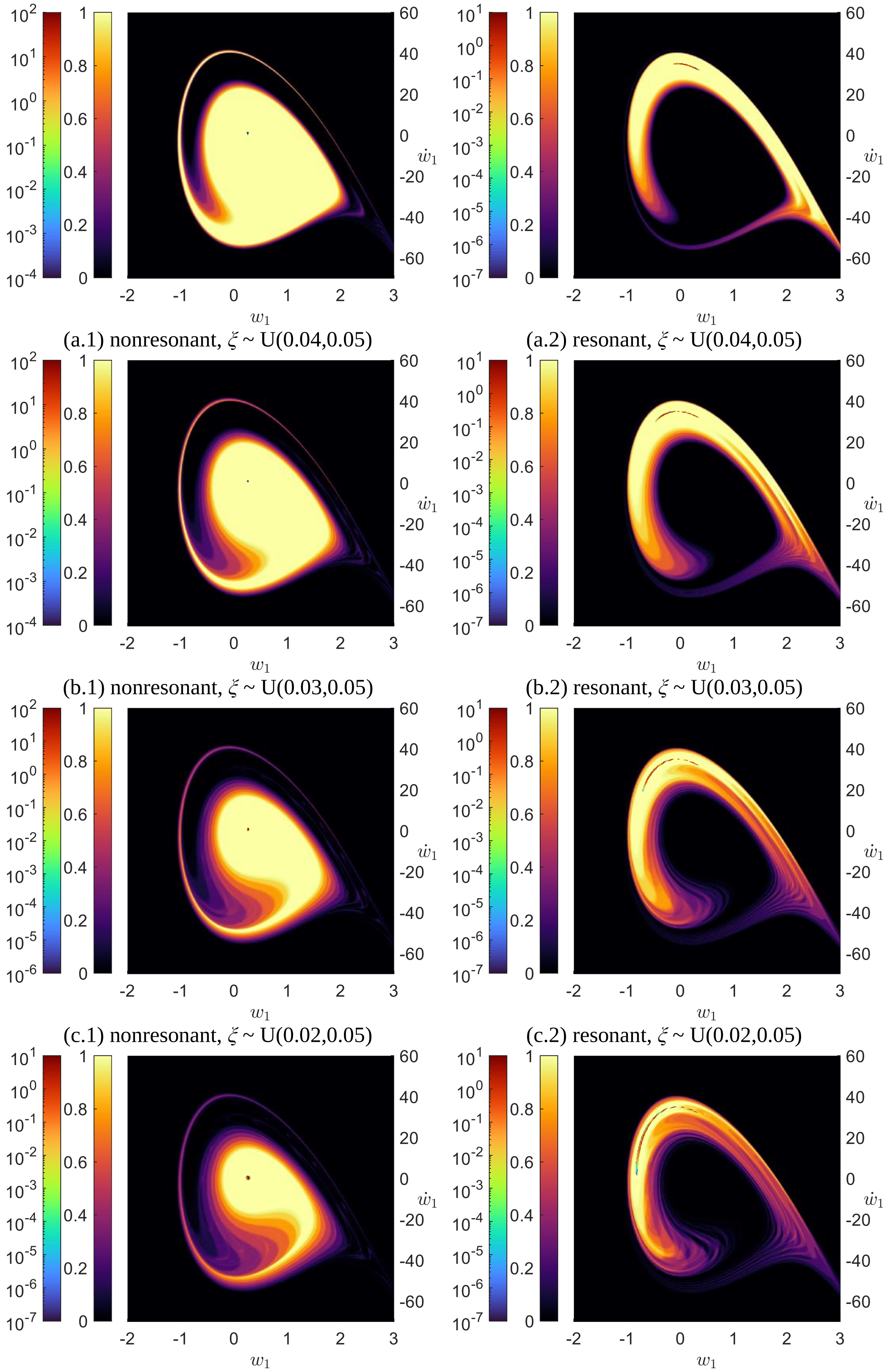

(a.1) nonresonant, ξ ~ U(0.04,0.05) (a.2) resonant, ξ ~ U(0.04,0.05)

(b.1) nonresonant, ξ ~ U(0.03,0.05) (b.2) resonant, ξ ~ U(0.03,0.05)

(c.1) nonresonant, ξ ~ U(0.02,0.05) (c.2) resonant, ξ ~ U(0.02,0.05)

(d.1) nonresonant, ξ ~ U(0.01,0.05) (d.2) resonant, ξ ~ U(0.01,0.05)

Figure 6.29 – Mean attractors' distributions (first color bar) and mean basins' distributions (second color bar) for varying damping ratio ξ distributions. A = 17V, Ω = 15

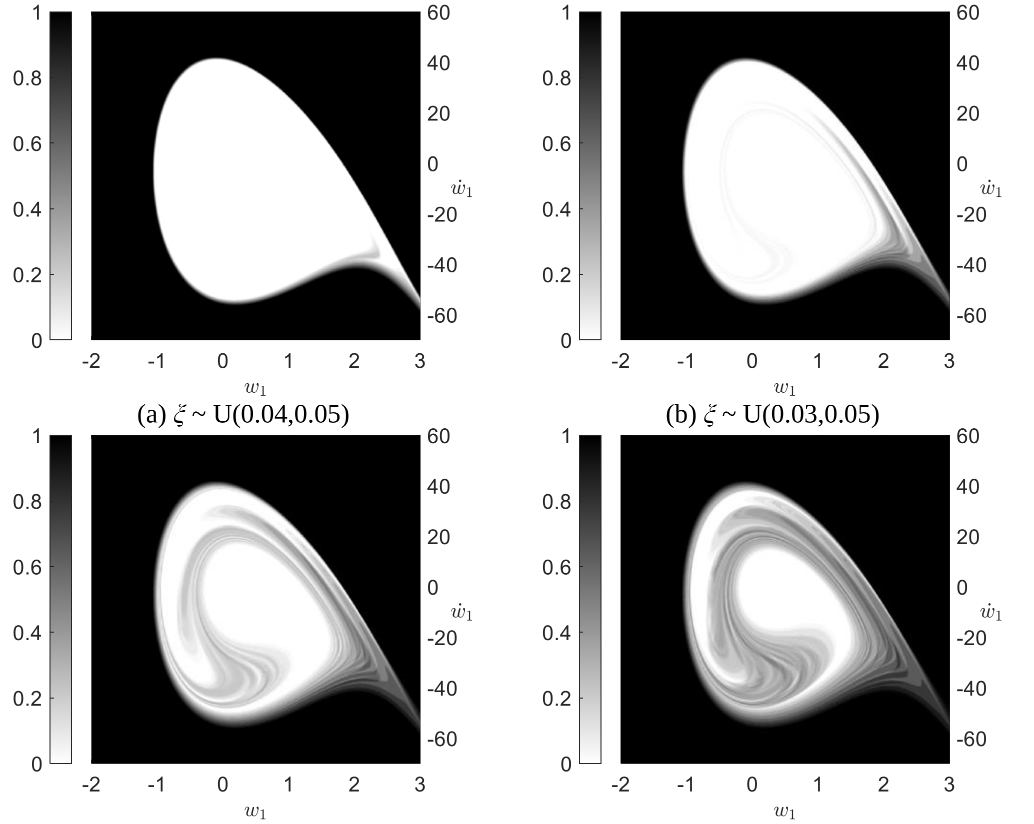

(a) ξ ~ U(0.04,0.05) (b) ξ ~ U(0.03,0.05)

(c) ξ ~ U(0.02,0.05) (d) ξ ~ U(0.01,0.05)

Figure 6.30 – Escape regions' distributions (color bar) for varying damping ratio ξ distributions. A = 17V, Ω = 15

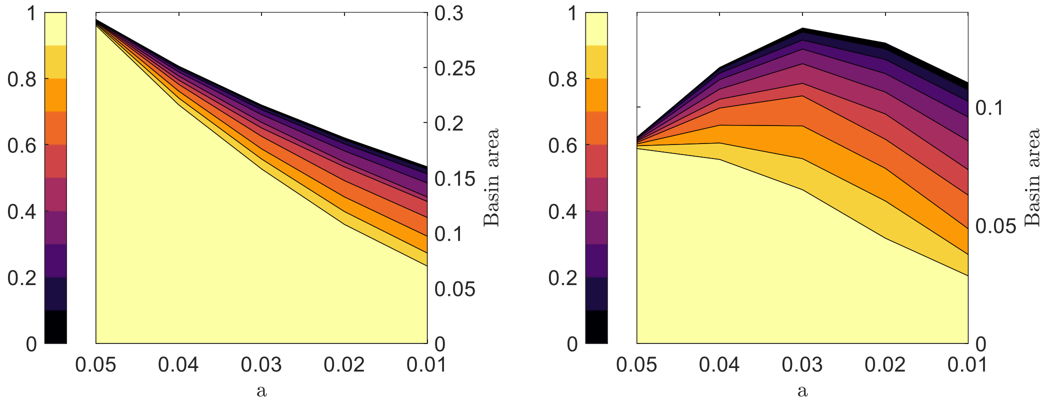

(a) nonresonant (b) resonant

Figure 6.31 – Integrity profile of the weighted basins area as a function of the lower parameter uncertainty boundary a for A = 17V, Ω = 15.
Color scale corresponds to the probability threshold p

Figure 6.31 displays the dynamic integrity profiles proposed in eq. (4.2) for the analyzed uncertainty cases as functions of the lower parameter boundary a. The first case, a = 0.05, corresponds to the deterministic result with ξ = 0.05. The nonresonant attractor shows a steady integrity decrease for all probability thresholds p. Surprisingly, the resonant basin shows an initial increase and inflection point p > 0.8, before decreasing with a, showing that the system can gain or lose integrity for mild uncertainty cases, depending on the adopted probability threshold *p*.

The effects of parametric uncertainty on the stable and unstable manifolds are depicted in Figure 6.32. The manifolds interactions and rate of mixing are illustrated in Figure 6.33. The mean structures diffuse over the phase-space as uncertainty increases, increasing the complexity of the flow structures in phase-space. For the lower uncertainty case, Figure 6.32(a) and Figure 6.33(a), the unstable manifold remains simple. However, the stable manifold is already diffused over a large region. There is already a diffusion of the saddle shown by the red crossing in Figure 6.33 (a). This reflects the basins topology in Figure 6.29(a), with large nondeterministic regions. The unstable manifolds, Figure 6.32(a.2, b.2, c.2, d.2), show regions of high probability, corresponding to the attractors' densities support observed in Figure 6.29, with the support of the nonresonant attractor localized in a small region, while the support of the resonant attractor spreads along a curve. The stable manifolds, Figure 6.32(a.1, b.1, c.1, d.1), display an increasingly complex structure as uncertainty increases, with increasing regions of intercession, as observed in Figure 6.33(d), which explains the erosion process quantified in Figure 6.31. However, the adopted probability space discretization must be taken into account, since the phase-space structures for each ξ-value are highly localized, and the probability space discretization through *n* collocation points may artificially insert discontinuities into the mean structures, needing for their correct display a larger value of *n*. This effect is known in the uncertainty quantification literature, motivating the development of adaptative discretization techniques of the probability space [172].

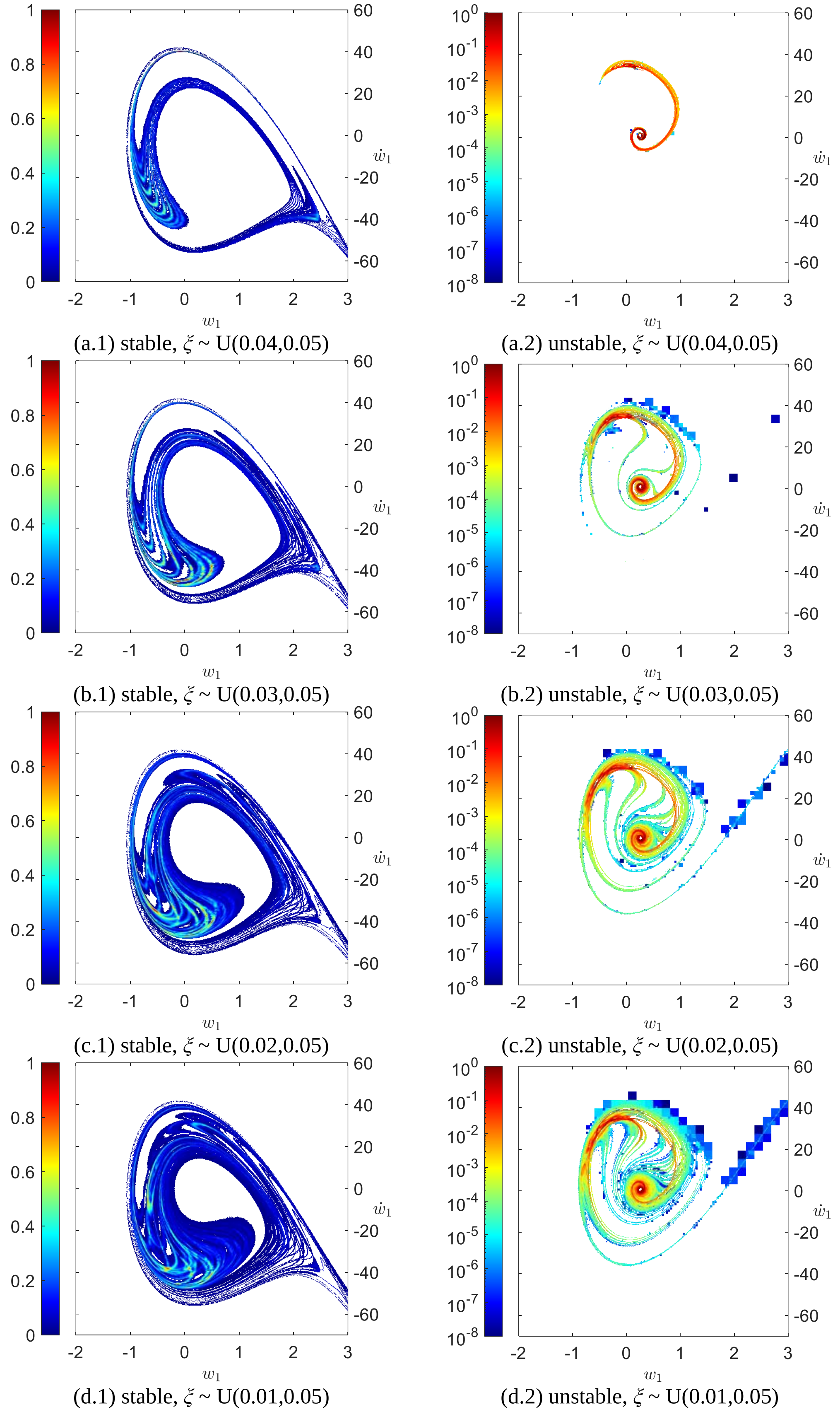

Figure 6.32 – Dependency of the stable and unstable manifolds' distributions (color bar) with the damping ratio ξ distributions. A = 17V, Ω = 15

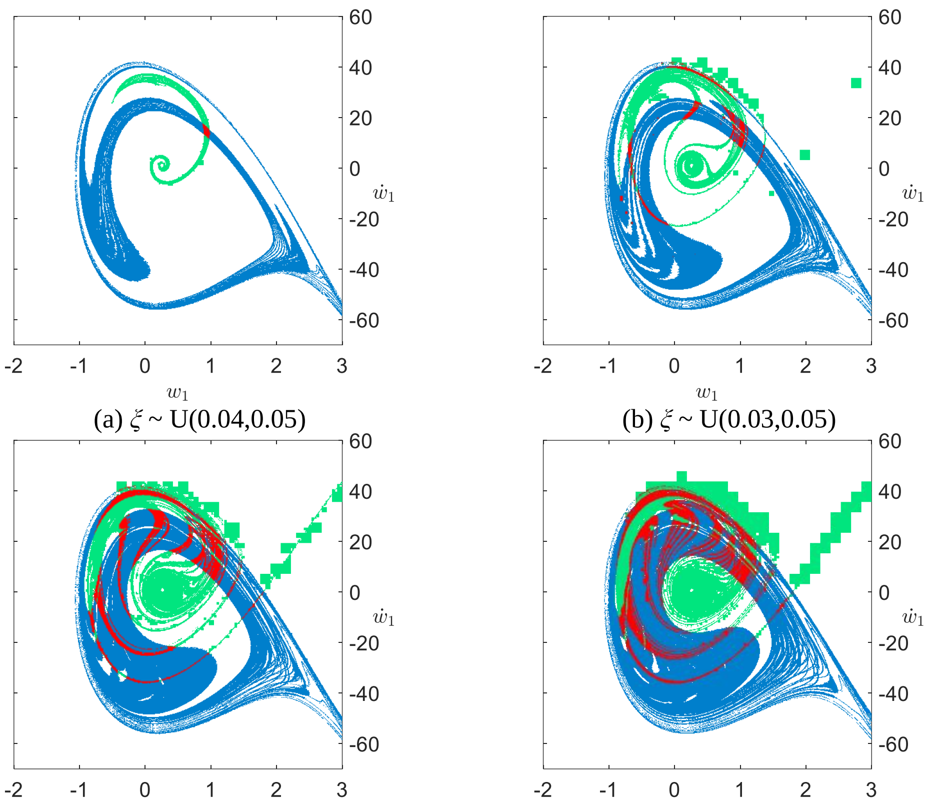

(a) ξ ~ U(0.04,0.05) (b) ξ ~ U(0.03,0.05)

(c) ξ ~ U(0.02,0.05) (d) ξ ~ U(0.01,0.05)

Figure 6.33 – Stable (blue), and unstable (green) manifolds superposition (in red) for different damping ratio distributions ξ. A = 17V, Ω = 15

A comparison of the cumulative number of integrated initial conditions against a hypothetical complete subdivision at level 18 with 16 initial conditions per box is given in Figure 6.34, for selected uncertainty boundaries, a. Again, the computational advantage of the proposed algorithm, Table 3.3, is evident, with ratios lower than 0.4, even for the highest uncertainty case analyzed.

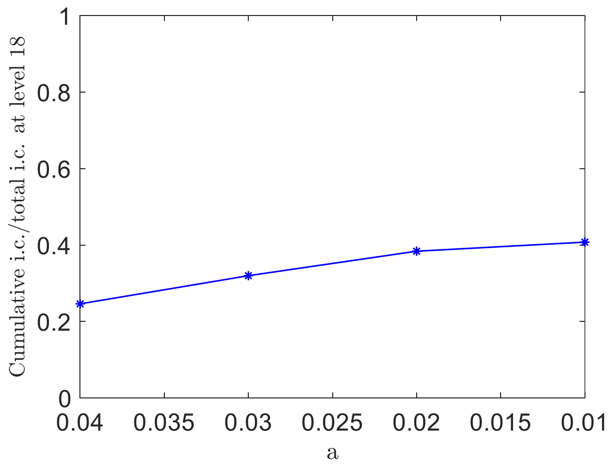

Figure 6.34 – Dependency of the cumulative integrated initial conditions ratio with the lower uncertainty boundary a. A = 17V, Ω = 15

7
Conclusions

Uncertainties in engineering systems are unavoidable and can drastically change their behavior. Also, noise is inevitable in the operational stages. The computational cost of both global dynamic and nondeterministic analysis makes it difficult to consider these phenomena simultaneously in a complex system. Trying to address these limitations, adaptative phase-space discretization strategies for the global analysis of nonlinear dynamical systems with competing attractors were proposed. These strategies made it possible to observe the influence of uncertainty on basins of attraction, attractors, and manifolds, and enable the quantification of dynamic integrity measures, as illustrated by the examples. Here, the contributions are highlighted, subdivided into two main aspects: the main formal and numerical contributions, resulting in the development of the proposed algorithms, and the phenomenological observations based on the selected applications, covering different bifurcation scenarios. Finally, a list of suggestions following the present research is given.

7.1.
Main formal and numerical contributions

Initially, the definitions of attractors and basins with nondeterministic effects were discussed. In the usual pushforward sense, attractors are regions in phase-space to which a set of initial conditions converge as time goes to infinity. However, this definition cannot be adopted when uncertainty is considered, with attractors being randomly distributed in phase-space. The solution was to consider not the attractors but their distributions in phase-space. Another feature of interest is the basin of attraction, defined as the set of all initial conditions in the phase space that converge asymptotically to a given attractor. The classical basin definition must also be modified when uncertainty is considered, being, in this case, random sets distributed according to a random parameter. Therefore, another definition, named stochastic basin of attraction, was adopted here. It consists of a probability map assigned to the entire phase-space, indicating the probability of a set of initial conditions converging to a given attractor. These two definitions, that is, attractor's distribution and stochastic basin of attraction, are dual through the transfer operators, a crucial property in the development of this thesis. Furthermore, they converge to the classical definition when the underlying dynamics are deterministic.

The Ulam method, a classical discretization method of flows in phase-space, was adopted in the present work. This method was described and extended here to nondeterministic cases, and, finally, a unified description was formulated based on the Perron-Frobenius, Koopman, and Foias linear operators. The many applications in the literature of the Ulam method to stochastic dynamical systems suggest that it is the most natural discretization method within the uncertainty framework.

Specifically, the Foias transfer operator governs the flow in the mean sense, allowing the application of the Ulam method to stochastic dynamical systems. The case with parameter uncertainty is more complicated to analyze. The phase-space of such cases was here augmented to accommodate the uncertain parameter space, which was also discretized. This allowed the computation of statistics of the global structures.

However, the phase-space discretization leads to numerical diffusion. The usual procedure in literature is to increase the resolution (discretization of phase-space), which increases the computational cost dramatically. Since there are regions in phase-space where the flow is unimportant, two adaptative phase-space discretization strategies to refine relevant regions, such as basins' boundaries, attractors' distributions, and manifolds, were proposed. Each strategy can be summarized in three main steps: identification, refinement, and calculation. The first strategy uses a heuristic basin boundary definition, whereas the second one considers the stable manifold of the saddles lying along the basin boundaries. Both strategies are capable of mitigating numerical diffusion in the analyzed cases, maintaining a low computational cost. Finally, binary and r-tree structures were used to organize the phase-space, with the r-tree structure leading to smaller computational costs within the refinement strategy.

The question of how to measure the dynamic integrity of nondeterministic systems was also addressed. A new integrity measure, based on previous definitions and on the classical global integrity measure, was proposed. It quantifies the global area of the basin of attraction for selected probability thresholds, thus providing the designer with information on the degree of safety of a given dynamical system.

7.2. Phenomenological observations

The developed numerical strategies were then applied to two widely used archetypal nonlinear oscillators, the Helmholtz and the Duffing oscillators, and to two microelectromechanical systems. The effects of uncertain parameters and noise on systems with coexisting solutions, nonlinear resonance, multiple potential wells, and escape to infinity, among others, were investigated. The proposed strategies mitigated the numerical diffusion, highlighting the real diffusion.

7.2.1. Helmholtz and the Duffing oscillators

The deterministic Helmholtz oscillator displayed three possible outcomes: a nonresonant attractor, a resonant attractor, and escape solutions. The adaptative discretization procedure obtained the attractors and the boundaries of the basins with high fidelity, even when the basin boundary becomes fractal and highly convoluted. It was demonstrated that the subdivision strategy could mitigate numerical diffusion, a common hindrance inherent to many phase-space discretization procedures found in the literature. A comparison with the initially refined discretization showed that the economy achieved by the proposed procedure could be as high as 90% for highly refined levels. Next, the Helmholtz oscillator with a random stiffness parameter was considered, with the uncertainty parameter defined as a truncated normal variable to prevent large spurious values. Mean basins and densities were obtained for varying uncertainty intensity, being the attractors' densities described by one-dimensional structures in the phase-space. As the uncertainty increases, broader regions along the basins' boundaries needed to be refined. Here, the economy of the proposed methodology was verified through a box count procedure. The results quantified the decrease of the safe basin area of both attractors, particularly the resonant one, with increasing uncertainty. For high uncertainty values, no set of initial conditions had a 100% probability of converging to the resonant attractor. The results were validated by a Monte Carlo analysis, demonstrating the efficiency of the proposed methodology. Increasing noisy excitation led to an increasing diffusion of the attractors, affecting particularly the resonant attractor which approaches the basin boundary. This led to a global bifurcation due to a connection between the resonant attractor and the saddle. After this bifurcation, the resonant basin vanished, and solutions either converged to the nonresonant attractor or escaped. The detailed analysis of the global bifurcation showed that formerly resonant solutions become long transients after a critical noise intensity. Long transient solutions were detected by the almost invariant eigenmeasures, identifying regions where solutions stayed for a long time with basins of attraction varying with the adopted final time horizon. The dependence of the basin on the time horizon identified here is important information for the integrity analysis, vibration control, and other applications where the transient response becomes important.

Next, the Duffing oscillator under harmonic excitation with added noise and uncertainties was investigated considering two sets of parameters: one leading to two potential wells with resonant and non-resonant attractors within each well, other leading to one periodic attractor coexisting with a chaotic attractor. The box count comparison showed that the base and the last discretization levels must be increased to obtain a significant computational economy as the number of coexisting attractors and, consequently, the basin competition increases. Therefore, deeper levels must be considered to attain a significant economy when compared to the full discretization of the phase-space. Regarding the effect of a random linear stiffness, addressed by considering the first parameter set, the nonresonant solutions were more sensitive to uncertainty, losing stability in the mean sense for larger uncertainty values, as corroborated by the erosion of the corresponding basin areas with the uncertainty level. However, all basins' areas with probability equal to one decreased steadily with the uncertainty, with large regions of phase-space showing high sensitivity, which should be considered in a dynamic integrity analysis. The effect of added noise excitation was investigated for the second parameter set. The adaptative discretization was able to refine both the chaotic attractor and its basin boundary. The proximity of the chaotic attractor to the basin boundary led to an attractor-saddle connection, which occurs even for low noise levels. The chaotic attractor became a long transient solution, with the basin of attraction being dependent on the time-horizon for large noise levels. Monte Carlo analysis also confirmed the result. The basin area followed the same pattern, indicating the stability loss of the chaotic attractor with noise. The attained economy depends on the noise level and, consequently, on the flow's diffusion level.

Finally, the parametrically excited Duffing oscillator with added noise was investigated. This allowed the analysis of a different scenario where a period-2 attractor and escape coexist, with increasing competition observed as the excitation amplitude increased. The cyclic component of the attractor lost stability as noise increased, with the attractor behaving almost cyclically. Again, depending on the noise level, the attractor can lose stability, behaving as a long transient solution, with the obtained basin depending on the adopted time-horizon. Time-history and spectrum analysis for varying noise confirmed these conclusions.

7.2.2. Microelectromechanical Systems

A growing interest in the mechanical behavior of Microelectromechanical Systems or MEMS in various engineering fields has been observed in recent decades. With the numerical procedure validated through the analysis of the two archetypal oscillators, the global dynamic analysis of two engineering problems, a microcantilever and a microarch, both electrically actuated, was conducted. In both cases, the equations of motion were derived based on a three-dimensional imperfect Rayleigh beam formulation.

The static nonlinear response of the microcantilever under DC voltage displayed two limit points, delimiting the unstable branch of solutions that separates the two stable branches, leading to a multistability range and hysteresis. If the imperfection magnitude is added as a second control parameter, the obtained surface exhibit the typical cusp geometry, where one stable solution may suddenly jump to an alternate outcome due to the existence of competing solutions. The prevailing solution was highly dependent on imperfection and noise levels. The pull-in instability was present in most cases, being the pull-in voltage sensitive to the imperfection level and sign. When the imperfection decreases the gap between the beam and the actuator plate, the pull-in voltage reduces, and the system becomes more susceptible to this type of instability. On the other hand, the pull-in load increases when the gap increases, and no static pull-in was observed after a certain threshold value. Also, the lowest natural frequency was significantly affected by the simultaneous effect of the DC voltage and geometric imperfection, becoming zero at the limit points in the region of the cusp catastrophe, where it showed two distinct vibration frequencies. The resonance curves of the imperfect microbeam under AC actuation exhibited a softening response since the load nonlinearity (which was of the softening type) was stronger than the geometric nonlinearities (which was of the hardening type) for small values of the initial gap. In these resonant regions, the coexistence of a stable non-resonant and a resonant branch was observed bending toward lower frequencies regions. As the forcing magnitude increased, it increased the multistability range. Also, a pull-in bandwidth developed, thus making the system more susceptible to dynamic instability. The imperfection decreased the values at which the pull-in band is formed. Therefore, higher imperfections increase the vulnerability of the microbeam to dynamic pull-in instability. In all cases, the resonant peak at a forcing frequency equal to half the natural frequency exhibited a softening behavior too, and led in some cases to pull-in bandwidth. As the imperfection level increased, the resonant peak at a third of the natural frequency also increased, leading to an additional resonance region that may influence the microbeam dynamic response.

The initial classical global dynamic analysis, without phase-space refinement, revealed that the erosion of the basins of attraction depends not only on the amplitude and frequency of the AC voltage but also on the imperfection level and the noise magnitude. As the noise level increased, the probability along the basin boundaries diffused, dramatically increasing the microbeam sensitivity to initial conditions. The influence of noise on the time response of competing attractors may lead to complex responses with successive jumps between the competing attractors. Both examples showed that attractors could disappear or merge depending on the noise level, significantly influencing the microbeam nonlinear dynamics, and the threshold value of the intensity for noise generating a transition from coexistence to extinction was estimated. Finally, these results were compared to the proposed refinement algorithm, showing that the results without refinement missed the transient characteristic of some basins. Furthermore, the refinement algorithm could separate the basins even for large noise levels, which showed that the loss of integrity occurs at lower noise levels compared to the classical analysis.

The microarch was the last analyzed model. It was taken as a clamped-clamped structure, with an initial stress-free curvature and imposed axial displacement. The axial displacement was condensed, and a flexural beam model was derived. Its static response under DC actuation displayed two limit points which delimited the unstable solutions branch and led to a multistability range and hysteresis. It was shown that two symmetric linear modes are the minimum necessary for qualitative analysis.

A reduced order model, based on the first two symmetric linear modes, was derived for the dynamics in the vicinity of a given static position, following the definition of nonlinear normal modes of Shaw and Pierre [202]. The free vibration response and the frequency response under AC actuation demonstrated the validity of the proposed model when compared against the classical 2-mode discretization. A main subharmonic resonant region was identified, with the main resonant region being excited only for low damping ratios. A pull-in band developed for increasing AC voltage at the subharmonic frequency. In all cases, a softening response was obtained due to the initial beam curvature and load.

The global dynamics in the subharmonic region were studied with the proposed refinement procedure. The manifolds were also obtained, and an r-tree phase-space structure was adopted in this analysis. A potential well with nonresonant and resonant solutions was observed, and the impact of different damping ratios and added noise was investigated. The basins and manifolds of the deterministic case demonstrated a convoluted partition of the phase-space for low damping ratios. Then, a low damping ratio case was investigated under noise, and the transient characteristic of the solutions was again observed. This was evidenced in the integrity profiles, which showed a Dover cliff when the noise amplitude varied and also a dependency on the adopted time-horizon. The manifolds under noise showed that, in the case of a long-transient solution, its basin merges with the stable manifold due to the diffusion effect. Finally, the uncertainty of the critical damping ratio was investigated, where a uniform distribution was adopted. The spread of the attractors along the bifurcation path as the interval increases was observed, again a distinct result in comparison to noisy cases. Their basins also spread over the phase-space. The integrity profile revealed the gradual integrity loss of both solutions. Finally, the manifold analysis demonstrated how they spread over the phase-space due to parameter uncertainty.

This work presented an alternative for the classical phase-space discretization, applying it to different dynamical systems under various bifurcation scenarios. In summary, the examples demonstrated the efficiency of the developed algorithms, based on the concept of operators, in the global analysis of dynamical systems. The relevant contributions enable the analysis, control, and design of systems at different scales, in a multiphysics context, considering unavoidable imperfections, uncertainties and noise. The thesis also highlights the role played by global analysis in unveiling the nonlinear response and actual safety of engineering systems in different environments and shows that the nondeterministic effects should be considered in global dynamics analyses.

7.2.3. Evaluation of Uncertainty Effects

Based on the summarized results described in the previous subsections, the following phenomena are observed:

For the stochastic cases, the influence of noise on the attractor's diffusion is more prominent than the diffusion of the basin boundaries. As the stochastic attractor increases, it approaches the basin boundary leading to a global bifurcation where the basin disappears and merges with other basins, generally after a very long transient. The proposed methodology is able to detect the long-transient solutions and, consequently, the basin loss of integrity for high noise intensity. The loss of integrity after very long transients induced by noise was observed in several cases, being this phenomenon validated through Monte-Carlo experiments. In such cases, for smaller numbers of periods of integration, the stochastic attractor seems to be stable, showing that integrity is time-dependent and that classical methods, such as Grid-of-Starts, may lead to wrong results. Finally, the manifolds' analysis suggested that this loss of integrity is associated with a stable manifold accretion.

The parameter uncertainty cases displayed other new phenomena as well. As predicted through Monte-Carlo, the occurrence of parametric uncertainty leads to the spread of the attractors along bifurcation paths. Contrary to the noisy case, basins are increasing diffused over large regions of phase-space, leading to a gradual decrease of the basin area for each probability threshold. For large uncertainties, basins may have no set of initial conditions in phase-space with a 100% probability of convergence to their attractors. Thus, the system outcome in these regions becomes unpredictable. Finally, random parameters in problems with complex dynamics result in cumulative manifold intersections as the uncertainty increases. Specifically, an aliasing effect, which is a common issue in the discretization of probability spaces, is observed in attractors' distributions, basins' boundaries, and manifolds.

The observations suggest that there is a strong relationship between the computational efficiency of the proposed strategies and the phase-space complexity. That is, simpler dynamics lead to a high computational economy. In all cases, the probability threshold p of the proposed integrity measure governs the basins' safety level. Finally, the examples show that nondeterminism is a potential hazard to be accounted for in the design of nonlinear structures.

7.3.
Suggestions for future works

Although this study has presented novel results regarding stochastic dynamic systems, it also demonstrates new demands for specific investigations that may be explored in future works. As a continuation of this thesis, the following research topics are suggested:

- Improvement of the subdivision strategy, focusing on reducing the number of integrated initial conditions and required memory, possibly employing analytical and semi-analytical methods, such as harmonic balance, multiple scales, homotopy, etc;
- Investigation of continuation strategies in the transfer operator space;
- Improvement of the subdivision strategy for the analysis of systems with parameter uncertainty – mitigation of the aliasing effect, reduction of the number of computed transfer operators;
- Investigation of different discretized spaces, substituting the space of constant functions by linear functions, for example;
- Comparison of the present technique with different strategies applied to the generator equation, such as finite differences, finite volumes, and finite elements;
- Global dynamic analysis of different multidimensional beam problems derived using the presented formulation, involving flexural-flexural, flexural-torsional, flexural-extensional interactions based on appropriate reduced order models for each case;
- Investigate other nondeterministic effects, such as multiparameter uncertainty, multiplicative noise, and colored noise;
- Global dynamic analysis of other continuous structures, formulated as reduced order models, such as hyperelastic membranes, shells, problems involving fluid-structure interaction, etc;
- Definition of other dynamical integrity measures for nondeterministic systems.
- Exploitation of dynamic integrity analysis and outcomes in a non-deterministic environment for systems safety evaluations.

References

1 Kiureghian, A. Der; Ditlevsen, O.: Aleatory or epistemic? Does it matter? **Struct. Saf.**, v. 31, n. 2, pp. 105–112, 2009. https://doi.org/10.1016/j.strusafe.2008.06.020

2 Papadrakakis, M.; Stefanou, G.; Papadopoulos, V. eds: **Computational Methods in Stochastic Dynamics**. v. 1, Dordrecht: Springer Netherlands, 2011.

3 Papadrakakis, M.; Stefanou, G.; Papadopoulos, V. eds: **Computational Methods in Stochastic Dynamics**. v. 2, Dordrecht: Springer Netherlands, 2013.

4 Mignolet, M. P.; Soize, C.: Stochastic reduced order models for uncertain geometrically nonlinear dynamical systems. **Comput. Methods Appl. Mech. Eng.**, v. 197, n. 45–48, pp. 3951–3963, 2008. https://doi.org/10.1016/j.cma.2008.03.032

5 Zhou, Y. B.: **Model Reduction For Nonlinear Dynamical Systems With Parametric Uncertainties**. 2012. Monograph (Sc.D.) - Massachusetts Institute of Technology, Cambridge, Massachusetts.

6 Koiter, W. T.: **The Stability of Elastic Equilibrium**. 1970.

7 Batista, R. C.; Gonçalves, P. B.: Non-linear lower bounds for shell buckling design. **J. Constr. Steel Res.**, v. 28, n. 2, pp. 101–120, 1994. https://doi.org/10.1016/0143-974X(94)90037-X

8 Galambos, T. V. ed: **Guide to Stability Design Criteria for Metal Structures**. John Wiley & Sons, 1998.

9 Perry, S. H.; Chilver, A. H.: The statistical variation of the buckling strengths of columns. **Proc. Inst. Civ. Eng.**, v. 61, n. 1, pp. 109–125, 1976. https://doi.org/10.1680/iicep.1976.3505

10 Gonçalves, P. B.; Santee, D. M.: Influence of uncertainties on the dynamic buckling loads of structures liable to asymmetric postbuckling behavior. **Math. Probl. Eng.**, v. 2008, pp. 1–24, 2008.

https://doi.org/10.1155/2008/490137

11 Xiu, D.: Fast numerical methods for stochastic computations: a review. **Commun. Comput. Phys.**, v. 5, n. 2–4, pp. 242–272, 2009

12 Gerritsma, M.; van der Steen, J.-B.; Vos, P.; Karniadakis, G.: Time-dependent generalized polynomial chaos. **J. Comput. Phys.**, v. 229, n. 22, pp. 8333–8363, 2010. https://doi.org/10.1016/j.jcp.2010.07.020

13 Mai, C. V.: **Polynomial Chaos Expansions For Uncertain Dynamical Systems - Applications In Earthquake Engineering**. 2016. Monograph (Sc.D.) - ETH Zürich, Zürich.

14 Luchtenburg, D. M.; Brunton, S. L.; Rowley, C. W.: Long-time uncertainty propagation using generalized polynomial chaos and flow map composition. **J. Comput. Phys.**, v. 274, pp. 783–802, 2014. https://doi.org/10.1016/j.jcp.2014.06.029

15 Arnold, L.: **Random Dynamical Systems**. Berlin, Heidelberg: Springer Berlin Heidelberg, 1998.

16 Han, X.; Kloeden, P. E.: **Random Ordinary Differential Equations and Their Numerical Solution**. v. 85, Singapore: Springer Singapore, 2017.

17 Lasota, A.; Mackey, M. C.: **Chaos, Fractals, and Noise**. v. 97, New York, NY: Springer New York, 1994.

18 Ulam, S. M.: **Problems in Modern Mathematics**. New York, NY: John Wiley & Sons, 1964.

19 Hsu, C. S.: A generalized theory of cell-to-cell mapping for nonlinear dynamical systems. **J. Appl. Mech.**, v. 48, n. 3, pp. 634–642, 1981. https://doi.org/10.1115/1.3157686

20 Hsu, C. S.: A theory of cell-to-cell mapping dynamical systems. **J. Appl. Mech.**, v. 47, n. 4, pp. 931–939, 1980. https://doi.org/10.1115/1.3153816

21 Guder, R.; Kreuzer, E. J.: Using generalized cell mapping to approximate invariant measures on compact manifolds. **Int. J. Bifurc. Chaos**, v. 07, n. 11, pp. 2487–2499, 1997. https://doi.org/10.1142/S0218127497001667

22 Hsu, C. S.; Chiu, H. M.: A cell mapping method for nonlinear deterministic and stochastic systems — part I: the method of analysis. **J. Appl. Mech.**, v. 53, n. 3, p. 695, 1986. https://doi.org/10.1115/1.3171833

23 Chiu, H. M.; Hsu, C. S.: A cell mapping method for nonlinear deterministic and stochastic systems — part II: examples of application. **J. Appl. Mech.**,

v. 53, n. 3, p. 702, 1986. https://doi.org/10.1115/1.3171834

24 Sun, J.-Q.; Hsu, C. S.: The generalized cell mapping method in nonlinear random vibration based upon short-time gaussian approximation. **J. Appl. Mech.**, v. 57, n. 4, pp. 1018–1025, 1990. https://doi.org/10.1115/1.2897620

25 Han, Q.; Xu, W.; Sun, J.-Q.: Stochastic response and bifurcation of periodically driven nonlinear oscillators by the generalized cell mapping method. **Phys. A Stat. Mech. its Appl.**, v. 458, pp. 115–125, 2016. https://doi.org/10.1016/j.physa.2016.04.006

26 Yue, X.; Wang, Y.; Han, Q.; Xu, Y.; Xu, W.: Transient responses of nonlinear dynamical systems under colored noise. **EPL (Europhysics Lett.**, v. 127, n. 2, p. 24004, 2019. https://doi.org/10.1209/0295-5075/127/24004

27 Yue, X.; Wang, Y.; Han, Q.; Xu, Y.; Xu, W.: Probabilistic response and stochastic bifurcation in a turbulent swirling flow. **J. Comput. Nonlinear Dyn.**, v. 14, n. 11, 2019. https://doi.org/10.1115/1.4044500

28 Han, Q.; Xu, W.; Hao, H.; Yue, X.: Global analysis of stochastic systems by the digraph cell mapping method based on short-time gaussian approximation. **Int. J. Bifurc. Chaos**, v. 30, n. 05, p. 2050071, 2020. https://doi.org/10.1142/S0218127420500716

29 Yue, X.; Xu, Y.; Xu, W.; Sun, J.-Q.: Probabilistic response of dynamical systems based on the global attractor with the compatible cell mapping method. **Phys. A Stat. Mech. its Appl.**, v. 516, pp. 509–519, 2019. https://doi.org/10.1016/j.physa.2018.10.034

30 Yue, X.; Xu, Y.; Xu, W.; Sun, J.-Q.: Global invariant manifolds of dynamical systems with the compatible cell mapping method. **Int. J. Bifurc. Chaos**, v. 29, n. 08, p. 1950105, 2019. https://doi.org/10.1142/S0218127419501050

31 Dellnitz, M.; Hohmann, A.: A subdivision algorithm for the computation of unstable manifolds and global attractors. **Numer. Math.**, v. 75, n. 3, pp. 293–317, 1997. https://doi.org/10.1007/s002110050240

32 Dellnitz, M.; Hohmann, A.; Junge, O.; Rumpf, M.: Exploring invariant sets and invariant measures. **Chaos An Interdiscip. J. Nonlinear Sci.**, v. 7, n. 2, pp. 221–228, 1997. https://doi.org/10.1063/1.166223

33 Dellnitz, M.; Junge, O.: On the approximation of complicated dynamical

behavior. **SIAM J. Numer. Anal.**, v. 36, n. 2, pp. 491–515, 1999. https://doi.org/10.1137/S0036142996313002

34 Yue, X.; Xu, W.; Zhang, Y.: Global bifurcation analysis of Rayleigh–Duffing oscillator through the composite cell coordinate system method. **Nonlinear Dyn.**, v. 69, n. 1–2, pp. 437–457, 2012. https://doi.org/10.1007/s11071-011-0276-z

35 Yue, X.; Lv, G.; Zhang, Y.: Rare and hidden attractors in a periodically forced Duffing system with absolute nonlinearity. **Chaos, Solitons & Fractals**, v. 150, p. 111108, 2021. https://doi.org/10.1016/j.chaos.2021.111108

36 Yue, X.; Xiang, Y.; Zhang, Y.; Xu, Y.: Global analysis of stochastic bifurcation in shape memory alloy supporter with the extended composite cell coordinate system method. **Chaos An Interdiscip. J. Nonlinear Sci.**, v. 31, n. 1, p. 013133, 2021. https://doi.org/10.1063/5.0024992

37 Lindner, M.; Hellmann, F.: Stochastic basins of attraction and generalized committor functions. **Phys. Rev. E**, v. 100, n. 2, p. 022124, 2019. https://doi.org/10.1103/PhysRevE.100.022124

38 Andonovski, N.; Lenci, S.: Six-dimensional basins of attraction computation on small clusters with semi-parallelized SCM method. **Int. J. Dyn. Control**, pp. 1–12, 2019. https://doi.org/10.1007/s40435-019-00557-2

39 Belardinelli, P.; Lenci, S.: A first parallel programming approach in basins of attraction computation. **Int. J. Non. Linear. Mech.**, v. 80, pp. 76–81, 2016. https://doi.org/10.1016/j.ijnonlinmec.2015.10.016

40 Belardinelli, P.; Lenci, S.: An efficient parallel implementation of cell mapping methods for MDOF systems. **Nonlinear Dyn.**, v. 86, n. 4, pp. 2279–2290, 2016. https://doi.org/10.1007/s11071-016-2849-3

41 Sun, J.-Q.; Xiong, F.-R.; Schütze, O.; Hernández, C.: **Cell Mapping Methods**. Singapore: Springer Singapore, 2019.

42 Klus, S.; Koltai, P.; Schütte, C.: On the numerical approximation of the Perron-Frobenius and Koopman operator. **J. Comput. Dyn.**, v. 3, n. 1, 2015. https://doi.org/10.3934/jcd.2016003

43 Dellnitz, M.; Froyland, G.; Junge, O.: The algorithms behind GAIO — set oriented numerical methods for dynamical systems. In: Fiedler, B. (ed.)

Ergodic Theory, Analysis, and Efficient Simulation of Dynamical Systems. Berlin, Heidelberg: Springer Berlin Heidelberg, pp. 145–174, 2001.

44 Padberg, K.; Thiere, B.; Preis, R.; Dellnitz, M.: Local expansion concepts for detecting transport barriers in dynamical systems. **Commun. Nonlinear Sci. Numer. Simul.**, v. 14, n. 12, pp. 4176–4190, 2009. https://doi.org/10.1016/j.cnsns.2009.03.018

45 Dellnitz, M.; Klus, S.; Ziessler, A.: A set-oriented numerical approach for dynamical systems with parameter uncertainty. **SIAM J. Appl. Dyn. Syst.**, v. 16, n. 1, pp. 120–138, 2017. https://doi.org/10.1137/16M1072735

46 Gerlach, R.; Koltai, P.; Dellnitz, M.: Revealing the intrinsic geometry of finite dimensional invariant sets of infinite dimensional dynamical systems. 2019. https://doi.org/10.48550/arXiv.1902.08824

47 Ziessler, A.; Dellnitz, M.; Gerlach, R.: The numerical computation of unstable manifolds for infinite dimensional dynamical systems by embedding techniques. **SIAM J. Appl. Dyn. Syst.**, v. 18, n. 3, pp. 1265–1292, 2019. https://doi.org/10.1137/18M1204395

48 Gerlach, R.; Ziessler, A.; Eckhardt, B.; Dellnitz, M.: A set-oriented path following method for the approximation of parameter dependent attractors. **SIAM J. Appl. Dyn. Syst.**, v. 19, n. 1, pp. 705–723, 2020. https://doi.org/10.1137/19M1247139

49 Koltai, P.: A stochastic approach for computing the domain of attraction without trajectory simulation. **Conf. Publ. 2011**, n. Special, pp. 854–863, 2011. https://doi.org/10.3934/proc.2011.2011.854

50 Koltai, P.; Volf, A.: Optimizing the stable behavior of parameter-dependent dynamical systems --- maximal domains of attraction, minimal absorption times. **J. Comput. Dyn.**, v. 1, n. 2, pp. 339–356, 2014. https://doi.org/10.3934/jcd.2014.1.339

51 Froyland, G.; Koltai, P.: Estimating long-term behavior of periodically driven flows without trajectory integration. **Nonlinearity**, v. 30, n. 5, pp. 1948–1986, 2017. https://doi.org/10.1088/1361-6544/aa6693

52 Klus, S.; Nüske, F.; Koltai, P.; Wu, H.; Kevrekidis, I.; Schütte, C.; Noé, F.: Data-driven model reduction and transfer operator approximation. **J. Nonlinear Sci.**, v. 28, n. 3, pp. 985–1010, 2018.

https://doi.org/10.1007/s00332-017-9437-7

53 Ding, J.; Li, T. Y.: Markov finite approximation of Frobenius-Perron operator. **Nonlinear Anal. Theory, Methods Appl.**, v. 17, n. 8, pp. 759–772, 1991. https://doi.org/10.1016/0362-546X(91)90211-I

54 Ding, J.; Du, Q.; Li, T. Y.: High order approximation of the Frobenius-Perron operator. **Appl. Math. Comput.**, v. 53, n. 2–3, pp. 151–171, 1993. https://doi.org/10.1016/0096-3003(93)90099-Z

55 Jin, C.; Ding, J.: A linear spline Markov approximation method for random maps with position dependent probabilities. **Int. J. Bifurc. Chaos**, v. 30, n. 03, p. 2050046, 2020. https://doi.org/10.1142/S0218127420500467

56 Bangura, R. M.; Jin, C.; Ding, J.: The norm convergence of a least squares approximation method for random maps. **Int. J. Bifurc. Chaos**, v. 31, n. 05, p. 2150068, 2021. https://doi.org/10.1142/S0218127421500681

57 Levien, R.: **The Elastica: A Mathematical History**. 2008.

58 Leine, R. I.: The historical development of classical stability concepts: Lagrange, Poisson and Lyapunov stability. **Nonlinear Dyn.**, v. 59, n. 1–2, pp. 173–182, 2010. https://doi.org/10.1007/s11071-009-9530-z

59 La Salle, J.; Lefschetz, S. eds: **Stability by Lyapunov's Direct Method with Applications**. v. 4, Elsevier, 1961.

60 Thompson, J. M. T.: Chaotic phenomena triggering the escape from a potential well. **Proc. R. Soc. A Math. Phys. Eng. Sci.**, v. 421, n. 1861, pp. 195–225, 1989. https://doi.org/10.1098/rspa.1989.0009

61 Soliman, M. S.; Thompson, J. M. T.: Integrity measures quantifying the erosion of smooth and fractal basins of attraction. **J. Sound Vib.**, v. 135, n. 3, pp. 453–475, 1989. https://doi.org/10.1016/0022-460X(89)90699-8

62 Thompson, J. M. T.; Bishop, S. R.; Leung, L. M.: Fractal basins and chaotic bifurcations prior to escape from a potential well. **Phys. Lett. A**, v. 121, n. 3, pp. 116–120, 1987. https://doi.org/10.1016/0375-9601(87)90403-8

63 Lenci, S.; Rega, G.: Optimal control of homoclinic bifurcation: theoretical treatment and practical reduction of safe basin erosion in the Helmholtz oscillator. **J. Vib. Control**, v. 9, n. 3–4, pp. 281–315, 2003. https://doi.org/10.1177/107754603030753

64 Lenci, S.; Rega, G.: Optimal control of nonregular dynamics in a Duffing

oscillator. **Nonlinear Dyn.**, v. 33, n. 1, pp. 71–86, 2003. https://doi.org/10.1023/A:1025509014101

65 Gonçalves, P. B.; Silva, F. M. A. da; Rega, G.; Lenci, S.: Global dynamics and integrity of a two-dof model of a parametrically excited cylindrical shell. **Nonlinear Dyn.**, v. 63, n. 1–2, pp. 61–82, 2011. https://doi.org/10.1007/s11071-010-9785-4

66 Guckenheimer, J.; Holmes, P.: **Nonlinear Oscillations, Dynamical Systems, and Bifurcations of Vector Fields**. v. 42, New York, NY: Springer New York, 1983.

67 Lenci, S.; Rega, G.; Ruzziconi, L.: The dynamical integrity concept for interpreting/ predicting experimental behaviour: from macro- to nano-mechanics. **Philos. Trans. R. Soc. A Math. Phys. Eng. Sci.**, v. 371, n. 1993, pp. 1–19, 2013. https://doi.org/10.1098/rsta.2012.0423

68 Rega, G.; Settimi, V.: Global dynamics perspective on macro- to nano-mechanics. **Nonlinear Dyn.**, v. 103, n. 2, pp. 1259–1303, 2021. https://doi.org/10.1007/s11071-020-06198-x

69 Lansbury, A. N.; Thompson, J. M. T.: Incursive fractals: a robust mechanism of basin erosion preceding the optimal escape from a potential well. **Phys. Lett. A**, v. 150, n. 8–9, pp. 355–361, 1990. https://doi.org/10.1016/0375-9601(90)90231-C

70 Thompson, J. M. T.; Soliman, M. S.: Fractal control boundaries of driven oscillators and their relevance to safe engineering design. **Proc. R. Soc. A Math. Phys. Eng. Sci.**, v. 428, n. 1874, pp. 1–13, 1990. https://doi.org/10.1098/rspa.1990.0022

71 Thompson, J. M. T.; Rainey, R. C. T.; Soliman, M. S.: Ship stability criteria based on chaotic transients from incursive fractals. **Philos. Trans. R. Soc. London. Ser. A Phys. Eng. Sci.**, v. 332, n. 1624, pp. 149–167, 1990. https://doi.org/10.1098/rsta.1990.0106

72 Lenci, S.; Rega, G.: Load carrying capacity of systems within a global safety perspective. Part II. Attractor/basin integrity under dynamic excitations. **Int. J. Non. Linear. Mech.**, v. 46, n. 9, pp. 1240–1251, 2011. https://doi.org/10.1016/j.ijnonlinmec.2011.05.021

73 Rega, G.; Lenci, S.: A global dynamics perspective for system safety From macro- to nanomechanics: analysis, control, and design engineering. **Appl.**

Mech. Rev., v. 67, n. 5, p. 050802, 2015. https://doi.org/10.1115/1.4031705

74 Lenci, S.; Orlando, D.; Rega, G.; Gonçalves, P. B.: Controlling nonlinear dynamics of systems liable to unstable interactive buckling. **Procedia IUTAM**, v. 5, pp. 108–123, 2012. https://doi.org/10.1016/j.piutam.2012.06.014

75 Orlando, D.; Gonçalves, P. B.; Lenci, S.; Rega, G.: Increasing practical safety of Von Mises truss via control of dynamic escape. **Appl. Mech. Mater.**, v. 849, pp. 46–56, 2016. https://doi.org/10.4028/www.scientific.net/AMM.849.46

76 Rega, G.; Lenci, S.: Identifying, evaluating, and controlling dynamical integrity measures in non-linear mechanical oscillators. **Nonlinear Anal. Theory, Methods Appl.**, v. 63, n. 5–7, pp. 902–914, 2005. https://doi.org/10.1016/j.na.2005.01.084

77 Benedetti, K. C. B.; Gonçalves, P. B.; Silva, F. M. A. da: Nonlinear oscillations and bifurcations of a multistable truss and dynamic integrity assessment via a Monte Carlo approach. **Meccanica**, v. 55, n. 12, pp. 2623–2657, 2020. https://doi.org/10.1007/s11012-020-01202-5

78 Lenci, S.; Rega, G. eds: **Global Nonlinear Dynamics for Engineering Design and System Safety**. v. 588, Cham: Springer International Publishing, 2019.

79 Thompson, J. M. T.: Dynamical Integrity: Three Decades of Progress from Macro to Nanomechanics. In: Lenci, S. and Rega, G. (eds.) **Global Nonlinear Dynamics for Engineering Design and System Safety**. Cham: Springer International Publishing, pp. 1–26, 2019.

80 Rega, G.: Nonlinear dynamics in mechanics: state of the art and expected future developments. **J. Comput. Nonlinear Dyn.**, v. 17, n. 8, 2022. https://doi.org/10.1115/1.4054112

81 Haller, G.; Ponsioen, S.: Exact model reduction by a slow–fast decomposition of nonlinear mechanical systems. **Nonlinear Dyn.**, v. 90, n. 1, pp. 617–647, 2017. https://doi.org/10.1007/s11071-017-3685-9

82 Touzé, C.; Vizzaccaro, A.; Thomas, O.: Model order reduction methods for geometrically nonlinear structures: a review of nonlinear techniques. **Nonlinear Dyn.**, v. 105, n. 2, pp. 1141–1190, 2021.

https://doi.org/10.1007/s11071-021-06693-9

83 Mazzilli, C. E. N.; Gonçalves, P. B.; Franzini, G. R.: Reduced-order modelling based on non-linear modes. **Int. J. Mech. Sci.**, v. 214, p. 106915, 2022. https://doi.org/10.1016/j.ijmecsci.2021.106915

84 Fonseca, F. M.; Gonçalves, P. B.: Nonlinear behavior and instabilities of a hyperelastic von Mises truss. **Int. J. Non. Linear. Mech.**, v. 142, n. February, p. 103964, 2022. https://doi.org/10.1016/j.ijnonlinmec.2022.103964

85 Hu, N.; Burgueño, R.: Buckling-induced smart applications: recent advances and trends. **Smart Mater. Struct.**, v. 24, n. 6, p. 063001, 2015. https://doi.org/10.1088/0964-1726/24/6/063001

86 Cao, Y.; Derakhshani, M.; Fang, Y.; Huang, G.; Cao, C.: Bistable structures for advanced functional systems. **Adv. Funct. Mater.**, v. 31, n. 45, p. 2106231, 2021. https://doi.org/10.1002/adfm.202106231

87 Fang, S.; Zhou, S.; Yurchenko, D.; Yang, T.; Liao, W.-H.: Multistability phenomenon in signal processing, energy harvesting, composite structures, and metamaterials: A review. **Mech. Syst. Signal Process.**, v. 166, n. February 2021, p. 108419, 2022. https://doi.org/10.1016/j.ymssp.2021.108419

88 Bovier, A.; den Hollander, F.: **Metastability. A Potential-Theoretic Approach**. v. 351, Cham: Springer International Publishing, 2015.

89 Serdukova, L.; Zheng, Y.; Duan, J.; Kurths, J.: Stochastic basins of attraction for metastable states. **Chaos An Interdiscip. J. Nonlinear Sci.**, v. 26, n. 7, p. 073117, 2016. https://doi.org/10.1063/1.4959146

90 Kraut, S.; Feudel, U.; Grebogi, C.: Preference of attractors in noisy multistable systems. **Phys. Rev. E**, v. 59, n. 5, pp. 5253–5260, 1999. https://doi.org/10.1103/PhysRevE.59.5253

91 Brunton, S. L.; Proctor, J. L.; Kutz, J. N.; Bialek, W.: Discovering governing equations from data by sparse identification of nonlinear dynamical systems. **Proc. Natl. Acad. Sci. U. S. A.**, v. 113, n. 15, pp. 3932–3937, 2016. https://doi.org/10.1073/pnas.1517384113

92 Pajonk, O.; Rosić, B. V.; Litvinenko, A.; Matthies, H. G.: A deterministic filter for non-gaussian bayesian estimation — applications to dynamical system estimation with noisy measurements. **Phys. D Nonlinear Phenom.**,

v. 241, n. 7, pp. 775–788, 2012. https://doi.org/10.1016/j.physd.2012.01.001

93 Champion, K.; Lusch, B.; Kutz, J. N.; Brunton, S. L.: Data-driven discovery of coordinates and governing equations. **Proc. Natl. Acad. Sci.**, v. 116, n. 45, pp. 22445–22451, 2019. https://doi.org/10.1073/pnas.1906995116

94 Gelß, P.; Klus, S.; Eisert, J.; Schütte, C.: Multidimensional approximation of nonlinear dynamical systems. **J. Comput. Nonlinear Dyn.**, v. 14, n. 6, 2019. https://doi.org/10.1115/1.4043148

95 Poon, L.; Grebogi, C.: Controlling complexity. **Phys. Rev. Lett.**, v. 75, n. 22, pp. 4023–4026, 1995. https://doi.org/10.1103/PhysRevLett.75.4023

96 Benedetti, K. C. B.; Gonçalves, P. B.: Nonlinear response of an imperfect microcantilever static and dynamically actuated considering uncertainties and noise. **Nonlinear Dyn.**, v. 107, n. 2, pp. 1725–1754, 2022. https://doi.org/10.1007/s11071-021-06600-2

97 Arnold, L.; Boxler, P.: Stochastic bifurcation: instructive examples in dimension one. In: **Diffusion Processes and Related Problems in Analysis, Volume II**. Boston, MA: Birkhäuser Boston, pp. 241–255, 1992.

98 Wei, W.; Xu, W.; Liu, J.: Stochastic P-bifurcation analysis of a class of nonlinear Markov jump systems under combined harmonic and random excitations. **Phys. A Stat. Mech. its Appl.**, v. 582, p. 126246, 2021. https://doi.org/10.1016/j.physa.2021.126246

99 Soliman, M. S.; Thompson, J. M. T.: Stochastic penetration of smooth and fractal basin boundaries under noise excitation. **Dyn. Stab. Syst.**, v. 5, n. 4, pp. 281–298, 1990. https://doi.org/10.1080/02681119008806101

100 Schenk-Hoppé, K. R.: Bifurcation scenarios of the noisy duffing-van der pol oscillator. **Nonlinear Dyn.**, v. 11, n. 3, pp. 255–274, 1996. https://doi.org/10.1007/BF00120720

101 Sharma, S. N.: A Kolmogorov-Fokker-Planck approach for a stochastic Duffing-van der Pol system. **Differ. Equations Dyn. Syst.**, v. 16, n. 4, pp. 351–377, 2008. https://doi.org/10.1007/s12591-008-0019-x

102 Xu, W.; He, Q.; Fang, T.; Rong, H.: Global analysis of stochastic bifurcation in Duffing system. **Int. J. Bifurc. Chaos**, v. 13, n. 10, pp. 3115–3123, 2003. https://doi.org/10.1142/S021812740300848X

103 Xu, W.; He, Q.; Fang, T.; Rong, H.: Stochastic bifurcation in duffing system subject to harmonic excitation and in presence of random noise. **Int. J. Non. Linear. Mech.**, v. 39, n. 9, pp. 1473–1479, 2004. https://doi.org/10.1016/j.ijnonlinmec.2004.02.009

104 Xu, W.; He, Q.; Fang, T.; Rong, H.: Global analysis of crisis in twin-well Duffing system under harmonic excitation in presence of noise. **Chaos, Solitons & Fractals**, v. 23, n. 1, pp. 141–150, 2005. https://doi.org/10.1016/j.chaos.2004.03.040

105 He, Q.; Xu, W.; Rong, H.; Fang, T.: Stochastic bifurcation in Duffing–Van der Pol oscillators. **Phys. A Stat. Mech. its Appl.**, v. 338, n. 3–4, pp. 319–334, 2004. https://doi.org/10.1016/j.physa.2004.01.067

106 Hsu, C. S.: Global analysis of dynamical systems using posets and digraphs. **Int. J. Bifurc. Chaos**, v. 05, n. 04, pp. 1085–1118, 1995. https://doi.org/10.1142/S021812749500079X

107 Green, P. L.; Worden, K.; Atallah, K.; Sims, N. D.: The benefits of Duffing-type nonlinearities and electrical optimisation of a mono-stable energy harvester under white Gaussian excitations. **J. Sound Vib.**, v. 331, n. 20, pp. 4504–4517, 2012. https://doi.org/10.1016/j.jsv.2012.04.035

108 Agarwal, V.; Zheng, X.; Balachandran, B.: Influence of noise on frequency responses of softening Duffing oscillators. **Phys. Lett. Sect. A Gen. At. Solid State Phys.**, v. 382, n. 46, pp. 3355–3364, 2018. https://doi.org/10.1016/j.physleta.2018.09.008

109 Cui, J.; Jiang, W.-A.; Xia, Z.-W.; Chen, L.-Q.: Non-stationary response of variable-mass Duffing oscillator with mass disturbance modeled as Gaussian white noise. **Phys. A Stat. Mech. its Appl.**, v. 526, p. 121018, 2019. https://doi.org/10.1016/j.physa.2019.04.254

110 Agarwal, V.; Yorke, J. A.; Balachandran, B.: Noise-induced chaotic-attractor escape route. **Nonlinear Dyn.**, v. 65, n. 6, pp. 1–11, 2020. https://doi.org/10.1007/s11071-020-05873-3

111 Cilenti, L.; Balachandran, B.: Transient probability in basins of noise influenced responses of mono and coupled Duffing oscillators. **Chaos An Interdiscip. J. Nonlinear Sci.**, v. 31, n. 6, p. 063117, 2021. https://doi.org/10.1063/5.0051103

112 Orlando, D.; Gonçalves, P. B.; Rega, G.; Lenci, S.: Influence of transient

escape and added load noise on the dynamic integrity of multistable systems. **Int. J. Non. Linear. Mech.**, v. 109, pp. 140–154, 2019. https://doi.org/10.1016/j.ijnonlinmec.2018.12.001

113 Silva, F. M. A. da; Gonçalves, P. B.: The influence of uncertainties and random noise on the dynamic integrity analysis of a system liable to unstable buckling. **Nonlinear Dyn.**, v. 81, n. 1–2, pp. 707–724, 2015. https://doi.org/10.1007/s11071-015-2021-5

114 Kamiński, M.; Corigliano, A.: Numerical solution of the Duffing equation with random coefficients. **Meccanica**, v. 50, n. 7, pp. 1841–1853, 2015. https://doi.org/10.1007/s11012-015-0133-0

115 Hajjaj, A. Z.; Jaber, N.; Ilyas, S.; Alfosail, F. K.; Younis, M. I.: Linear and nonlinear dynamics of micro and nano-resonators: Review of recent advances. **Int. J. Non. Linear. Mech.**, v. 119, p. 103328, 2020. https://doi.org/10.1016/j.ijnonlinmec.2019.103328

116 Younis, M. I.: **MEMS Linear and Nonlinear Statics and Dynamics**. v. 20, Boston, MA: Springer US, 2011.

117 Debéda, H.; Dufour, I.: Resonant microcantilever devices for gas sensing. In: **Advanced Nanomaterials for Inexpensive Gas Microsensors**. Elsevier, pp. 161–188, 2020.

118 Das, K.; Batra, R. C.: Symmetry breaking, snap-through and pull-in instabilities under dynamic loading of microelectromechanical shallow arches. **Smart Mater. Struct.**, v. 18, n. 11, p. 115008, 2009. https://doi.org/10.1088/0964-1726/18/11/115008

119 Batra, R. C.; Porfiri, M.; Spinello, D.: Electromechanical Model of Electrically Actuated Narrow Microbeams. **J. Microelectromechanical Syst.**, v. 15, n. 5, pp. 1175–1189, 2006. https://doi.org/10.1109/JMEMS.2006.880204

120 Akhavan, H.; Roody, B. S.; Ribeiro, P.; Fotuhi, A. R.: Modes of vibration, stability and internal resonances on non-linear piezoelectric small-scale beams. **Commun. Nonlinear Sci. Numer. Simul.**, v. 72, pp. 88–107, 2019. https://doi.org/10.1016/j.cnsns.2018.12.006

121 Batra, R. C.; Porfiri, M.; Spinello, D.: Review of modeling electrostatically actuated microelectromechanical systems. **Smart Mater. Struct.**, v. 16, n. 6, pp. R23–R31, 2007. https://doi.org/10.1088/0964-1726/16/6/R01

122 Najar, F.; Nayfeh, A. H.; Abdel-Rahman, E. M.; Choura, S.; El-Borgi, S.: Dynamics and Global Stability of Beam-based Electrostatic Microactuators. **J. Vib. Control**, v. 16, n. 5, pp. 721–748, 2010. https://doi.org/10.1177/1077546309106521

123 Ruzziconi, L.; Bataineh, A. M.; Younis, M. I.; Cui, W.; Lenci, S.: Nonlinear dynamics of an electrically actuated imperfect microbeam resonator: experimental investigation and reduced-order modeling. **J. Micromechanics Microengineering**, v. 23, n. 7, p. 075012, 2013. https://doi.org/10.1088/0960-1317/23/7/075012

124 Nayfeh, A. H.; Younis, M. I.; Abdel-Rahman, E. M.: Reduced-Order Models for MEMS Applications. **Nonlinear Dyn.**, v. 41, n. 1–3, pp. 211–236, 2005. https://doi.org/10.1007/s11071-005-2809-9

125 Younis, M. I.; Nayfeh, A. H.: A Study of the Nonlinear Response of a Resonant Microbeam to an Electric Actuation. **Nonlinear Dyn.**, v. 31, n. 1, pp. 91–117, 2003. https://doi.org/10.1023/A:1022103118330

126 Hajjaj, A. Z.; Alfosail, F. K.; Jaber, N.; Ilyas, S.; Younis, M. I.: Theoretical and experimental investigations of the crossover phenomenon in micromachined arch resonator: part I—linear problem. **Nonlinear Dyn.**, v. 99, n. 1, pp. 393–405, 2020. https://doi.org/10.1007/s11071-019-05251-8

127 Hajjaj, A. Z.; Alfosail, F. K.; Jaber, N.; Ilyas, S.; Younis, M. I.: Theoretical and experimental investigations of the crossover phenomenon in micromachined arch resonator: part II—simultaneous 1:1 and 2:1 internal resonances. **Nonlinear Dyn.**, v. 99, n. 1, pp. 407–432, 2020. https://doi.org/10.1007/s11071-019-05242-9

128 Ghayesh, M. H.; Farokhi, H.; Amabili, M.: Nonlinear dynamics of a microscale beam based on the modified couple stress theory. **Compos. Part B Eng.**, v. 5035, pp. 318–324, 2013. https://doi.org/10.1016/j.compositesb.2013.02.021

129 Farokhi, H.; Ghayesh, M. H.: Size-dependent parametric dynamics of imperfect microbeams. **Int. J. Eng. Sci.**, v. 99, pp. 39–55, 2016. https://doi.org/10.1016/j.ijengsci.2015.10.014

130 Farokhi, H.; Ghayesh, M. H.; Amabili, M.: Nonlinear dynamics of a geometrically imperfect microbeam based on the modified couple stress theory. **Int. J. Eng. Sci.**, v. 68, pp. 11–23, 2013.

https://doi.org/10.1016/j.ijengsci.2013.03.001

131 Abdel-Rahman, E. M.; Younis, M. I.; Nayfeh, A. H.: Characterization of the mechanical behavior of an electrically actuated microbeam. **J. Micromechanics Microengineering**, v. 12, n. 6, pp. 759–766, 2002. https://doi.org/10.1088/0960-1317/12/6/306

132 Younis, M. I.; Abdel-Rahman, E. M.; Nayfeh, A. H.: A reduced-order model for electrically actuated microbeam-based MEMS. **J. Microelectromechanical Syst.**, v. 12, n. 5, pp. 672–680, 2003. https://doi.org/10.1109/JMEMS.2003.818069

133 Dai, H. L.; Wang, L.: Size-dependent pull-in voltage and nonlinear dynamics of electrically actuated microcantilever-based MEMS: A full nonlinear analysis. **Commun. Nonlinear Sci. Numer. Simul.**, v. 46, pp. 116–125, 2017. https://doi.org/10.1016/j.cnsns.2016.11.004

134 Ruzziconi, L.; Bataineh, A. M.; Younis, M. I.; Lenci, S.: An Imperfect Microbeam Electrically Actuated: Experimental Investigation and Parameter Identification. In: **ASME 2012 International Design Engineering Technical Conferences and Computers and Information in Engineering Conference**. American Society of Mechanical Engineers, pp. 87–94, 2012.

135 Ruzziconi, L.; Younis, M. I.; Lenci, S.: Parameter identification of an electrically actuated imperfect microbeam. **Int. J. Non. Linear. Mech.**, v. 57, pp. 208–219, 2013. https://doi.org/10.1016/j.ijnonlinmec.2013.08.003

136 Alkharabsheh, S. A.; Younis, M. I.: Dynamics of MEMS Arches of Flexible Supports. **J. Microelectromechanical Syst.**, v. 22, n. 1, pp. 216–224, 2013. https://doi.org/10.1109/JMEMS.2012.2226926

137 Ghayesh, M. H.: Functionally graded microbeams: Simultaneous presence of imperfection and viscoelasticity. **Int. J. Mech. Sci.**, v. 140, n. February, pp. 339–350, 2018. https://doi.org/10.1016/j.ijmecsci.2018.02.037

138 Caruntu, D. I.; Martinez, I.; Knecht, M. W.: Parametric resonance voltage response of electrostatically actuated Micro-Electro-Mechanical Systems cantilever resonators. **J. Sound Vib.**, v. 362, pp. 203–213, 2016. https://doi.org/10.1016/j.jsv.2015.10.012

139 Caruntu, D. I.; Botello, M. A.; Reyes, C. A.; Beatriz, J. S.: Voltage–Amplitude Response of Superharmonic Resonance of Second Order of

Electrostatically Actuated MEMS Cantilever Resonators. **J. Comput. Nonlinear Dyn.**, v. 14, n. 3, pp. 1–8, 2019. https://doi.org/10.1115/1.4042017

140 Hu, Y. C.; Chang, C. M.; Huang, S. C.: Some design considerations on the electrostatically actuated microstructures. **Sensors Actuators A Phys.**, v. 112, n. 1, pp. 155–161, 2004. https://doi.org/10.1016/J.SNA.2003.12.012

141 Das, K.; Batra, R. C.: Pull-in and snap-through instabilities in transient deformations of microelectromechanical systems. **J. Micromechanics Microengineering**, v. 19, n. 3, p. 035008, 2009. https://doi.org/10.1088/0960-1317/19/3/035008

142 Awrejcewicz, J.; Krysko, V. A.; Pavlov, S. P.; Zhigalov, M. V.; Kalutsky, L. A.; Krysko, A. V.: Thermoelastic vibrations of a Timoshenko microbeam based on the modified couple stress theory. **Nonlinear Dyn.**, 2019. https://doi.org/10.1007/s11071-019-04976-w

143 Dai, H. L.; Wang, L.; Ni, Q.: Dynamics and pull-in instability of electrostatically actuated microbeams conveying fluid. **Microfluid. Nanofluidics**, v. 18, n. 1, pp. 49–55, 2014. https://doi.org/10.1007/s10404-014-1407-x

144 Dehrouyeh-Semnani, A. M.; Mostafaei, H.; Nikkhah-Bahrami, M.: Free flexural vibration of geometrically imperfect functionally graded microbeams. **Int. J. Eng. Sci.**, v. 105, pp. 56–79, 2016. https://doi.org/10.1016/j.ijengsci.2016.05.002

145 Ilyas, S.; Alfosail, F. K.; Younis, M. I.: On the response of MEMS resonators under generic electrostatic loadings: theoretical analysis. **Nonlinear Dyn.**, v. 97, n. 2, pp. 967–977, 2019. https://doi.org/10.1007/s11071-019-05024-3

146 Ilyas, S.; Alfosail, F. K.; Bellaredj, M. L. F.; Younis, M. I.: On the response of MEMS resonators under generic electrostatic loadings: experiments and applications. **Nonlinear Dyn.**, v. 95, n. 3, pp. 2263–2274, 2019. https://doi.org/10.1007/s11071-018-4690-3

147 Vig, J. R.; Kim, Y.: Noise in microelectromechanical system resonators. **IEEE Trans. Ultrason. Ferroelectr. Freq. Control**, v. 46, n. 6, pp. 1558–1565, 1999. https://doi.org/10.1109/58.808881

148 Andò, B.; Baglio, S.; Trigona, C.; Dumas, N.; Latorre, L.; Nouet, P.:

Nonlinear mechanism in MEMS devices for energy harvesting applications. **J. Micromechanics Microengineering**, v. 20, n. 12, p. 125020, 2010. https://doi.org/10.1088/0960-1317/20/12/125020

149 Alsaleem, F. M.; Younis, M. I.; Ouakad, H. M.: On the nonlinear resonances and dynamic pull-in of electrostatically actuated resonators. **J. Micromechanics Microengineering**, v. 19, n. 4, p. 045013, 2009. https://doi.org/10.1088/0960-1317/19/4/045013

150 Ruzziconi, L.; Younis, M. I.; Lenci, S.: An electrically actuated imperfect microbeam: Dynamical integrity for interpreting and predicting the device response. **Meccanica**, v. 48, n. 7, pp. 1761–1775, 2013. https://doi.org/10.1007/s11012-013-9707-x

151 Steven Greene, M.; Liu, Y.; Chen, W.; Liu, W. K.: Computational uncertainty analysis in multiresolution materials via stochastic constitutive theory. **Comput. Methods Appl. Mech. Eng.**, v. 200, n. 1–4, pp. 309–325, 2011. https://doi.org/10.1016/j.cma.2010.08.013

152 Zhu, C.; Zhu, P.; Liu, Z.: Uncertainty analysis of mechanical properties of plain woven carbon fiber reinforced composite via stochastic constitutive modeling. **Compos. Struct.**, v. 207, pp. 684–700, 2019. https://doi.org/10.1016/j.compstruct.2018.09.089

153 Silva, F. M. A. da; Soares, R. M.; Prado, Z. J. G. N. Del; Gonçalves, P. B.: Intra-well and cross-well chaos in membranes and shells liable to buckling. **Nonlinear Dyn.**, v. 102, n. 2, pp. 877–906, 2020. https://doi.org/10.1007/s11071-020-05661-z

154 Lazarov, B. S.; Schevenels, M.; Sigmund, O.: Topology optimization with geometric uncertainties by perturbation techniques. **Int. J. Numer. Methods Eng.**, v. 90, n. 11, pp. 1321–1336, 2012. https://doi.org/10.1002/nme.3361

155 Rodrigues, L.; Silva, F. M. A. da; Gonçalves, P. B.: Influence of initial geometric imperfections on the 1:1:1:1 internal resonances and nonlinear vibrations of thin-walled cylindrical shells. **Thin-Walled Struct.**, v. 151, n. April, p. 106730, 2020. https://doi.org/10.1016/j.tws.2020.106730

156 Fina, M.; Weber, P.; Wagner, W.: Polymorphic uncertainty modeling for the simulation of geometric imperfections in probabilistic design of cylindrical shells. **Struct. Saf.**, v. 82, p. 101894, 2020.

https://doi.org/10.1016/j.strusafe.2019.101894

157 Agarwal, N.; Aluru, N. R.: Stochastic Analysis of Electrostatic MEMS Subjected to Parameter Variations. **J. Microelectromechanical Syst.**, v. 18, n. 6, pp. 1454–1468, 2009. https://doi.org/10.1109/JMEMS.2009.2034612

158 Fiedler, B. ed: **Handbook of Dynamical Systems**. v. 2, Elsevier B.V., 2002.

159 Hasselblatt, B.; Katok, A. eds: **Handbook of Dynamical Systems**. v. 1A, Elsevier B.V., 2002.

160 Hasselblatt, B.; Katok, A. eds: **Handbook of Dynamical Systems**. v. 1B, Elsevier B.V., 2006.

161 Hasselblatt, B.; Broer, H.; Takens, F. eds: **Handbook of Dynamical Systems**. v. 3, Elsevier B.V., 2010.

162 Bollt, E. M.; Santitissadeekorn, N.: **Applied and Computational Measurable Dynamics**. Philadelphia, PA: Society for Industrial and Applied Mathematics, 2013.

163 Nayfeh, A. H.; Balachandran, B.: **Applied Nonlinear Dynamics**. New York: Wiley, 1995.

164 Kovacic, I.; Brennan, M. J. eds: **The Duffing Equation: Nonlinear Oscillators and Their Behaviour**. Chichester, UK: John Wiley & Sons, Ltd, 2011.

165 Michel, A. N.; Hou, L.; Liu, D.: **Stability of Dynamical Systems**. Boston, MA: Birkhäuser Boston, 2008.

166 Michel, A. N.; Wang, K.; Hu, B.: **Qualitative Theory of Dynamical Systems - The Role of Stability Preserving Mappings**. New York, NY: Marcel Dekker, 2001.

167 Michel, A. N.; Miller, R. K.: **Qualitative Analysis of Large Scale Dynamical Systems**. v. 134, London: Academic Press, 1977.

168 Siddiqi, A. H.: **Functional Analysis and Applications**. Singapore: Springer Singapore, 2018.

169 Chaskalovic, J.: **Mathematical and Numerical Methods for Partial Differential Equations**. Cham: Springer International Publishing, 2014.

170 Papoulis, A.; Pillai, S. U.: **Probability, Random Variables, and Stochastic Processes**. McGraw-Hill Higher Education, 2002.

171 Augustin, F.; Rentrop, P.: Stochastic Galerkin techniques for random ordinary differential equations. **Numer. Math.**, v. 122, n. 3, pp. 399–419, 2012. https://doi.org/10.1007/s00211-012-0466-8

172 Le Maître, O. P.; Knio, O. M.: **Spectral Methods for Uncertainty Quantification**. Dordrecht: Springer Netherlands, 2010.

173 Sullivan, T. J.: **Introduction to Uncertainty Quantification**. v. 63, Cham: Springer International Publishing, 2015.

174 Zhang, Z.; Karniadakis, G. E.: **Numerical Methods for Stochastic Partial Differential Equations with White Noise**. v. 196, Cham: Springer International Publishing, 2017.

175 Øksendal, B.: **Stochastic Differential Equations**. Berlin, Heidelberg: Springer Berlin Heidelberg, 2003.

176 Xie, W.-C.: Random processes and stochastic differential equations. In: **Dynamic stability of structures**. New York, NY: Cambridge, pp. 155–233, 2006.

177 Duan, J.; Wang, W.: **Effective Dynamics of Stochastic Partial Differential Equations**. Elsevier, 2014.

178 Ochs, G.: Random attractors: robustness, numerics and chaotic dynamics. In: **Ergodic Theory, Analysis, and Efficient Simulation of Dynamical Systems**. Berlin, Heidelberg: Springer Berlin Heidelberg, pp. 1–30, 2001.

179 Silva, F. M. A. da; Gonçalves, P. B.; Del Prado, Z. J. G. N.: Influence of physical and geometrical system parameters uncertainties on the nonlinear oscillations of cylindrical shells. **J. Brazilian Soc. Mech. Sci. Eng.**, v. 34, n. spe2, pp. 622–632, 2012. https://doi.org/10.1590/S1678-58782012000600011

180 Ding, J.; Yien Li, T.; Zhou, A.: Finite approximations of Markov operators. **J. Comput. Appl. Math.**, v. 147, n. 1, pp. 137–152, 2002. https://doi.org/10.1016/S0377-0427(02)00429-6

181 Bollt, E. M.; Billings, L.; Schwartz, I. B.: A manifold independent approach to understanding transport in stochastic dynamical systems. **Phys. D Nonlinear Phenom.**, v. 173, n. 3–4, pp. 153–177, 2002. https://doi.org/10.1016/S0167-2789(02)00659-0

182 Črnjarić-Žic, N.; Maćešić, S.; Mezić, I.: Koopman operator spectrum for random dynamical systems. **J. Nonlinear Sci.**, v. 30, n. 5, pp. 2007–2056,

2020. https://doi.org/10.1007/s00332-019-09582-z

183 Koltai, P.: **Efficient Approximation Methods For The Global Long-Term Behavior Of Dynamical Systems - Theory, Algorithms And Examples**. 2010. Monograph (Sc.D.) - Technischen Universität München, Munich.

184 Guder, R.; Kreuzer, E. J.: Control of an adaptive refinement technique of generalized cell mapping by system dynamics. **Nonlinear Dyn.**, v. 20, n. 1, pp. 21–32, 1999. https://doi.org/10.1023/A:1008352418599

185 Guder, R.; Kreuzer, E.: Basin boundaries and robustness of nonlinear dynamic systems. **Arch. Appl. Mech.**, v. 69, n. 8, pp. 569–583, 1999. https://doi.org/10.1007/s004190050244

186 Lukaszyk, S.: A new concept of probability metric and its applications in approximation of scattered data sets. **Comput. Mech.**, v. 33, n. 4, pp. 299–304, 2004. https://doi.org/10.1007/s00466-003-0532-2

187 Klünker, A.; Padberg-Gehle, K.; Thiffeault, J.-L.: Open-flow mixing and transfer operators. **Philos. Trans. R. Soc. A Math. Phys. Eng. Sci.**, v. 380, n. 2225, pp. 8–10, 2022. https://doi.org/10.1098/rsta.2021.0028

188 Hsu, C. S.: **Cell-to-Cell Mapping**. v. 64, New York, NY: Springer New York, 1987.

189 Thompson, J. M. T.: Designing against capsize in beam seas: recent advances and new insights. **Appl. Mech. Rev.**, v. 50, n. 5, p. 307, 1997. https://doi.org/10.1115/1.3101710

190 Soliman, M. S.; Gonçalves, P. B.: Chaotic behaviour resulting in transient and steady-state instabilities of pressure loaded shallow spherical shells. **J. Sound Vib.**, v. 259, n. 3, pp. 497–512, 2003. https://doi.org/10.1006/jsvi.2002.5163

191 Nayfeh, A. H.; Mook, D. T.: **Nonlinear Oscillations**. Wiley, 1995.

192 Moon, F. C.: **Chaotic Vibrations**. Wiley, 2004.

193 Thompson, J. M. T.; Stewart, H. B.: **Nonlinear Dynamics and Chaos**. Chichester, England: Wiley, 2002.

194 Thompson, J. M. T.: **Instabilities and Catastrophes in Science and Engineering**. Chichester: Wiley, 1982.

195 Burkardt, J.: **The Truncated Normal Distribution**. Department of Scientific Computing, Florida State University, 2014.

196 Gonçalves, P. B.; Silva, F. M. A. da; Prado, Z. J. G. N. Del: Transient and steady state stability of cylindrical shells under harmonic axial loads. **Int. J. Non. Linear. Mech.**, v. 42, n. 1, pp. 58–70, 2007. https://doi.org/10.1016/j.ijnonlinmec.2006.12.011

197 Cataldo, E.; Soize, C.: Voice signals produced with jitter through a stochastic one-mass mechanical model. **J. Voice**, v. 31, n. 1, pp. 111.e9-111.e18, 2017. https://doi.org/10.1016/j.jvoice.2016.01.001

198 Soliman, M. S.; Thompson, J. M. T.: Global dynamics underlying sharp basin erosion in nonlinear driven oscillators. **Phys. Rev. A**, v. 45, n. 6, pp. 3425–3431, 1992. https://doi.org/10.1103/PhysRevA.45.3425

199 Han, S. M.; Benaroya, H.; Wei, T.: Dynamics of transversely vibrating beams using four engineering theories. **J. Sound Vib.**, v. 225, n. 5, pp. 935–988, 1999. https://doi.org/10.1006/jsvi.1999.2257

200 Allgower, E. L.; Georg, K.: **Numerical Continuation Methods**. v. 13, Berlin, Heidelberg: Springer Berlin Heidelberg, 1990.

201 Prado, Z. J. G. N. Del: **Acoplamento E Interação Modal Na Instabilidade Dinâmica De Cascas Cilíndricas**. 2001. Monograph (Sc.D.) - Pontifícia Universidade Católica do Rio de Janeiro, Rio de Janeiro.

202 Shaw, S. W.; Pierre, C.: Normal Modes for Non-Linear Vibratory Systems. **J. Sound Vib.**, v. 164, n. 1, pp. 85–124, 1993. https://doi.org/10.1006/jsvi.1993.1198

203 Dankowicz, H.; Schilder, F.: **Recipes for Continuation**. Philadelphia, PA: Society for Industrial and Applied Mathematics, 2013.

204 Jaeger, L.; Kantz, H.: Homoclinic tangencies and non-normal Jacobians — Effects of noise in nonhyperbolic chaotic systems. **Phys. D Nonlinear Phenom.**, v. 105, n. 1–3, pp. 79–96, 1997. https://doi.org/10.1016/S0167-2789(97)00247-9

205 Crespo da Silva, M. R. M.; Glynn, C. C.: Nonlinear Flexural-Flexural-Torsional Dynamics of Inextensional Beams. I. Equations of Motion. **J. Struct. Mech.**, v. 6, n. 4, pp. 437–448, 1978. https://doi.org/10.1080/03601217808907348

206 Crespo da Silva, M. R. M.; Glynn, C. C.: Nonlinear Flexural-Flexural-Torsional Dynamics of Inextensional Beams. II. Forced Motions. **J. Struct. Mech.**, v. 6, n. 4, pp. 449–461, 1978.

https://doi.org/10.1080/03601217808907349

207 Crespo da Silva, M. R. M.: Non-linear flexural-flexural-torsional-extensional dynamics of beams—I. Formulation. **Int. J. Solids Struct.**, v. 24, n. 12, pp. 1225–1234, 1988. https://doi.org/10.1016/0020-7683(88)90087-X

208 Crespo da Silva, M. R. M.: Non-linear flexural-flexural-torsional-extensional dynamics of beams—II. Response analysis. **Int. J. Solids Struct.**, v. 24, n. 12, pp. 1235–1242, 1988. https://doi.org/10.1016/0020-7683(88)90088-1

209 Crespo da Silva, M. R. M.; Zaretzky, C. L.: Nonlinear flexural-flexural-torsional interactions in beams including the effect of torsional dynamics. I: Primary Resonance. **Nonlinear Dyn.**, v. 5, n. 1, pp. 3–23, 1994. https://doi.org/10.1007/BF00045077

210 Zaretzky, C. L.; Crespo da Silva, M. R. M.: Nonlinear flexural-flexural-torsional interactions in beams including the effect of torsional dynamics. II: Combination resonance. **Nonlinear Dyn.**, v. 5, n. 2, pp. 161–180, 1994. https://doi.org/10.1007/BF00045674

211 Carvalho, E. C.; Gonçalves, P. B.; Rega, G.; Prado, Z. J. G. N. Del: Influence of axial loads on the nonplanar vibrations of cantilever beams. **Shock Vib.**, v. 20, n. 6, pp. 1073–1092, 2013. https://doi.org/10.3233/SAV-130823

212 Carvalho, E. C.: **Vibrações Não Lineares E Não Planares E Instabilidade Dinâmica De Barras Esbeltas**. 2013. Monograph (Sc.D.) - Pontifical Catholic University of Rio de Janeiro, Rio de Janeiro.

213 Nayfeh, A. H.; Pai, P. F.: **Linear and Nonlinear Structural Mechanics**. Wiley, 2004.

214 Love, A. E. H.: **A Treatise on the Mathematical Theory of Elasticity**. New York: Dover, 1944.

Appendix A
Formulation of imperfect Rayleigh beams

The present formulation follows the works of [205–211] where Euler-Bernoulli beams are modeled, with nonlinearities up to the third order with the effect of rotary inertias also considered [212]. The kinematics of an imperfect beam is defined with respect to three curvilinear coordinate systems: the deformed axes (ξ, η, ζ), the undeformed axes (ξ_0, η_0, ζ_0), and the reference axes (X, Y, Z). The undeformed axes correspond to a stress-free configuration and define a Lagrangian frame of reference, while the deformed axes define an Eulerian frame of reference. The undeformed arclength is identified by s, while the deformed arclength is identified by $\tilde{s}$. All three frames are illustrated in Figure A1.

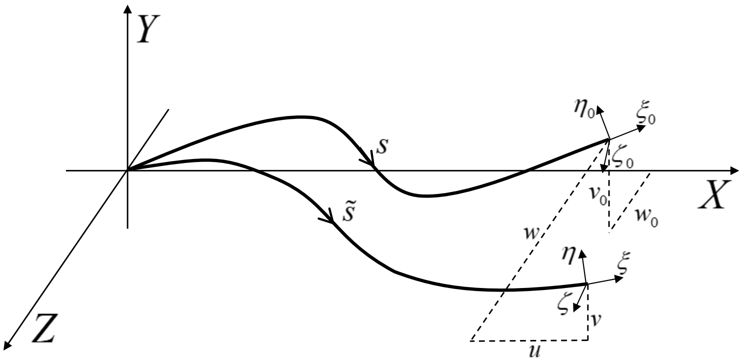

Figure A1 – Orientation of imperfect undeformed and deformed frames with respect to the reference axis

A.1
Rotation matrices, Euler angles, curvatures, and angular velocities

The relation between the reference frame with each configuration is given by matrices $[T]$ and $[T_0]$. By applying three successive rotations, the reference axes are transformed into one of the curvilinear axes:

$$\begin{Bmatrix} i_\xi \\ i_\eta \\ i_\zeta \end{Bmatrix} = [T] \begin{Bmatrix} i_X \\ i_Y \\ i_Z \end{Bmatrix}, \tag{A1}$$

$$\begin{Bmatrix} i_{\xi_0} \\ i_{\eta_0} \\ i_{\zeta_0} \end{Bmatrix} = [T_0] \begin{Bmatrix} i_X \\ i_Y \\ i_Z \end{Bmatrix}, \tag{A2}$$

where $\{i_\xi, i_\eta, i_\zeta\}$, $\{i_{\xi 0}, i_{\eta 0}, i_{\zeta 0}\}$, and $\{i_X, i_Y, i_Z\}$ are unit vectors of the axes (ξ, η, ζ), (ξ_0, η_0, ζ_0) and (X, Y, Z), respectively. The matrices $[T]$ and $[T_0]$ are functions of Euler angles ψ, θ, and ϕ,

$$[T] = \begin{bmatrix} 1 & 0 & 0 \\ 0 & \cos\bar{\phi} & \sin\bar{\phi} \\ 0 & -\sin\bar{\phi} & \cos\bar{\phi} \end{bmatrix} \begin{bmatrix} \cos\bar{\theta} & 0 & -\sin\bar{\theta} \\ 0 & 1 & 0 \\ \sin\bar{\theta} & 0 & \cos\bar{\theta} \end{bmatrix} \begin{bmatrix} \cos\bar{\psi} & \sin\bar{\psi} & 0 \\ -\sin\bar{\psi} & \cos\bar{\psi} & 0 \\ 0 & 0 & 1 \end{bmatrix}, \tag{A3}$$

$$[T_0] = \begin{bmatrix} 1 & 0 & 0 \\ 0 & \cos\phi_0 & \sin\phi_0 \\ 0 & -\sin\phi_0 & \cos\phi_0 \end{bmatrix} \begin{bmatrix} \cos\theta_0 & 0 & -\sin\theta_0 \\ 0 & 1 & 0 \\ \sin\theta_0 & 0 & \cos\theta_0 \end{bmatrix} \begin{bmatrix} \cos\psi_0 & \sin\psi_0 & 0 \\ -\sin\psi_0 & \cos\psi_0 & 0 \\ 0 & 0 & 1 \end{bmatrix}, \tag{A4}$$

where $\bar{\alpha} = \alpha + \alpha_0$. Given that $[T]$ and $[T_0]$ are rotation matrices, the following properties hold:

$$\begin{aligned} [T_0]^{-1} &= [T_0]^*, \\ [T]^{-1} &= [T]^*. \end{aligned} \tag{A5}$$

where * denotes transposition. A complete description of Euler rotations can be found in [212, 213]. To summarize, the transformations from the reference axes to the deformed or undeformed configurations are schematized below.

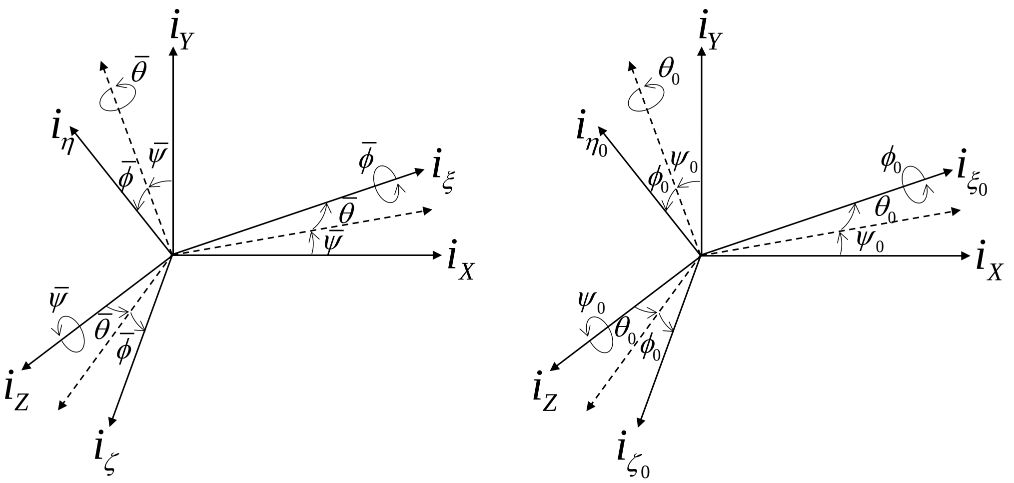

(a) (b)

Figure A2 – Transformation from the material axes to the (a) deformed and (b) undeformed configuration using Euler angles

By definition, the $\{i_\xi, i_\eta, i_\zeta\}$ and $\{i_{\xi 0}, i_{\eta 0}, i_{\zeta 0}\}$ frames are orthogonal. Therefore, the following property holds:

$$i_j \cdot i_k = \delta_{jk}, \tag{A6}$$

for j,k as (ξ, η, ζ) or (ξ_0, η_0, ζ_0). Differentiating the relation (A6) results in

$$\begin{cases} i_j \cdot di_k = -di_j \cdot i_k, \\ i_j \cdot di_j = 0, \end{cases} \tag{A7}$$

defining antisymmetric relations between the undeformed and deformed axes and their derivatives. This property will be observed in the construction of the curvature and angular velocity matrices.

With the definition of the derivatives of the deformed and undeformed axes, the curvature and angular velocity matrices are obtained. Differentiating (A1) and (A2) with respect to the undeformed configuration (Lagrangian frame) and using property (A5) results in

$$\begin{Bmatrix} i_\xi \\ i_\eta \\ i_\zeta \end{Bmatrix}' = [T]'[T]^* \begin{Bmatrix} i_\xi \\ i_\eta \\ i_\zeta \end{Bmatrix}, \tag{A8}$$

$$\begin{Bmatrix} i_{\xi_0} \\ i_{\eta_0} \\ i_{\zeta_0} \end{Bmatrix}' = \left[T_0\right]' \left[T_0\right]^* \begin{Bmatrix} i_{\xi_0} \\ i_{\eta_0} \\ i_{\zeta_0} \end{Bmatrix}. \tag{A9}$$

where $(\ )' = d/ds$. The curvature matrices relate the curvilinear axes spatial derivative with itself. By inspecting the expressions (A8) and (A9) one obtains

$$\left[K\right] = \left[T\right]' \left[T\right]^* = \begin{bmatrix} 0 & \bar{\kappa}_\zeta & -\bar{\kappa}_\eta \\ -\bar{\kappa}_\zeta & 0 & \bar{\kappa}_\xi \\ \bar{\kappa}_\eta & -\bar{\kappa}_\xi & 0 \end{bmatrix}, \tag{A10}$$

$$\left[K_0\right] = \left[T_0\right]' \left[T_0\right]^* = \begin{bmatrix} 0 & \kappa_{\zeta_0} & -\kappa_{\eta_0} \\ -\kappa_{\zeta_0} & 0 & \kappa_{\xi_0} \\ \kappa_{\eta_0} & -\kappa_{\xi_0} & 0 \end{bmatrix}, \tag{A11}$$

where the curvatures are given by

$$\begin{aligned} \bar{\kappa}_\xi &= i_\eta{}' \cdot i_\zeta = \bar{\phi}' - \bar{\psi}' \sin\bar{\theta}, \\ \bar{\kappa}_\eta &= i_\zeta{}' \cdot i_\xi = \bar{\psi}' \sin\bar{\phi} \cos\bar{\theta} + \bar{\theta}' \cos\bar{\phi}, \\ \bar{\kappa}_\zeta &= i_\xi{}' \cdot i_\eta = \bar{\psi}' \cos\bar{\phi} \cos\bar{\theta} - \bar{\theta}' \sin\bar{\phi}, \end{aligned} \tag{A12}$$

$$\begin{aligned} \kappa_{\xi_0} &= i_{\eta_0}{}' \cdot i_{\zeta_0} = \phi_0{}' - \psi_0{}' \sin\theta_0, \\ \kappa_{\eta_0} &= i_{\zeta_0}{}' \cdot i_{\xi_0} = \psi_0{}' \sin\phi_0 \cos\theta_0 + \theta_0{}' \cos\phi_0, \\ \kappa_{\zeta_0} &= i_{\xi_0}{}' \cdot i_{\eta_0} = \psi_0{}' \cos\phi_0 \cos\theta_0 - \theta_0{}' \sin\phi_0, \end{aligned} \tag{A13}$$

Next, the expression (A1) is differentiated with respect to time. Applying property (A5) results in

$$\begin{Bmatrix} i_\xi \\ i_\eta \\ i_\zeta \end{Bmatrix}^\bullet = \left[T\right]^\bullet \left[T\right]^* \begin{Bmatrix} i_\xi \\ i_\eta \\ i_\zeta \end{Bmatrix}, \tag{A14}$$

where $(\ )^\bullet = d/dt$. The angular velocity matrix relates the time derivative of the curvilinear axes to themselves. Inspecting the expression (A14) results in the definition

$$[\omega]=[T]^{\bullet}[T]^{*}=\begin{bmatrix} 0 & \omega_{\zeta} & -\omega_{\eta} \\ -\omega_{\zeta} & 0 & \omega_{\xi} \\ \omega_{\eta} & -\omega_{\xi} & 0 \end{bmatrix}, \tag{A15}$$

where the angular velocities are

$$\begin{aligned} \omega_{\xi} &= \dot{i}_{\eta}\cdot i_{\zeta} = \dot{\phi}-\dot{\psi}\sin\bar{\theta}, \\ \omega_{\eta} &= \dot{i}_{\zeta}\cdot i_{\xi} = \dot{\psi}\sin\bar{\phi}\cos\bar{\theta}+\dot{\theta}\cos\bar{\phi}, \\ \omega_{\zeta} &= \dot{i}_{\xi}\cdot i_{\eta} = \dot{\psi}\cos\bar{\phi}\cos\bar{\theta}-\dot{\theta}\sin\bar{\phi}, \end{aligned} \tag{A16}$$

In contrast with the curvature definition, the undeformed configuration is time-independent, resulting in a zero undeformed angular velocity. Additionally, the curvatures can be determined directly from the angular velocity matrix [ω] by applying Kirchhoff's kinetic analogy [214].

A.2
Kinematics

A beam element with undeformed and deformed lengths ds and $d\tilde{s}$ is considered. The perfect length dx is also specified since the stress-free configuration is not the reference frame. The geometric relations between $d\tilde{s}$ and ds with the perfect length are shown in Figure A3.

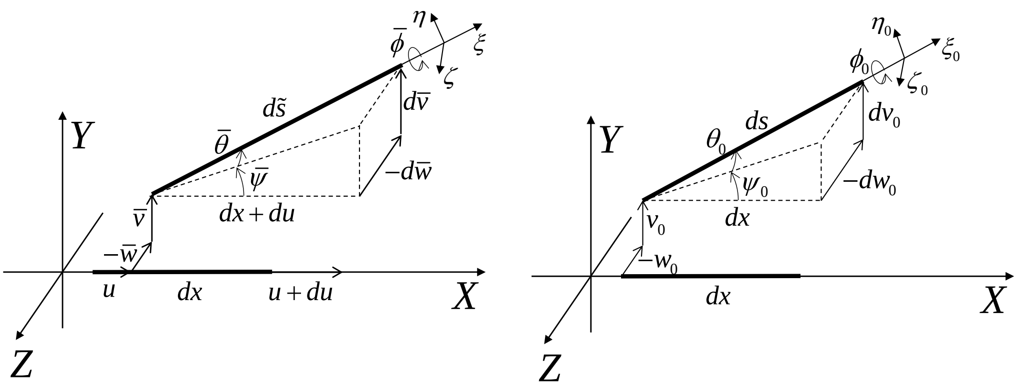

Figure A3 – Geometric relations (a) $d\tilde{s} - dx$ and (b) $ds - dx$

From Figure A3, the deformed and undeformed lengths $d\tilde{s}$ and ds are written as functions of the reference length dx and the initial and total displacements,

$$d\tilde{s}^2 = \left(dx + du\right)^2 + d\overline{v}^2 + d\overline{w}^2, \tag{A17}$$

$$ds^2 = dx^2 + dv_0^2 + dw_0^2. \tag{A18}$$

The variation of the reference length with respect to the Lagrangian frame, x', is obtained from eq. (A18), resulting in

$$x' = \sqrt{1 - v_0'^2 - w_0'^2}. \tag{A19}$$

being dependent only on the imperfections. Therefore, if the system is perfect, then eq. (A19) will be constant, and the reference and Lagrangian frames will coincide, as expected. Similarly, the variation of the deformed length with respect to the Lagrangian frame, $\tilde{s}'$, is obtained from eq. (A17) and eq. (A19), resulting in

$$\tilde{s}' = \sqrt{\left(u' + \sqrt{1 - v_0'^2 - w_0'^2}\right)^2 + \overline{v}'^2 + \overline{w}'^2}. \tag{A20}$$

Trigonometric relations between the Euler angles and displacements can also be obtained from Figure A3. The deformed configuration, Figure A3a, gives

$$\begin{aligned} \sin\overline{\psi} &= \frac{\overline{v}'}{\sqrt{\overline{v}'^2 + \left(u' + \sqrt{1 - v_0'^2 - w_0'^2}\right)^2}}, \\ \cos\overline{\psi} &= \frac{u' + \sqrt{1 - v_0'^2 - w_0'^2}}{\sqrt{\overline{v}'^2 + \left(u' + \sqrt{1 - v_0'^2 - w_0'^2}\right)^2}}, \end{aligned} \tag{A21}$$

$$\begin{aligned} \sin\overline{\theta} &= \frac{-\overline{w}'}{\sqrt{\overline{v}'^2 + \overline{w}'^2 + \left(u' + \sqrt{1 - v_0'^2 - w_0'^2}\right)^2}}, \\ \cos\overline{\theta} &= \frac{\sqrt{\overline{v}'^2 + \left(u' + \sqrt{1 - v_0'^2 - w_0'^2}\right)^2}}{\sqrt{\overline{v}'^2 + \overline{w}'^2 + \left(u' + \sqrt{1 - v_0'^2 - w_0'^2}\right)^2}}, \end{aligned} \tag{A22}$$

while the undeformed configuration, Figure A3b, gives

$$\sin\psi_0 = \frac{v_0'}{\sqrt{1-w_0'^2}},$$
$$\cos\psi_0 = \frac{\sqrt{1-v_0'^2-w_0'^2}}{\sqrt{1-w_0'^2}}, \tag{A23}$$

$$\sin\theta_0 = -w_0',$$
$$\cos\theta_0 = \sqrt{1-w_0'^2}. \tag{A24}$$

The elongation of the beam's principal axis is defined based on eq. (A20), and is given by

$$\Delta_e = \frac{d\tilde{s}-ds}{ds} = \sqrt{\left(u' + \sqrt{1-v_0'^2-w_0'^2}\right)^2 + \bar{v}'^2 + \bar{w}'^2} - 1. \tag{A25}$$

With this expression, the deformation in any point of a transversal section can be readily obtained, assuming that warping, transversal shear strain, and Poisson's effect are negligible.

A.3
Small strain tensor

For the definition of the small strain tensor, see Figure A1. Initially, a point P_0 of the undeformed configuration is considered, located at (x, v_0, w_0) in the reference frame $\{i_X, i_Y, i_Z\}$. This point then moves to a new position $(0, \eta_0, \zeta_0)$ in the undeformed frame $\{i_{\xi 0}, i_{\eta 0}, i_{\zeta 0}\}$. Therefore, the final position vector R_s is the sum of the vector in the reference frame and the vector in the undeformed frame,

$$R_s = x i_X + v_0 i_Y + w_0 i_Z + \eta_0 i_{\eta_0} + \zeta_0 i_{\zeta_0}. \tag{A26}$$

Similarly, a point P of the deformed configuration is considered with coordinates $(x+u, v+v_0, w+w_0)$ in the reference frame $\{i_X, i_Y, i_Z\}$. Then it moves to a new position $(0, \eta, \zeta)$ in the deformed frame $\{i_\xi, i_\eta, i_\zeta\}$. Finally, the position vector $R_{\tilde{s}}$ of the final location is the sum of the vector in the reference frame and the vector in the deformed frame,

$$R_{\tilde{s}} = \left(x+u\right)i_X + \bar{v}i_Y + \bar{w}i_Z + \eta i_\eta + \zeta i_\zeta . \tag{A27}$$

The total derivative of the undeformed position vector R_s with respect to the undeformed frame is given by

$$dR_s = \left(x' i_X + v_0' i_Y + w_0' i_Z\right)ds + \eta i_{\eta_0}{}' ds + \zeta i_{\zeta_0}{}' ds + i_{\eta_0} d\eta + i_{\zeta_0} d\zeta , \tag{A28}$$

where the approximations $\eta_0 \approx \eta, \zeta_0 \approx \zeta, d\eta_0 \approx d\eta, d\zeta_0 \approx d\zeta$ are considered since warping is neglected. Similarly, differentiating the deformed position vector $R_{\tilde{s}}$ with respect to the undeformed frame results in

$$dR_{\tilde{s}} = \left[\left(x'+u'\right)i_X + \bar{v}' i_Y + \bar{w}' i_Z\right]ds + \eta i_\eta{}' ds + \zeta i_\zeta{}' ds + i_\eta d\eta + i_\zeta d\zeta . \tag{A29}$$

Using eqs. (A8) and (A9), the derivatives of the unit vectors in expressions (A28) and (A29) can be simplified, resulting in

$$\begin{aligned} dR_s = &\left\{x', v_0', w_0'\right\} \cdot \left\{i_X, i_Y, i_Z\right\}^* ds + \\ &\left\{\zeta\kappa_{\eta_0} - \eta\kappa_{\zeta_0}, -\zeta\kappa_{\xi_0}, \eta\kappa_{\xi_0}\right\} \cdot \left\{i_{\xi_0}, i_{\eta_0}, i_{\zeta_0}\right\}^* ds + \\ &\left\{0, d\eta, d\zeta\right\} \cdot \left\{i_{\xi_0}, i_{\eta_0}, i_{\zeta_0}\right\}^* , \end{aligned} \tag{A30}$$

$$\begin{aligned} dR_{\tilde{s}} = &\left\{x'+u', \bar{v}', \bar{w}'\right\} \cdot \left\{i_X, i_Y, i_Z\right\}^* ds + \\ &\left\{\zeta\bar{\kappa}_\eta - \eta\bar{\kappa}_\zeta, -\zeta\bar{\kappa}_\xi, \eta\bar{\kappa}_\xi\right\} \cdot \left\{i_\xi, i_\eta, i_\zeta\right\}^* ds + \\ &\left\{0, d\eta, d\zeta\right\} \cdot \left\{i_\xi, i_\eta, i_\zeta\right\}^* . \end{aligned} \tag{A31}$$

Finally, by substituting eqs. (A1), (A2), and (A19) into eqs. (A30) and (A31), they can be recast with respect to a single frame of reference, which gives

$$\begin{aligned} dR_s = &\left(\left\{\sqrt{1-v_0'^2-w_0'^2}, v_0', w_0'\right\} ds + \left\{\zeta\kappa_{\eta_0} - \eta\kappa_{\zeta_0}, -\zeta\kappa_{\xi_0}, \eta\kappa_{\xi_0}\right\} \cdot \left[T_0\right] ds + \right. \\ &\left.\left\{0, d\eta, d\zeta\right\} \cdot \left[T_0\right]\right) \cdot \left\{i_X, i_Y, i_Z\right\}^* \end{aligned} \tag{A32}$$

$$\begin{aligned} dR_{\tilde{s}} = &\left(\left\{\sqrt{1-v_0'^2-w_0'^2} + u', \bar{v}', \bar{w}'\right\} ds + \left\{\zeta\bar{\kappa}_\eta - \eta\bar{\kappa}_\zeta, -\zeta\bar{\kappa}_\xi, \eta\bar{\kappa}_\xi\right\} \cdot \left[T\right] ds + \right. \\ &\left.\left\{0, d\eta, d\zeta\right\} \cdot \left[T\right]\right) . \left\{i_X, i_Y, i_Z\right\}^* \end{aligned} \tag{A33}$$

The expressions (A32) and (A33) are fully nonlinear, and, differently from the formulation presented in [213], they are all referred to the reference frame $\{i_X, i_Y, i_Z\}$, which facilitates the understanding of the displacements and rotations.

The Lagrange strain tensor

$$\frac{1}{2}\left(dR_{\tilde{s}} \cdot dR_{\tilde{s}} - dR_s \cdot dR_s\right) \tag{A34}$$

is considered to obtain strains with respect to the Lagrangian frame $\{i_X, i_Y, i_Z\}$. If the full nonlinear expressions (A32) and (A33) are used, the resulting strains will contain higher-order terms. By considering small initial and total displacements and rotations, the transformation matrices $[T]$ and $[T_0]$ are close to the identity. Therefore, by also neglecting higher-order terms, the eq. (A34) is approximated as

$$\frac{1}{2}\left(dR_{\tilde{s}} \cdot dR_{\tilde{s}} - dR_s \cdot dR_s\right) \approx \{ds, d\eta, d\zeta\} \cdot \varepsilon \cdot \{ds, d\eta, d\zeta\}^* \tag{A35}$$

where ε is the small strain tensor with components

$$\begin{aligned}
\varepsilon_{\xi\xi} &= \Delta_e - \eta\left(\bar{\kappa}_\zeta - \kappa_{\zeta_0}\right) + \zeta\left(\bar{\kappa}_\eta - \kappa_{\eta_0}\right), \\
\varepsilon_{\xi\eta} &= -\frac{1}{2}\zeta\left(\bar{\kappa}_\xi - \kappa_{\xi_0}\right), \\
\varepsilon_{\xi\zeta} &= \frac{1}{2}\eta\left(\bar{\kappa}_\xi - \kappa_{\xi_0}\right), \\
\varepsilon_{\eta\eta} &= \varepsilon_{\zeta\zeta} = \varepsilon_{\eta\zeta} = 0,
\end{aligned} \tag{A36}$$

and Δ_e is the principal axis normal strain, defined in eq. (A25).

A.4
Generalized Lagrangian

The undeformed frame $\{i_{\xi 0}, i_{\eta 0}, i_{\zeta 0}\}$ is assumed as the energy referential to calculate the Lagrangian. First, it is necessary to derive the kinetic and potential energies, T and U, respectively. The kinetic energy is composed of translational and rotational portions. By taking the undeformed frame $\{i_{\xi 0}, i_{\eta 0}, i_{\zeta 0}\}$ as the principal axes of inertia, the inertia tensor becomes diagonal, simplifying the formulation. Therefore, the kinetic energy is

$$T = \int_S \frac{1}{2}\left\{ m\left(\dot{u}^2 + \dot{v}^2 + \dot{w}^2\right) + J_\xi \omega_\xi{}^2 + J_\eta \omega_\eta{}^2 + J_\zeta \omega_\zeta{}^2 \right\} ds, \tag{A37}$$

where m is the linearly distributed mass, J_ξ, J_η, and J_ζ are the linearly distributed rotational inertia, S is the undeformed beam length, and the angular velocities are defined in (A16). The imperfections do not contribute to the kinetic energy since they are time independent. Lastly, the rotational inertias are defined as

$$\begin{aligned} J_\xi &= \iint_A \rho\left(\eta^2 + \zeta^2\right) d\eta d\zeta, \\ J_\eta &= \iint_A \rho \zeta^2 d\eta d\zeta, \\ J_\zeta &= \iint_A \rho \eta^2 d\eta d\zeta, \end{aligned} \tag{A38}$$

where ρ is the density, and A is the sectional area.

A linear elastic constitutive model is considered to obtain the potential energy,

$$\sigma = \mathbf{C} : \varepsilon, \tag{A39}$$

where σ is the Cauchy stress tensor, ε is the small strain tensor defined in (A36), and **C** is the fourth-order elastic constitutive tensor, which is also diagonal with respect to the undeformed principal axes of inertia, (ξ_0, η_0, ζ_0). The potential strain energy is then

$$U = \frac{1}{2}\int_S \left\{ -\lambda \Delta_e + D_\xi\left(\bar{\kappa}_\xi - \kappa_\xi\right)^2 + D_\eta\left(\bar{\kappa}_\eta - \kappa_\eta\right)^2 + D_\zeta\left(\bar{\kappa}_\zeta - \kappa_\zeta\right)^2 \right\} ds \tag{A40}$$

with the curvatures defined in (A12) and (A13). The stiffness constants are

$$\begin{aligned} D_u &= \iint_A \left(\mu_1 + 2\mu_2\right) d\eta d\zeta, \\ D_\xi &= \iint_A \mu_2\left(\eta^2 + \zeta^2\right) d\eta d\zeta, \\ D_\eta &= \iint_A \left(\mu_1 + 2\mu_2\right)\zeta^2 d\eta d\zeta, \\ D_\zeta &= \iint_A \left(\mu_1 + 2\mu_2\right)\eta^2 d\eta d\zeta, \end{aligned} \tag{A41}$$

where μ_1 and μ_2 are the first and second Lamé parameters. The term λ is introduced to simplify the formulation for cases where Δ_e is negligeable and where it is not, following [206]. Finally, the Lagrangian $\mathcal{L} = T - U$ is

$$\begin{aligned}\mathcal{L} = \frac{1}{2}\int_S &\Big\{ m\left(\dot{u}^2 + \dot{v}^2 + \dot{w}^2\right) + J_\xi\left(\dot{\phi} - \dot{\psi}\sin\bar{\theta}\right)^2 + \\ &J_\eta\left(\dot{\psi}\sin\bar{\phi}\cos\bar{\theta} + \dot{\theta}\cos\bar{\phi}\right)^2 + J_\zeta\left(\dot{\psi}\cos\bar{\phi}\cos\bar{\theta} - \dot{\theta}\sin\bar{\phi}\right)^2\Big\}\, ds - \\ &\frac{1}{2}\int_S \Big\{ D_\xi\left(\phi' - \bar{\psi}'\sin\bar{\theta} + \psi_0'\sin\theta_0\right)^2 + \\ &D_\eta\left(\bar{\psi}'\sin\bar{\phi}\cos\bar{\theta} + \bar{\theta}'\cos\bar{\phi} - \psi_0'\sin\phi_0\cos\theta_0 - \theta_0'\cos\phi_0\right)^2 + \\ &D_\zeta\left(\bar{\psi}'\cos\bar{\phi}\cos\bar{\theta} - \bar{\theta}'\sin\bar{\phi} - \psi_0'\cos\phi_0\cos\theta_0 + \theta_0'\sin\phi_0\right)^2 - \lambda\Delta_e\Big\}\, ds.\end{aligned} \tag{A42}$$

A.5
Equations of motion

Hamilton's principle establishes that the trajectory between two instants t_1 and t_2 is the path which makes stationary the functional

$$\mathcal{H} = \int_{t_1}^{t_2} \mathcal{L}\, dt\,. \tag{A43}$$

By considering nonconservative forces, the extended Hamiltonian takes the form,

$$\mathcal{H} = \int_{t_1}^{t_2} \mathcal{L} + W_{nc}\; dt. \tag{A44}$$

The work of the external nonconservative forces, considering external distributed loads Q_α and damping coefficients c_α, results in

$$\delta W_{nc} = \int_S \left\{ Q_u^{nc}\delta u + Q_v^{nc}\delta v + Q_w^{nc}\delta w + Q_\phi^{nc}\delta\phi \right\} ds, \tag{A45}$$

where

$$Q_\alpha^{nc} = Q_\alpha - c_\alpha\dot{\alpha}, \qquad \alpha = \{u, v, w, \phi\}. \tag{A46}$$

Therefore, eq. (A44) is, in variational form,

$$\delta\mathcal{H} = \int_{t_1}^{t_2} \delta\mathcal{L} + \delta W_{nc}\ dt = \int_{t_1}^{t_2}\int_S \delta l + \left\{ Q_u^{nc}\delta u + Q_v^{nc}\delta v + Q_w^{nc}\delta w + Q_\phi^{nc}\delta\phi \right\} ds dt = 0, \tag{A47}$$

where ℓ is the kernel of the Lagrangian,

$$\mathcal{L} = \int_S \ell\ ds. \tag{A48}$$

The Lagrangian (A48) is a functional of the type $\mathcal{L}(x,t,u,v,w,\phi,u',v',w',\phi',\dot{u},\dot{v},\dot{w},\dot{\phi},\dot{u}',\dot{v}',\dot{w}',\dot{\phi}',\lambda)$, with sixteen state variables plus the Lagrange multiplier. The imperfections are known a priori. Thus, they are not state variables. Four differential equations are obtained from (A47) by applying the calculus of variations,

$$G_u' = \left[A_\psi \frac{\partial\psi}{\partial u'} + A_\theta \frac{\partial\theta}{\partial u'} - \lambda \frac{u' + \sqrt{1 - v_0'^2 + w_0'^2}}{2(1+\Delta_e)} \right]' = \frac{d}{dt}\left(\frac{\partial\ell}{\partial\dot{u}}\right) - Q_u^{nc}, \tag{A49}$$

$$G_v' = \left[A_\psi \frac{\partial\psi}{\partial v'} + A_\theta \frac{\partial\theta}{\partial v'} - \lambda \frac{\bar{v}'}{2(1+\Delta_e)} \right]' = \frac{d}{dt}\left(\frac{\partial\ell}{\partial\dot{v}}\right) - Q_v^{nc}, \tag{A50}$$

$$G_w' = \left[A_\theta \frac{\partial\theta}{\partial w'} - \lambda \frac{\bar{w}'}{2(1+\Delta_e)} \right]' = \frac{d}{dt}\left(\frac{\partial\ell}{\partial\dot{w}}\right) - Q_w^{nc}, \tag{A51}$$

$$A_\phi = Q_\phi^{nc}, \tag{A52}$$

with the Lagrange multiplier, in extensional cases, given by

$$\lambda = -2D_u\Delta_e, \tag{A53}$$

and the terms A are

$$A_\alpha = \frac{\partial\ell^2}{\partial t\partial\dot{\alpha}} + \frac{\partial\ell^2}{\partial x\partial\alpha'} - \frac{\partial\ell}{\partial\alpha}, \qquad \alpha = (\psi,\theta,\phi), \tag{A54}$$

The boundary conditions of the extensional beam are

$$\left\{\frac{\partial \ell}{\partial \phi'}\delta\phi - G_u\delta u - G_v\delta v - G_w\delta w + H_u\delta u' + H_v\delta v' + H_w\delta w'\right\}\Bigg|_{s=0}^{s=L} = 0, \tag{A55}$$

and the boundary conditions of the inextensional beam are

$$\begin{aligned}&\left\{\frac{\partial \ell}{\partial \phi'}\delta\phi - G_u\delta u - G_v\delta v - G_w\delta w + \left[H_v - \frac{H_u}{(1+u')}\bar{v}'\right]\delta v' + \right.\\ &\qquad\left.\left[H_w - \frac{H_u}{(1+u')}\bar{w}'\right]\delta w'\right\}\Bigg|_{s=0}^{s=L} = 0.\end{aligned} \tag{A56}$$

The variations of the Euler angles ψ and θ with respect to the state variables are obtained by deriving eqs. (A21) and (A22). Finally, the terms H are

$$H_\beta = \frac{\partial \ell}{\partial \psi'}\frac{\partial \ell}{\partial \beta'} + \frac{\partial \ell}{\partial \theta'}\frac{\partial \ell}{\partial \beta'}, \qquad \beta = (u, v, w). \tag{A57}$$

The eqs. (A49) to (A52) form a nonlinear system without an analytical solution. Thus, an approximate solution is necessary to analyze the beam motion. The exact equations of motion for the imperfect beam are obtained by substituting eqs. (A54), the definitions of the Euler angles, eqs. (A21), (A22), (A23), and (A24), and the axial elongation, eq. (A25), into eqs. (A49), (A50), (A51), and (A52). If the axial elongation is relevant, then eq. (A53) is applied [207, 208]. If it is not, that is, if the beam can be assumed inextensional, then eq. (A53) is not applied. Instead, the axial elongation, eq. (A25), is imposed equal to zero, rendering the axial displacement as

$$u' = \sqrt{1-\bar{v}'^2 - \bar{w}'^2} - \sqrt{1 - v_0'^2 - w_0'^2}, \tag{A58}$$

and then the axial equation, (A49), is solved for the Lagrange multiplier, see [205, 206]. In both extensional and inextensional cases, the resulting equations are difficult to analyze due to the strong nonlinearities. In this thesis, following [205–208], the equations of motion are expanded in Taylor series of the state variables, $u, v, w, \phi,$ and the imperfections, $v_0, w_0, \phi_0,$ up to the third order.

Appendix B
Constant tensors resulting from the Galerkin expansion of the microarch problem

$$\mathbf{A}_{in} = \int_0^1 (1-w_0)^2 F_i F_n \, ds, \tag{B1}$$

$$\mathbf{A}_{ijn} = \int_0^1 2(1-w_0) F_i F_j F_n \, ds, \tag{B2}$$

$$\mathbf{A}_{ijkn} = \int_0^1 F_i F_j F_k F_n \, ds, \tag{B3}$$

$$\mathrm{B}_{in} = \int_0^1 (1-w_0)^2 F_i^{\mathrm{iv}} F_n \, ds, \tag{B4}$$

$$\mathrm{B}_{ijn} = \int_0^1 2(1-w_0) F_i^{\mathrm{iv}} F_j F_n \, ds, \tag{B5}$$

$$\mathrm{B}_{ijkn} = \int_0^1 F_i^{\mathrm{iv}} F_j F_k F_n \, ds, \tag{B6}$$

$$\mathbf{C}_n = u_B \int_0^1 (1-w_0)^2 w_0'' F_n \, ds, \tag{B7}$$

$$\begin{aligned} \mathbf{C}_{in} = u_B \left(\int_0^1 (1-w_0)^2 F_i'' F_n \, ds - \int_0^1 2(1-w_0) w_0'' F_i F_n \, ds \right) - \\ \int_0^1 d^2 w_0' F_i' ds \int_0^1 (1-w_0)^2 w_0'' F_n \, ds, \end{aligned} \tag{B8}$$

$$\mathbf{C}_{ijn} = -u_B\left(\int_0^1 2\left(1-w_0\right)F_i''F_jF_n\,ds - \int_0^1 w_0''F_iF_jF_n\,ds\right) -$$
$$\int_0^1 \frac{d^2}{2}F_i'F_j'ds\int_0^1\left(1-w_0\right)^2 w_0''F_n\,ds - \tag{B9}$$
$$\int_0^1 d^2w_0'F_j'ds\left(\int_0^1\left(1-w_0\right)^2 F_i''F_n\,ds - \int_0^1 2\left(1-w_0\right)w_0''F_iF_n\,ds\right),$$

$$\mathbf{C}_{ijkn} = -\int_0^1 \frac{d^2}{2}F_k'F_j'ds\left(\int_0^1\left(1-w_0\right)^2 F_i''F_n\,ds - \int_0^1 2\left(1-w_0\right)w_0''F_iF_n\,ds\right) -$$
$$\int_0^1 d^2w_0'F_k'ds\left(\int_0^1 2\left(1-w_0\right)F_i''F_jF_n\,ds - \int_0^1 w_0''F_iF_jF_n\,ds\right) + \tag{B10}$$
$$u_B\int_0^1 F_i''F_jF_kF_n\,ds,$$

$$\mathbf{C}_{ijkln} = \int_0^1 \frac{d^2}{2}F_k'F_l'ds\left(\int_0^1 2\left(1-w_0\right)F_i''F_jF_n\,ds - \int_0^1 w_0''F_iF_jF_n\,ds\right) -$$
$$\int_0^1 d^2w_0'F_l'ds\int_0^1 F_i''F_jF_kF_n\,ds, \tag{B11}$$

$$\mathbf{C}_{ijklmn} = -\int_0^1 \frac{d^2}{2}F_l'F_m'\,ds\int_0^1 F_i''F_jF_kF_n\,ds, \tag{B12}$$

$$\mathbf{D}_n = u_B\int_0^1\left(1-w_0\right)^2 w_0^{\mathrm{iv}}F_n\,ds + u_B\int_0^1\left(1-w_0\right)^2 d^2\left\{w_0'\left(F_i''w_0'\right)'\right\}'F_n\,ds, \tag{B13}$$

$$\mathbf{D}_{in} = \int_0^1 w_0'F_i'''ds\int_0^1\left(1-w_0\right)^2\left(w_0'' + 2\frac{d^2}{\beta_u}w_0^{\mathrm{iv}}\right)F_n\,ds +$$
$$u_B\left(\int_0^1 2\left(1-w_0\right)^2\left(F_i^{\mathrm{iv}} - w_0^{\mathrm{iv}}F_i\right)F_n\,ds\right) +$$
$$\int_0^1 \frac{d^2}{\beta_u}\left(1-w_0\right)^2\left(w_0'^2F_i'''\right)''F_n\,ds +$$
$$\int_0^1 d^2w_0'F_i'ds\int_0^1\left(1-w_0\right)^2 w_0^{\mathrm{iv}}F_n\,ds - \tag{B14}$$
$$\int_0^1 \frac{d^2}{\beta_u}\left(1-w_0\right)^2 w_0'F_j'''F_i'''F_n\,ds +$$
$$\int_0^1\left(1-w_0\right)^2 d^2\left(F_i''w_0''w_0' + F_i'w_0''^2 + F_i'\left(w_0'w_0''\right)'\right)'F_n\,ds,$$

$$
\begin{aligned}
\mathbf{D}_{ijn} = & \int_0^1 F_i' F_j''' ds \int_0^1 \left(1-w_0\right)^2 \left(w_0'' + 2\frac{d^2}{\beta_u} w_0^{\mathrm{iv}} \right) F_n \, ds + \\
& u_B \left(\int_0^1 \left(4\left(1-w_0\right) F_i^{\mathrm{iv}} - w_0^{\mathrm{iv}} F_i \right) F_j F_n \, ds \right) + \\
& \int_0^1 w_0' F_j''' ds \left(\int_0^1 \left(1-w_0\right)^2 \left(F_i'' + 2\frac{d^2}{\beta_u} F_i^{\mathrm{iv}} \right) F_n \, ds - \right. \\
& \left. \int_0^1 2\left(1-w_0\right) \left(w_0'' + 2\frac{d^2}{\beta_u} w_0^{\mathrm{iv}} \right) F_i F_n \, ds \right) + \\
& \int_0^1 \frac{d^2}{2} F_i' F_j' ds \int_0^1 \left(1-w_0\right)^2 w_0^{\mathrm{iv}} F_n \, ds + \\
& \int_0^1 d^2 w_0' F_i' ds \left(\int_0^1 2\left(1-w_0\right)^2 F_i^{\mathrm{iv}} F_n \, ds - \int_0^1 2\left(1-w_0\right) w_0^{\mathrm{iv}} F_j F_n \, ds \right) - \qquad \text{(B15)} \\
& \int_0^1 2d^2 \left(1-w_0\right) F_j \left(F_i' w_0''^2 + F_i' \left(w_0' w_0'' \right)' \right)' F_n \, ds + \\
& \int_0^1 \left\{ d^2 \left(1-w_0\right)^2 \left(F_i'' F_j' w_0'' + F_j' \left(F_i'' w_0' \right)' + w_0' \left(F_i'' F_j' \right)' - \right. \right. \\
& \left. \left. \frac{F_i' F_j' w_0'''}{2} \right)' F_n \right\} ds + \int_0^1 2\frac{d^2}{\beta_u} \left(1-w_0\right)^2 \left(w_0' F_j' F_i''' \right)'' F_n \, ds + \\
& \int_0^1 2\frac{d^2}{\beta_u} \left(1-w_0\right) F_j \left(w_0'^2 F_i''' \right)'' F_n \, ds - \\
& \int_0^1 2d^2 \left(1-w_0\right) F_j \left(F_i'' w_0'' w_0' + w_0' \left(F_i'' w_0' \right)' \right)' F_n \, ds,
\end{aligned}
$$

$$
\begin{aligned}
\mathbf{D}_{ijkn} = {} & \int_0^1 F_j' F_k''' ds \int_0^1 (1-w_0)^2 \left(F_i'' + 2\frac{d^2}{\beta_u} F_i^{\mathrm{iv}} \right) F_n \, ds - \\
& \int_0^1 F_j' F_k''' ds \int_0^1 2(1-w_0) \left(w_0'' + 2\frac{d^2}{\beta_u} w_0^{\mathrm{iv}} \right) F_i F_n \, ds + \\
& \int_0^1 w_0' F_k''' ds \int_0^1 \left(w_0'' + 2\frac{d^2}{\beta_u} w_0^{\mathrm{iv}} \right) F_i F_j F_n \, ds - \\
& \int_0^1 w_0' F_k''' ds \int_0^1 2(1-w_0) \left(F_i'' + 2\frac{d^2}{\beta_u} F_i^{\mathrm{iv}} \right) F_j F_n \, ds - \\
& u_B \int_0^1 2 F_i^{\mathrm{iv}} F_j F_k F_n \, ds + \\
& \int_0^1 \frac{d^2}{2} F_j' F_k' ds \left(\int_0^1 2(1-w_0) w_0^{\mathrm{iv}} F_i F_n \, ds - \int_0^1 2(1-w_0)^2 F_i^{\mathrm{iv}} F_n \, ds \right) - \\
& \int_0^1 d^2 w_0' F_k' ds \left(\int_0^1 4(1-w_0) F_i^{\mathrm{iv}} F_j F_n \, ds - \int_0^1 w_0^{\mathrm{iv}} F_i F_j F_n \, ds \right) + \\
& \int_0^1 d^2 (1-w_0) F_k \left(F_i' F_j' w_0''' \right)' F_n \, ds + \\
& \int_0^1 d^2 F_j F_k \left(F_i' w_0''^2 + F_i' \left(w_0' w_0'' \right)' \right)' F_n \, ds + \\
& \int_0^1 d^2 (1-w_0)^2 \left(F_j' \left(F_i'' F_k' \right)' \right)' F_n \, ds - \\
& \int_0^1 2d^2 (1-w_0) F_k \left(F_i'' F_j' w_0'' + F_j' \left(F_i'' w_0' \right)' + w_0' \left(F_i'' F_j' \right)' \right)' F_n \, ds + \\
& \int_0^1 d^2 F_j F_k \left(F_i'' w_0'' w_0' + w_0' \left(F_i'' w_0' \right)' \right)' F_n \, ds + \\
& \int_0^1 \frac{d^2}{\beta_u} (1-w_0)^2 \left(F_j' F_k' F_i''' \right)'' F_n \, ds + \\
& \int_0^1 4\frac{d^2}{\beta_u} (1-w_0) F_k \left(w_0' F_j' F_i''' \right)'' F_n \, ds + \\
& \int_0^1 \frac{d^2}{\beta_u} F_j F_k \left(w_0'^2 F_i''' \right)'' F_n \, ds - \\
& \int_0^1 \frac{d^2}{\beta_u} (1-w_0)^2 F_k' F_j''' F_i''' F_n \, ds + \\
& \int_0^1 2\frac{d^2}{\beta_u} (1-w_0) F_k w_0' F_j''' F_i''' F_n \, ds,
\end{aligned}
\qquad \text{(B16)}
$$

$$
\begin{aligned}
\mathbf{D}_{ijkln} = & \int_0^1 F_k' F_l''' ds \int_0^1 \left(w_0'' + 2\frac{d^2}{\beta_u} w_0^{\mathrm{iv}} \right) F_i F_j F_n \, ds - \\
& \int_0^1 F_k' F_l''' ds \int_0^1 2(1-w_0) \left(F_i'' + 2\frac{d^2}{\beta_u} F_i^{\mathrm{iv}} \right) F_j F_n \, ds + \\
& \int_0^1 w_0' F_l''' ds \int_0^1 \left(F_i'' + 2\frac{d^2}{\beta_u} F_i^{\mathrm{iv}} \right) F_j F_k F_n \, ds + \\
& \int_0^1 d^2 w_0' F_i' ds \int_0^1 2F_i^{\mathrm{iv}} F_j F_k F_n \, ds + \\
& \int_0^1 \frac{d^2}{2} F_k' F_l' ds \left(\int_0^1 w_0^{\mathrm{iv}} F_i F_j F_n \, ds - \int_0^1 4(1-w_0) F_i^{\mathrm{iv}} F_j F_n \, ds \right) - \\
& \int_0^1 F_k F_l \frac{d^2}{2} \left(F_i' F_j' w_0''' \right)' F_n \, ds - \\
& \int_0^1 2(1-w_0) F_l d^2 \left(F_j' \left(F_i'' F_k' \right)' \right)' F_n \, ds + \\
& \int_0^1 d^2 F_k F_l \left(F_i'' F_j' w_0'' + F_j' \left(F_i'' w_0' \right)' + w_0' \left(F_i'' F_j' \right)' \right)' F_n \, ds + \\
& \int_0^1 2\frac{d^2}{\beta_u} (1-w_0) F_l \left(F_j' F_k' F_i''' \right)'' F_n \, ds + \\
& \int_0^1 2\frac{d^2}{\beta_u} F_k F_l \left(w_0' F_j' F_i''' \right)'' F_n \, ds + \\
& \int_0^1 2\frac{d^2}{\beta_u} (1-w_0) F_l F_k' F_j''' F_i''' F_n \, ds - \int_0^1 \frac{d^2}{\beta_u} w_0' F_k F_l F_j''' F_i''' F_n \, ds,
\end{aligned}
\tag{B17}
$$

$$
\begin{aligned}
\mathbf{D}_{ijklmn} = & \int_0^1 \left(F_i'' + 2\frac{d^2}{\beta_u} F_i^{\mathrm{iv}} \right) F_j F_k F_n \, ds \int_0^1 F_l' F_m''' \, ds + \\
& \int_0^1 2F_i^{\mathrm{iv}} F_j F_k F_n \, ds \int_0^1 \frac{d^2}{2} F_l' F_m' \, ds + \int_0^1 d^2 F_l F_m \left(F_j' \left(F_i'' F_k' \right)' \right)' F_n \, ds + \\
& \int_0^1 \frac{d^2}{\beta_u} F_l F_m \left(F_j' F_k' F_i''' \right)'' F_n \, ds - \int_0^1 \frac{d^2}{\beta_u} F_l F_m F_k' F_j''' F_i''' F_n \, ds.
\end{aligned}
\tag{B18}
$$